2019

Damage Detection Using Destructive Testing of a Reinforced Concrete Slab

Michael Edward Daves
University of Mississippi

DAMAGE DETECTION USING DESTRUCTIVE TESTING OF A REINFORCED CONCRETE SLAB

A Thesis
presented in partial fulfillment of requirements
for the degree of Master of Science
in the Department of Civil Engineering
The University of Mississippi

by

MICHAEL EDWARD DAVES

May 2019

ABSTRACT

Visual inspection is one of the primary tools for evaluating the health of bridges as more reach or exceed their intended lifespan. Bridge deterioration must be monitored to ensure continued safety, so owners need maintenance reports to decide on corrective actions. Strategic repair can offer asset managers the benefit of saving money and time; thus, knowing where to locate and what type of repairs can be challenging when relying on visual techniques alone. A tool designed to aid bridge inspectors is the SHE^tm program, which quantitatively measures damage location and severity for any set of time data.

This paper aims to provide insight into progressively damaged concrete modal behavior as well as prove SHE^tm capabilities of damage detection. A 1200-pound test slab acted as the central span of a 1:12 scale model of an on-campus reinforced concrete bridge. Tri-axial accelerometers captured data which was analyzed of frequency responses and mode shapes for each damage condition. This work employed a genetic algorithm using 24 damage indices to compare different damage cases. An optimized plot showing damage location and severity was output for each comparison.

Two types of slab damage were induced to simulate stiffness and mass changes. The slab was first cut with a concrete saw at 8 separate instances. The 8 cuts produced 7 different damage cases, each modeling progressive stiffness change. Using the grid pattern made from the cuts, a demolition hammer then removed blocks of approximately known mass. The total of 15 extracted blocks created an additional 13 damage cases, each modeling progressive mass decrease.

The results from the genetic algorithm were similar for both stiffness and mass change cases. Damage location was accurately determined in and around the areas where cuts were made and blocks had been removed. Damage severity was most accurate for stiffness change cases. While the 24 damage indices varied, the Curvature Difference and Strain Energy Difference provided the best average results for both stiffness and mass changes. Note that these indices apply to this model only, but the procedure can be repeated for other infrastructure.

DEDICATION

This thesis is dedicated to my friends and family who have helped me during my two years of graduate work. It is especially dedicated to my grandmother, Maybelle Daves, who sadly passed away during my time in graduate school. In particular, I would like to thank my mother and father, Mike and Ashley Daves, for their support and love. I love you both.

LIST OF ABBREVIATIONS AND SYMBOLS

CDF	Curvature damage factor
CDF_KR	Damage Factor Curvature (resultant)
CDF_KS	Damage Factor Curvature (spatial)
COMAC	Coordinate modal assurance criterion
$COMAC_KR$	Coordinate Modal Assurance Criterion of Curvature (resultant)
$COMAC_KS$	Coordinate Modal Assurance Criterion of Curvature (spatial)
COMAC$\boldsymbol{\phi}$	Coordinate Modal Assurance Criterion of Mode Shape
CSV	Comma separated values
DAQ	Data acquisition
DC	Damage case
DI	Damage index
DiffF	Flexibility Difference
$Diff_KR$	Curvature Difference (resultant)
$Diff_KS$	Curvature Difference (spatial)
DiffUR	Strain Energy Difference (resultant)
DiffUS	Strain Energy Difference (spatial)
Diff$\boldsymbol{\phi}$	Mode Shape Difference
DivF	Flexibility Division
Div_KR	Curvature Division (resultant)
Div_KS	Curvature Division (spatial)

DivUR	Strain Energy Division (resultant)
DivUS	Strain Energy Division (spatial)
Div$\boldsymbol{\phi}$	Mode Shape Division
DLV	Damage location vector
EMA	Experimental modal analysis
FEA	Finite element analysis
FFT	Fast Fourier transform
FRF	Frequency response function
FV	Fitness value
FWD	Falling weight deflectometer
GA	Genetic algorithm
GPR	Ground penetrating radar
MA	Modal analysis
MS	Mode shape
NCITEC	National Center for Intermodal Transportation for Economic Competitiveness
NCPA	National Center for Physical Acoustics
NDT	Non-destructive testing
NI	National Instruments
PercF	Flexibility Percentage
PercUR	Strain Energy Percentage (resultant)
PercUS	Strain Energy Percentage (spatial)

P_{MFI}	Flexibility Probability
P_{γ}	Strain Energy Probability
SHE	Structural health evaluation
UPV	Ultrasonic pulse velocity
Z_{MFI}	Flexibility Z-score
Z_{γ}	Strain Energy Z-score

ACKNOWLEDGMENTS

I would like to give my complete appreciation and gratitude to my advisor and friend, Dr. Elizabeth Ervin. None of this would have been possible without you. I knew you would push me and you did and I am all the better for it. I would like to express my thanks for Dr. Christopher Mullen and Dr. Hakan Yasarer for their services as committee members. I would also like to thank Stephen Zeng for his help and friendship throughout this research. Finally, I would like to thank the University of Mississippi for the facilities and resources to conduct my research.

TABLE OF CONTENTS

LIST OF TABLES

LIST OF FIGURES

1. INTRODUCTION

1.1 Motivation and Literature

Ever more structures within the United States are approaching and exceeding their intended life span without retrofit or reconstruction. As structural members increase in age, they decrease in maximum yield strength due to damage ranging from abrupt impacts to gradual fatigue over time. Damage has been defined by Prasad and Shesu as any departure from original properties that may cause "undesirable stresses, displacements, or vibrations on the structure" [1]. These deviations over time can lead to infinite possibilities where structures may become unstable or unfit to continue to function as it was originally designed. The typical method used to determine whether a structure is considered unsafe is to perform a visual inspection. As America's infrastructure continues to decay, a growing need exists for the ability to quickly, effectively, and economically determine the structural capability of buildings, bridges, dams, etc.

In 1971 the Federal Highway Administration (FHWA) implemented the National Bridge Inspection Program. The program implemented a standard technique in the United States for bridge inspection which utilized a visual inspection along with other hand tools [2]. The average inspection is time-consuming and expensive, even more so for larger scale bridges. Each of the 614,387 bridges in the U.S. as of 2017 requires visual inspection by a specially trained inspector at a particular return interval [2,3]. Considering this heavy demand with aging structures, a need exists for more autonomous and less subjective monitoring of bridges. For now, no technology is proven for establishing bridge health; therefore, machine aids or testing equipment do not

entirely negate visual inspection. Innovative inspection tools can decrease inspection area, time, and cost as well as point trained inspectors to the most severe damage.

Many bridge engineers today often turn to non-destructive testing (NDT) of bridges in order to determine damage severity in hopes of evaluating remaining structural capacity. NDT techniques for concrete come in various forms. One particular method that is growing in popularity is the use of Ground Penetrating Radar (GPR). Multiple companies utilize GPR in order to gather knowledge of the state of the rebar within bridge decks. The GPR scanning unit can be used on ground or in air which is useful for bridges with areas that are difficult to access [4]. GPR is limited in its effectiveness depending on the pre-existing conditions of the bridge under inspection. Factors such as concrete permeability, density of reinforcement layout, and deck saltwater residue will all adversely affect the accuracy of the GPR results [5].

Another popular product series is based on the Ultrasonic Pulse Velocity (UPV) method. This method utilizes a wave sent through concrete and measures information about cracks as well as homogeneity of the concrete. Humboldt's HC-6390 UPV tester is one example of a packaged tool which inspectors can order and quickly employ. This specific UPV tester has a variable range of amplitude from 250-1000V and can take up to 30 samples per test [6]. A UPV test is well suited for determining the elastic moduli for concrete as well. A study by Pesic et al. measured the static and dynamic moduli of 5 reinforced concrete beams. This study found that, for calculating structural capabilities relatively new concrete, the static modulus of elasticity parameter found from cylinder compression tests should be used; however, for concrete older than 60 days, the dynamic modulus of elasticity is needed to calculate the compressive strength and static modulus. The dynamic modulus of elasticity was then determined using UPV [7]. Although UPV can determine concrete material properties, the location of cracks is limited to

local detection. One study found that the sensors for determining crack location and depth should not be more than 200mm apart in order to maintain reasonable level of accuracy [8]. Such a limited range of sensor placement means that the inspector needs to have a good idea of where a crack is before starting the test. Still, even if the locations of cracks are known and the crack depth and concrete properties are found with UPV, the state of the rebar is still not addressed.

Combining multiple NDT methods for a concrete structure may support an overall quantifiable value for damage, but it will come at costs: expense, time, training, effort, limitations, etc. A specific weakness of NDT tools and methods is that they operate typically operate at relatively high frequencies. The high frequency range is ideal for precise damage determination but limits the technology to localized areas. This difference means that only local effects can be measured instead of overall structural stability; however, the average fundamental frequencies of full scale bridges are less than 100Hz. In order to gather a more global idea of damage and state of the structure, methods utilizing lower frequencies should be used.

Modal analysis (MA) through induced vibrations is an NDT method which uses the relatively low natural frequencies of a bridge. The goal of MA is the output of deflection modes for a structure from which an engineer can understand bridge dynamic characteristics. Observed properties may lead to rough qualitative conclusions regarding damage. Other quantities can measure the change in modal parameters of a structure over time. For instance, change in the damping properties of a reinforced concrete slab can provide a measure of damage. Ahmed studied the change in natural frequencies of a reinforced concrete slab before and after inducing damage. The results showed a quantifiable measure for shift in frequencies. When this shift was compared to the damping properties, Ahmed found that damage could be measured on a case by case basis, but their method was inconsistent when considering the progressive levels of damage

[9]. MA is often used with the modelling approach since stiffness and mass are known. Modelling is accurate and economical but is performed in an ideal cyber environment which does not represent real world conditions.

An alternative and a popular approach to MA is experimental modal analysis (EMA). The benefits of utilizing EMA are that results are data oriented rather than mathematically determined. Experimental methods always introduce real factors which can be impossible or quite difficult to simulate for a computer model. EMA is effective in measuring the modal response parameters of any structure. As an example, Azam and Khan in 2015 were able to show the accuracies of EMA for a reinforced concrete slab when compared to theoretical calculations. After the experiment, they found that the percent error of his experimental versus theoretical results varied from 7%– 17%, a relatively low number for the experimental realm [10]. Note that entire conferences are dedicated to EMA and System Identification (SI); the latter is the direct determination of realistic stiffness and mass matrices.

In some cases, a researcher may choose to conduct a simulation rather than use theoretical approaches in order to reinforce their findings for an experiment. One modelling approach to EMA may be Finite Element Analysis (FEA). Banwell et al. attempted to correlate the two procedures, and their results showed that the lower the natural frequency, the lower the percent error was between the EMA and FEA results [11]. Structural engineers are normally most concerned with the lowest natural frequencies of their structures, and therefore these findings held to bolster the accuracy of EMA for critical frequency ranges. Performing experiments on in-service structures can be difficult, so modelling studies are prevalent. For this reason, improvements in experimental modal analysis (EMA) should be pursued.

The two main steps of employing EMA are data generation and data processing. Data is captured by a sensor experiencing some excitation: structural vibrations are induced into structures in many different ways. For smaller structures, a handheld hammer may input a known pulse. Medium-sized structures may be better excited by an installed actuator which creates a steady harmonic force. Larger structures serve as greater challenges due to massive inertia and high value. A three span curved steel girder bridge, 152 feet in length, was examined by Womack et al. under static and dynamic loads. In order to induce dynamic vibrations in the bridge, an eccentric mass shaker outputting 89kN (20,000lbf) of force was used. Natural frequencies were determined for the bridge within 0-20Hz, but no information is known about natural frequencies greater than 20Hz due to shaker bandwidth limits [12].

Sudden impacts or pulses are normally preferred excitation since harmonic loads are difficult to apply to large structures, such as full-scale bridges or buildings. These loads must be very carefully controlled such that they do not overload the bridge, damaging it while inspecting. Some custom-built machines exist that use a weight-dropping mechanism to send vibrations through a large structure, limited only by relative mass. For instance, the University of Arkansas possesses a machine labelled as a falling weight deflectometer (FWD). The FWD is mounted on a custom-built truck and can be positioned wherever space allows to strike the bridge undergoing analysis in order to induce a pulse [13].

Requiring no special machinery, a preferable source of vibration is operational excitation. The terms operational and ambient may be used interchangeably or may be disputed as two different excitation means; here, both are the force conditions caused during active operation. Ambient excitation utilizes various forces including test vehicles, traffic, and wind. For example, shutting down one lane for inspection still permits cars and trucks to pass over the bridge causing

structural motion. Farrar et al. found that ambient vibrations are the "only practical method" to induce vibrations in large bridges [14]. The negative aspect to this approach is that the input is uncontrolled, and thus a random noise component is introduced into the next step, data processing.

The Fast Fourier Transform (FFT) method is widely used to convert the time history sensor data into the frequency domain. With the FFT comes windowing and/or filtering of the data signals to decrease noise, a modal analyzer's greatest foe. Experimental noise is one reason computer generated mode shapes and operational deflection shapes can look vastly different; the other factor is decoupled eigenvalue analysis versus coupled measured signals.

Resonant frequencies and their associated deflections can be studied in order to specifically understand the structure undergoing analysis. While useful, most inspection agencies are mainly concerned with the status of a structure after a return period or a destructive event. Therefore, a data set can be gathered after initial construction and then again after a structural change. In order to compare both sets of data, mode shape comparisons prove more stable than time histories or resonant peaks, and researchers apply many different methods that are introduced in Table 3-1. This work is a part of a series out of the Multi Function Dynamics Lab at the University of Mississippi that introduces new quantitative metrics using the differences among matching mode shapes to detect damage. The newest version is employed herein; this includes three-dimensional analysis and artificially intelligent output.

A damage index (DI) is a relatively simple equation meant to extract damage from frequency information, such as mode shape changes. One specific DI is the damage location vector (DLV), the simplest calculation possible. This indicator is the direct difference between the FFTs for two different damage cases. The simplicity of the calculation is what makes DLV

so attractive. It can compute multiple damage cases while relying strictly on the data taken from the structure [15]. DLV does have its limits; for instance, the data must have a significant amount of change in the FRF plots for DLV to be as effective as it has proven to be. A study by Gao et al. suggests that DLV yields more accurate results than direct comparison of modal properties when natural frequencies shift by relatively small amounts (around 0.01Hz) after a stiffness reduction [16]. Albeit simple in nature and quick in processing, DLV requires too heavily on ideally captured data. Gathering sufficient amounts of quality data from real world bridges outside of a laboratory setting can prove to be difficult politically and/or physically.

Another measure for damage is the shift in natural frequencies on the FRF plots between damage cases. As the equations for natural frequency states, changes in stiffness are directly related to the natural frequencies of a structure. Benedetti et al. and Faizan showed this relation by experimentally damaging a reinforced concrete beam by inducing cracks. Comparing the undamaged state data with the damaged state data, the natural frequencies found in the beam decreased in value on the frequency spectrum [17,18]. Nozarian and Esfandiari took a similar approach in analyzing frequency shift; they computationally determined the decrease in natural frequency with a decrease in stiffness in trusses [19]. While stiffness is directly related to natural frequency, mass is indirectly related. The natural frequency equation states that as mass decreases, the natural frequencies of the structure will increase in value. Though global damage is useful to determine for any structure, shifts in natural frequencies do not address damage location.

This work focuses on destructive testing, so one goal was to simulate real world damage scenarios as accurately as possible in a laboratory setting. Progressive damage was also induced by multiple cases in which the structural integrity of a test bridge would be increasingly

impacted in a negative way. Simulated cracking was studied with the assistance of a concrete saw. Numerous causes can generate cracking in concrete slabs. For instance, a heavy impact by a hammer can cause cracks in unpredicted locations as well as unseen microscopic cracks. Cracks can and often also form during the curing process of concrete. Newly constructed bridges have been known to have early cracks, some due to improper procedure, but others are a mystery [20]. A quick and economical method to verify crack effects on the bridge before opening the bridge up for public use would be beneficial.

Another type of common real world progressive damage is physical mass loss. One example of this would be after an extreme event, possibly a collision, where relatively large pieces of concrete had completely separated from the main structure; the severity of the damage is visually inspected, but the overall stability effects are unknown. Aging also causes mass loss in the form of spalling, where small pieces separate over time due to various reasons such as delamination of rebar from the concrete. Delamination underneath concrete decks often leads to areas of concrete falling form the bridge. Not only does the loss of concrete weaken the bridge, it exposes the rebar to the environment. Xing found that asymmetrical delamination had a greater effect on the structural capabilities of a reinforced concrete slab [21]. Simulated mass loss was studied herein with the assistance of the crack checkerboard and a demolition hammer. Other types of damage which can be common for some bridges are corrosion from salt, fires, and general weathering due to freeze-thaw action, but this analysis does not cover these sets of damage.

1.2 Thesis

This paper will discuss the EMA of a reinforced concrete slab under progressive damage conditions and analyze damage detection and severity. The damage conditions chosen for the

analysis were stiffness changes through cracks and mass changes through mass loss. A sledgehammer with a force transducing tip was used to induce vibrations. In order to gather the data from the vibration response of the slab, 3 tri-axial accelerometers were utilized. The time history data was then input into the SHE^{TM} program for analysis. SHE^{TM} is a modal analysis program which processes time history data in order to detect damage location and severity. Peaks in the FRF plots from the data pointed toward the natural frequencies of the slab for each damage condition. The changes in mode shapes that occur at the natural frequencies are one factor which can show structural changes in the slab. By experimentally comparing the FRF plots from one case to another, the shift in natural frequency location should reliably show damage within the slab. For this experiment, the data would come from a concrete slab; however, since SHE^{TM} only needs time history data, the equipment could be set-up for various materials and structural configurations.

In this work, damage detection and damage severity were the two main results. The data from the SHE^{TM} program provided changes in modal parameters of the slab. The GA combined the results from SHE^{TM} into a total of 24 damage indices in order to provide "best fit" plots displaying relative damage values and locations. By combining the uses of the GA and SHE^{TM} program, an overall quantitative result for level of damage can be found for the slab in this experiment.

The purpose of this research study is to develop a program which will accurately detect damage within any structure. Creating a user interface which less technically trained users can use on full scale bridges will decrease the amount of training needed in order to utilize the equipment. In doing so, bridges can be accurately assessed for damaged and a more quantitative diagnosis of health can be assigned. Accurate damage detection will reveal areas to be repaired

and avoid more general closures as well as determine critically ill bridges that may be in danger of collapse.

1.3 Organization

This paper will document the destructive testing of a concrete slab. The original bridge was disassembled, moved, and reassembled in a separate facility; Chapter 2 compares the 2014 as-built bridge and the 2019 relocated bridge. Chapter 3 examines dynamic response to analyze changes in stiffness via cutting. In Chapter 4, damage due to mass loss is evaluated by the software for location and severity. Discussion includes result sensitivity as compared to sensor loss caused by block removal. Chapter 5 presents damage detection conclusions from the stiffness/mass portions and then states their significance to bridge inspection. The accuracy of SHE^{TM} with GA is analyzed in order to determine the best damage indices for this slab.

2. PROCEDURE

2.1 Introduction

The destructive damage goal was to simulate real world scenarios in which overall structural integrity would be impacted. A top priority is certainly cracking, whether from new condition or from freeze-thaw aging. This chapter will address the effects of artificial cracking on a test slab. Another type of relatively common damage is physical mass loss, such as spalling or impact; these scenarios are discussed later in Chapter 4.

2.2 Bridge Background

The small-scale bridge was originally designed and built by the Multi Function Dynamics Lab along with a team of students, faculty, and staff. Funding for bridge construction was provided by a grant awarded to Dr. Elizabeth Ervin from the National Center for Intermodal Transportation for Economic Competitiveness (NCITEC). It was modelled after an existing on-campus bridge at a 1:12 scale apart from a 6 inch slab thickness. Wooden forms were hand built and a total of eight separate pieces of concrete were poured. Components included two internal "T-shaped" piers, two external piers, and four slabs. Note that the concrete from the pour was subjected to a slump test which resulted in approximately 9.25 inches. Two compression tests were also performed using tests cylinders and yielded an average compressive strength of around 7,100 psi. The bridge was then assembled, and 57 self-leveling epoxy pads were poured. Fifty-

five of these pads were poured on the center test slab. A single pad was poured in the center of each side slab. The pads served as connection points to the bridge for a single tri-axial accelerometer to be attached during testing. Figure 2-1 shows the finished product installed in the National Center for Physical Acoustics (NCPA) [22].

Figure 2-1 Experimental Set-up (2014 Study, Located in the NCPA)

2.3 2014 Test Series

Prior experiments focused on nondestructive changes in the global boundary conditions of the central slab. Eight cases were presented with various objectives: one of which is shown in the yellow circle in Figure 2-1. He achieved this result by applying a sheet of changeable strips that included rubber pads of varying thicknesses and hardness. The first case examined was considered the as-built baseline which was also considered the control case for the experimental series. Being the control, the baseline consisted of the bridge exactly how it was first assembled with no additions or changes made to any of its supports.

During each test, in order to excite the center slab, a demolition hammer with an attached force transducer on the tip was used to tap the angled wooden block on the edge of the slab. The

word “tap” is used here because the force it took to excite the bridge was relatively small compared to the force that a sledgehammer might normally be used to create which would involve a full swing. A single accelerometer recorded the output from the shock load. This hammer-accelerometer duo created a single input-single output system for recording signal via a single module in a National Instruments (NI) Data Acquisition (DAQ) chassis. The signal was then fed into a laptop running LabView® software, and this stored captured data as comma separated (.csv) files compatible with SHE™.

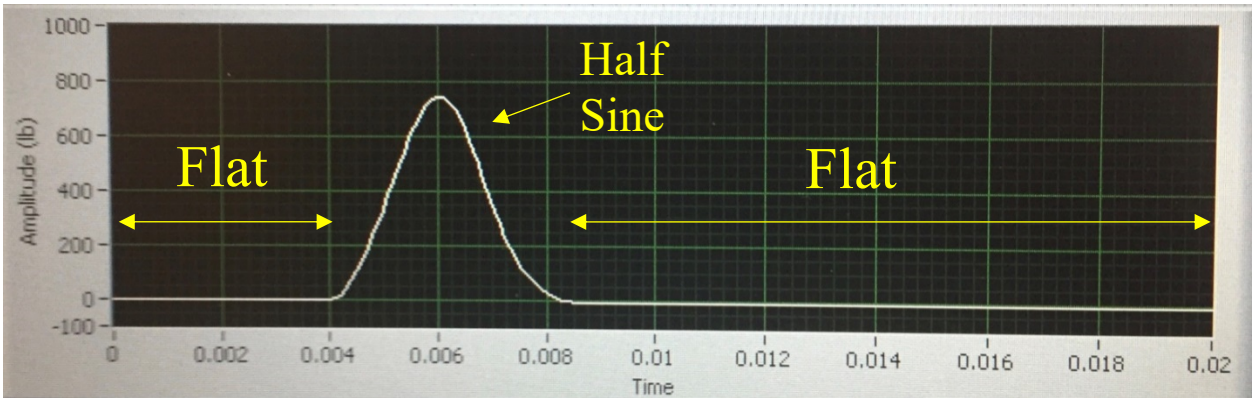

Figure 2-2 Acceptable Hammer Hit

Tap testing for each case began with applying super glue to the top of an epoxy pad and attaching the accelerometer to it. Once an adequate amount of time had passed for the superglue to dry, the bridge was ready for a pulse from the hammer. An adequate tap from the hammer was vital to prevent noise. The time history plot from each hit is examined before acceptance. An example of an acceptable hit is seen in Figure 2-2. The main criterion is a relatively smooth line before and after the curve. The most common example of a rejected hit is a double or even triple hit. Repeated hits can be difficult to physically feel sometimes when contacting with the structure, but they will show in the hammer’s time history plot. For the 2014 studies, the ideal

range for applied force was 600 to 800 pounds and was recorded over a full second. Hits above 800 pounds may contain too much noise or perhaps even exceed the limits of the accelerometer. Hits below 600 pounds may not provide enough force in order to induce an appropriate response from the slab; however, low hits are rare with the 12-pound sledgehammer. After a successful tap and having saved the outputs, the accelerometer was removed from the pad, superglue was applied to the next pad, and the process began again. All 57 pads were tested sequentially.

After Worley's test series was completed, the project funding also ended. The bridge was then moved piece by piece to a new location on the campus. The bridge's piers and external slabs were leveled, followed by the placement of the central slab. Since the bridge had been physically moved to a new location, the boundary conditions were anticipated to be different, yet still relatively similar. This work will first examine a new baseline control case, and a comparison to the prior study which serves to introduce experimental modal analysis (EMA).

2.4 2019 Test Series

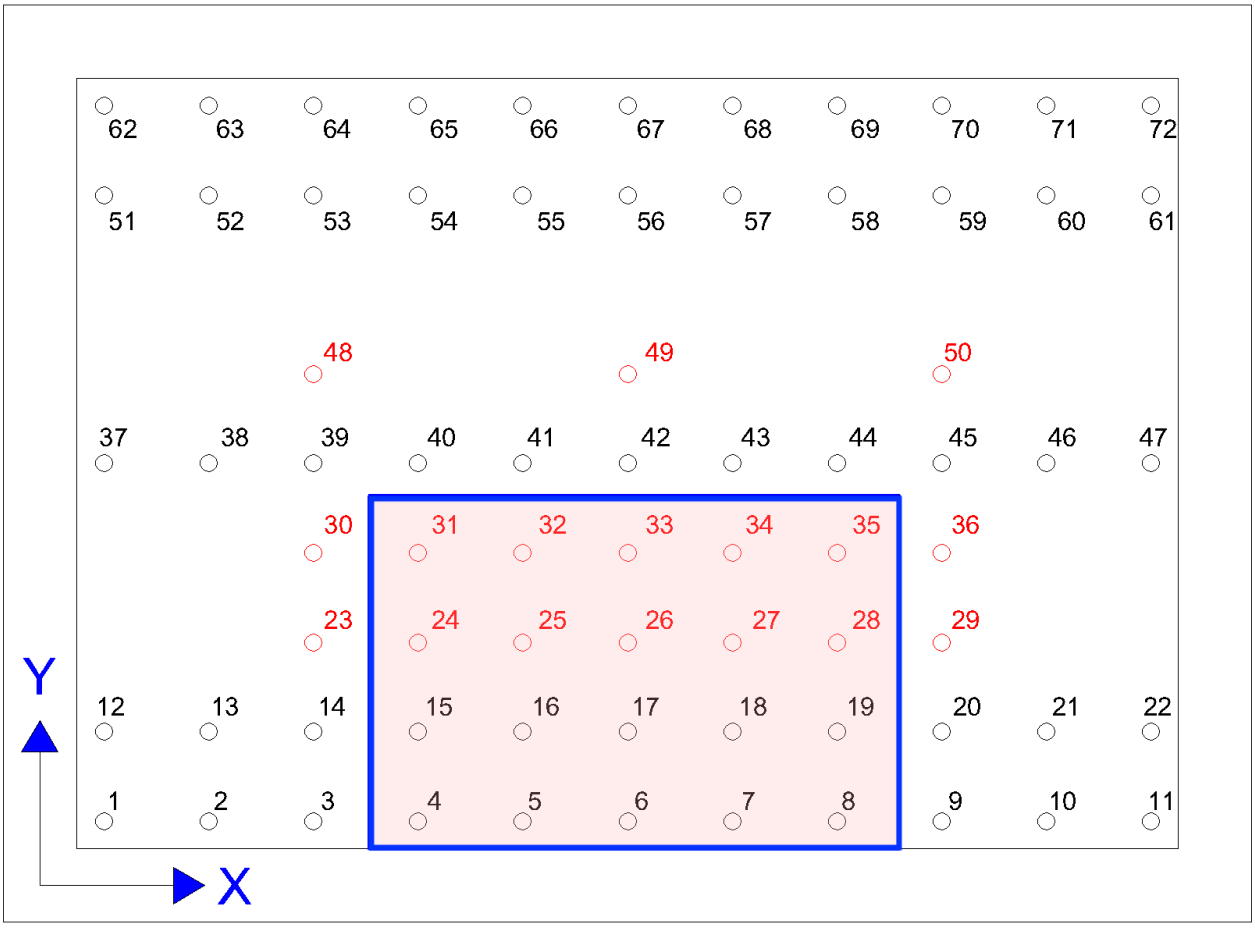

Figure 2-3 Added Node Points and Planned Damage Area (2019 Study)
Blue = damage area
Red = new node points

In contrast to Worley's testing, this experimental series is destructive and progressive damage causes sensor loss. If the 57 original sensor points are kept, an insufficient number of pads will remain left at the end of testing to accurately determine damage. Therefore, an

additional 17 self levelling epoxy pads were poured in and around the area planned for damage bringing the total amount of epoxy pads to 74.

Figure 2-3 presents a layout of the new and existing sensor points. The newly added points are denoted in red while the planned damage area is outlined in blue.

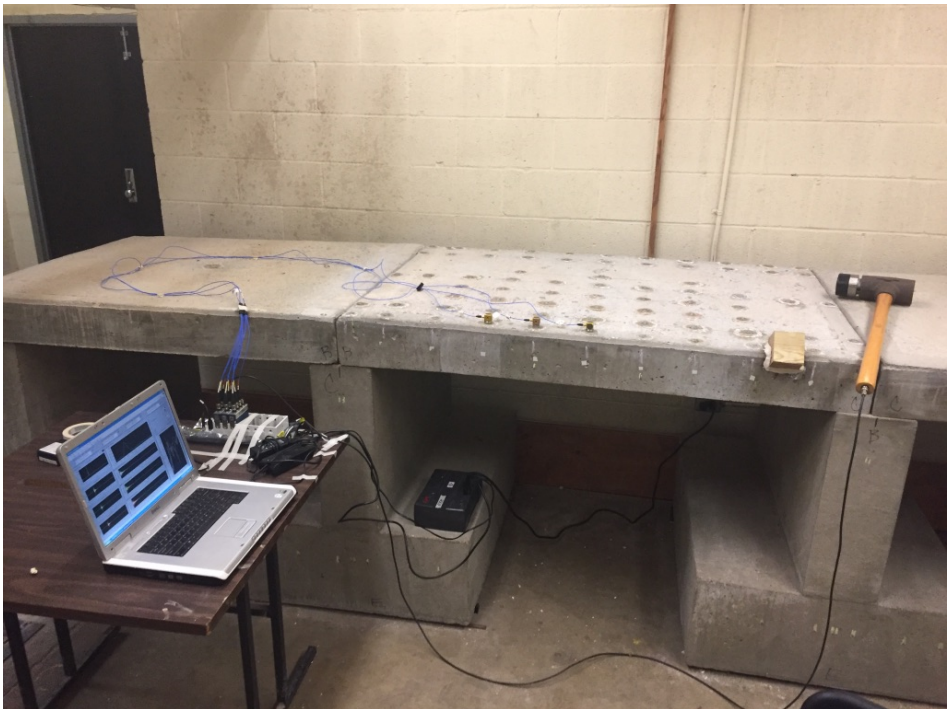

Figure 2-4 Experimental Set-up (2019 Study, located in Anderson Hall)

This experiment employed three accelerometers to capture data for 21 test cases. Each of the accelerometers was made by PCB Piezotronics (Model Number: 356B18). Accelerometers 1, 2, and 3 fed into National Instruments Modules (Model Number: NI 9234) 1, 2, and 3, respectively, while each Module had been plugged into the DAQ chassis (Model Number: cDAQ-9172). The same sledgehammer with a different force transducer tip sensitive to 1mV/lbf (PCB Piezotronics, Model Number: 086D50) was plugged into the first module along with

Sensor 1. This configuration created a single input-multiple output system. All ten data channels were fed into a laptop running NI LabVIEW. A full equipment set layout is seen in Figure 2-4.

Worley's superglue method was a very time-consuming method, and the total cumulative test time was extensive having one sensor and eight test cases. For the current experiment, 21 test cases with 17 more nodes would take an unnecessary amount of time despite having 3 sensors. The previous method for sensor attachment was therefore inadequate. In order to decrease test time, steel washers were glued to 74 epoxy pads. Factory magnetic attachments were screwed into the accelerometers to quickly secure and remove each sensor.

The first case tested was the baseline, or control. This also led to an ideal force range used for the hammer-accelerometer duo of 400 to 600 pounds, 200 pounds less than Worley's range. The reason behind this change is the sensitivity of the accelerometers. The prior test's accelerometer was calibrated for 100.7 mV/g while the current sensors were calibrated to an average of 1016 mV/g. Thus, the sensors in this experiment are a magnitude higher in sensitivity than the single accelerometer used in the 2014 test. The sensitivity in the time domain also affects the ideal time history recording length. Originally, a full second was plotted so as to not miss any frequencies that may show after the impact form the hammer; however, no significant peaks were noted in the second half the time domain. The recorded length was shortened in order to reduce unnecessary noise at the end of the recorded signal. Also, in order to best record the local damage results as well as keep the file size for each test a manageable size, the sample rate was set to 4,400 samples per second.

One last change was made to the prior testing process to minimize cord noise. A "single file" configuration of the accelerometers meant that the cords linking the sensors to the DAQ chassis would likely come in contact with each other. Whenever cords touch, they are more

likely to move, so the possibility for added noise is increased. Preventing cord motion was especially important since they were resting on the slabs which were also undergoing vibrations from the hammer. In order to counteract the noise, the start point of Sensor 1 became node point 1, Sensor 2 became node point 12, and Sensor 3 became node point 37. From this configuration, the sensors were shifted to the right. For instance, Sensor 1 was moved to Node 2, Sensor 2 to Node 13, and Sensor 3 to Node 38. Note that for each case, Sensor 1 was rotated 90 degrees clockwise when was placed on Node 10. This rotation was required because the wooden hit block would interfere with the sensor's cable. Therefore, the accelerometer was rotated, and the data was adjusted within the .csv file. In short, the X direction data was switched to the negative Y direction and *vice versa*.

2.5 SHE™ Usage

The main two goals of the SHE™ program are to produce mode shapes and then use those modes shapes as comparisons for damage detection. The preferable inputs are tri-axial signals with respect to time. As tests were performed for each damage case, the data gathered from the accelerometers was stored as .csv files. Each sensor gathered results from the X, Y, Z, and time domains. As shown in Figure 2-4, the "X" direction is the longitudinal direction of the bridge, the "Y" direction is transverse sway, and the "Z" direction is vertical acting upwards (parallel with the direction of gravity).

When input into SHE™, this data was first used to create a time history plot. Figure 2-5 is an example of the time history plot from the baseline test case. While the time domain was not the main focus, it serves as an initial check if the data was reliable. The accelerometers serves as an "output-only" scheme, meaning that operational or ambient excitation is considered. All

responses should show exponential decay with varying magnitudes. Any other errors can be identified at this step before continuing on to frequency domain.

The next step is performing a Fast Fourier Transform (FFT) on the temporal data. Three plots are produced for each full SHE^{TM} analysis. Figure 2-6 presents the first plot of direct FFT output. Since the hammer recording is not used, the terms FFT and frequency response function (FRF) are interchangeable. The second FRF plot consists of the same data but now normalized based upon the highest amplitude to reveal for very low amplitudes. Finally, the third plot alters the data by smoothing it with a factor determined by the user.

These figures contain four subplots. The first three in Figure 2-6 show the FRFs of the data in the X, Y, and Z domains. Each subplot contains 74 FFTs, which correlated to the accelerometer data from all 74 node points on the bridge. Experimental modal analysis considers every peak important in these three plots, but this is far too excessive for practical use. Thus, the fourth plot takes the cumulative sum of all three directions; later, a resultant concept is also used with the goal of presenting just one trace for overall peak-picking.

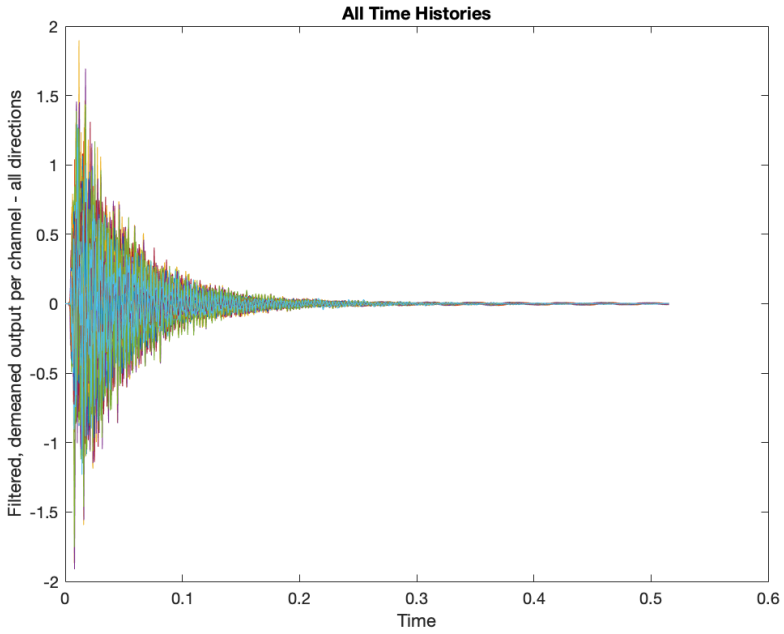

Figure 2-5 Baseline Time Histories

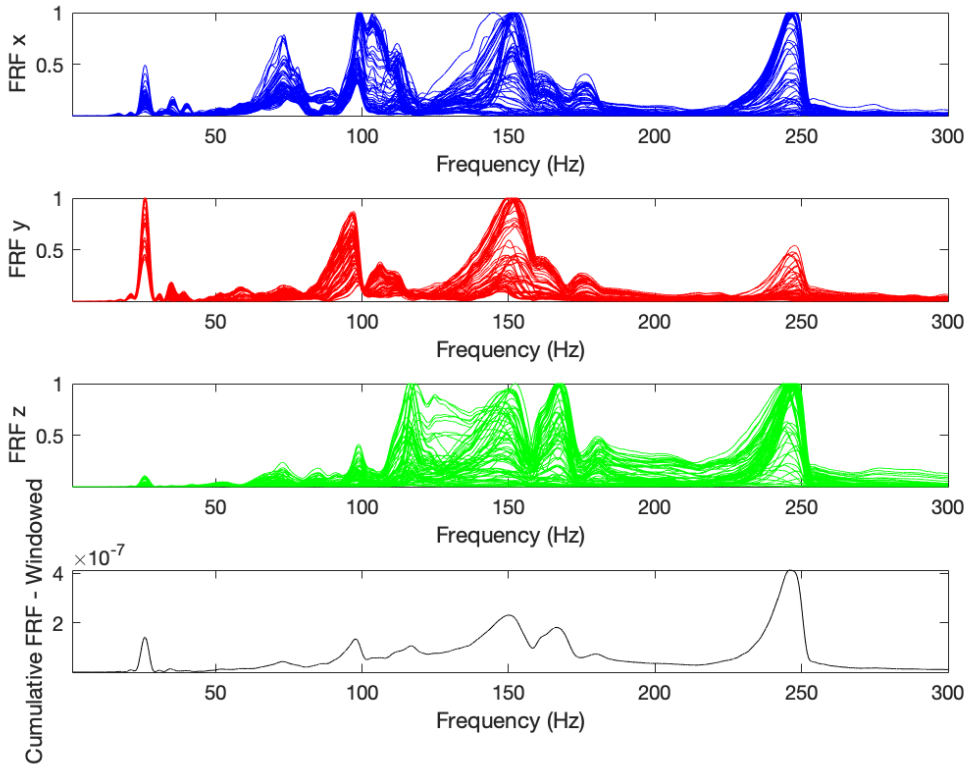

Figure 2-6 Normalized Frequency Response Functions (Baseline)

At this point, the cumulative FRF is examined for any local peaks. The plots from the other directions can aid the user in determining stable versus unstable peaks. Ultimately, it will be the user who confirms that a peak is a resonant frequency, so much guidance is provided. Once cumulative magnitude peaks have been determined, the program asks for ranges in order to select local maximums. These local maxima mark the frequencies for which to plotted slab behavior if excited precisely at that respective frequency, i.e. potential mode shapes, but these results need to be cleansed. Not all local maximums will be true mode shapes, and the false positives can be discarded so that only the real mode shapes of the structure under analysis are left.

Additionally, the cumulative graph can prove to be misleading for frequency identification. While the cumulative plot makes it easy to visually spot peaks, sometimes a heavy amplitude in one direction can dwarf in size a smaller but important amplitude in another. That is, should there be a high peak in the Y direction at 50Hz, for example, and a lesser peak in the Z direction at 47Hz, the cumulative plot might not show much of a peak at 47Hz but rather 49.5Hz. For this reason, every mode shape of the structure may not lie exactly on every peak but sometimes a little to the right or left of the peak. Therefore, it is important to always check the X, Y, and Z directions when looking at the plotted mode shapes to verify their behavior based upon the amplitude of the plots in each direction.

After the mode shapes have been selected, an appropriate amplification factor is applied in order to better visually analyze their actual shape. Shape visualization will be important for late mode matching in SHE^{TM} as well as noting trends or unusual behaviors. Mode shape magnitudes vary widely depending on the frequency range: note how relatively small the amplitudes of low frequency FRFs are in Figure 2-6. Too low of an amplification factor makes

it difficult to determine any definable modal characteristics. Too high of an amplification factor causes the mode shape to be so deformed that it may sometimes be impossible to describe. Thus, a single amplification factor is unsuitable to be applied to all mode shapes at once (a SHE^{TM} improvement is proposed here).

Modal characteristics may include bending, axial stretching/compressing, and torsional rotation. In order to fix the amplification problem, the SHE^{TM} program must be run multiple times and groups of modes with similar magnitudes plotted. The user then analyzes each potential mode's behavior for uniqueness and characteristic behavior. Identification of three-dimensional coupled experimental modes can be challenging, and the baseline slab results are presented herein. Once all mode shapes have been determined, the last step is storing all modal information into one .mat file with an "undamaged" and "damaged" prefix. The data within the undamaged and damaged files is the same apart from the names of the variables within the .mat file itself. The particular named variables will be important later when cases will be compared to each other. Fortunately, an amplification factor is not needed to complete this step.

Table 2-1 2019 Baseline Mode Shape Descriptions

Experimental Freq. (Hz)	Characteristic Mode Description
1.985	Translation in the Y (side-sway)
3.599	Compression in the Y
6.901	Translation in the Y (side-sway)
10.335	Tension in the Y
14.046	Translation in the Y (side-sway), Torsion about the Z
17.285	Compression in the Y
25.846	Translation in the Y (side-sway), Torsion about the X
30.680	Tension in the Y
34.554	Tension in Y, Torsion about the Z
40.120	Compression in Y (left side), Tension in Y (right side)
45.068	Compression in Y (left side), Tension in Y (right side)
52.018	Torsion about the Z
58.724	Torsion about the Z
72.852	Compression in Y
86.621	Tension in Y
97.738	Compression in Y
103.825	Tension in the Y
106.120	Compression in Y, bend in negative Z
116.715	Compression in Y (left side), Tension in Y (right side), bend in positive Z
125.146	Torsion about the Z, bend in positive Z
150.000	Torsion about the Z
166.325	Tension in the Y, Torsion about the X
179.753	Torsion about the Z, bend in positive Z
246.077	High order sine shape in X and Y
275.146	Compression in Y (left side), Tension in Y (right side), Torsion about Z

The baseline condition for the concrete bridge model contained 23 distinct mode shapes, each with their own characteristic deflected shape. Side-sway modes were towards the lower end of the spectrum (less than 50Hz) while bending modes emerged at the higher end (greater than 100Hz). The torsional modes appeared scattered throughout the frequency domain. The upper

limit of 300Hz was arbitrary, but massive structures are very rarely globally damaged by high frequency excitation.

For the low range mode shapes, the first identified mode shape denoted was on the edge of the data acquisition limits at 1.985Hz. At such a low level, a professional technician is recommended in order avoid false positives or DC level interference. As a rule of thumb, anything below 1Hz requires special attention. Fortunately, the lower a mode shape is in frequency, the less difference it takes to find two distinct mode shapes. In other words, a mode shape at 2Hz could be quite different and unique from a mode shape at 3Hz; however, a mode shape at 174Hz, for example, is most likely very similar to a mode shape at 175Hz. For this reason, the mode shape at 1.985Hz is relatively close to 1Hz but is still far enough away that no false positives were noted. It is important to note that this 1.985Hz mode shape was not seen in any other damage cases except for damage case 19 and 20, which both involve relatively heavy mass loss.

The next mode shape at 3.599Hz was the fundamental mode shape for most damage cases. Its primary shape was a compression in the Y-axis. The right side of the slab did compress more than the left denoting a higher order level of compression. Upon running damage detection, this particular mode shape did not match well to others discussed further in Chapters 3 and 4.

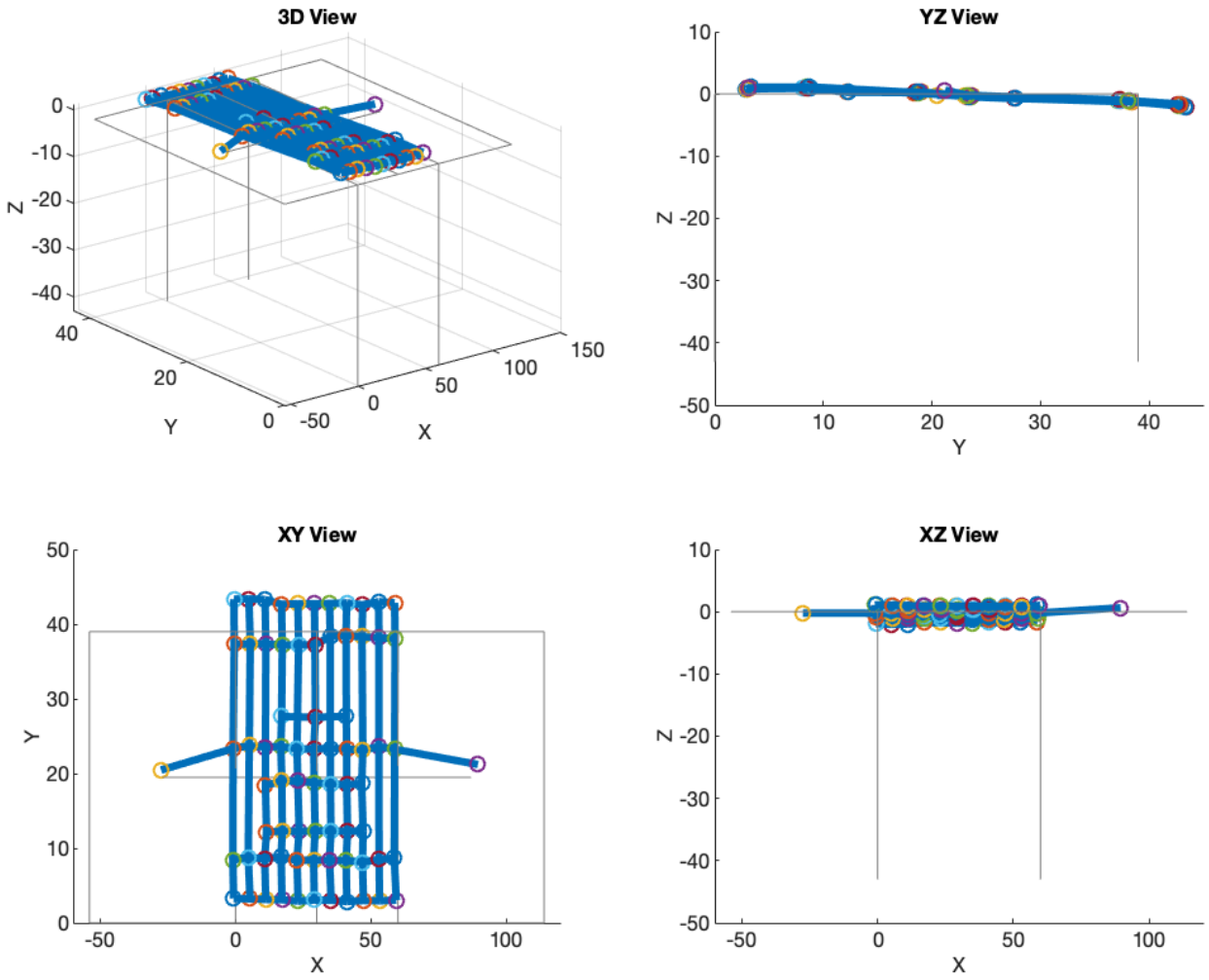

Figure 2-7 Baseline Mode Shape at 25.846Hz (2019 Study)

Illustrated in Figure 2-7, the most significant mode shape was found at 25.846Hz. Relatively simple to describe, modal behavior consisted of a sway in the positive Y axis and a clockwise rotation about the positive X axis. The two side slabs also showed a sway in the positive Y axis but not to the same magnitude of the main slab. This particular mode shape was seen in all the frequency spectrum plots for all damage cases; this mode shape kept its characteristics and maintained a peak within 25 to 27Hz. This particular mode shape is a good visual measurement to show the change in the behavior of the slab as the damage progressed throughout the experiment.

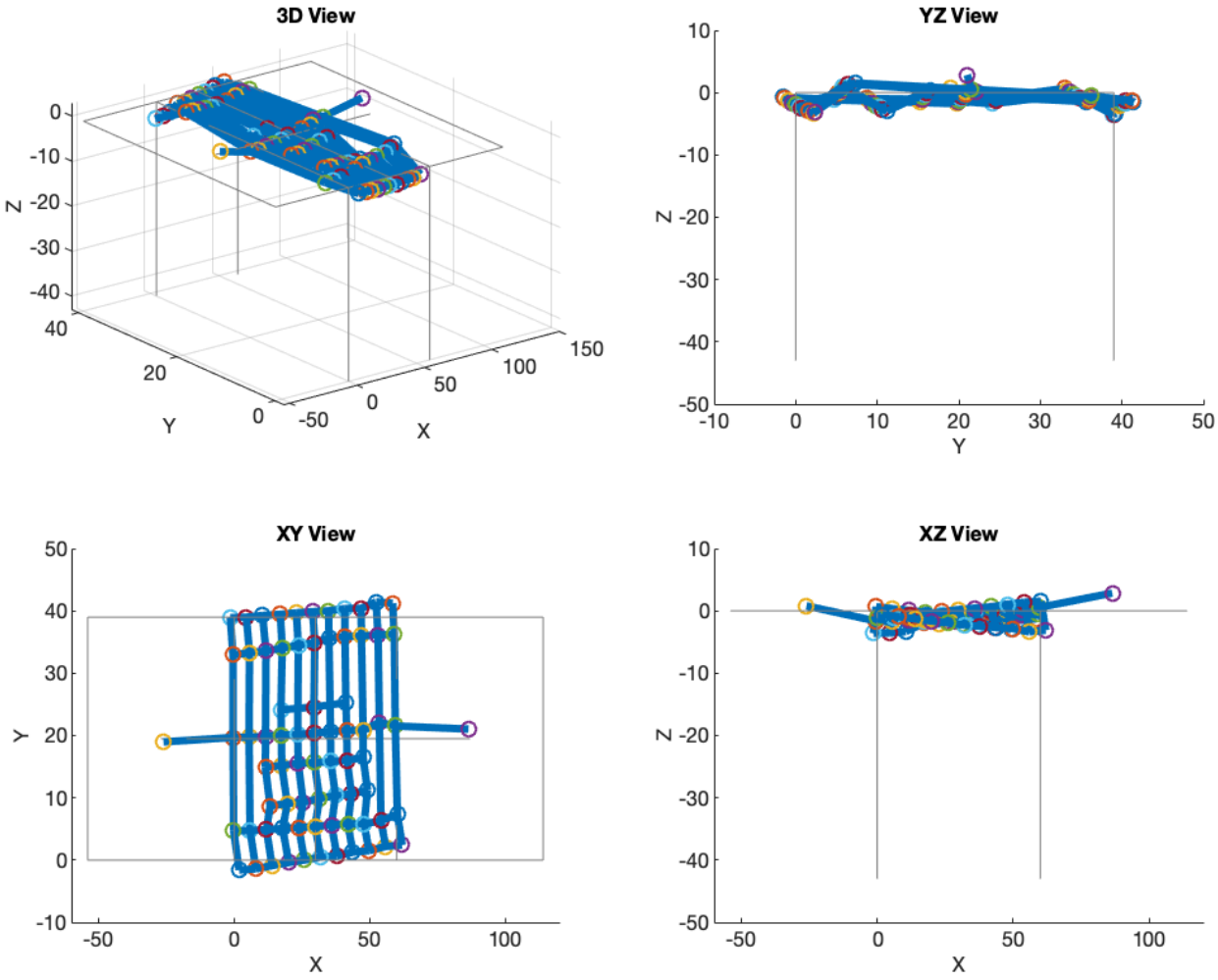

Figure 2-8 Baseline Mode Shape at 52.018Hz (2019 Study)

Progressing down Table 2-1 from 25Hz, most peaks involve tensions and compressions in the side-sway direction. Purely torsional modes are not seen until around 52Hz; this plot is displayed in Figure 2-8. The mode shape does possess other movements outside of the torsion about the Z-axis but they are not definable behaviors.

The second and third highest magnitude peaks on Figure 2-6 were initially seen as distinct and valuable mode shapes. Later study shows that the modes at 150.000Hz and 166.325Hz are unstable. Identification reliability is introduced by smaller peaks near these

relatively large peaks that were showing similar shapes at the peak shapes. Data acquisition jargon of “mirror” and “ringdown” are often applied to these cases, and the result is a repeated mode shape for multiple frequencies. In these cases, true mode shapes are hard to find; one suggestion is to examine at very specific frequencies along one side of the peak.

Another option is a more in-depth look into the X, Y, and Z directions; when examining the peaks at 150Hz and 166.325Hz. Both specific frequencies and X, Y, and Z were examined but neither method resulted in a positive showing one or two distinct mode shapes. The same problem was encountered by Worley during his initial base line tests as well. The frequency range 150Hz to 170Hz is therefore considered to be unreliable when matching mode shapes.

2.6 2014 vs 2019 Baseline Mode Shapes

Matching modes takes an experienced eye to choose a true match or not. In fact, the more experience the better. The unique and characteristic motions of each mode shape should be compared at a global rather than local level. A factor to always keep in mind is that matched modes should be as similar as possible except in magnitude.

The current baseline will now be compared to the published baseline, and the modes are very likely to change for several reasons. Worley showed that boundary conditions play a vital role in mode shapes for this concrete slab. During the campus move, the bridge’s global boundary conditions might have changed, but the concrete-to-concrete connections at the target slab’s ends certainly changed. Internal slab damage might have also occurred: no external damage was observed. The new baseline test case possessed new modal characteristics and behavior when compared to the prior baseline, but despite the differences in the two baselines, similarities were still expected. This comparison serves as practice for Chapters 3 and 4, in which mode shapes of the damage cases will be matched.

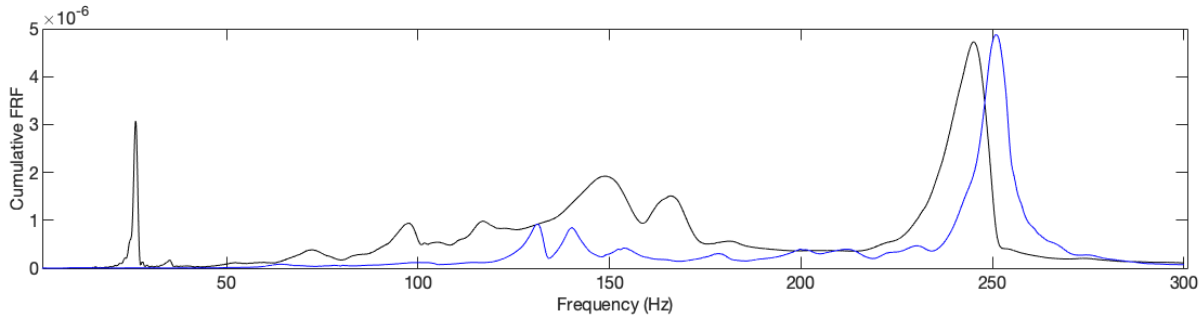

Figure 2-9 Baseline Comparison
Linear (0-300Hz) (2014 = Blue; 2019 = Black)

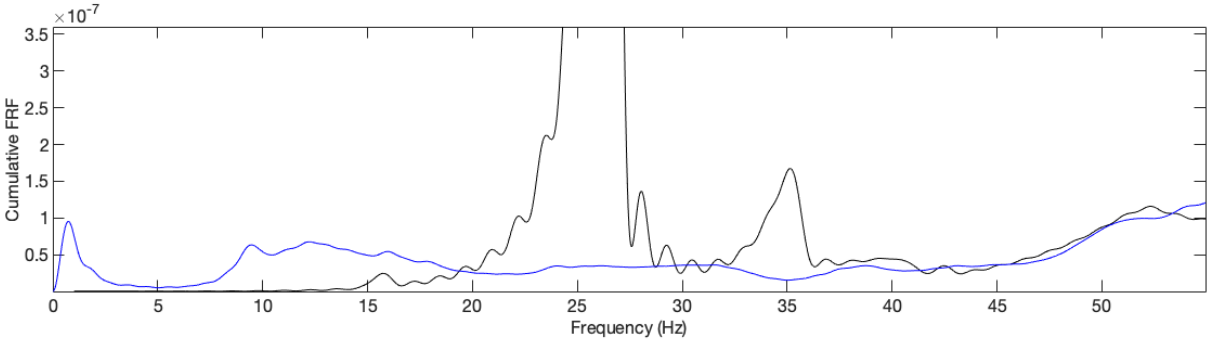

Figure 2-10 Baseline Comparison (0-60Hz)
Linear (0-50Hz) (2014 = Blue; 2019 = Black)

Table 2-2 Baseline MS Descriptions (2014 Study)

Experimental Freq. (Hz)	Characteristic Mode Description
12.227	Translation in the y-direction (sidesway) – rigid body motion
64.170	Torsion about the x-axis and translation in the y-direction
78.232	Torsion about the x-axis and torsion about the z-axis
98.916	Strong Torsion of the center slab around the z-axis and bending in the positive z-direction
114.629	Torsion about the z-axis but fixed in the bottom left corner - bending in the z-direction
153.828	First order bending in the negative z-direction – minor slab torsion about the z-axis
178.389	Bending in the positive z-direction, torsion about the y-axis and x-axis, and translation in the negative x-direction
199.785	Bending in the positive z-direction with translation in the positive y-direction
224.414	Bending in the positive z-direction until midspan where the bending is ~0 and then bending in the negative z-direction also torsion about the x-axis (negative)

Figure 2-9 presents the frequency domain comparison between the 2014 data set and the 2019 data set. A key area is the frequency range up to 50Hz, designated as the “low” frequency region. As previously stated, the lower frequency range contained more sway modes than the higher frequency range. Mass dominates for concrete since it is a very dense material and normally used in larger quantities. The sway movement in certain modes will then have a heightened effect on the slab when compared to other modal behaviors like bending. The higher mass content of the concrete means a greater inertia when it begins to move under vibrations. The modal acceleration of the concrete is what makes the lower frequency range especially important when studying the structural integrity of the bridge.

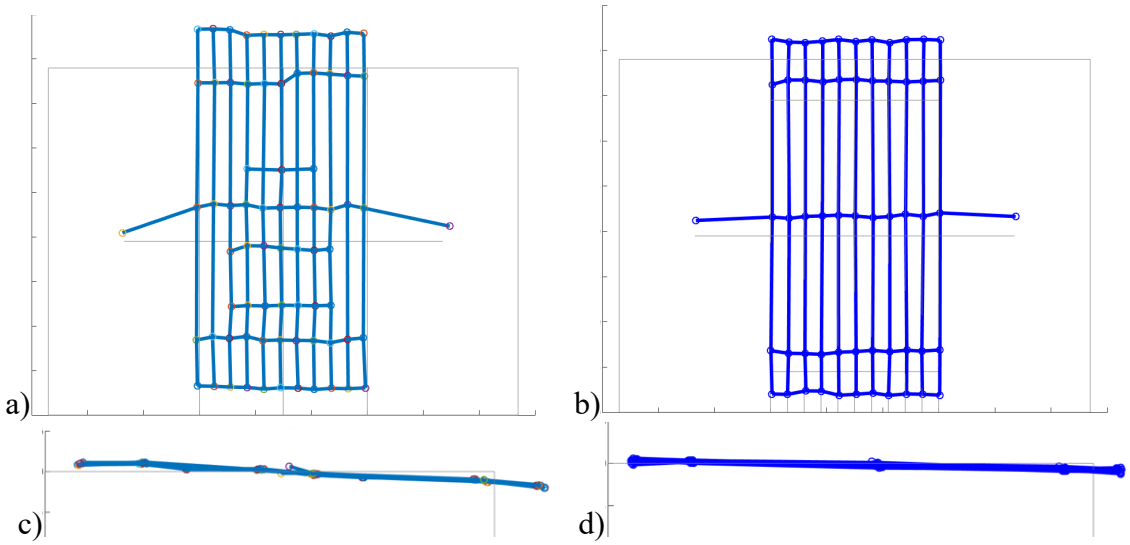

Figure 2-11 2019 vs 2014 Baseline Mode Shape Match (low frequency)
a) 2019 at 25.846Hz (XY View)
b) 2014 at 12.227Hz (XY View)
c) 2019 at 25.846Hz (YZ View)
d) 2014 at 12.227Hz (YZ View)

An important aspect to keep in mind when viewing the FRFs in Figure 2-9 and Figure 2-10 is that the magnitude of each plotted line is not a clear defining measure when comparing two frequency response plots. Instead, the overall shape and location of peaks are two aspects that they describe the behavior or the bridge at each test. A quick glance at Figure 2-10 reveals that the 2014 baseline response in the low frequency range did not match up very well with the baseline tested in this experiment. Even though the blue line (Worley) matched somewhat closely with the red line (this analysis) for certain parts of the low frequency range, the peaks were not coordinated. Examining Table 2-2 in reference to Table 2-1 and only considering the low frequency range, the only one mode matched. Figure 2-11 show a side by side comparison of the only match in the low frequency range. Each view presents a specific modal behavior in which to compare one mode shape to the other. The XY view possesses a side-sway motion in the Y-axis. The YZ view provides a rotation or torsion response about the X-axis. The side-sway

is also shown the YZ view as well. The modes are approximately 13Hz apart indicating a stiffness increase from the original test site to the new testing area. The stiffness change is most likely due to the reassembly and leveling of the bridge since no relative damage was done to the slab.

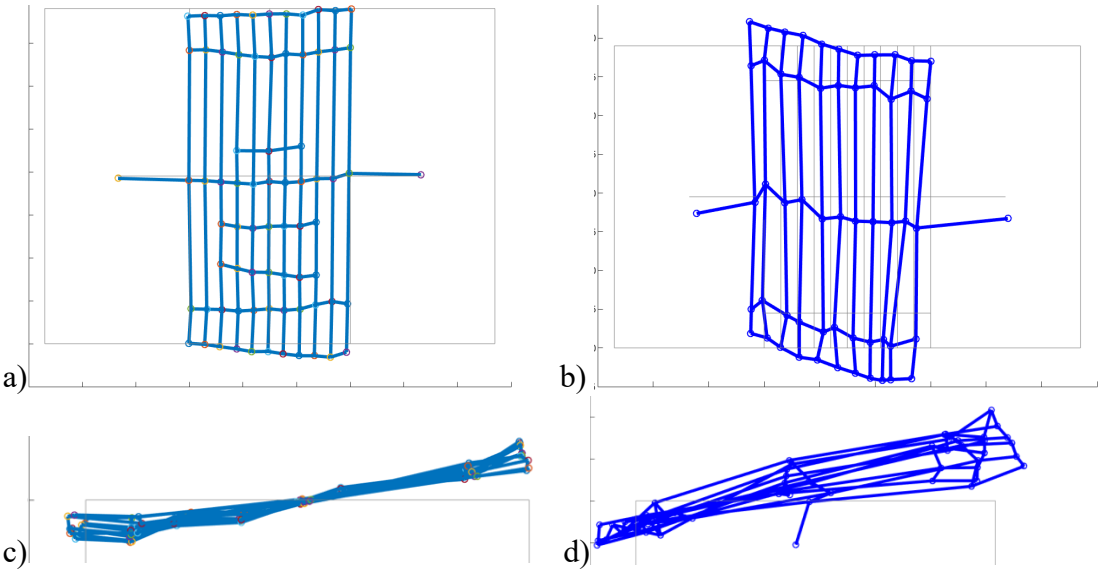

Figure 2-12 2019 vs 2014 Baseline Mode Shape Match (high frequency)
a) 2019 Baseline at 166.325Hz (XY View)
b) 2014 Baseline at 178.389Hz (XY View)
c) 2019 Baseline at 166.325Hz (YZ View)
d) 2014 Baseline at 178.389Hz (YZ View)

The frequencies greater than 50Hz as seen in Figure 2-9 contain better potential matches since local motions are more likely. No particular frequency peaks matched; nonetheless, a few peaks were relatively close. The mode shapes examination revealed only two cases with matching characteristic motions. The first case was the match between Worley's mode shape at around 12Hz and the mode shape from this analysis around 25Hz as discussed.

The second case is seen in Figure 2-12. The two mode shapes are not completely identical but are still relatively close enough in fit to discuss. The altered differences in the two shapes are likely due to the transport of the slab from its original location. The change in location

also likely contributed to the difference in frequency. The slight change in shape and increase in frequency suggest an increase in stiffness for this particular mode match. An increase in stiffness internally would not make sense for the slab, thus the change in boundary conditions is most likely what caused this mode shape to increase in frequency.

2.7 Conclusions

Direct frequency comparisons between Worley's baseline and this baseline proved to be unsuccessful. Few peaks were close in frequency, and the mode shapes at those peaks did not match. Two pairs of modes were examined although each mode shape occurred at a frequency more than 10Hz different than its respective match. Data acquisition could have been one influencing factor, but physical changes were more likely the cause. Frequency differences were attributed to the new boundary conditions when the bridge was reassembled for this experiment. Solely comparing the mode shapes of the two cases revealed mismatched mechanisms.

3. STIFFNESS CHANGE

3.1 Introduction

Moving ahead to destructive testing, this chapter focuses on a relative stiffness change within the center test slab. In order to induce a stiffness change, the slab was sequentially cut with a standard concrete saw, creating 7 damaged cases for SHE™. At a width of approximately ¼ inch, each cut was intended to decrease stiffness with negligible changes to the mass. As the basic equation for natural frequency $\left(\omega = \sqrt{\frac{k}{m}}\right)$ suggests, stiffness and natural frequency are directly related. Therefore, a decrease in natural frequency is expected as the relative stiffness decreases with each progressive cut. The detection goals are both location of the cut and its effect on overall stiffness of the slab.

a)  b) 

Figure 3-1 Crack Induction
a) Bracing/Clamp
b) Concrete Saw Cutting

Before each cut, precautionary measures were taken. Intense vibrations from the concrete saw might shift the center test slab. Worley's experiment proved that the boundary conditions have a very significant impact on mode shapes and therefore damage detection [22]. In order to prevent moving of the slab during cutting a custom wooden "clamp" was constructed and applied each time a cut was made. Two of the clamps in Figure 3-1a were installed, and then cutting commenced as in Figure 3-1b. Note that no major change was later seen in the data to support that the saw vibration caused any significant frequency shift, except perhaps the baseline.

3.2 Damage Cases 1 to 7

Figure 3-2 shows the layout of the eight artificial cracks followed by drawings of the cracks for each respective damage case in Figure 3-3. The centers of concrete bridge spans may sometimes experience the most deflection and possess the highest internal stresses. Thus, damaging the test slab's center will in turn be damaging the most critical portion of the slab. Additionally, roadway bridges such as overpasses normally have the center span points over traffic. The cuts performed in this analysis simulate cracks in the vital central region, and the cut order was selected to show progressive effects. Although on the top surface, the induced cracks also simulate possible results of an over-height vehicle impact. Note that for all cuts, no rebar was ever encountered by the saw.

The first cut started at the edge of the center slab between nodes 5 and 6 and extended towards the middle of the slab until stopping between nodes 33 and 34 (see Figure 3-2). All target region cuts ranged from 3 to 3.5 inches deep. As the transverse cut approached the slab's centerline, the saw blade was gradually pulled up creating an incline to zero depth. During each cut, water was applied to the cut region in order to act as a coolant for the diamond blade as well as an attempt to reduce dust level. Keeping the saw straight while making the initial cut proved to be difficult at first, but it was easier to keep the saw on track as the cut deepened. As the cut grew deeper, it became more difficult to prevent blade tilt that might widen the walls. Then the slab was swept and vacuumed, and the testing procedure as described in Chapter 2 ensued. Henceforth, the abbreviation "DC" will be used for a specified Damage Case with a number.

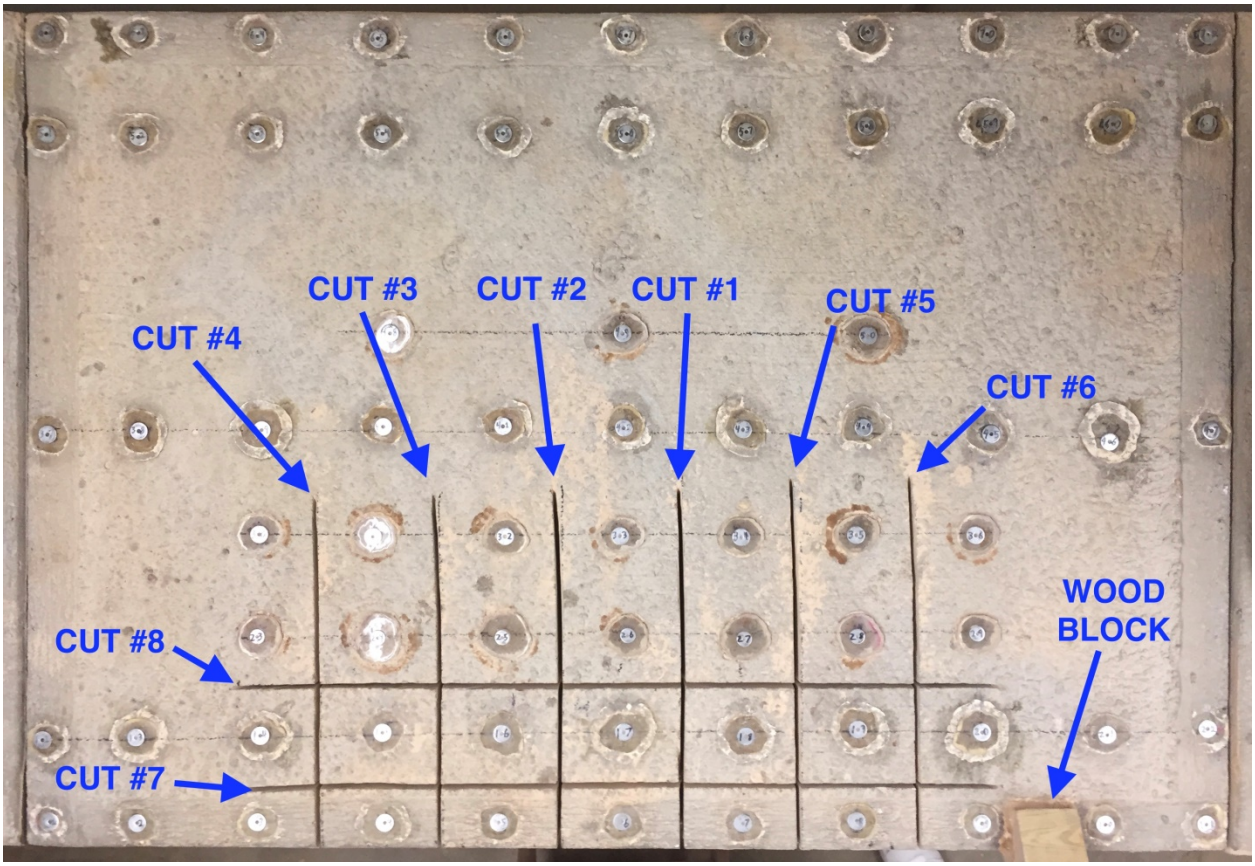

Figure 3-2 Damage Cut Layout and Order

Each cut was performed in a similar fashion to the first cut. Cuts #1 through 6 were kept as uniform as possible, but slight curvature occurred near the centerline. For DC6 and 7, the two longitudinal Cuts #7 and 8 were kept at the same depth until inclines at each end. Each DC consisted of one additional cut added apart from DC3. DC3 in Figure 3-3 displays 2 added cuts from DC2.

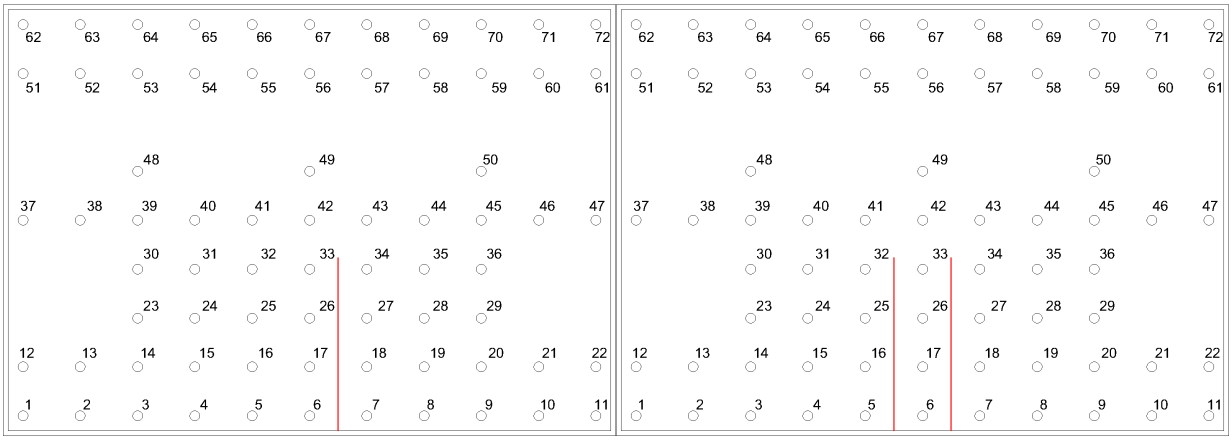

a)

b)

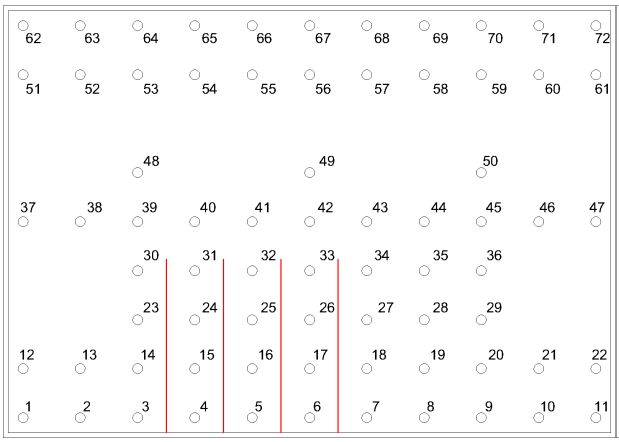

c)

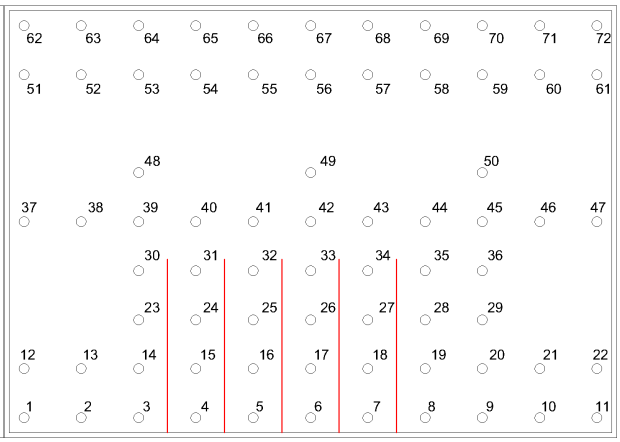

d)

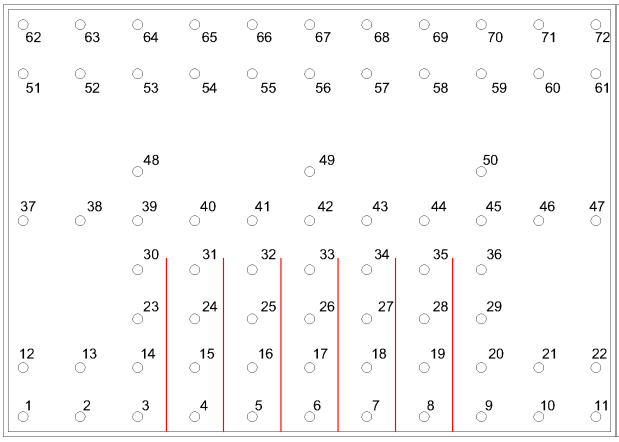

e)

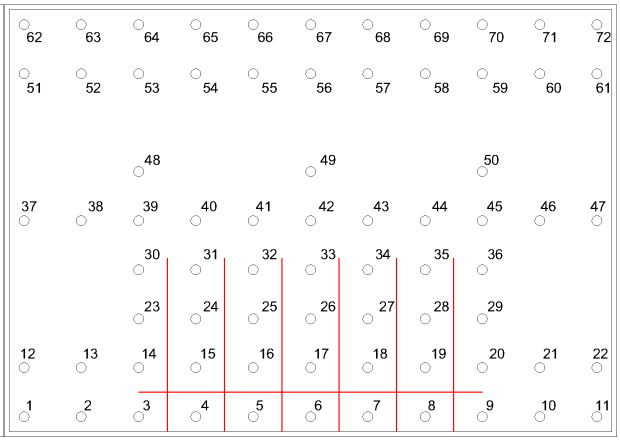

f)

Figure 3-3. *Progressive Cut Order (to be continued)*

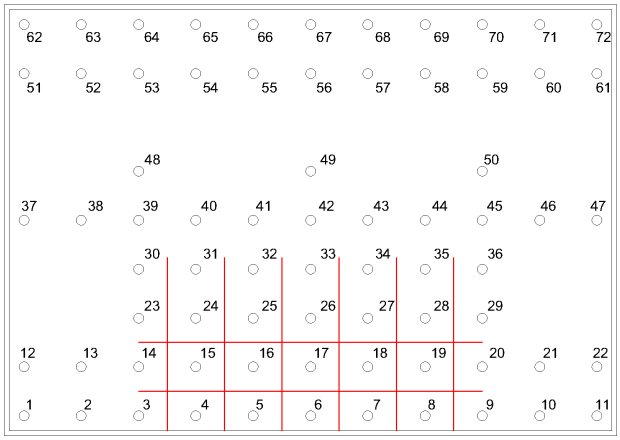

g)

Figure 3-3 Progressive Cut Order
a) DC1 b) DC2
c) DC3 d) DC4
e) DC5 f) DC6
g) DC7

3.3 Frequency Comparison

Matching mode shapes is one of the most important steps in running the SHE™ program. Every mode shape for every structural configuration is different, and differences among modes leads to damage detection. Accuracy can depend upon properly matching mode shapes that are both relatively close in frequency as well as characteristic motion, such as bending, torsion, or axial. The mode matching process currently requires a trained user, but even then, issues can arise. For instance, two matching mode shapes that possess the same shape but are symmetrically flipped about one or more axes are commonly named mirror modes. Although these modes may have the same mechanism, their dissimilar orientation will not work for the software. This study will consider several subsets of modes that might be selected by a user.

Among the seven stiffness damage comparisons of DC1-7, three were analyzed in-depth while others were permitted fewer mode subsets. The first in-depth damage case comparison, DC1 to DC7, compares the initial cut to the final cut and thus provides results for cumulative

stiffness change. The second in-depth comparison was DC1 and DC2, which involved only one transverse cut. This sequential damage comparison studies incremental stiffness change. The third main comparison was between the baseline case and DC1. While this also compares one cut, the undamaged as-built versus initially damaged acts as a measure of sensitivity and a control of procedures. For instance, noise can be introduced by instruments capturing signals or by frequency domain calculations.

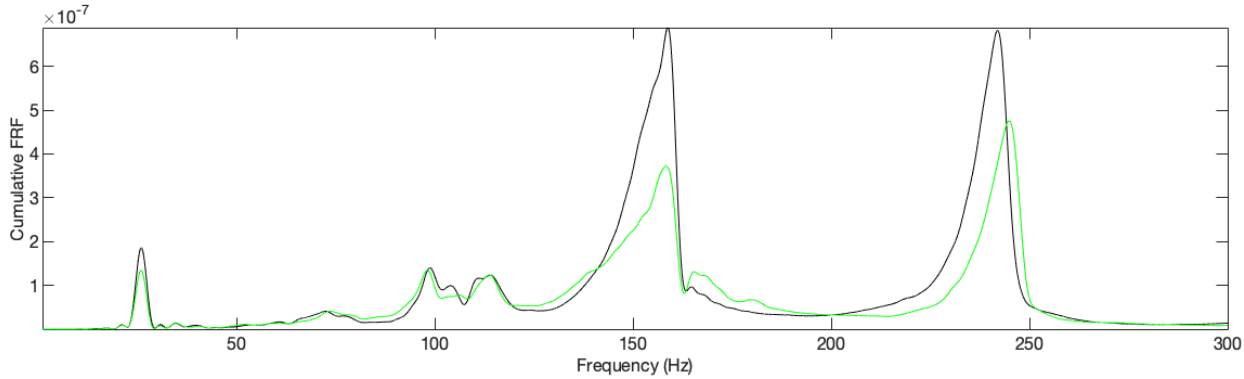

Figure 3-4 Cumulative Frequency Output for DC1 (Green) and DC7 (Black)

The responses shown in Figure 3-4 provide knowledge regarding natural frequency changes varying from DC1 (green) to DC7 (black). In general, the amplitudes of DC7 are greater than those of DC1. This could be caused by more motion being felt as damage has been induced; however, it could also be that more of the 25 hammer impacts were on the upper end of the acceptable range.

The resonant peaks of Figure 3-4 reveal further clues to slab behavior. With 7 more cuts, DC7 should have lower stiffness than DC1, so each pair of peaks should show the DC1 (green) peak to the left of the DC7 (black) peak. For peaks higher than 100Hz, this expectation held true. Peak shift results were mixed for peaks under 100Hz, which are structurally significant.

Another way of illustrating the differences between frequency response functions is Damage Location Vector (DLV) from Section 1.1. This damage detection technique is subtraction of the two outputs, and the SHE™ software plots these values by physical location. For DC1 to DC7, DLV in Figure 3-5 appears to possess random damage locations: this comparison should show damaged points (no green or blue) in X = 20 to 40 and Y = 0 to 15. This figure does not reflect the expected outcome, and neither did the other six stiffness case comparisons. Thus, DLV is deemed unreliable, and frequency content alone remains in question.

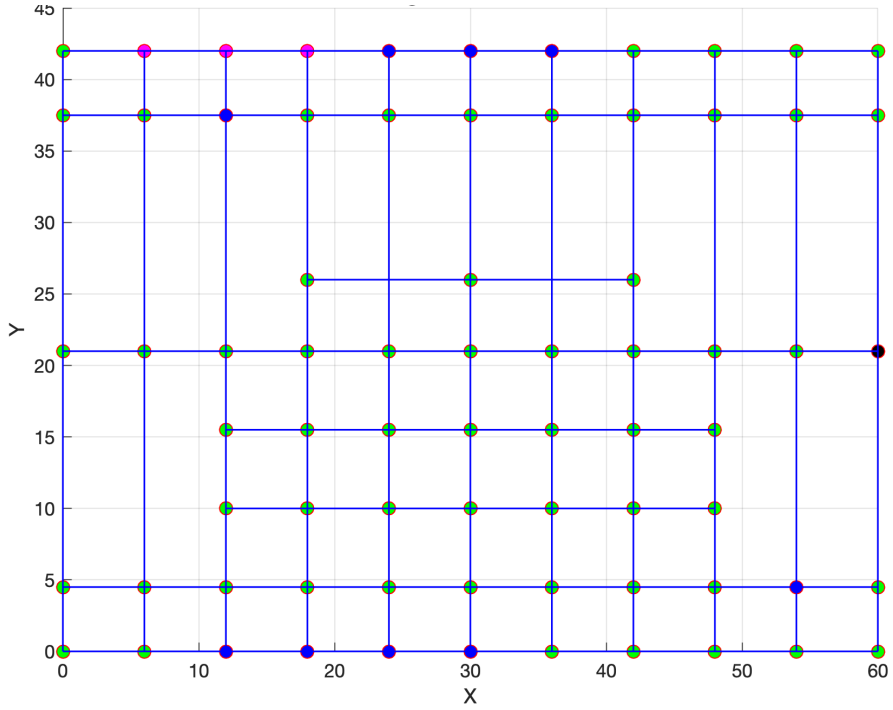

Figure 3-5 Example of DLV (DC1 to DC7)

Waterfall plots were created to display an overall view of natural frequency changes for all stiffness damage cases. Figure 3-6 and Figure 3-7 provide resonant peaks for the first 7 damage cases. Frequency peaks of matched mode shapes from successive cases are marked by a

solid orange line while matched modal peaks but not immediately successive are marked by a dashed blue line. The higher amplitudes above 60Hz mask smaller peaks, so Figure 3-7 provides a closer view at the 0-50Hz range. As discussed in Section 2.5 , mode shapes in the 150-160Hz range were unstable and thus unreliable. Also, the peak around 242Hz was prominent, but its shape was difficult to distinguish. For these two reasons, Figure 3-6 only shows the FRF from 0 to 125Hz.

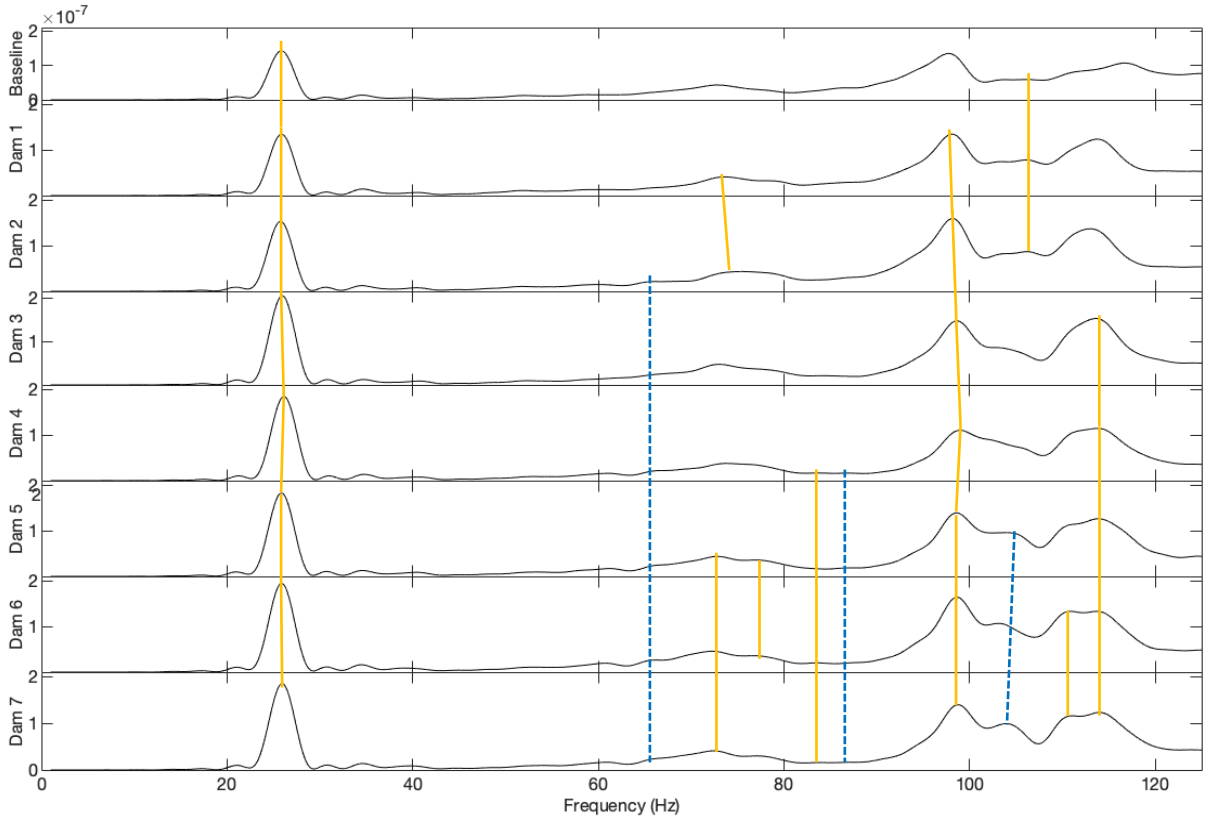

Figure 3-6 Cumulative Stiffness Waterfall (Baseline-DC7, 0-125Hz)
Orange Line = Consecutive Peaks

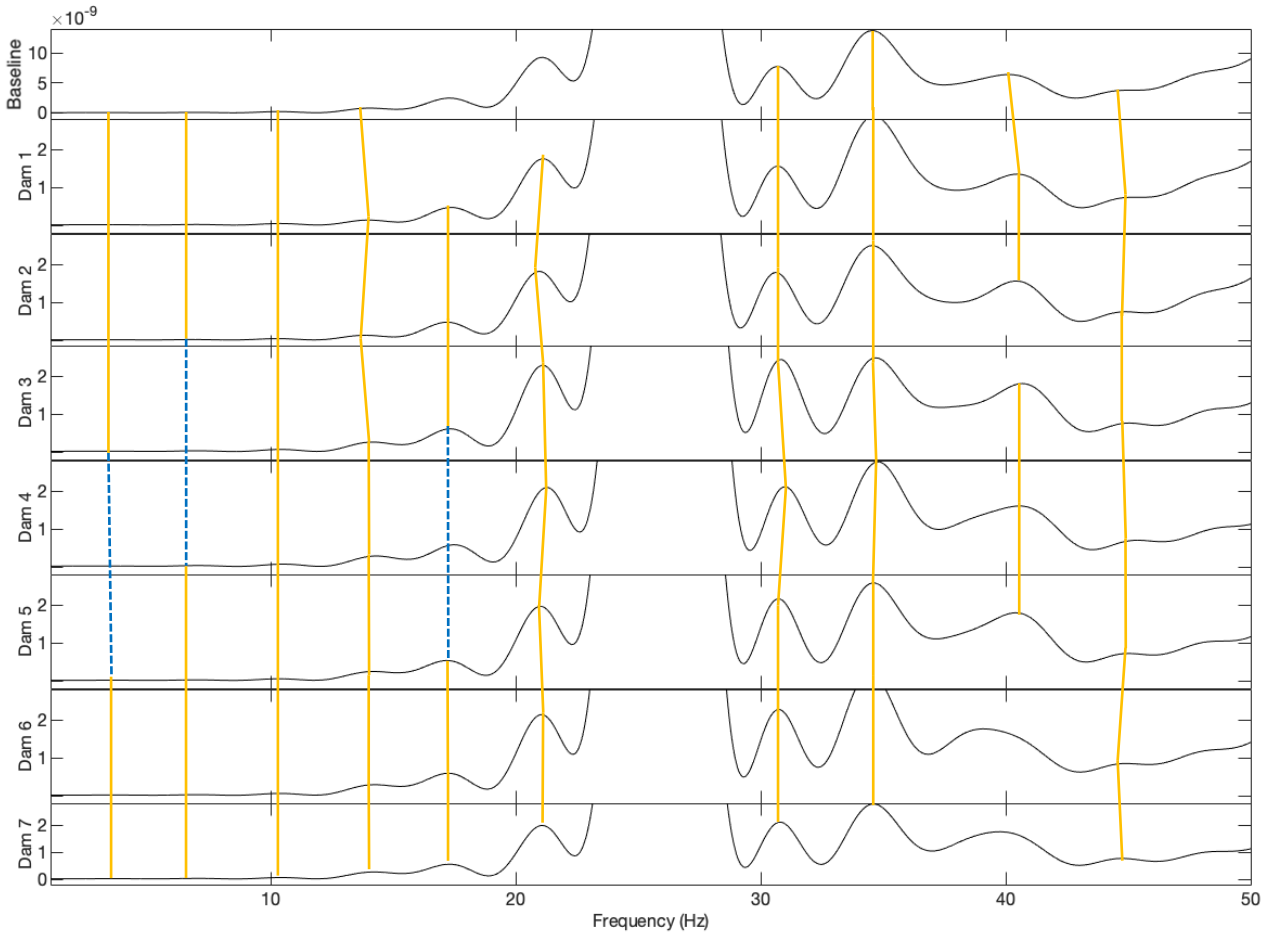

Figure 3-7 Cumulative Stiffness Waterfall (Baseline-DC7, 0-50Hz)
Orange Line = Consecutive Peaks

Mode shapes are required to truly understand the nature of peak shifts. If one only considers the waterfall plots of Figure 3-6 and Figure 3-7, it can seem that the slab's properties were unaffected when particular cuts were made. A general trend of the peak shifting up or down on the frequency spectrum in the waterfall plots is difficult to determine on visual inspection alone. Before cutting took place, the hypothesis was that a clearly visible shift in peaks would show on the waterfall plot. That hypothesis was proven wrong.

A few isolated areas on the waterfall plots show a relatively small change in peak location, but overall most lines denoting peaks are approximately straight. No peak was ever measured to be at the exact same frequency in one DC when compared to another; however, the

straight lines in the waterfall plots prove that very little change took place at most peaks for DC1 to DC7. The waterfall plots then prove that the slab kept its structural stiffness despite the localized damage that had been done to it. The strength of the slab is again likely due to the fact that the concrete saw never encountered the rebar.

Every frequency value for every matching peak in all damage cases for the waterfall plots was found to vary less than 4Hz. Therefore, that the waterfall plots alone, like the FRF overlays, are an inadequate measurement for damage detection for the stiffness cases of this slab. Another method is needed in order to properly determine damage within the slab.

3.4 GA/Procedure

The next step is damage detection using the experimental modal analysis output (undamaged.mat, damaged.mat) and matched modes. Individual damage indices were previously available, but more have been (and can be) added. Then, an artificially intelligent process selects likely damaged location, estimates damage severity, and states best damage indicator. Genetic algorithm (GA) software is being developed by Stephen Zeng, PhD Candidate in the Multi Function Dynamics Lab, Civil Engineering Department. The GA plots used herein are generated from SHE^{TM} with his algorithm. The GA plot produced from the algorithm is one of the main focus points of the research in determining where the damage is as well as to what degree.

A target vector is required as user input into GA. This vector is based upon *a priori* knowledge of approximately where the damage in a system would be. The target vector consists of an array of numbers representing node points for each respective structure. The entries are either 0 corresponding to nodes expected to have no damage or 1 corresponding to nodes expected to have damage. For example, if a cut on the slab passed between Nodes 46 and 47, then the target vector would have a value of 1 in the 46th and 47th position within its array while

all the remaining 70 positions would be 0. Note that target vectors used herein were strictly binary; that is, only values of 1 or 0 were inputs. Other options should be considered for optimizing the target vector, and no automatic processes have been developed to aid a user in deciding the vector. Therefore, the target vector should be created by an experienced individual.

Before the GA computation stage, the software generates 51 plots that represent individual damage indices (DI) along individual axes, thanks to tri-axial input data. These DI are combined into the 24 resultant indices provided in Table 3-1. GA then uses these as inputs to find the most suited DI for damage detection in this specific case. A weight coefficient is output that provides a measure of accuracy with a fit of 1 being the best fit and 0 being no correlation. The highest ranked DI should always be inspected, but the user must be sure to look at the second and third ranked indices as well. In some cases, the lower-ranked DI still possess a fit of 0.8 or 0.9, meaning large influence on the damage plots.

Table 3-1 Damage Indices List

DI Number	Name	Symbol
1	COMAC in Mode Shape	COMAC$\boldsymbol{\phi}$
2	Difference in Mode Shape	Diff$\boldsymbol{\phi}$
3	Division in Mode Shape	Div$\boldsymbol{\phi}$
4	Difference in Flexibility	DiffF
5	Division in Flexibility	DivF
6	Percentage in Flexibility	PercF
7	Z-score in Flexibility	Z_{MFI}
8	Probability in Flexibility	P_{MFI}
9	COMAC in Curvature (S)	$COMAC_KS$
10	COMAC in Curvature (R)	$COMAC_KR$
11	Difference in Curvature (S)	$Diff_KS$
12	Difference in Curvature (R)	$Diff_KR$
13	Division in Curvature (S)	Div_KS
14	Division in Curvature (R)	Div_KR
15	Curvature Damage Factor (S)	CDF_KS
16	Curvature Damage Factor (R)	CDF_KR
17	Difference in Strain Energy (S)	DiffUS
18	Difference in Strain Energy (R)	DiffUR
19	Division in Strain Energy (S)	DivUS
20	Division in Strain Energy (R)	DivUR
21	Percentage in Strain Energy (S)	PercUS
22	Percentage in Strain Energy (R)	PercUR
23	Z-score in Strain Energy	$Z_{\boldsymbol{\gamma}}$
24	Probability in Strain Energy	$P_{\boldsymbol{\gamma}}$

R = Resultant, S = Spatial

If for some reason the final GA plot does not line up with the known damaged area, the user must dig deeper into the 41 plots in order to determine why. For instance, if one of the nodes on the slab that was tested was showing a false positive for its damage indicated value, the user could examine the directional X, Y, and Z plots for that particular “best suited” method. If a very strong portion of the X plot exists which matches the same location of the false positive

found in the final GA plot, then perhaps there exists a particular pair of modes that were not well matched and must be removed. Removing a poor match or noisy sensor data may change results drastically. A different calculation method may be chosen as the best for damage detection during the second round of GA. If so, the supporting 41 plots should be evaluated again in the same manner that they initially were.

3.5 GA Plot

The final visualization GA plot is the deliverable that contains the information to diagnose problematic areas of a structure. An example of this plot, Figure 3-9 shows a fitness value (FV) in its title. The FV represents the relative accuracy of GA and thus the matching of the DI to damage location. That is, high variance in damage location and severity will often result in a high FV; however, it is important to note that a low FV does not always mean successful damage detection: the fit can be good for the wrong location, for instance.

Figure 3-9 is a layout of all 72 node points used in this work. While Nodes 73 and 74 (the adjacent slab nodes) were helpful in describing the mode shapes, they generated a great deal of variance and were removed for this step in order to improve FV. At each node point, the number within the circle represents relative change of the final GA result. In short, each node point for one DC case is compared to its matching node point in a separate DC. The greater the difference in two node points, the greater the damage value within the circle at that particular node point. The color code from Figure 3-8 is employed for viewing ease: note that the thresholds are arbitrary, but green to red/black shows increasing levels of change.

The shown damage percentages are relative in nature, and actual values carry different weights specifically depending on the two compared damage cases. For instance, a 67% damage value at some node for DC1 to DC7 would be more severely damaged than the same point with a

67% damage value for DC1 to DC2. First, DC1 to DC7 involves far more cumulative damage, so 67% also means more. Second, the damage level must be checked between the 72 nodes to ensure that results above the noise level are maintained.

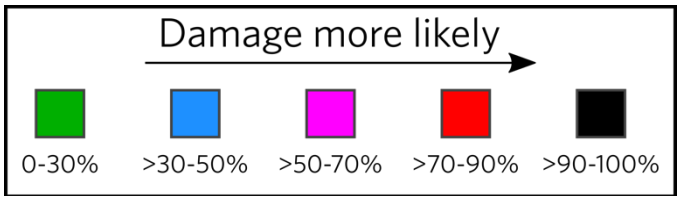

Figure 3-8 Damage Level Scale

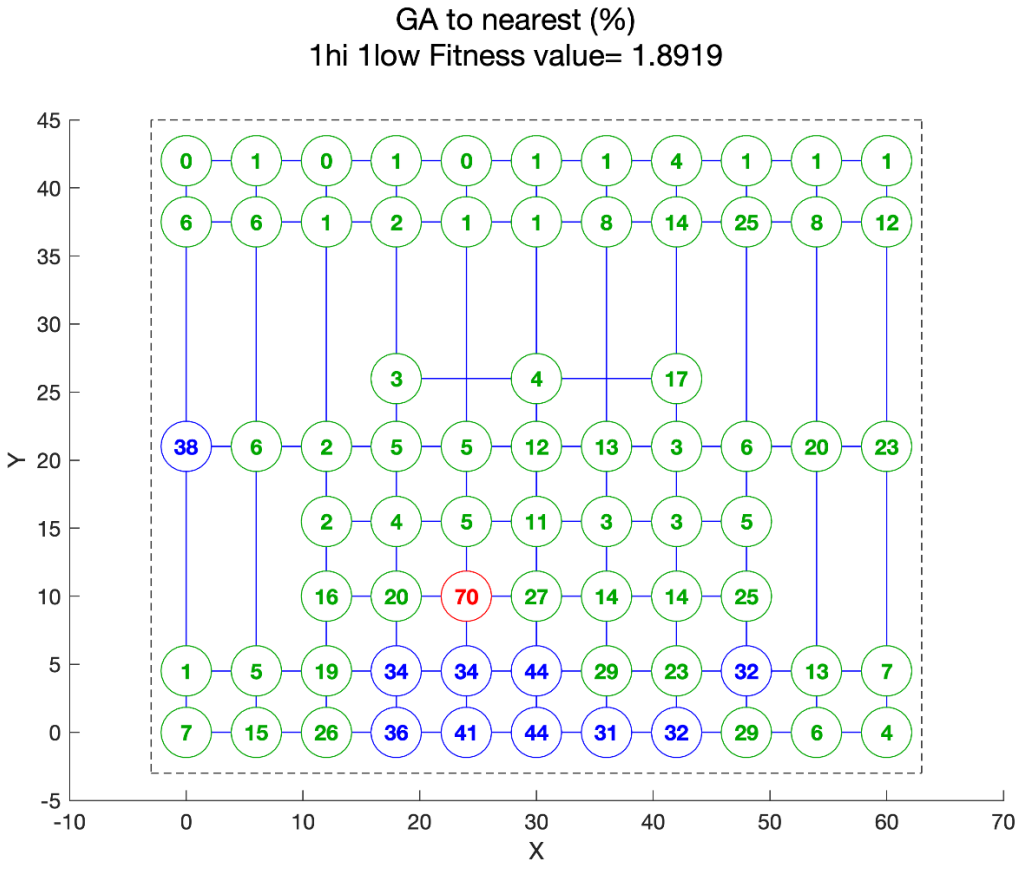

Figure 3-9 GA Plot Example (DC1-DC2)

3.6 Modal Subsets

Since GA results can vary upon selected modes, each of the three main damage comparisons were analyzed for multiple mode subsets. These subsets contained different practical combinations of initially matched modes that a user might select. Note that this is not an exhaustive search, just an introductory effort. As follows, each subset has a corresponding number with it for quick recall.

Subset 1 is the "Nominal" mode subset. After matching the modes for any damage case comparison, the initial set of matched modes were termed as the Nominal subset. From this set, different combinations of modes were analyzed, all in the same manner.

Subset 2 is the "25Hz (sway)" mode subset. As discussed in Section 2.5, the mode shape at 25Hz was the most reliable mode shape throughout the experiment. Analyzing this mode shape comparison alone is a good test of SHE^{TM} capability. Also, the mode shape at 25Hz possessed a relatively simple behavior, primarily made up of a sway motion.

Subset 3 is the "High Frequency" mode subset. As the name might suggest, this subset is a combination of only modes above 60Hz. The FRF plots showed that the slab behaved differently in the low versus to high frequency ranges. Therefore, this subset will isolate the high frequency range for analysis.

Subset 4 is the "Low Frequency" mode subset, corresponding to the inverse of subset 3. That is, this subset is a combination of only modes below 60Hz. For the DC1 to DC7 comparison, the name of this subset was replaced by "Mode Shape 1 Only" since just one matched mode (near 3Hz) occurred in this frequency region.

Subset 5 is the "Mode Shape 1 Removed" mode subset. The first mode shape can be noisy due to signal loss, so removing this mode was intended to reduce the total noise in the

mode shape grouping. Thus, this subset uses all the Nominal subset mode matches except for the first mode match.

Subset 6 is the “1 High, 1 Low” mode subset. One well-matching mode from the high frequency range and one from low frequency range were chosen to analyze as a pair. This subset represents the minimum input for both frequency ranges.

Subset 7 is the “Close Fit” mode subset. The mode combination was chosen based upon reinspection of the Nominal mode shape set. Acting as a very experienced and critical inspector, the mode matches were further narrowed down so that only prime modes were used. A new subroutine was written to overlay normalized mode shapes to assist in this step. This subset is quite subjective depending how closely the user defines a match.

Subset 8 is the “Best Guess” mode subset. A trial-and-error study was conducted, and this subset provides the combination of modes that resulted in the lowest GA fitness value. The Best Guess subset was not determined until the previous seven subsets had been completed. At this point the user will have seen the results from the other subsets and could foresee other matched sets.

3.7 Evaluation Criteria

In this work, damage detection accuracy is based upon four criteria. The 8 subsets for each damage case comparison were analyzed based upon these metrics. Both qualitative and quantitative measures are required, but any thresholds are entirely arbitrary and based on experience.

The first criterion is the fitness value (FV) itself. Since FV represents GA’s accuracy, any subset with a fitness value over 2.0 may be considered here to possess skewed results due to

noise or poor mode matches. Any FV less than 2.0 is considered to be adequate and aids the user being able to trust the damage detection results for that particular subset.

The second criterion is the maximum damage value, or the greatest damage percentage of all 72 node points on the GA plot. On average, a damage value above 0.95 is considered adequate since it likely shows good separation from undamaged locations. Note that the highest damage value can be subjective depending on the physical damage done to the structure, and this experiment was expected to cause relatively heavy damage around the cut areas. A weakness of this criterion is that the maximum damage value only indicates the highest value for a single node, lacking information on overall damage level.

The third criterion addresses this shortcoming on Criterion 2 by comparing damage percentages for unexpected ("Zeroes") versus expected ("Ones") locations from the target vector. The two averaged values present an indicator of how well the target vector fits a damage case comparison. Ideally, average values expected for damaged and undamaged percentages will be as close as possible to 100% and 0%, respectively. The ratio of expected damaged to undamaged values is then employed for direct comparison, but this ratio seems highly variable. Here, a good ratio is deemed to be 6.00 or higher by experience and familiarity with this structure. Anything lower than 6.00 seems to possess damage too scattered around the slab or too close in damage value. Even though different damage comparisons will result in different amounts of damage, the target vector comparison should still work, and an acceptable ratio of 6.00 or higher is then used for almost all scenarios in this study.

The fourth and final criterion is a qualitative personal judgment. This decision of "accept" or "reject" is solely the user's and is based on their experience. Factors include knowledge of mode matching and other elements of the SHE^{TM} program as well as structural and

material behavior. A judgment of acceptable means that the final damage detection GA plot can be trusted to proficiently show damage in the structure. A broad look is taken when examining the GA plot, and the user focuses on how damage percentages are distributed. The user analyzes personally acceptable error by considering any outlying damaged points. Also, the severity of the damage is considered: the more structural change between the two damage cases, the more expected damaged nodes with higher values. Furthermore, the user reflects upon the results for Criteria 1, 2, and 3. For instance, even Criteria 2 and 3 are acceptable, a poor fitness value combined with poor damage location could lead a user to reject this damage detection scenario.

3.8 GA Results

Every damage case comparison was recorded on a GA Results table (i.e. Table 3-2). Providing the user an idea of how well the subsets worked as a whole, each table begins with FV statistics for the 8 mode subsets. The results for each of the 4 criteria are progressively listed down the table. Underneath the first criterion, the average error per sensor is noted. The sensor error average is calculated by dividing the fitness value by the number of sensors for that respective DC. Immediately below the sensor error is the DI that the GA chose as the best fit for that respective subset; more information on that DI can be found in Table 3-1. For each and every case presented in this study, the best DI's fit value was 100%. The averages of the zeros and ones from the target vector are shown along with the ratio and final judgment.

Table 3-2 DC1-DC7 Results

	Subset Group Data:	Number of Subsets **8**	Mean Fitness Value **2.4689**	Max Fitness Value **3.5127**	Min. Fitness Value **1.7620**	Standard Deviation **0.6562**		
Sub-Set Number	1	2	3	4	5	6	7	8
Sub-Set Name	Nominal	25Hz (Sway)	High Frequency	MS 1 Only	MS 1 Removed	Lowest FV	Close Fit	1 High, 1 Low
Criterion 1: Fitness Value	**2.0300**	**3.5127**	**2.7534**	**2.9633**	**1.9643**	**1.762**	**1.818**	**2.9471**
Avg. Error per Sensor	2.82%	4.88%	3.82%	4.12%	2.73%	2.45%	2.53%	4.09%
Best GA Damage Index (1.00)	(15) CDFS	(18) diffUR	(12) diffkR	(11) diffkS	(11) diffkS	(12) diffkR	(18) diffUR	(16) CDFR
Criterion 2: Max Damage Value	**0.9618**	**0.7599**	**0.9758**	**0.9998**	**0.8949**	**0.9618**	**0.9682**	**0.9960**
AVG. (zeroes):	10.50%	18.52%	5.67%	18.91%	9.47%	10.50%	4.26%	16.77%
AVG. (ones):	63.12%	31.94%	48.19%	47.57%	63.83%	63.10%	67.70%	46.12%
Criterion 3: Ones/ Zeroes	**6.01**	**1.72**	**8.50**	**2.52**	**6.74**	**6.01**	**15.88**	**2.75**
Criterion 4: Judgment	**accept**	**reject**	**reject**	**reject**	**accept**	**accept**	**accept**	**reject**

Table 3-2 provides results for DC1 and DC7 while Figure 3-10 shows the GA plot for the Nominal subset. Looking straight to the first criterion, only half of the subsets "passed" the 20 threshold. Relatively speaking, the highest fitness value of 3.5127 in subset 2 is still not a very high number compared to the maximum value of 72; however, for the purpose of this analysis, the SHE^{TM} program worked well enough that the threshold for the fitness values was made more stringent.

Considering the second criterion, all but two subsets passed. A high pass rate of all subsets is expected for this damage comparison since the relative change in damage is high compared to the other stiffness change DCs. Seven new cuts have been made into the slab from DC1 to DC7, so the maximum damage values should be very close to one. Such is the case with subset 4.

The target vector ratio in criterion 3 covered a broad range for the 8 subsets. Subset 7 possessed one of the highest ratios in the entire experiment with 15.88. The range of which the target vector ratio covers for this damage comparison suggests that the target vector alone cannot help the GA provide accurate information. Both the matched mode sets along with a well-planned target vector are needed to truly display results as accurate as possible.

Examining the judgment section, subset 3 is an example of a case when the judgment call carries more weight. If a subset meets the thresholds for the first three criteria, then it will have an accept label for the judgement call. In the case of subset 3, two of the three preceding criteria pass the threshold mark. Also note that the fitness value, although outside of the threshold, is not the largest value of the subset group. The user must be the one to make the call of whether or not to give the accept or reject label and trust the related GA plot. Note that the difference algorithm for strain energy and curvature seems to work the best for DC1 to DC7 comparison.

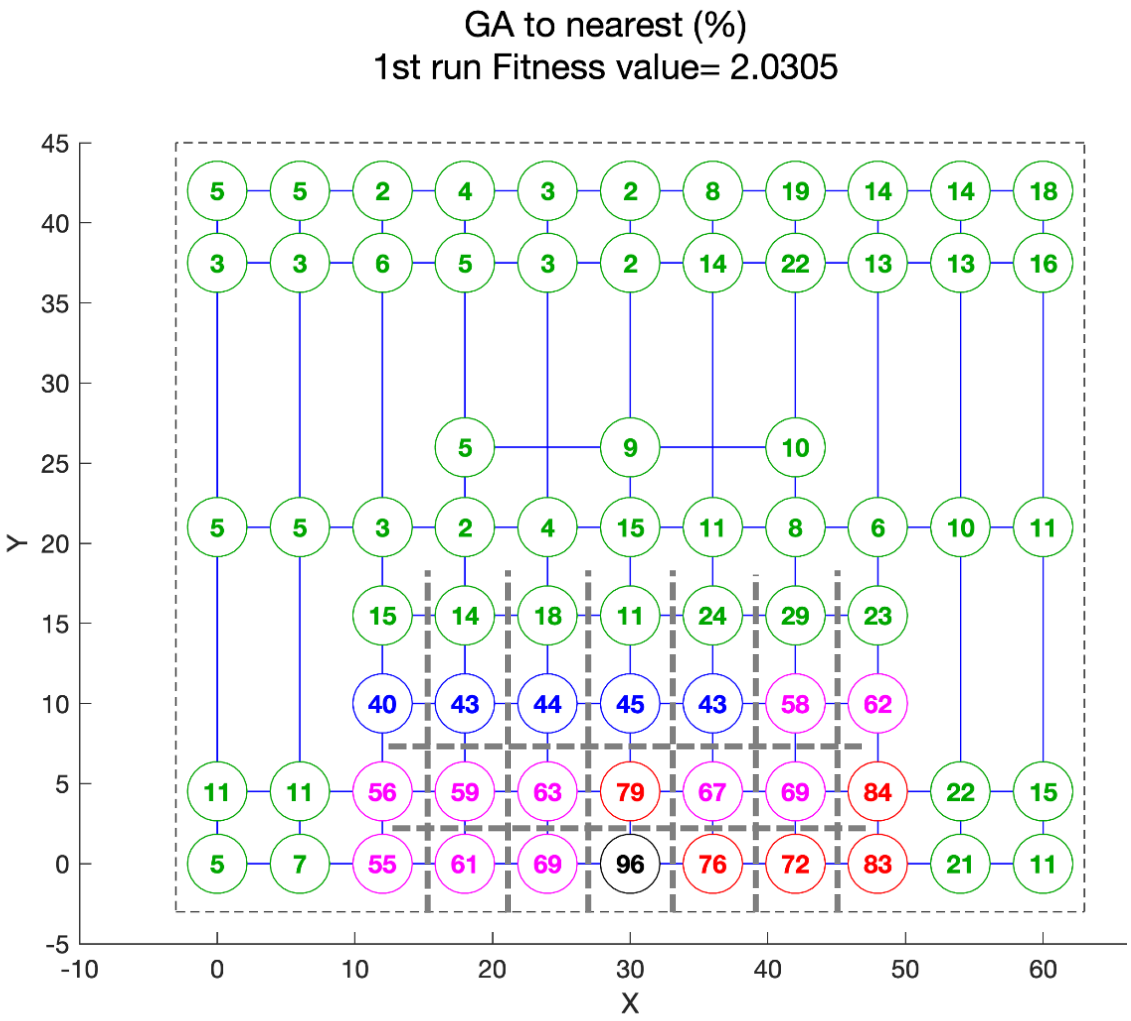

Figure 3-10 DC1-DC7 (Nominal)
Gray lines indicate cuts

Table 3-3 DC1-DC2 Results

Subset Group Data:	Number of Subsets	Mean Fitness Value	Max Fitness Value	Min. Fitness Value	Standard Deviation		
	8	**1.8498**	**1.9936**	**1.7040**	**0.0980**		
Sub-Set Number	1	2	3	4	5	6	7	8
Sub-Set Name	Nominal	25Hz (Sway)	High Frequency	Low Frequency	MS 1 Removed	1 High, 1 Low	Close Fit	Best Guess
Criterion 1: Fitness Value	**1.8381**	**1.7384**	**1.704**	**1.9501**	**1.834**	**1.8989**	**1.9936**	**1.8415**
Avg. Error per Sensor	2.55%	2.41%	2.37%	2.71%	2.55%	2.64%	2.77%	2.56%
Best GA Damage Index (1.00)	(3) divMS	(5) divF	(17) diffUS	(21) percuss	(3) divMS	(5) divF	(1) COMAC	(3) divMS
Criterion 2: Max Damage Value	**0.5761**	**0.6036**	**0.9083**	**0.9038**	**0.6128**	**0.7020**	**0.4177**	**0.5982**
AVG. (zeroes):	7.41%	7.32%	6.21%	8.21%	7.70%	10.95%	9.74%	7.02%
AVG. (ones):	37.17%	49.63%	50.45%	38.93%	38.73%	43.33%	35.52%	37.20%
Criterion 3: Zeroes/ Ones	**5.02**	**6.78**	**8.13**	**4.74**	**5.03**	**3.96**	**3.65**	**5.30**
Criterion 4: Judgment	**accept**	**reject**	**accept**	**accept**	**accept**	**reject**	**reject**	**accept**

Table 3-3 provides results for DC1 and DC2. The fitness value range is smaller than the range in Table 3-2, which is expected considering the relatively small damage change in the two cases. Note that all of the subsets' fitness values are within the threshold, thereby making the first criterion a poor choice in distinguishing good and bad subsets for this DC comparison. The low average fitness value does show SHE^{TM}'s efficiency with damage cases of relatively small stiffness change. Only two subsets pass the threshold for the second criterion. Stiffness changes are normally difficult to predict without previous calculation and analysis of a structure. The relatively low maximum damage values suggest that the slab was not affected severely from the first to the second cut. Note that a lower maximum damage value will make damage location more difficult unless the node points away from the damaged area possess low damage values such as 5 or less. The pass rate for the third criterion is the same as the second criterion; only two subsets pass. Most nodes assigned a zero value on the target vector most likely possessed more than 5 for their respective damage values and therefore decreased the target vector ratio. Thus, DC1 to DC2 will rely more on the fourth criterion since the pass rate of the preceding three criteria is low compared to the pass rate of DC1 to DC7. Note that no particular DI seems to repeat for this damage case comparison suggesting that for relatively small damage case comparisons, the best DI will be chosen on a case by case basis.

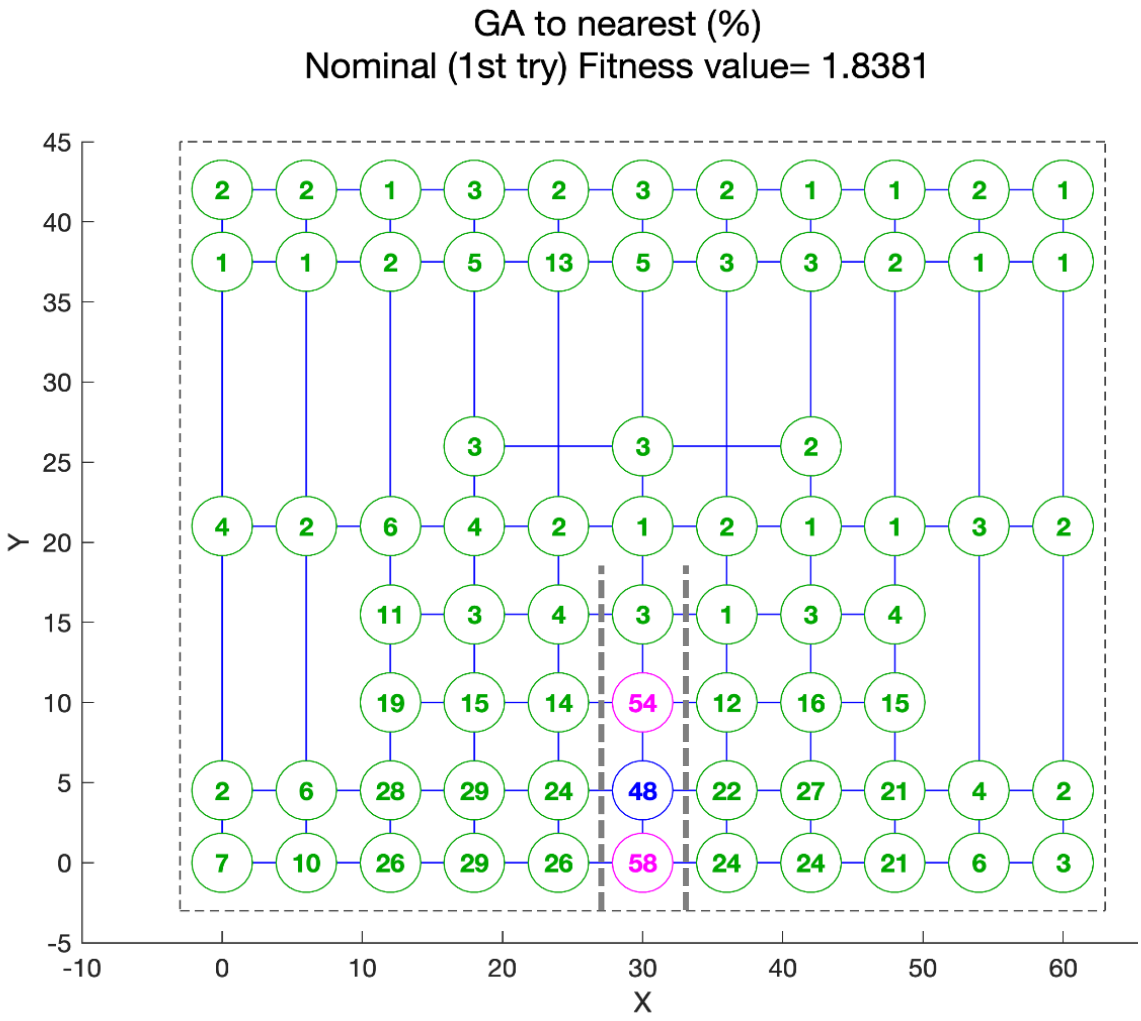

Figure 3-11 DC1-DC2 (Nominal)
Gray lines indicate cuts

Table 3-4 Baseline-DC1 Results

	Subset Group Data:	Number of Subsets **8**	Mean Fitness Value **2.0741**	Max Fitness Value **2.3913**	Min Fitness Value **1.4277**	Standard Deviation **0.2901**		
Subset Number	1	2	3	4	5	6	7	8
Subset Name	Nominal	25Hz (Sway)	High Frequency	Low Frequency	Mode Shape 1 Removed	1 High, 1 Low	Close Fit	Best Guess
Criterion 1: Fitness Value	**2.0585**	**1.4277**	**2.1845**	**2.1435**	**2.0847**	**2.3913**	**2.2952**	**2.0072**
Avg. Error per Sensor:	2.86%	1.98%	3.03%	2.98%	2.90%	3.32%	3.19%	2.79%
Best GA Damage Index (1.00):	(17) diffUS	(17) diffUS	(17) diffUS	(17) diffUS	(17) diffUS	(1) COMAC	(1) COMAC	(17) diffUS
Criterion 2: Max Damage Value	**0.7075**	**0.9990**	**0.5622**	**0.4576**	**0.6454**	**0.2879**	**0.4309**	**0.7083**
AVG. (zeroes):	11.17%	5.63%	10.94%	12.29%	12.02%	10.11%	12.84%	11.10%
AVG. (ones):	34.23%	61.98%	28.21%	31.00%	36.72%	11.16%	19.59%	40.37%
Criterion 3: Zeroes/Ones	**3.06**	**11.01**	**2.58**	**2.52**	**3.05**	**1.10**	**1.53**	**3.64**
Criterion 4: Judgment	**accept**	**accept**	**reject**	**reject**	**reject**	**reject**	**reject**	**accept**

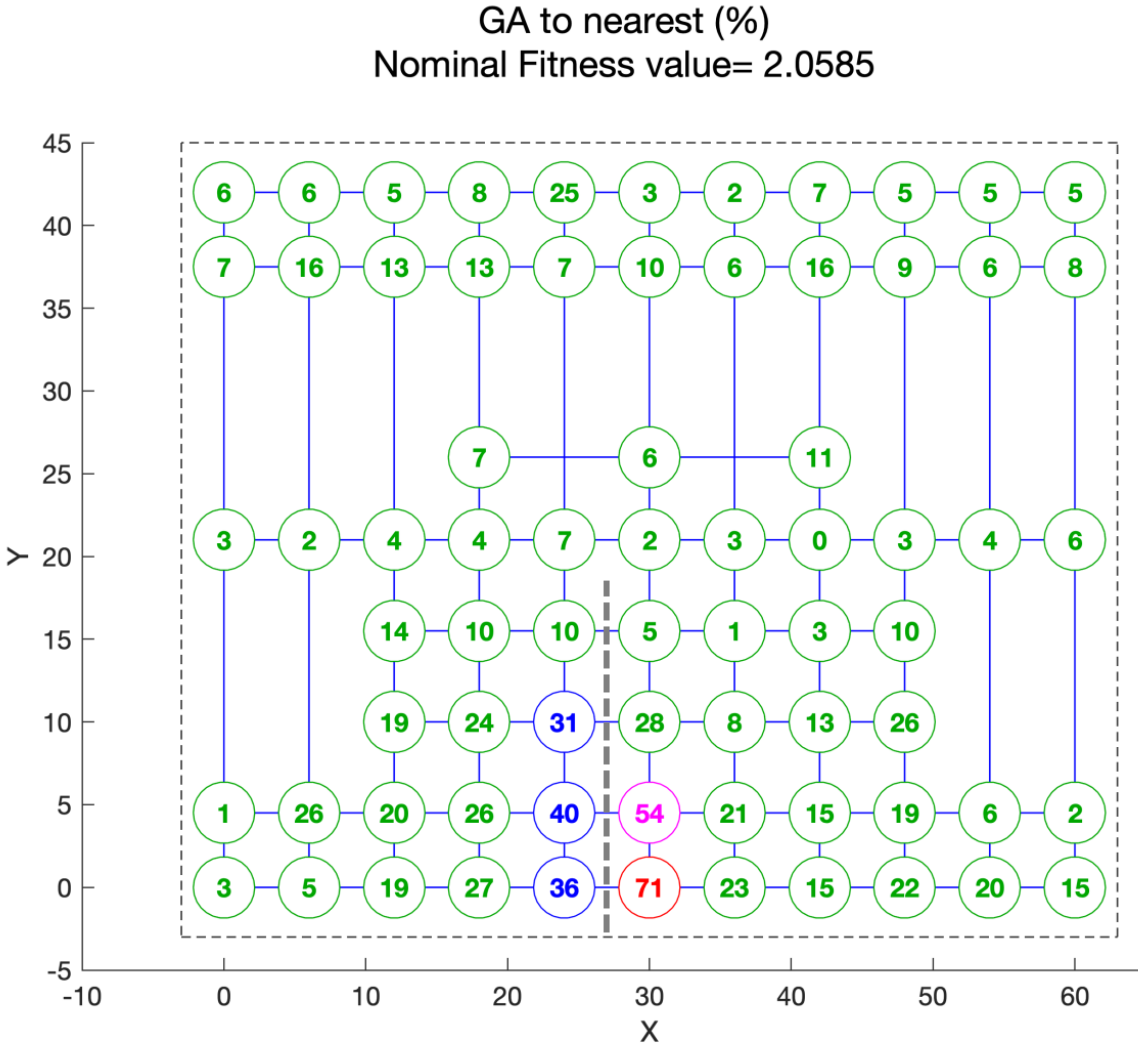

Figure 3-12 Baseline-DC1 (Nominal)
Gray line indicates cut

Table 3-4 provides results for Baseline and DC1. This particular damage case comparison was more difficult than the previous two considering that not as many mode shapes were matched in subset 1. Also, many false positives are displayed in this Table 3-4. The majority of the subsets pass the first criterion, and the two subsets that do not pass are relatively close to passing as well. The second criterion has a large variance over the 8 subsets suggesting a scattered and random pattern for damage location. The third criterion backs up the results from

the second with all but one subset having values less than 3.1. As stated for Table 3-3, one cut within the slab did not show a relatively large change. Analyzing the slab from its originally undamaged state to its initial damaged state is expected to display higher values for the target ratio. Having two of eight subsets receive an "accept" label suggests that the damage case comparison as a whole is not an accurate result of the damage within the slab. One observation that is not a false positive is the chosen DI being Strain Energy Difference for the majority of the subsets. The repeated picking of this DI by the GA aids in the robustness of the particular algorithm in damage detection.

Table 3-5 DC1-(DC3, DC4, DC5, DC6)

Damage Case Number:	DC1-DC3	DC1-DC4	DC1-DC5	DC1-DC6
Criterion 1: Fitness Value	**2.1224**	**1.8824**	**1.7536**	**1.879**
Avg. Error per Sensor	2.95%	2.61%	2.44%	2.61%
Best Damage Index from GA (1.00):	(11) diffkS	(17) diffUS	(18) diffUR	(17) diffUS
Criterion 2: Max Damage Value	**0.9953**	**0.9237**	**0.9977**	**0.9498**
AVG. (zeroes):	11.72%	6.59%	10.34%	4.47%
AVG. (ones):	63.29%	69.24%	69.96%	65.25%
Criterion 3: Zeroes/Ones	**5.40**	**10.51**	**6.77**	**14.58**
Criterion 4: Judgment	accept	accept	accept	accept

Table 3-5 displays the results for the remaining damage cases analyzed for the stiffness loss portion of the experiment. The damage cases in Table 3-5 were recorded after analyzing the results from the first three tables. One observation showed that subset 1 of all three of the main damage comparison cases received an “accept” label for the final criterion and passed the majority of the other criteria. Therefore, only the Nominal subsets were recorded for the secondary damage comparisons. Apart from the DC1 to DC3, all damage comparison passed all four criteria. The Strain Energy Difference and Curvature Difference DI’s were also present, and the DC1 to DC3 comparison is relatively close to passing first and third criteria as well. The repeated acceptable labels for all four damage comparisons bolster the reliability of the SHE™ program for certain damage limits.

3.9 Conclusions

The Nominal mode showed the most accurate results on average of any other subset when comparing all results from the DCs for the stiffness change section of this testing. Recall that the Nominal subset mode matching combinations were chosen based off initial examination of the mode shapes and were therefore the first set of modes matched. This conclusion points towards the robustness of the GA when it comes to choosing modes to match. Since the Nominal subsets were not always the best choices for each damage comparison, improvement is still expected with better matching. Precise and specialized matching should lead to lower fitness value and improved displays of damage.

Note that examinations of the FRF overlay and waterfall plots proved to be insufficient for adequate damage severity determination.

4. MASS LOSS

4.1 Introduction

While Chapter 3 discussed stiffness change damage cases, Chapter 4 will focus on the second type of damage in this work, mass loss. Mass changes within the slab should affect modal properties on a more global scale as compared to stiffness changes. In order to mimic spalling over time, a total of 15 individual blocks were progressively removed to generate Damage Cases 8 to 20. Three different sizes of blocks were taken from the slab, and each row had its own size of block to be removed; thus, this analysis is organized by row as shown Figure 4-1.

For the mass loss studies, Damage Case 7 (all cuts, Figure 3-2) is considered the baseline case. For DC8 through DC18, only one block (Blocks 1-11) was removed at a time. Cases 19 and 20 included removal of two Blocks 12-13 and 14-15, respectively.

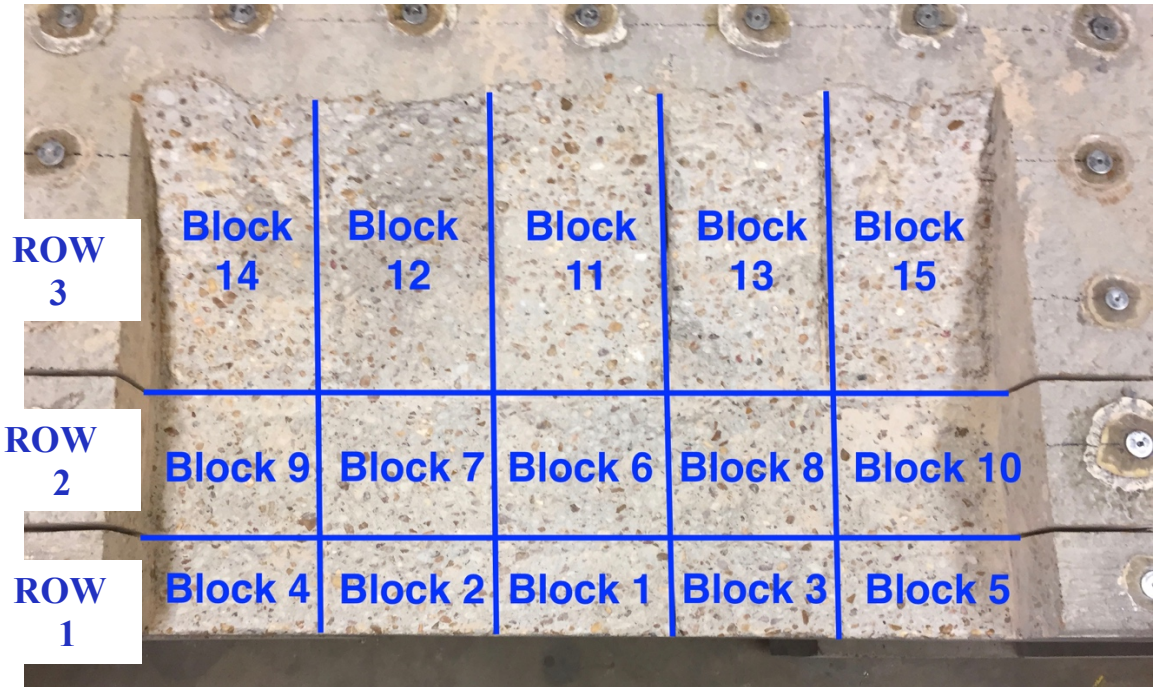

Figure 4-1 Block Removal Order Layout

4.2 Block Removal Procedure

A picture of the chipping process is shown in Figure 4-2. A demolition hammer was carefully used to chip a horizontal line the width of the respective block to be removed. Once a groove was created, more pressure was applied to the block. After less than a minute, the block separated from the slab along a relatively flat plane at a 3-inch depth. Separating along a plane kept approximately uniform mass loss in each block for each row.

Figure 4-3 provides photographs of the chipped results as four damage cases. This chipping process continued sequentially for blocks from Rows 1 and 2; however, the Row 3 blocks were not rectangular. For the third row, Block 11 was removed at a sloping angle up to the surface, removing two sensor pads and creating DC18 (Figure 4-3c). Blocks 12 through 15 were chipped at an angle close to the incline of the cuts on either side of them; DC19 and DC20 saw the removal of 2 angled blocks per damage case.

Figure 4-2 Picture of Chipping Process (Removal of Block 2)

The approximate volume of blocks in the first, second, and third rows are 54, 132, and 132 cubic inches, respectively. Using 150 pounds per cubic foot, the approximate mass of blocks in the first, second, and third rows are 4.7, 11.5, and 11.5 pounds, respectively. Each block removal from Row 1 correlated to a 0.36% mass loss relative to the undamaged slab. Also, blocks removed from rows 2 and 3 correlated to a 0.88% mass loss relative to the undamaged slab. Even though blocks from Row 3 were not similar in shape to the blocks in Row 2, the volume of the Row 3 blocks still approximately matched the volume of the blocks in Row 2. For this reason, the volume and mass values of the blocks in Rows 2 and 3 are reported as equal. A summary is provided in Table 4-1.

a)  b) 

c)  d) 

Figure 4-3 Photographs of DCs (Mass Loss)
a) DC8 (Block 1 removed)
b) DC13 (Block 6 removed)
c) DC18 (Block 11 removed)
d) DC20 (Block 14 & 15 removed)

4.3 Sensor Loss

An important factor that may affect the mass loss study's results is the loss of sensor data. As testing proceeded with each mass loss damage case, node points were removed along with block extractions, but data was always taken for 74 points during testing. The accelerometers were sequentially placed on pads, and when encountering a removed node, the sensor was then placed in a padded storage container on a table independent of the slab. The bridge was hit by the hammer per standard testing procedure, and data was recorded by the sensor in the external box as if "dead" sensor, or one that records only surrounding signal noise. This did not work though,

as the isolation was insufficient; a later decision was made to decrease the analyzed sensor number as damage progressed.

Fewer sensor points mean less overall slab data. The initial addition of 17 node points served to somewhat counteract data loss in the areas of block removal. The cumulative frequency response plots were deemed adequately precise for this analysis. Still, when compared to the stiffness change cases, the mass loss cases will not possess the same degree of damage accuracy. The stiffness cases have the benefit of utilizing 72 node points of data while the mass loss cases ranged from 71 to 52 node points: see Table 4-1. Although 52 node points were adequate, accurate damage location became increasingly difficult as sensor points were lost, and DC19 and DC20 were particularly affected by the removal of 4 sensor points each.

4.4 Order of Analysis

If the original baseline is used as the basis for comparison, the mass loss cases would include the damage from the stiffness change cases. This portion of the experiment is intended to focus on mass loss only; therefore, the damage cases for the mass loss portion use DC7 as their new baseline. A breakdown of the progressive total percent mass loss with respect to the slab in DC7 is provided on Table 4-1. The table describes the order of each damage case comparison made as well as the total number of sensor data points available for each case. Note that the amount of mass lost per block increases with each row in the slab. Table 4-1 quantitatively summarizes a quantitative view of the changes between each mass loss DC as well as helps interpretation of case comparison results.

Table 4-1 Mass and Sensor Loss Data

Row Number	Removed Block Number(s)	Damage Case Comparison	Mass Change (%)	Total Mass Loss (%)	Total Number of Sensors
Row 1	1	7 to 8	0.36	0.36	71
	2	7 to 9	0.36	0.72	70
	3	7 to 10	0.36	1.07	69
	4	7 to 11	0.36	1.43	68
	5	7 to 12	0.36	1.79	67
Row 2	6	7 to 13	0.88	2.67	66
	7	7 to 14	0.88	3.54	65
	8	7 to 15	0.88	4.42	64
	9	7 to 16	0.88	5.30	63
	10	7 to 17	0.88	6.17	62
Row 3	11	7 to 18	0.88	7.05	60
	12, 13	7 to 19	1.75	8.80	56
	14, 15	7 to 20	1.75	10.55	52

The damage case comparisons in the mass loss portion of this analysis were analyzed under 2 mode subsets. Chapter 3 proved that the Nominal mode subset, on average, provided the most optimal results on a consistent basis. This would be a trained inspector's most inclusive set of matched modes. Each case comparison was then further analyzed using a Close Fit or "Cleansed" mode subset using stricter fit guidelines, permitting the user to create a smaller list of matched modes. The goal of the cleansed sets was to potentially improve upon the accuracy of the GA results. All comparisons were analyzed using the same four criteria from Section 3.7.

As an example, the damage case comparison of DC7 to DC13 is examined in detail as it contained the best matched modes. The GA plot for the Nominal mode subset for this

comparison is seen in Figure 4-4. This mass loss case has Row 1 blocks completely removed and the first block from Row 2 removed, as shown in Figure 4-3b. Note that the area in outlined in the solid black rectangle is the primary area for damage detection. This rectangle will act as a windowed zoom view for later discussed damage case comparisons. Six blocks have been removed, and the associated lost sensors are represented by missing grid readings inside the black rectangle.

Although the fitness value is above the 2.00 threshold, this plot is still excellent in overall communicating the results of the mass loss effects of this analysis. Note the precision of the damage detection. The highest damage values are close to the Y=0 slab edge as well as close to the X=12,48 edges of the mass removal area. All damage values above 30%, apart from one 31% outlier, are within 6 inches of the mass loss area with the most known damage. Therefore, the visual conclusion is the region shows a reasonable damage pattern with maximum single points of 96%-97% change.

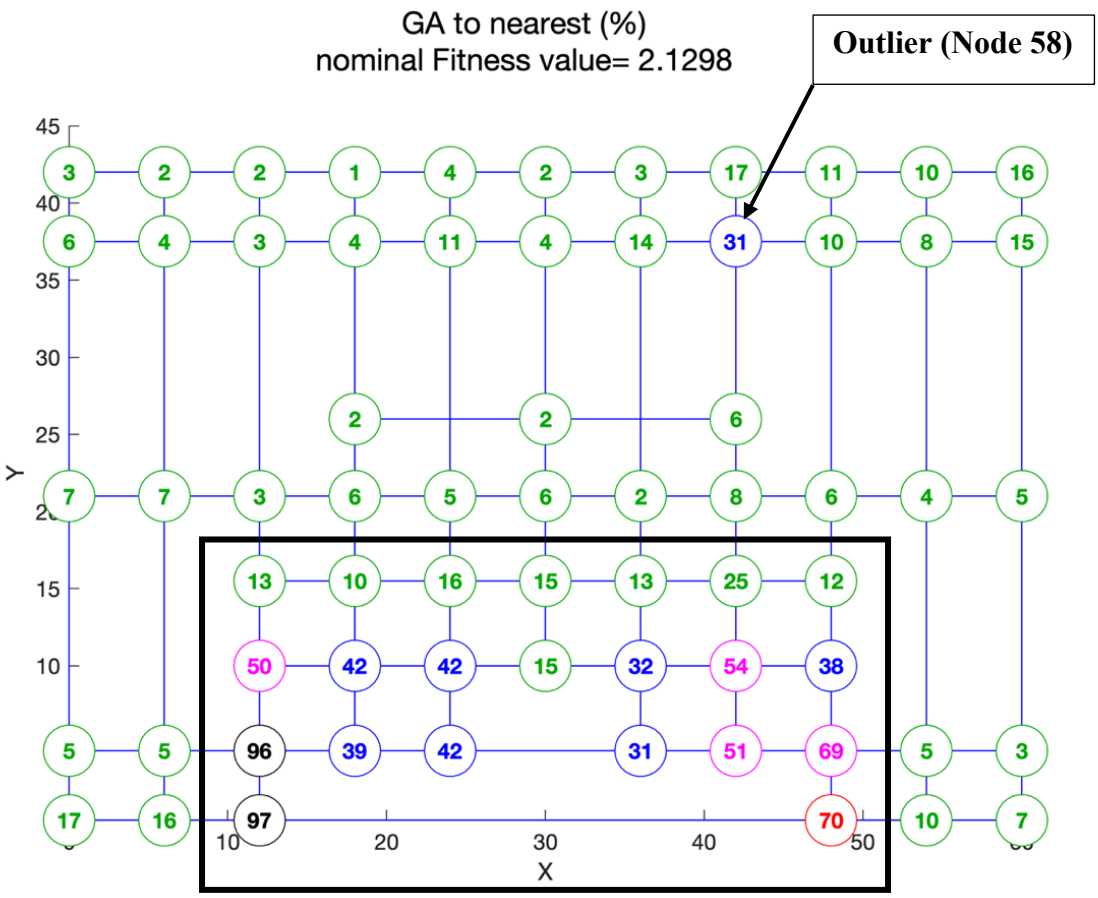

Figure 4-4 GA Plot of DC7 to DC13 (Nominal) with Zoomed Window

The single, relatively high damage value point that is not near the mass loss area is considered a false positive node. This outlier belongs to sensor Node 58 on the slab as denoted in Figure 4-4. During analysis of the mode shapes, the majority of damage cases showed Node 58 possessing either higher amplitudes or dissimilar behavior to the other sensor points around it. Further study of the other cases revealed the same GA results with Node 58 on average possessing a higher damage value than its immediately surrounding points. The washer on which this sensor was supported was checked, and the epoxy base was also examined; the sensor employed was examined and even switched. Still, no anomalies could be seen to determine what caused this unusual behavior. This anomaly of Node 58 has led to planning future work. Even

with a consistent outlier, the results still gave a well-defined description of damage location and severity.

The damage case comparison of DC7 to DC13 was also analyzed for two additional mode subsets. The Nominal subset had 12 matched mode shapes, but the cleansed subset had 8 modes with a stricter level of mode matching. A further subset was chosen to narrow down the matched modes to only the best four matched modes for the DC7 to DC13 case only. The GA plots for these three cases were remarkably similar: even with different numbers of matched modes, the results provide consistent answers with relatively accurate damage detection.

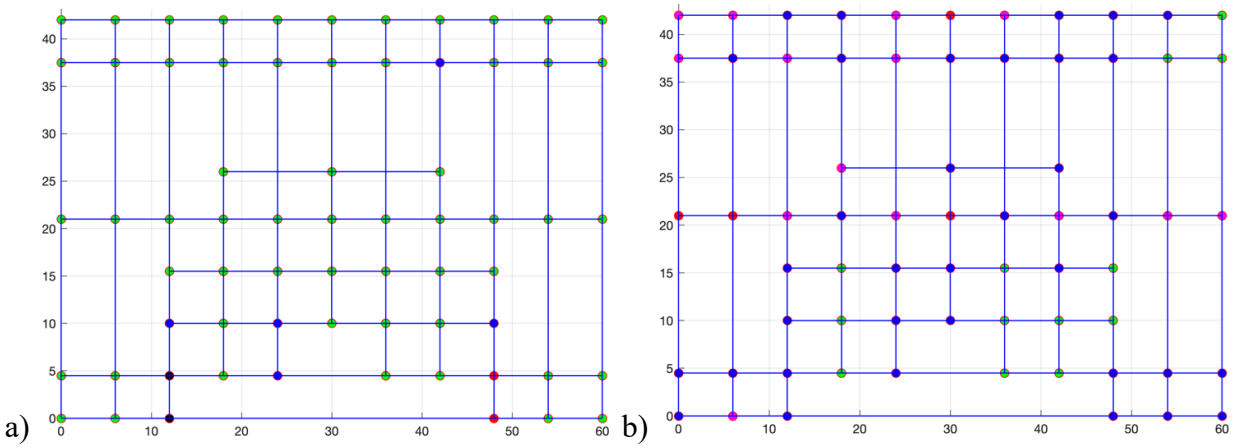

Figure 4-5 DC7 to DC13 Resultant Damage Indices
a) 11, Modal Curvature Difference (Spatial)
b) 9, COMAC for Modal Curvature (Spatial)

For this DC7 to DC13, the GA program output best fit damage indicators along with their weights. The Spatial Curvature Difference (DiffkS) was chosen by GA to be the best fit (100%) damage index for all mode subsets. A plot for this particular DI is seen in Figure 4-4a. The DiffkS plot showed the most damage around the expected area. One of the more poorly matched (0.0001% ≅ 0%) damage indices for this case was the Modal Curvature COMAC (COMACkS)

as seen in Figure 4-5b. The COMACkS plot showed scattered damage across the entire slab. Visual inspection of the color differences and locations between the two DI plots reinforce the results from the GA. Since the GA labelled Figure 4-5a as “well fit” and Figure 4-5b as “poor fit,” the results are reliable for this damage case.

All damage cases for the mass loss portion of this analysis are discussed in order of block removal, beginning with Block 1. The Nominal mode subset results are first discussed before the reduced cleansed mode subset.

4.5 Row 1

The progression of damage for the first row alone is presented in Figure 4-6. Visual inspection of these GA plots shows positive qualitative results for damage detection near removed blocks. Note that the red diamond in each zoomed GA plot represents the lost sensor from each respective DC. As anticipated, the most immediate points around the mass loss area show higher damage values when compared to other points. Another positive result is the precision of the damage indicated: all points with a damage value of 30% or higher are within approximately 6 inches of the mass loss area.

A trend also appeared for the first row. The two node points left and right (with respect to the X-axis, along Y=0) of the mass loss area carried the highest damage values for the total available points, but the points immediately above (with respect to the Y-axis, for Y>0) the mass loss area did not show a significant damage increase. Still, these sensor points possessed a higher average damage value than other sensor points on the slab. As each damage case comparison progressed, the number of points with a non-green color increased in area indicating a spread in damage. Thus, the spread of damage then directly correlates to the spread of mass loss.

Table 4-2 Row 1 Criteria (Nominal)

Damage Case Number:	DC7 to DC8	DC7 to DC9	DC7 to DC10	DC7 to DC11	DC7 to DC12
Criterion 1: Fitness Value	**1.5725**	**1.7115**	**1.9039**	**1.8198**	**1.7418**
Avg. Error per Sensor	2.21%	2.45%	2.76%	2.68%	2.60%
Best Damage Index from GA (1.00):	(17) diffUS	(17) diffUS	(17) diffUS	(12) diffkR	(11) diffkS
Criterion 2: Max Damage Value:	**73.51%**	**86.40%**	**87.58%**	**98.09%**	**78.39%**
AVG. (zeroes):	7.33%	5.53%	6.97%	9.06%	8.70%
AVG. (ones):	49.27%	43.53%	41.64%	57.02%	59.05%
Criterion 3: Zeroes/Ones	**6.72**	**7.87**	**5.98**	**6.29**	**6.79**
Criterion 4: Judgment	**accept**	**accept**	**accept**	**accept**	**accept**

Provided in Table 4-2, each of the five damage case comparisons received an acceptable label and passed the majority of the four criteria. The Node 58 outlier of Section 4.4 was only found in the DC7 to DC8 and DC7 to DC12 cases; the outlying value varied from 30% to 32%, which is a relatively low threshold. Also, the damage induced in the slab has both symmetrical (DC8, 10, 12) and asymmetrical (DC9, 11) cases. Upon examining the damage cases for the first row, none are exactly as quantitatively and qualitatively expected. One possibility for this non-uniformity is the location of the hammer hit with respect to the slab. Since the hammer was striking the slab in an asymmetrical location at an angle non-normal to any slab face, the vibrations thus could have caused an asymmetric response. The second possibility is that perhaps

the damage induced was not as uniform as intended. Asymmetric damage would likely skew damage result symmetry but should still yield an accurate damage location for mass loss.

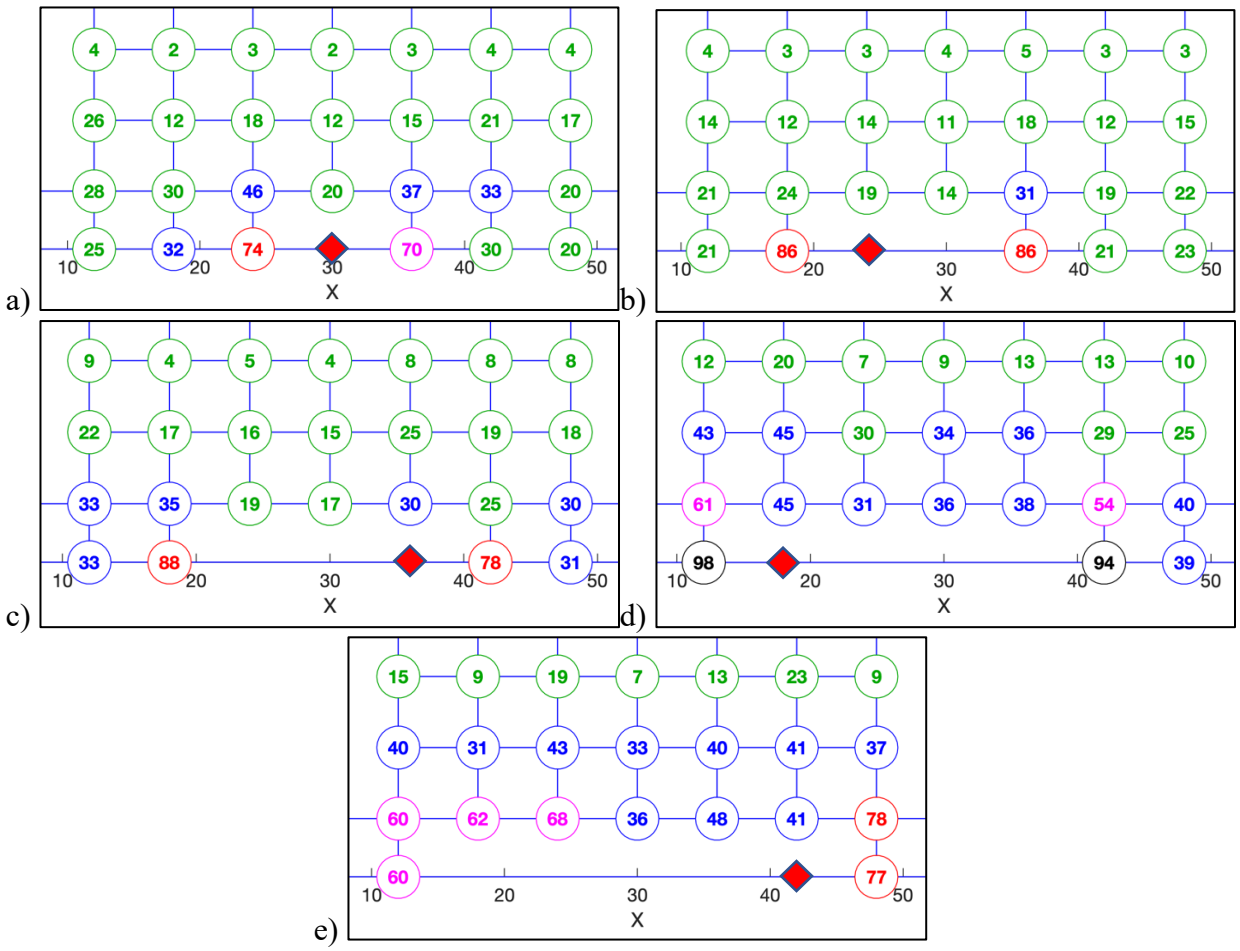

Figure 4-6 Nominal GA Plots for Row 1
a) Zoomed DC7 to 8 b) Zoomed DC7 to 9
c) Zoomed DC7 to 10 d) Zoomed DC7 to 11
e) Zoomed DC7 to 12

4.6 Row 2

Table 4-3 provides the results for damage detection on Row 2. The first three GA case comparisons were similar to those of the first row apart. In general, the damage values to the right and left (with the X-axis, along Y=0) of the newly removed mass areas were higher than the

values in other parts of the slab, except for the first row of sensor points. Since Row 2 was measured after Row 1's removal, it therefore makes sense for the damage values nearest the mass loss area edges on the first row (Nodes 3 and 7) to be high. All damaged value points above 30% were now within approximately 12 inches of the mass loss region. Note that the outlier at Node 58 varied from 24% to 42% and Table 4-3 presents the four criteria for all five cases.

Table 4-3 Row 2 Criteria (Nominal)

Damage Case Number:	DC7 to DC13	DC7 to DC14	DC7 to DC15	DC7 to DC16	DC7 to DC17
Criterion 1: Fitness Value	**2.1297**	**1.9746**	**1.932**	**2.0453**	**2.0076**
Avg. Error per Sensor	3.23%	3.04%	3.02%	3.25%	3.23%
Best Damage Index from GA (1.00):	(11) diffkS	(11) diffkS	(12) diffkR	(12) diffkR	(12) diffkR
Criterion 2: Max Damage Value	**96.73%**	**75.27%**	**88.23%**	**85.53%**	**92.73%**
AVG. (zeroes):	11.01%	9.55%	11.11%	8.80%	8.84%
AVG. (ones):	53.09%	56.53%	62.20%	50.58%	52.26%
Criterion 3: Zeroes/Ones	**4.82**	**5.92**	**5.60**	**5.75**	**5.91**
Criterion 4: Judgment	**accept**	**accept**	**accept**	**accept**	**accept**

The two latter cases of Row 2 are considered to successfully global detect damage; however, the third lines of nodes (Y=12) show insignificant (green) change though adjacent to removed block and sensor (red diamond). A further dispersion of damage would make sense considering the progressive nature of the mass loss area. Furthermore, the transverse spread

towards the centerline (with the Y-axis, for Y>0) had previously been greater than that longitudinally with the X-axis. Now, growth in occurring in neither direction as all points outside the zoomed areas showed green. Although having the most mass loss, DC7 to DC16 and DC7 to DC17 only have seven and six damages values over 50%, respectively. While the final case for Row 2 is very precise in its damage location, the GA plot also contains false negatives which would cause an inspector to possibly miss other damaged areas of the bridge. A possible cause is mode matching, which needs a further sensitivity study.

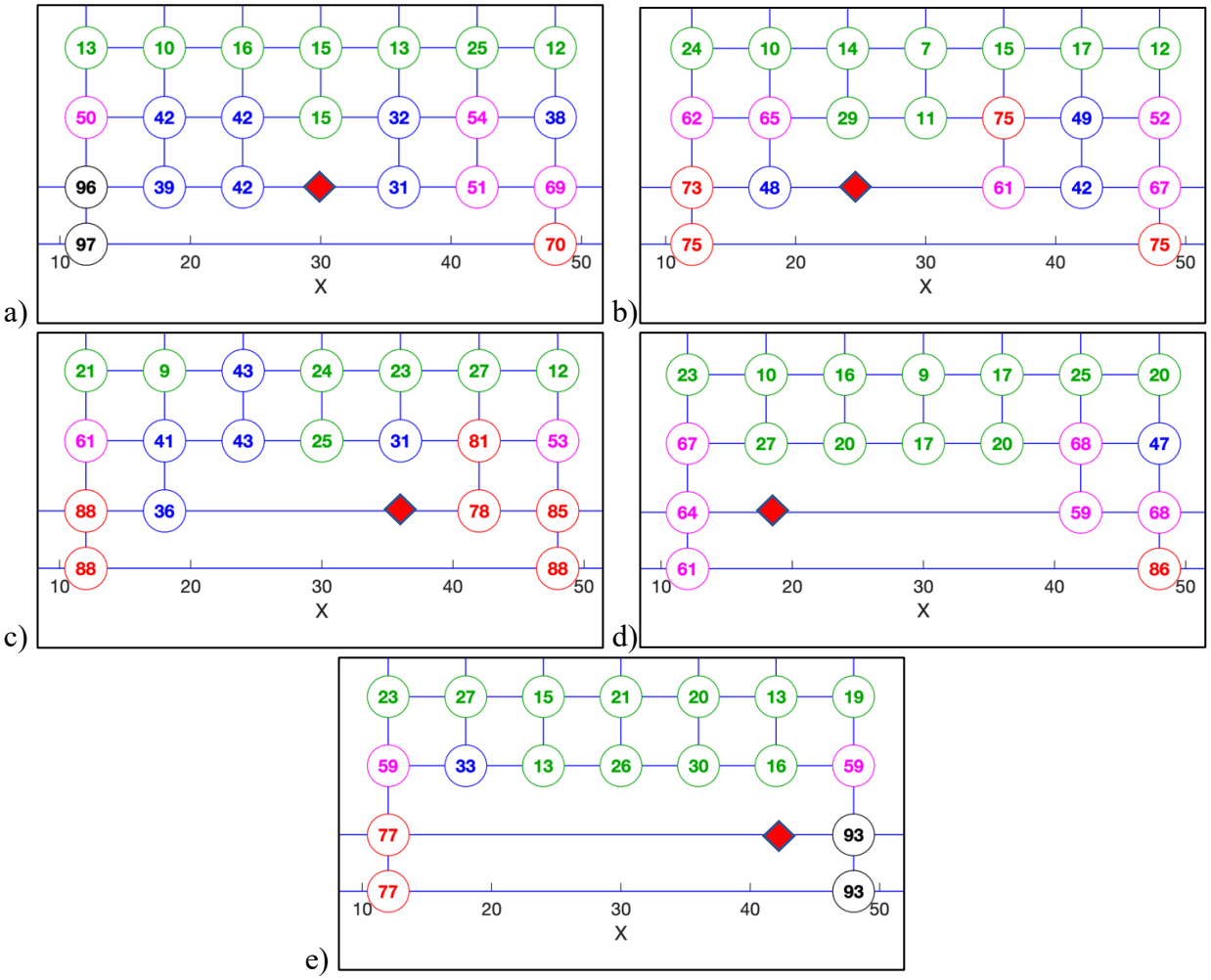

Figure 4-7 Nominal GA Plots for Row 2
a) Zoomed DC7 to 13 b) Zoomed DC7 to 14
c) Zoomed DC7 to 15 d) Zoomed DC7 to 16
e) Zoomed DC7 to 17

4.7 Row 3

Recall that (1) each Row 3 block had the same mass as Row 2; (2) each block removed held two sensor points; and (3) two blocks were removed for DC19 and DC20. Figure 4-8 displays the GA plots for the third row. The full, non-zoomed views are shown due to the increased spread of damage. The first comparison for Row 3 had a cumulative mass loss of 7.05%, and 60 available sensors remaining form the starting 72. For DC7 to DC19 and DC7 to

DC20, the cumulative mass loss was 8.80% and 10.55%, respectively. The final two damage case comparisons also had 56 available sensors for DC7 to DC19 and 52 available sensors for DC7 to DC20. Since the final two comparisons saw the largest change in mass and available sensors, the GA plots show a greater change in-between the 3 plots corresponding to Row 3. A greater number of non-green node points begin to appear and become more dispersed, and overall node values are higher on average than compared to DC7 to DC8.

Throughout the GA plots for Row 3, the longitudinal points aside Rows 1 and 2 maintained the highest values. More and more node points with higher values appeared as damage progressed. This overall increase in high values outside the expected damaged area lowered the ratio of the target vector values below the expected threshold provided in Table 4-4. This skew might also be due to the loss of damaged area sensors, doubled or quadrupled in these cases, which is certainly shown in the lower maximum damage values. The outlier at Node 58 appears at 29% to 50% in all damage case comparisons.

Table 4-4 Row 3 Criteria (Nominal)

Damage Case Number:	DC7 to DC18	DC7 to DC19	DC7 to DC20
Criterion 1: Fitness Value	**2.6987**	**2.78**	**2.6639**
Avg. Error per Sensor	4.50%	4.96%	3.70%
Best Damage Index from GA (1.00):	(12) diffkR	(16) CDFR	(15) CDFS
Criterion 2: Max Damage Value	**90.82%**	**77.73%**	**71.72%**
AVG. (zeroes):	16.32%	22.41%	19.52%
AVG. (ones):	43.72%	44.46%	42.66%
Criterion 3: Zeroes/Ones	**2.680**	**1.98**	**2.19**
Criterion 4: Judgment	**accept**	**accept**	**accept**

Despite the issues with the Row 3 results, the GA plots are accepted for all three cases. An inspector would know where to start looking for damage; while DC7 to DC18 is a bit conservative, DC7 to DC19 and DC7 to DC20 are a bit liberal. The locations of the latters' false positives may indicate a possible mode match issue.

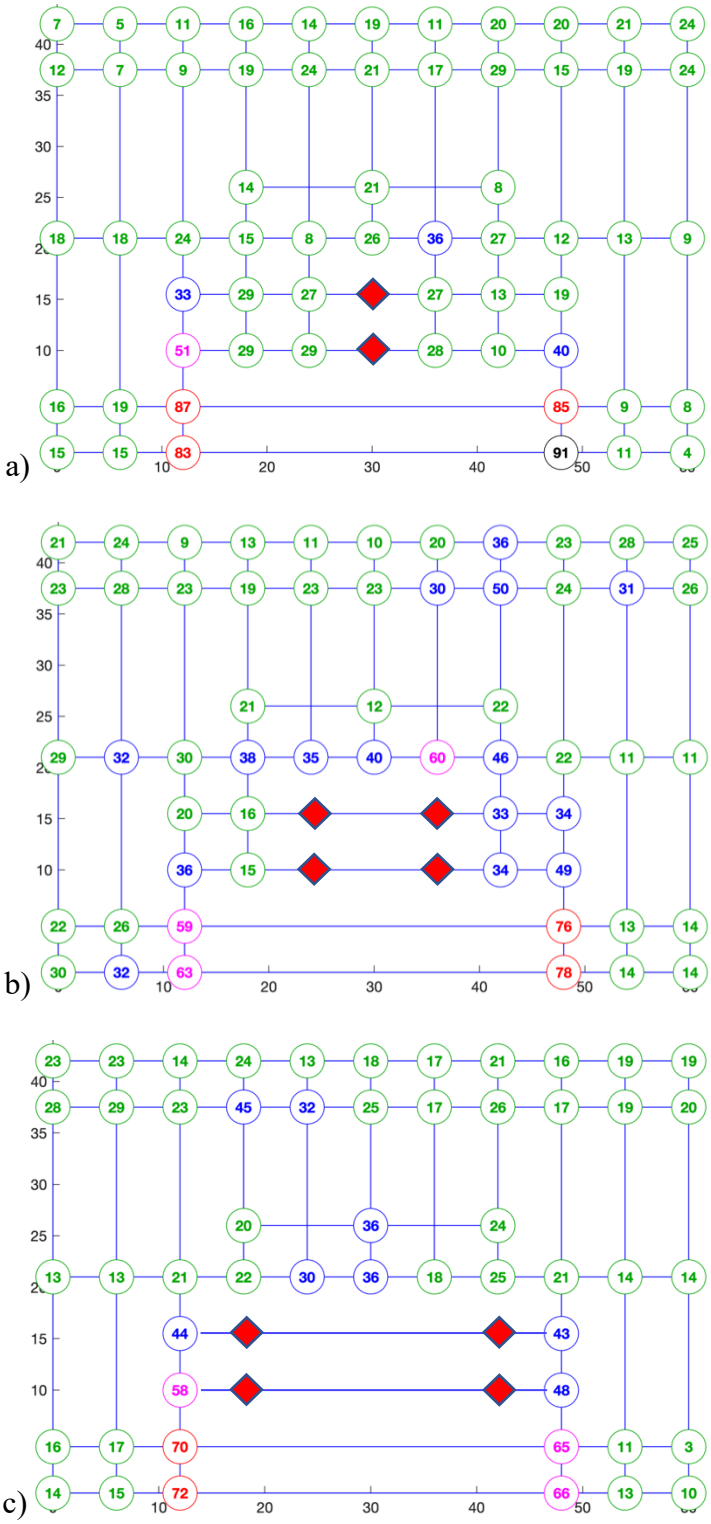

Figure 4-8 Nominal GA Plots for Row 3
a) DC7 to 18
b) DC7 to 19
c) DC7 to 20

4.8 Discussion of Modes

The thirteen damage cases for the mass loss portion were also analyzed under Chapter 3's "Cleansed" subset. From the modes used in this chapter (the "Nominal" subset), better fitting modes were selected as the cleansed subset. A better fit would require a more experienced user but should mean improved damage detection. Upon comparing the GA plots for the Cleansed subset to the Nominal subset, few differences were noted. For instance, Figure 4-9 shows a side by side comparison of the two subsets for DC7 to DC13. Both are successful, but the Nominal subset shows more asymmetry, likely caused by one of the four eliminated modes. Another difference is that the higher average damage values near the mass loss area as well as the lower fitness value for the Cleansed subset. The outlier is certainly much more prominent in the Nominal subset.

An argument could be made that the Cleansed subset technically is a better fit; however, the fit is not a significant improvement from the Nominal subset. The damage within the slab is still adequately located, and the severity is reasonable. Thus, for this particular damage subset comparison, it is not necessary to improve upon the initial mode matches by narrowing down the set of matched modes.

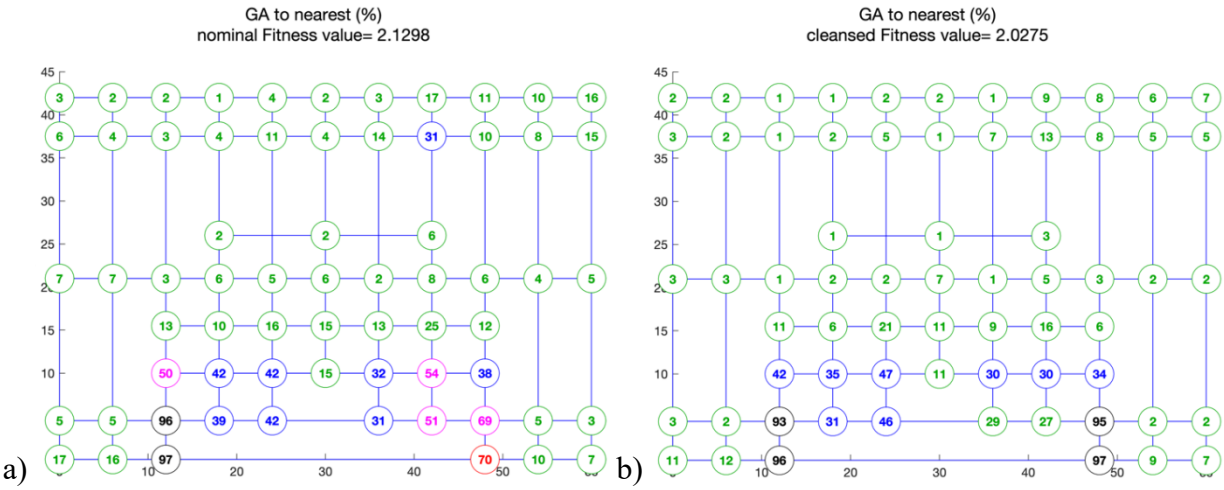

Figure 4-9 DC7-DC13 GA Plot Subset Comparison
a) Nominal (12 modes)
b) Cleansed (8 modes)

The comparisons and contrasts determined between the Nominal and Cleansed subsets for DC7 to DC13 also apply to the remaining twelve damage cases for the mass loss portion. The average damage values for both subsets varied but were still approximately the same for all damage cases. The outlier might have been stronger in one or the other subset, but it still remained. The results from the two subsets show the consistency in the capabilities of the SHE™ program: each subset used a different number of matched modes and still provided accurate results. This outcome translates well for full scale structures. Accessing areas of certain structures can be difficult or impossible which means less available sensor locations. Having less locations can cause the user to miss certain mode shapes and therefore have less mode shapes to match. This analysis determined, that even with limited data, the damage location should provide relatively accurate results for this slab.

4.9 Conclusions

All cumulative damage GA plots displayed appropriate damage location and severity for the mass loss portion. From DC8 to DC16, the four criteria for choosing GA plots were used to

analyze damage detection. The same criteria for DC17 to DC20 comparisons showed values that were outside of the threshold used for the experiment despite the plots being adequate. One cause for the negative results could be that the subjective thresholds need to be adjusted: the most drastic mass and sensor loss take place between the last four cases.

Mode matching is always a challenge, and less sensor points also leads to less smooth mode shapes. The smoother a mode shape plot is, the easier a user can define and match it. For this experiment, enough sensor points were present for all cases to visually determine mode shapes; however, the GA was forced to work with less and less points which may have slightly skewed the results. Figure 4-10 shows the change in the criteria for different damage cases as sensors were lost. The target vector ratio did not show any trends of loss of accuracy until after DC17 when it declined. The maximum damage value showed no trends at all for every DC. The fitness value did seem to react similar to the target vector ratio. After DC17 the fitness value began to steadily increase, thereby indicating a lower fit. Therefore, the target vector ratio and fitness value do show slight trends towards the end of the damage cases, but not enough data was taken in order to draw conclusive results on a link between available sensors and accuracy of damage detection. The average error per sensor is therefore used in order to quantify the accuracy of the results.

Table 4-2, Table 4-3, and Table 4-4 provide the average error per sensor. The averages of this error for Rows 1, 2, and 3 were 2.54%, 3.15%, and 4.38% respectively. This trend shows the increasing error of the available sensors as node points were removed. Thus, the sensor error did increase as damage progressed; however, the final error remained a reasonable level in order to consider all GA plots accurate.

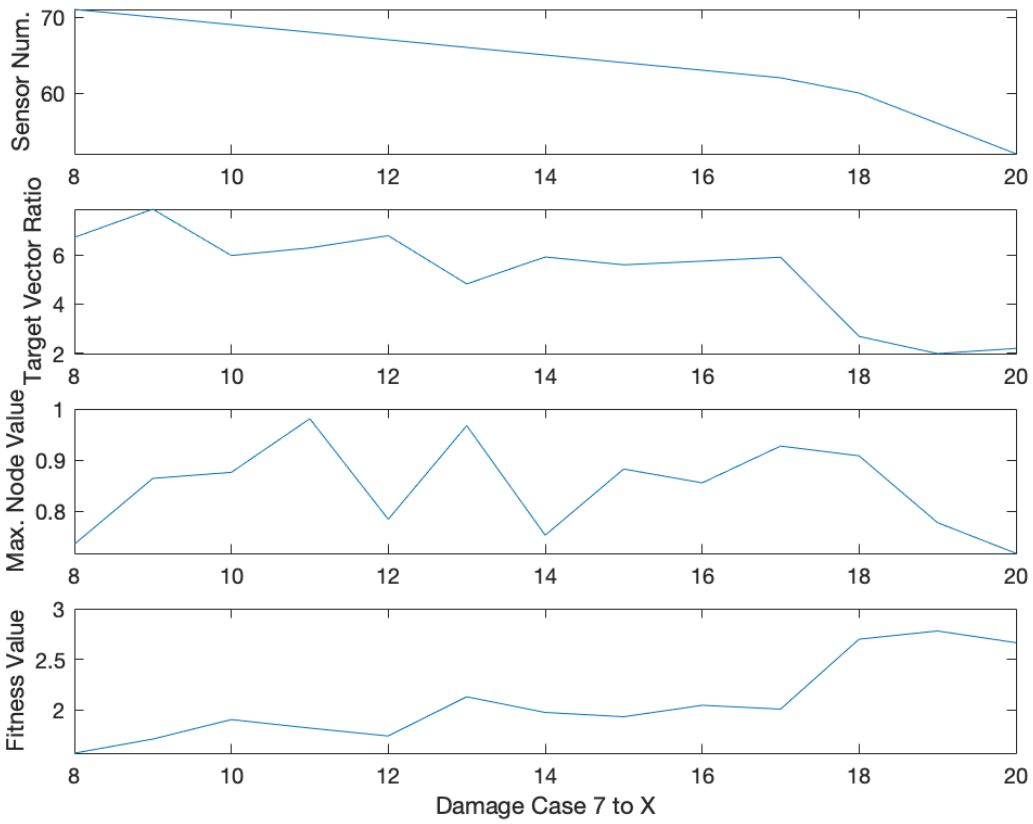

Figure 4-10 Damage Criteria by Sensor Loss Comparison

One last factor that contributed to the decrease in passing criteria was the spread of higher damage values on the slab. The damage spread greatly affected the target vector ratio criterion. Throughout the experiment, the target vector had values of 1 for all sensors points immediately above and aside the damaged area. As seen in previous GA plots, the highest damaged values were in the same location as the values of 1 set in the target vector. The further the damage progressed, the more dispersed points with higher damage values became. By the last damage case, several high damage values were outside of the expected damage area for the target vector. The varied damage led to a lower ratio of the 1 to 0 values of the target vector since an increased number of higher damaged values did not match the values assigned 1.

The majority of results from Chapter 4 proved to be reliable and reasonable. The accuracy of damage detection was adequate even with the loss of sensor points. This analysis was stopped after block 15 was removed with the idea that damage location would be impossible to miss by an inspector on a full-scale bridge. The later tests show that even with significant mass loss damage detection is still possible; however, significant mass loss is usually easier to detect than significant stiffness loss. For this reason, no further testing was deemed necessary for this analysis.

5. CONCLUSIONS

5.1 Summary

Visual inspection is a primary tool for evaluating bridge health. A tool designed to aid bridge inspectors is the SHE™ program, which determines damage location and severity from time data. This research provides insight into a progressively damaged 1200-pound reinforced concrete test slab. Tri-axial accelerometers captured data and mode shapes were analyzed to first compare two different boundary conditions of the undamaged span.

The slab was damaged in such manners as to simulate both stiffness and mass changes. The slab was first cut with a concrete saw at 8 separate instances. The 8 cuts produced 7 different damage cases, each modeling progressive stiffness change and representing cracking found in most concrete bridge decks. Using the grid pattern made from the cuts, a demolition hammer then removed blocks of approximately known mass. The total of 15 extracted blocks created an additional 13 damage cases, each modeling progressive mass decrease as found with concrete spalling over time.

Data processing included a genetic algorithm using 24 damage indices to compare a total of 21 different damage states. An optimized plot of the central test slab showing damage location and severity was output for each comparison, and the results were similar for both stiffness and mass change cases. Damage location was accurately determined in and around the areas where cuts were made and blocks had been removed. Damage severity was more accurate for the stiffness change cases over the mass loss cases. The Curvature Difference and Strain Energy

Difference provided the best average results for both stiffness and mass changes. Overall, curvature proved sensitive to damage.

Note that the specific results from this analysis apply to this experiment's test slab, but the procedure can absolutely be repeated for other infrastructure. This is especially valuable as more bridges as more reach or exceed their intended lifespan. Knowledge of where and when to make repairs can assist inspectors and asset managers.

5.2 Results and Discussion

Worley's 2014 study altered global boundary conditions for the same slab in this analysis. His findings suggested that the modal parameters of the slab were sensitive to any change in boundary conditions [22]. The results herein compared the FRF plots and matched mode shapes. Recall that after the 2014 study, the scale model bridge was disassembled, moved, and reassembled. Few similarities were determined in the FRF plots, and only one pair of modes were somewhat successfully matched although approximately 14Hz different. Therefore, the two studies were incomparable. In fact, a field study on a bridge deck revealed that natural frequencies can vary up to 34% when undergoing boundary shifts [23].

Four decision criteria were developed in order to determine the accuracy of damage detection. The GA results are first evaluated by fitness value to ensure an acceptable fit. Then relative maximum damage value and target vector ratio show variation above noise levels. Lastly, a subjective judgment call by the experienced inspector determines if the result is reasonable.

Multiple mode subsets were examined for the seven damage cases created by artificially cracking the slab. The Nominal subset was the first subset processed for each damage case comparison and consisted of all mode matches performed by a potential user. All plots from the

Nominal subset displayed relatively accurate damage location and values. The stiffness change analysis then shifted to a sensitivity analysis on mode selections: eight subsets were created for 3 separate damage comparisons. The results were purely mode shape based and showed that the Nominal subset was most consistently accurate for relative damage detection and severity. Analysis of the remaining 7 subsets still revealed that the optimal subset was the Nominal subset; therefore, GA is capable of producing relatively accurate results even without optimized matched modes. A possible reason for the GA providing positive results could be due to the crack width in the slab. The scaled crack width would be approximately 3 inches for a full scale bridge, which is a relatively large amount of damage. Thus, damage detection is more defined.

Fifteen blocks were removed from the slab to generate 13 additional damage cases. When compared to the fully cracked baseline of Damage Case 7, all DC8 through DC17 GA plots displayed appropriate relative damage location and severity. Rows 1 and 2 represented maximum slab mass losses of 1.79% and 6.17%, respectively. Row 3 had a total of 10.55% mass loss, and later cases did have some introduction of error as damage dispersion. The likely reason was a loss of sensitivity due to instrumentation. As each block was removed, at least one sensor attachment point was lost: data capture locations decreased from 72 nodes to 52 nodes.

Two mode subsets were also examined. The result for a reduced subset was qualitatively the same when compared that of the Nominal subset. Similar to the stiffness change cases, this conclusion supports the effectiveness of the GA despite a varying number of matched modes.

5.3 Significance

An important component which makes SHE^{TM} quite versatile is that it uses any time history data for processing results. Thus, it can analyze dynamic responses from most sensors for most materials. This versatility is important because the experimental set-up for this study will

not suit every structure; however, the same order of processing data can be repeated. Note that the results from this analysis apply only to the test slab in this experiment, but they may suggest possible responses from similar structures.

For instance, the concrete used for the test slab possessed a yield strength of approximately 7000psi, making it relatively stiffer than most concrete mixes used in full scale bridges. If a replica of the test slab were poured with 3000psi concrete, stiffness differences are expected to cause modal response changes but likely subtle ones. However, the SHE^{TM} program will run likewise and output results for the new slab, and expectations are that similar relative severity detection will occur. At this time, though, no predictions for a full scale bridge are made on damage indicators or even damage sensitive features.

When considering full scale active structures, permission for access can be difficult to obtain. Administrative approval and traffic control are often barriers to data collection. In order for damage detection to be possible using SHE^{TM}, at least two states of data must be acquired. The first set would ideally be collected at the time of completion for the respective structure in order to establish an undamaged as-built baseline. The results from this analysis support that continued intermittent data collection as inspection will yield results for damage detection. A second set of data could also be obtained at any point in the future after a structurally damaging event. Either method will help inspectors to monitor and diagnose bridge health.

Understanding what feature of a structure best demonstrates damage is valuable to engineers and researchers. The SHE^{TM} program ranks all 24 calculated resultant DIs in order of how well each DI fit the final GA plot. For all damage cases and all subsets, a minimum of one DI possessed a 100% (or 1.0) relative match to the GA plot. Figure 5-1 displays the total counts that a particular DI was chosen as the comparisons' best fit, also known as the optimal DI. Note

that Figure 5-1d is a bar chart for all DIs that were ranked second in overall match: second best matches can potentially be 80%-99% matched and thus be included.

The most popular algorithms were curvature algorithms: difference ($Diff_kS$ and $Diff_kR$) and damage factor (CDF_kS and CDF_kR). DI numbers 9 through 16 in Table 3-1 utilize curvature and were chosen for 12 out the 20 total damaged case comparisons. Additionally, the difference algorithm was chosen 15 out of the same 20 damaged cases, making it the most popular method of calculation.

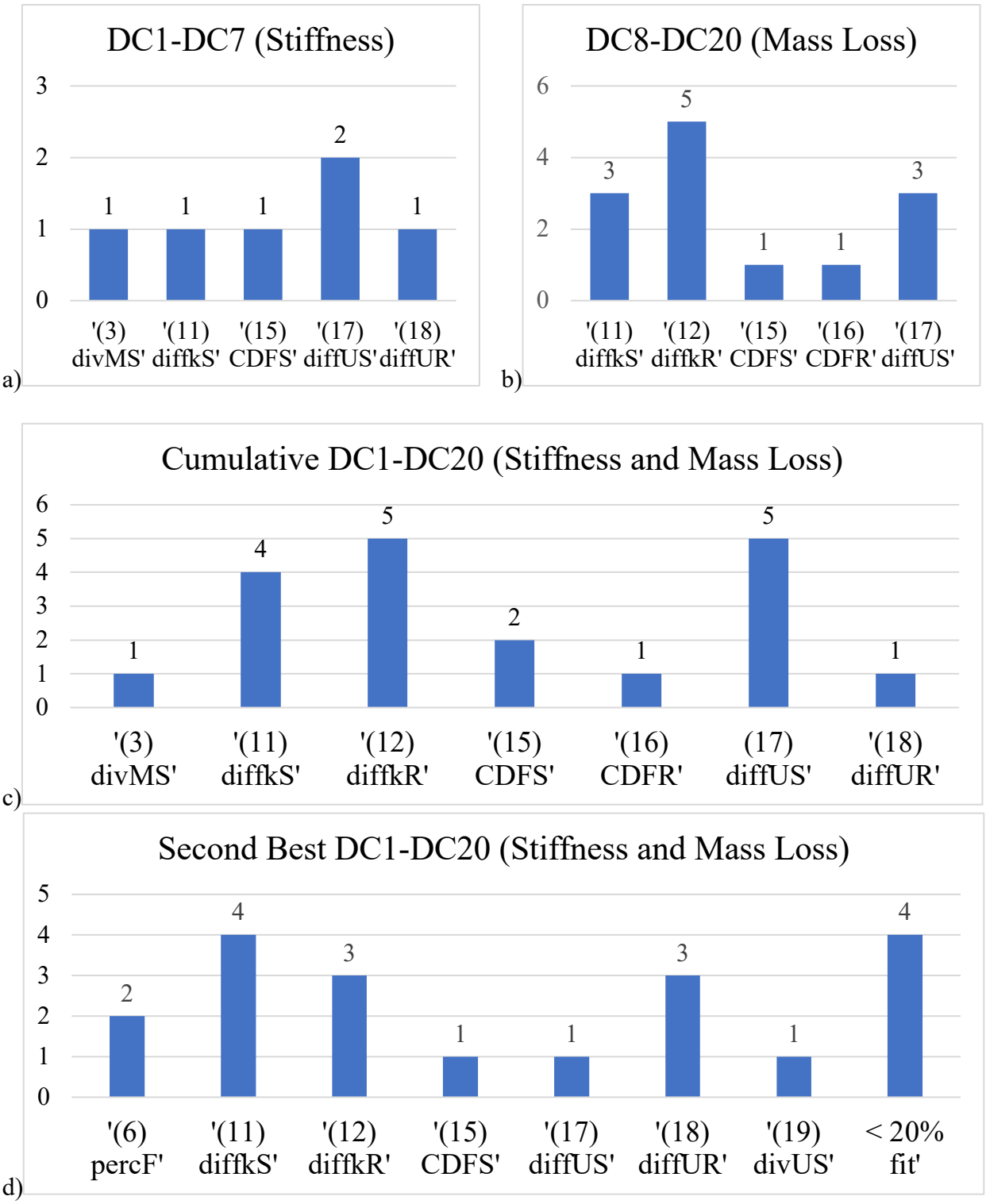

Figure 5-1 Count of GA-Selected Damage Index for All Nominal Cases
a) Optimal Stiffness Cases DC1-7 b) Optimal Mass Loss Cases DC8-20
c) Optimal & d) Second Best Stiffness and Mass Loss Cases DC1-20

5.4 Lessons Learned

- Shifts in boundary conditions matter and can mask smaller relative damage detection for stiffness or mass changes. Moving the same bridge assembly between 2014 and 2019 prevented frequency comparison.
- Data acquisition choices have an enormous effect on damage detection ability. Signal noise levels can mask small physical shifts.
- The Baseline to DC1 comparison was rejected, perhaps due for two reasons. The first is a shift in the slab, and thus boundary conditions, during the initial cut. The second reason is potentially the relatively low damage induced.
- The four decision criteria should be used to describe the overall result from any GA analysis. The thresholds will most definitely need to be changed if applied to another structure.
- The GA output plots are valuable in cracking and spalling cases. Excessive spalling might cause a problem due to sensor loss. Additionally, the GA method worked well for several matched mode sets, which bodes well for algorithm stability.
- The curvature parameter was chosen as the optimal damage sensitive feature, and difference was the best algorithm. Thus, for this structure, curvature could be further examined to extract more local information.

5.5 Future Work

This experiment analyzed a reinforced concrete slab, the results from which might be similar to other active or experimental concrete structures. While an older version of SHE^{TM} has been used in the past on full scale structures, the newly improved version used in this analysis has not. The newest form of SHE^{TM} is fully capable of operating on full scale structures

though changes in parameters within LabVIEW would be required. Adaptive testing techniques would also aid in damage detection. That is, the sensor layout for the first round of analysis may include evenly spaced points which would cover the entire bridge deck for example. In order to save testing time, the initial sensor point layout would possess relatively large spans between each point. After damage is located, a second round of testing would utilize a more concentrated sensor layout in the area of damage.

The SHE^{TM} program is not limited to concrete materials only. Even with similar geometries, steel structures are unlikely to show similar results to this analysis: the modes may have entirely different characteristics due to the material properties, frequency differences, and noise levels. A previous study using an earlier version of SHE^{TM} without GA noted that damage detection varied too greatly for a laboratory-sized structure [24]. Thus, future work should examine the DI choices and accuracy of the SHE^{TM} program for scaled structures built primarily of steel as well as full scale structures built from various materials.

The spatial and resultant difference in curvature DIs showed positive results in damage detection for this analysis. The same DIs may work well for damage detection for similar bridge deck structures, even if different steel and concrete combinations, but the remaining 22 DIs should not be disregarded either. In addition to physical differences, the difference in curvature DI was not always the best match (8 to 20). Accurate damage detection was still achieved for all Nominal subset damage cases despite which DI was chosen as the best match.

SHE^{TM} with GA is largely responsible for the consistent positive damage detection results; however, it does currently require a human component in order to match mode shapes and create a target vector. Matching among mode shapes is performed using visual inspection by an experienced user. This work does not provide mode matching techniques; future work will

attempt to automate the mode matching process. This would make the SHE™ program and detection process more user friendly in a non-laboratory setting for less technically experienced users. The binary target vector is also chosen by an experienced user with physical understanding of the damage. This analysis does not discuss choosing target vector techniques or experiment with different target vector orders. Future work may automate the target vector as well as test the effectiveness of non-binary target vectors [27].

Ultimately, a single software package is desired for various companies and agencies to use in order to determine relative damage severity. Automating the mode matching portion will remove the need for a user to undergo specific training in order to use the program. Also, developing an algorithm which will choose a target vector will eliminate the need for an inspector to know or assume where existing damage locations.

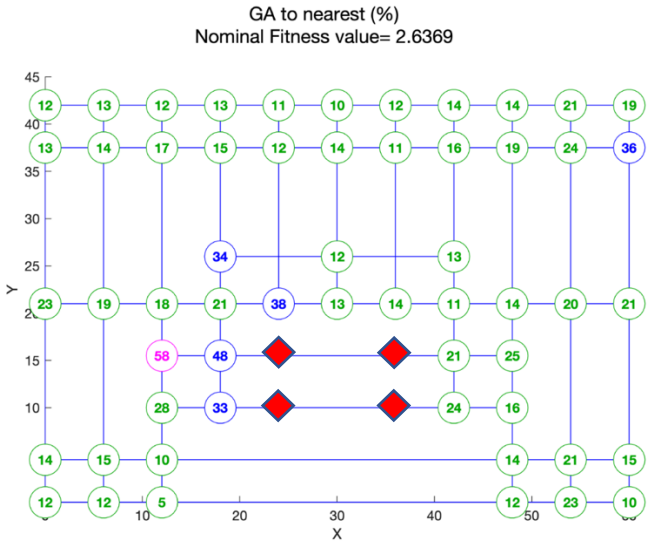

Figure 5-2 DC18 to DC19
(High Damage, Sequential)

The need for intermittent inspection without an as-built baseline is also important. A challenging comparison of incremental damage is shown in Figure 5-2; this sample sequential comparison tests the accuracy of SHE^{TM}. The GA results from DC18 to 19 did not meet qualitative expectations as the 58% maximum occurred in the wrong location. Six damage values were over 30 percent, barely confirmative; of the 6 values, only 3 were appropriately located next to the mass loss area. Even though this was only a single analysis, the results suggest that using a relatively high damage condition as a baseline for damage detection may yield inconclusive results for this slab.

a)  b) 

Figure 5-3 Node 58 Demolition
a) Partial Damage
b) Full Damage

Upon completion of all 21 data acquisitions, no further damage was scheduled for the test slab in this experiment. Node 58 was the consistent outlier point of nearly every mode shape was further examined. As shown in Figure 5-3, this region was cut, chipped, and examined. No signs of internal cracking, air pockets, or irregularly sized aggregate were found. No signal interference was detected, so the presence of the reoccurring outlying point is unknown.

LIST OF REFERENCES

[1] Prasad DR, Seshu DR. Study on change in modal parameters of RC beams due to fatigue type damage. Asian J Civ Eng 2010;11:521–32.

[2] Moore M, Phares B, Graybeal B, Rolander D, Washer G. Reliability of Visual Inspection for Highway Bridges (FHWA-RD-01-020). vol. II. 2000.

[3] American Society of Civil Engineers. ASCE 2017 Infrastructure Report Card. 2017.

[4] Roberts R. Inside the Bridge Inspection Toolbox. Artic Struct Test 2015:28–30.

[5] Wisconsin DOT. Structure Inspection Manual, Part - NDE and PDE Testing, Chapter 10 - GPR. 2014.

[6] MATEST. Ultrasonic pulse velocity tester. Matest Co 2019. http://www.matest.com/en/product/c372m-ultrasonic-pulse-velocity-tester (accessed April 1, 2019).

[7] Pešić N, Živanović S, Dennis J, Hargreaves J. Experimental and finite element dynamic analysis of incrementally loaded reinforced concrete structures. Eng Struct 2015;103:15–27. doi:10.1016/j.engstruct.2015.07.037.

[8] Kumar SA, Santhanam M. Detection of Concrete Damage Using Ultrasonic Pulse Velocity Method. Indian Soc. Non-Destructive Test. Hyderabad Chapter, 2006.

[9] Ahmed MS. Damage Detection in Reinforced Concrete Square Slabs Using Modal Analysis and Artificial Neural Network. Nottingham Trent, 2016.

[10] Azam MA, Khan QUZ. Experimental Modal Analysis of Reinforced Concrete Girder using Appropriated Excitation Technique. Int J Civ Environ Eng 2015;20:25–33.

[11] Banwell G, Mohr S, Rothberg S, Roberts J. Using Experimental modal Analysis to Validate a Finite Element Model of a Tennis Racket. Procedia Eng 2012;34:688–93. doi:10.1016/j.proeng.2012.04.117.

[12] Womack K, Halling M, Bott S. Static and Dynamic Testing of a Girder Bridge in Salt Lake City, Utah. vol. 13. 2001.

[13] Grimmelsman KA, Eric V, Carreiro JL, Rawn JD. Rapid Bridge Condition Screening by Falling Weight Deflectometer. 2014.

[14] Farrar CR, Duffey TA, Cornwell PJ. Excitation methods for bridge structures. Proc. IMAC 17, 17th Int. Modal Anal. Conf., vol. 7, 1999, p. 1063–8.

[15] Bernal D. Load Vectors for Damage Localization. J Eng Mech 2000;128:1–16.

[16] Gao Y, Spencer BF, Bernal D. Experimental Verification of the Flexibility-Based Damage Locating Vector Method. vol. 133. 2007.

[17] Faizan M. Damage Assessment of Rc Beam in Terms of its Stiffness and Modal Characteristics. J Ind Pollut Control 2017;33:1437–41.

[18] Benedetti A, Pignagnoli G, Tarozzi M. Damage Identification of Cracked Reinforced Concrete Beams Through Frequency Shift. Mater Struct Constr 2018;51.

[19] Nozarian MM, Esfandiari A. Structural Damage Identification using Frequency Response Function. Mater Forum 2008;33:443–9.

[20] Deng Y, Phares B, Harrington D. Causes of Early Cracking in Concrete Bridge Decks. CP Road Map Br 2016:1–6.

[21] Xing S, Halling MW, Barr PJ. Delamination Detection of Reinforced Concrete Decks Using Modal Identification. J Sensors 2012;2012:1–17.

[22] Worley SB. Development and Validation of the Structural Health Evaluation. Master's

Thesis. University of Mississippi, 2014.

[23] Barr PJ, Halling MW, Womack KC. Influence of Changes in Boundary Conditions on Bridge Response n.d.

[24] Baker E. An Experimental Investigation of a Reinforced Steel Frame Via Structural Dynamics. Honor's Thesis. University of Mississippi, 2016.

[25] National Instruments LabView 2018, Austin, TX.

[26] MathWorks MATLAB, R2019a, Natick, MA.

[27] Zeng, Stephen. "Damage Indices Using Genetic Algorithms." PhD Dissertation (pending May 2020), Civil Engineering, the University of Mississippi.

APPENDIX A: BASELINE MODE SHAPE

Mode Shape 1: 1.980Hz

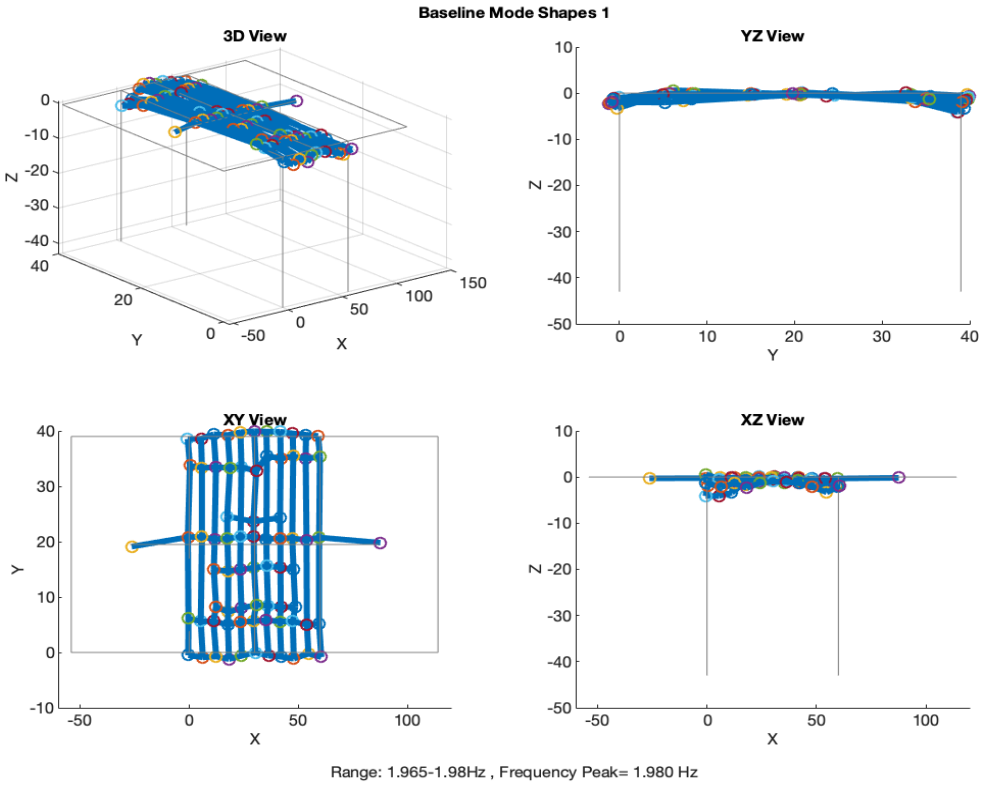

Mode Shape 2: 3.599Hz

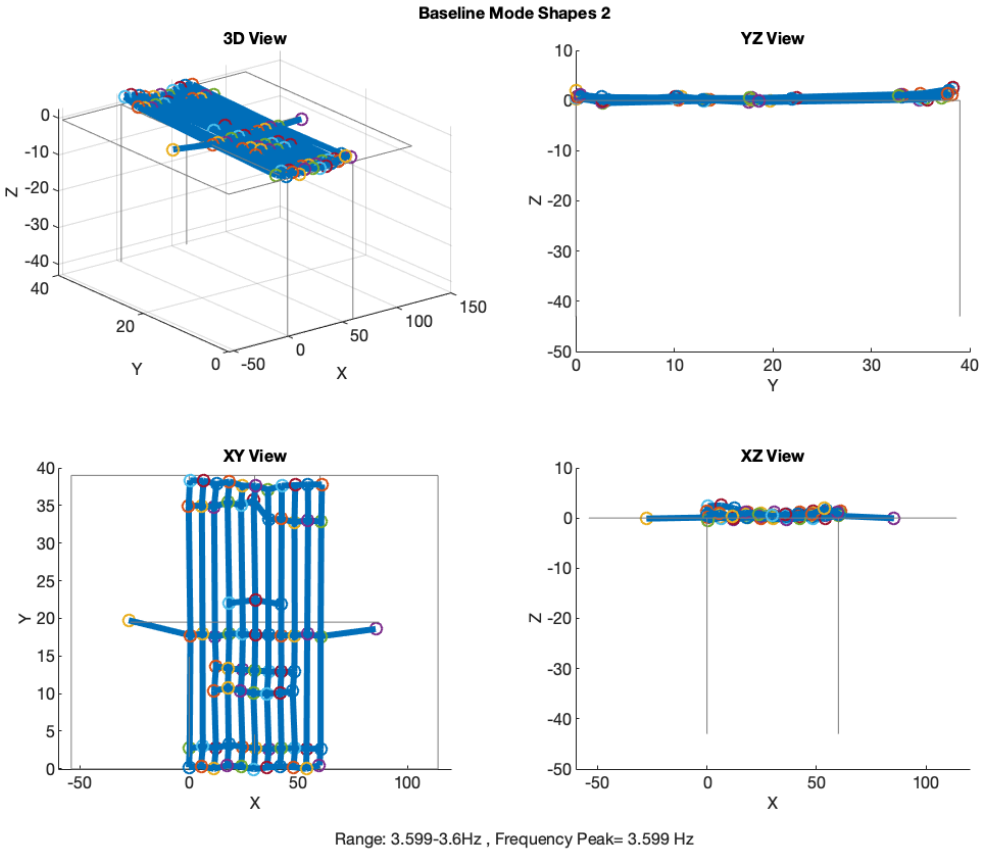

Mode Shape 3: 6.901Hz

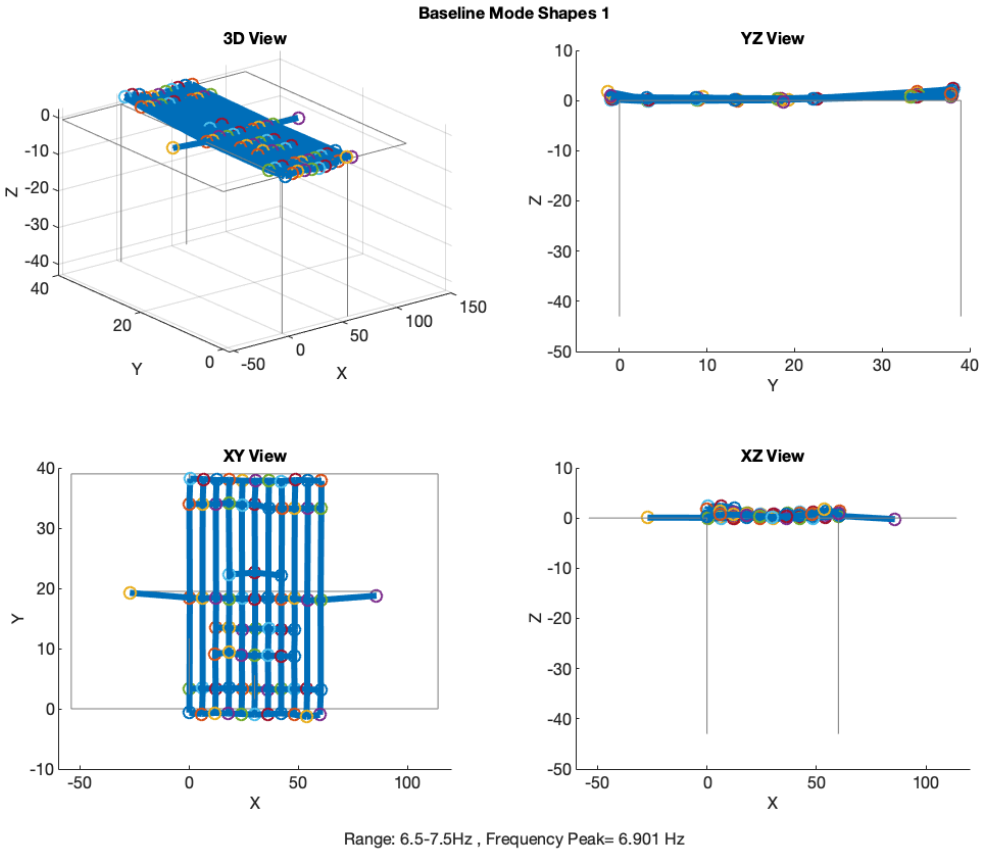

Mode Shape 4: 10.335Hz

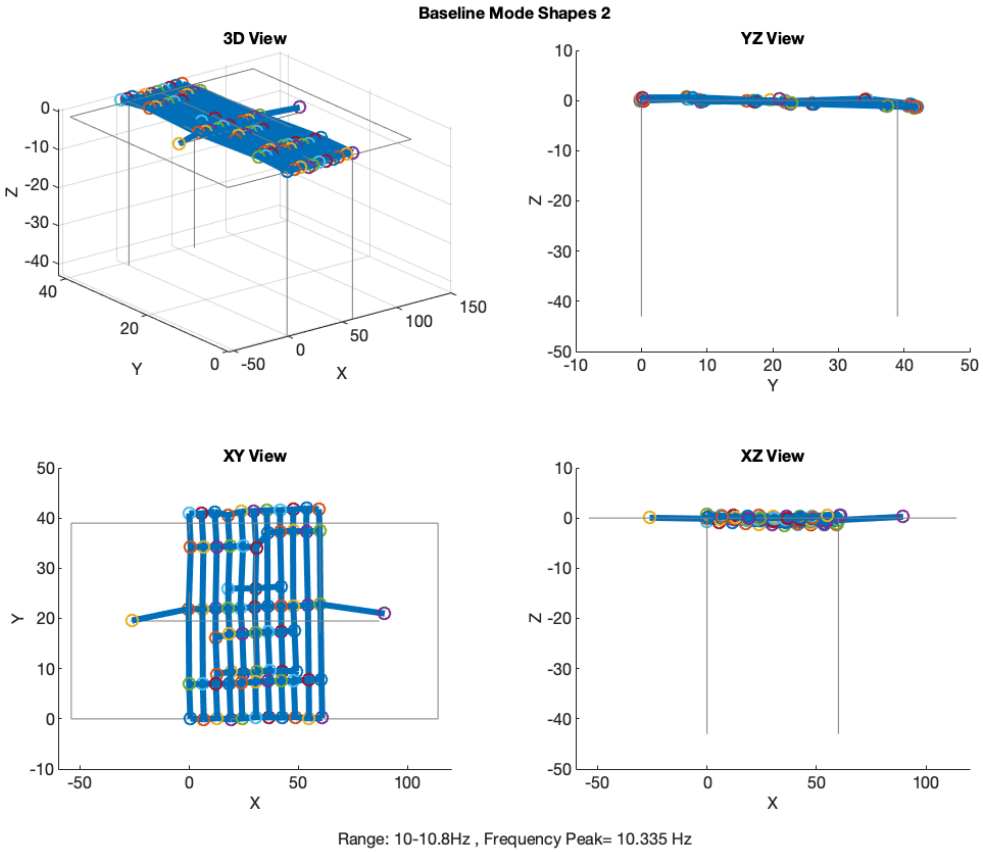

Mode Shape 5: 14.046Hz

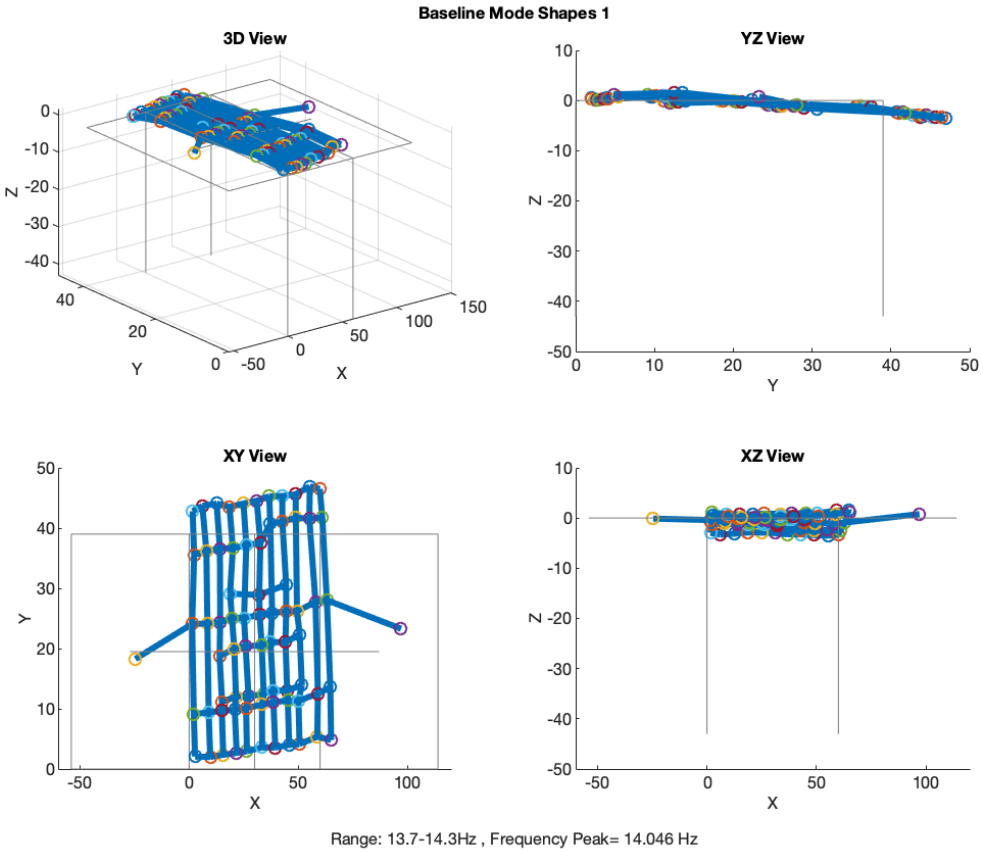

Mode Shape 6: 17.285Hz

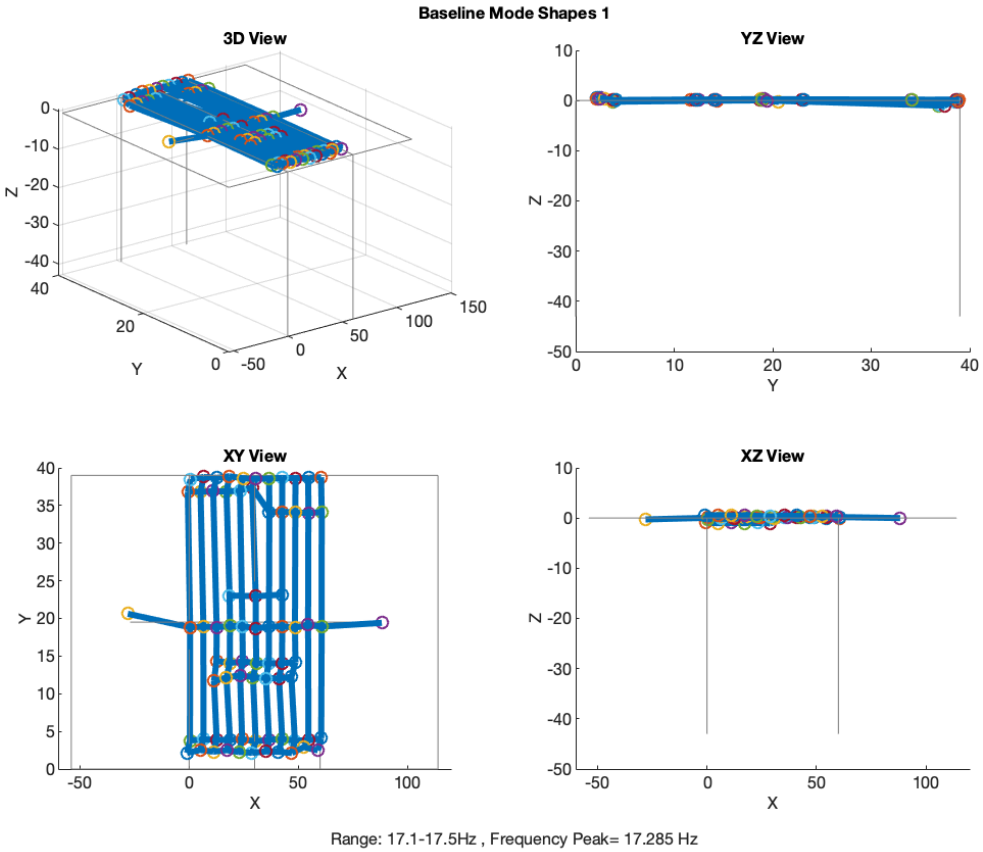

Mode Shape 7: 25.846Hz

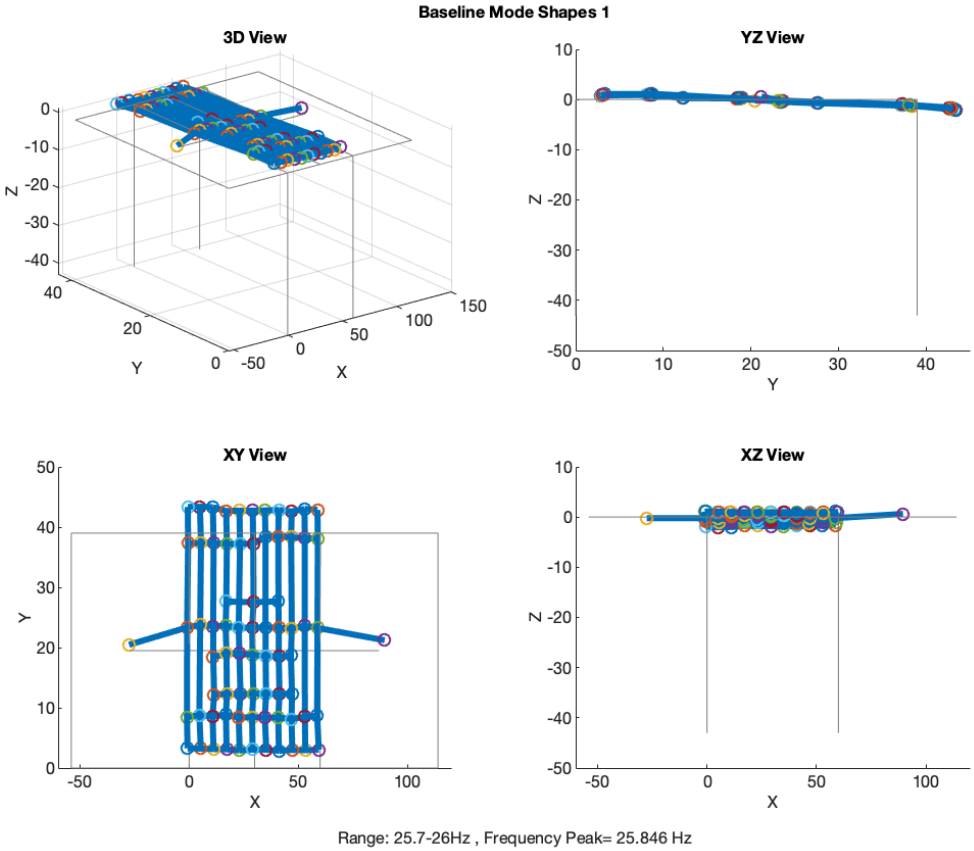

Mode Shape 8: 60.680Hz

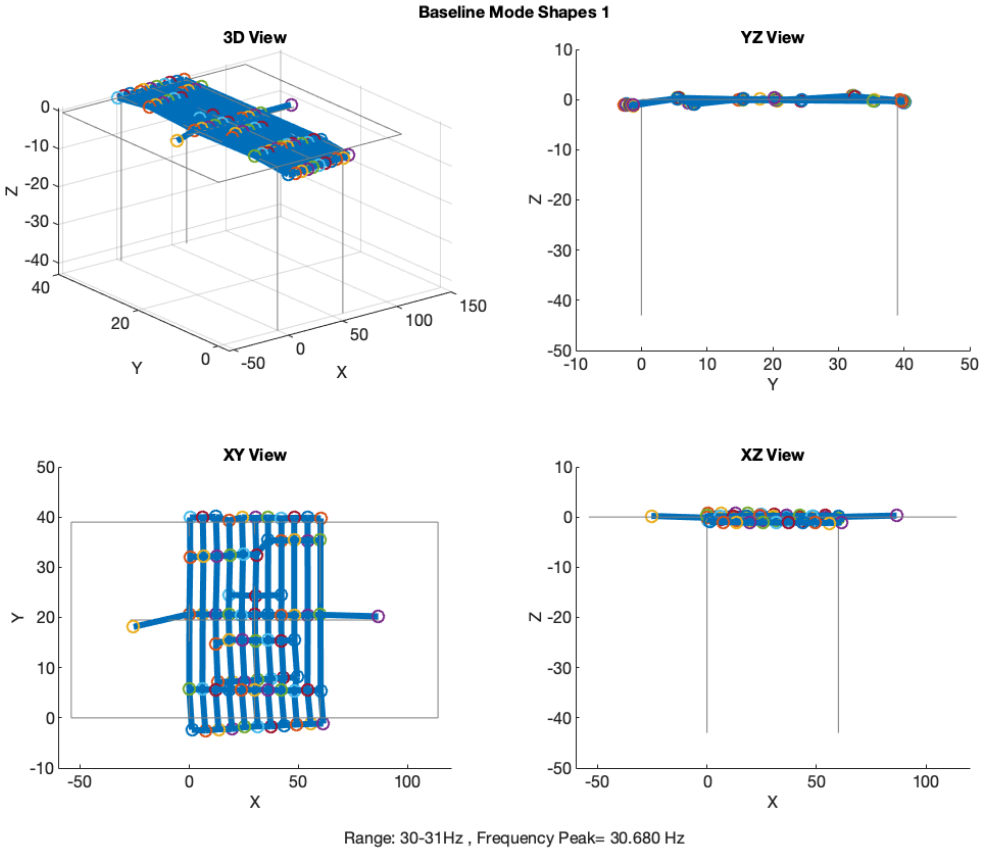

Mode Shape 9: 34.554Hz

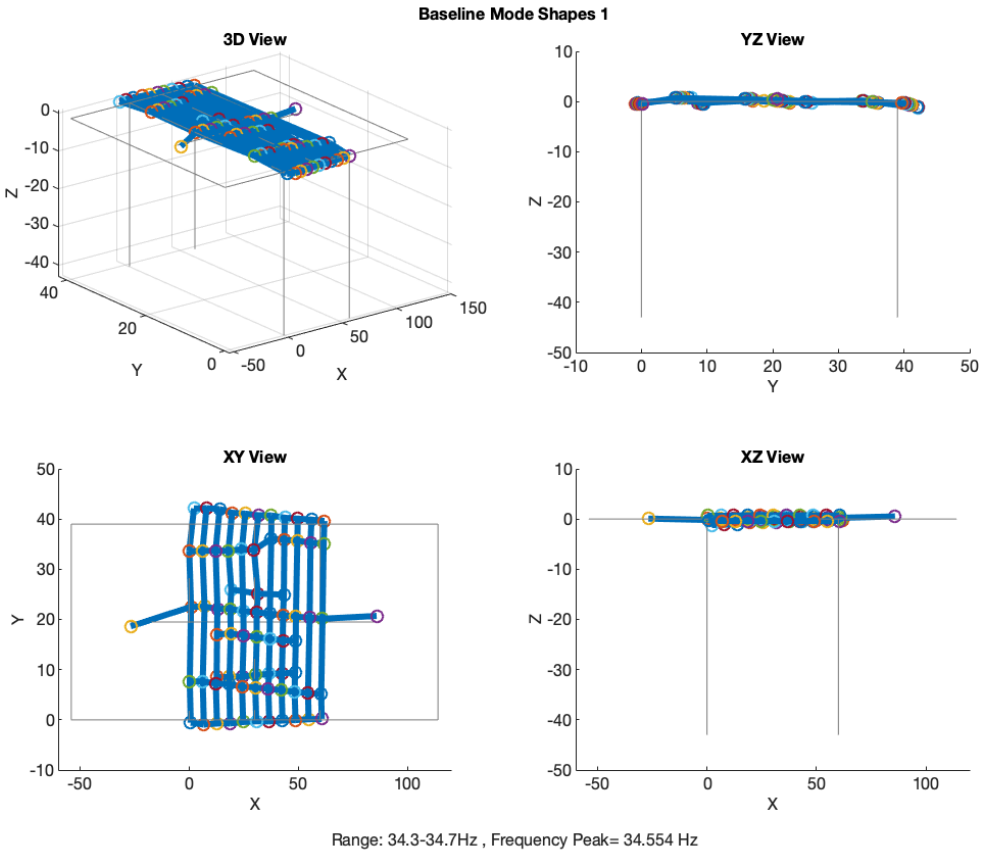

Mode Shape 10: 40.120Hz

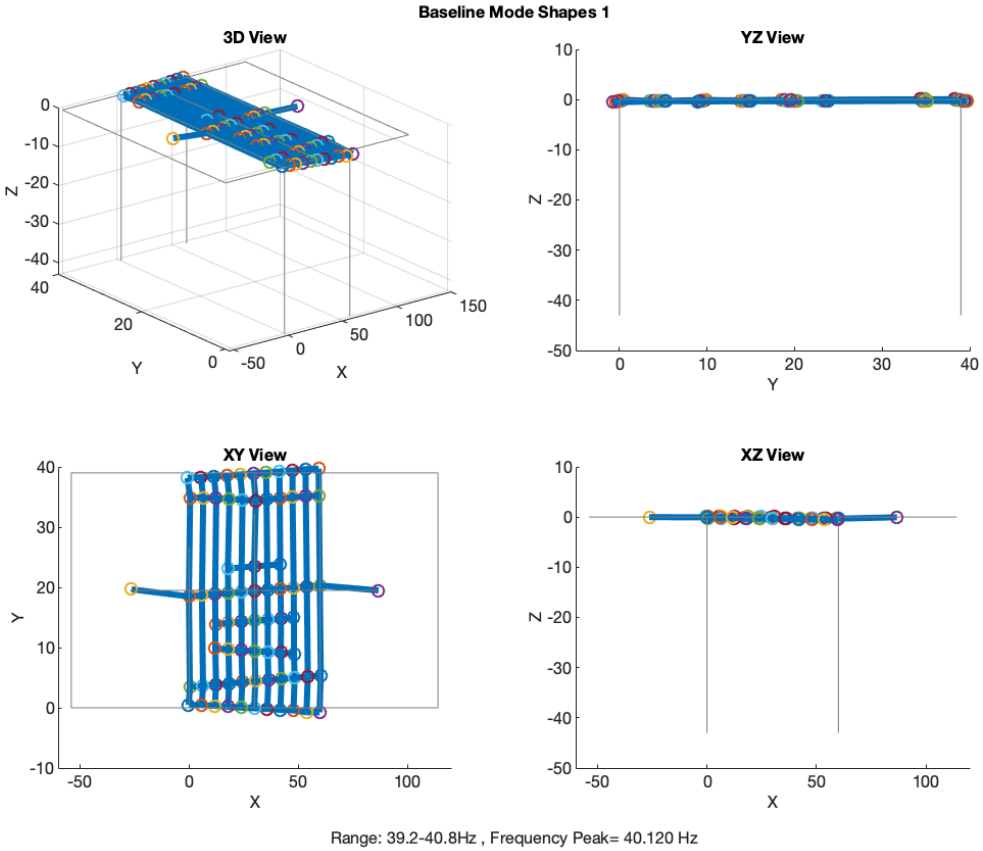

Mode Shape 11: 45.068Hz

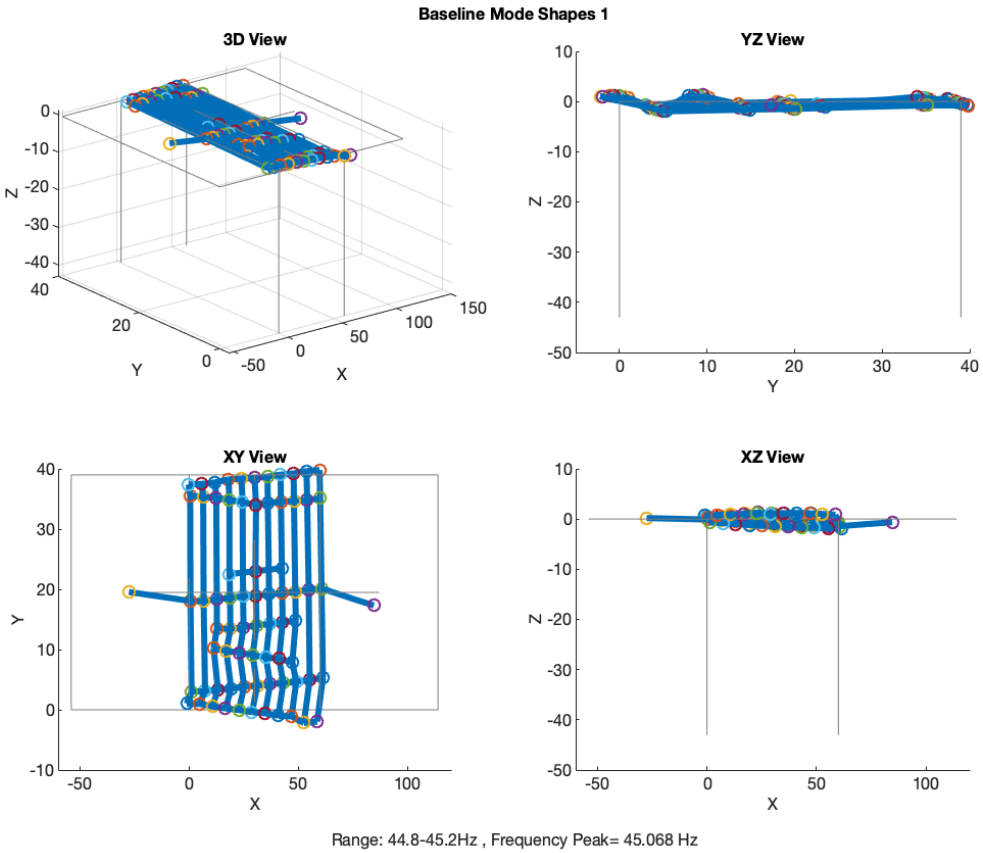

Mode Shape 12: 52.018Hz

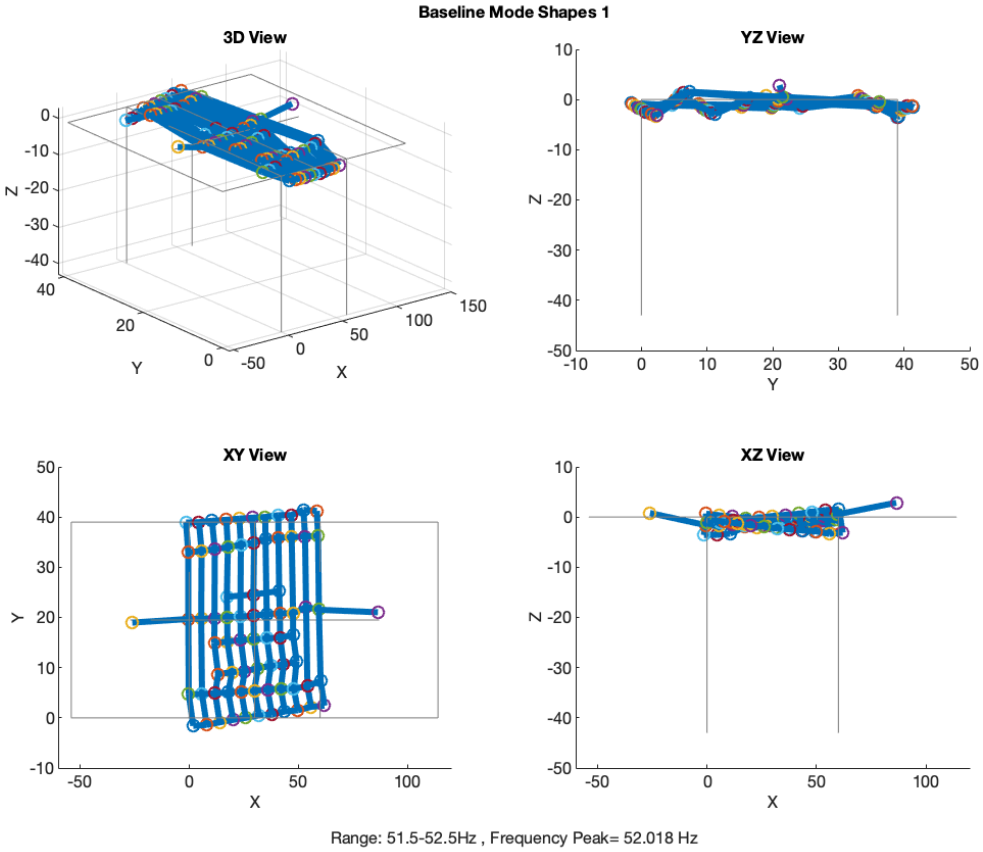

Mode Shape 13: 58.724Hz

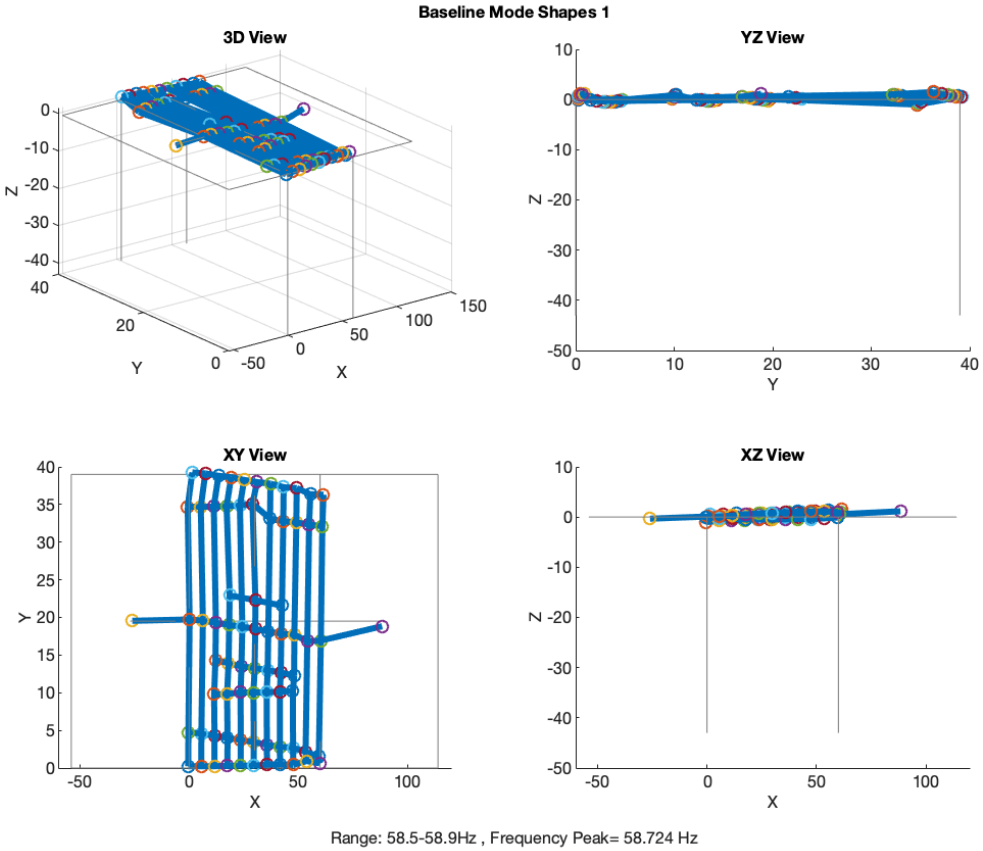

Mode Shape 14: 72.852Hz

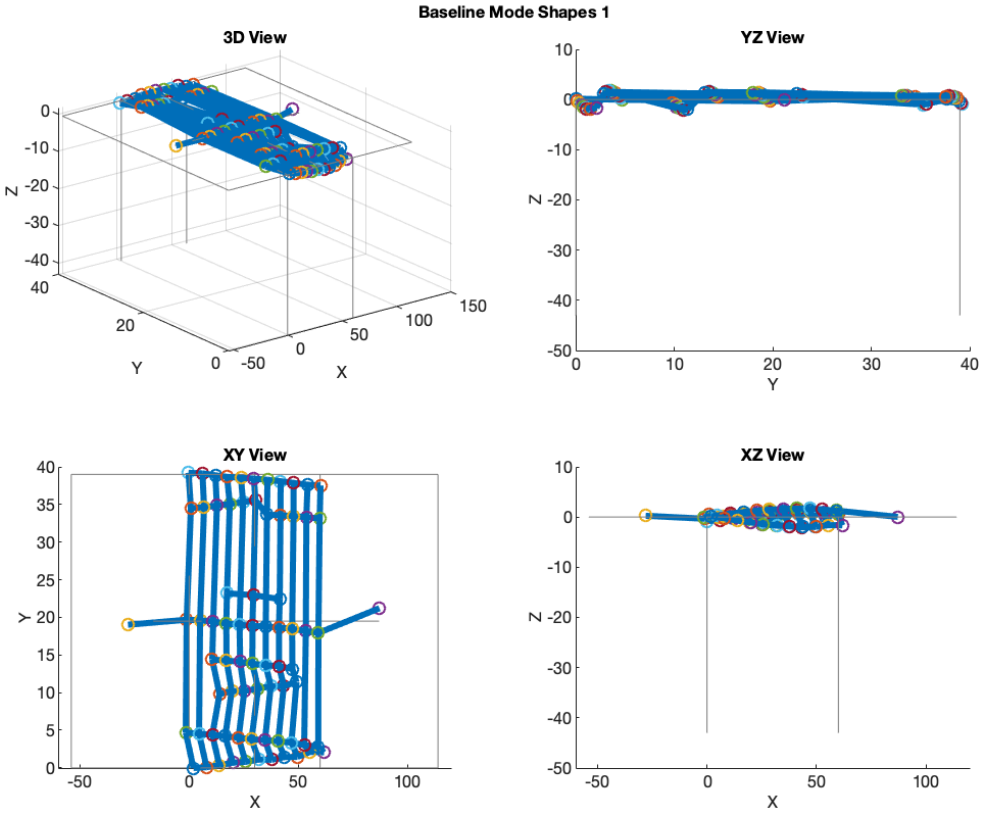

Mode Shape 15: 86.621Hz

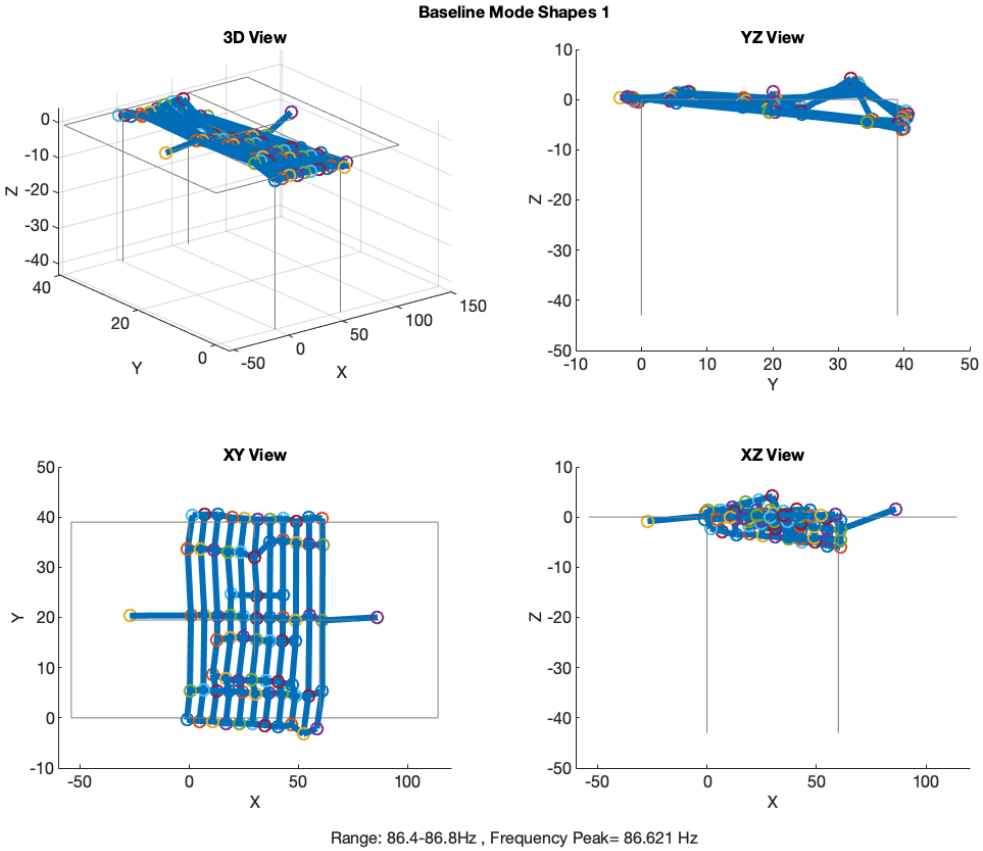

Mode Shape 16: 97.738Hz

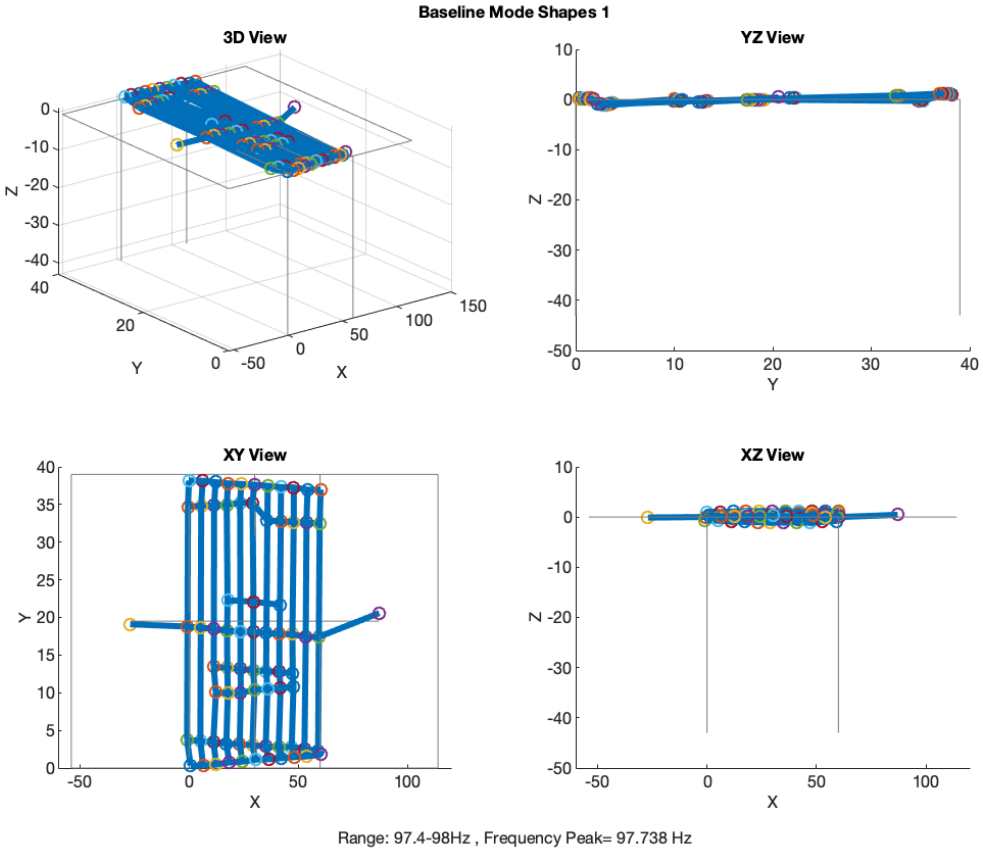

Mode Shape 17: 103.825Hz

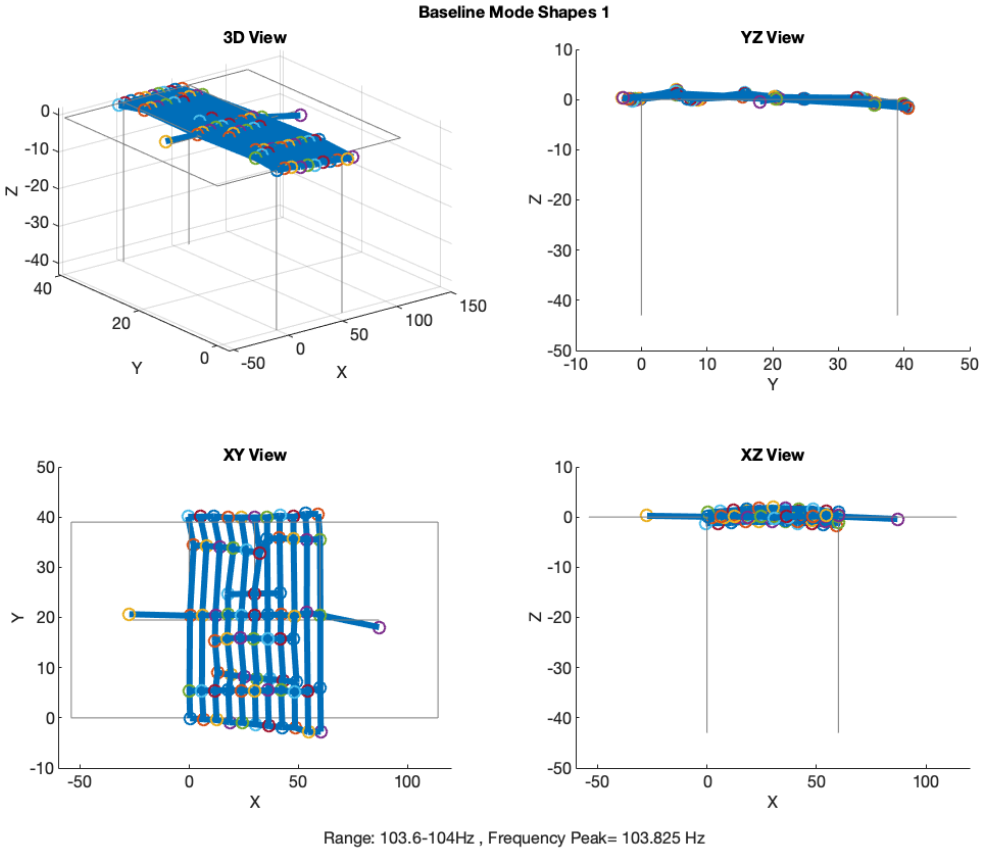

Mode Shape 18: 106.120Hz

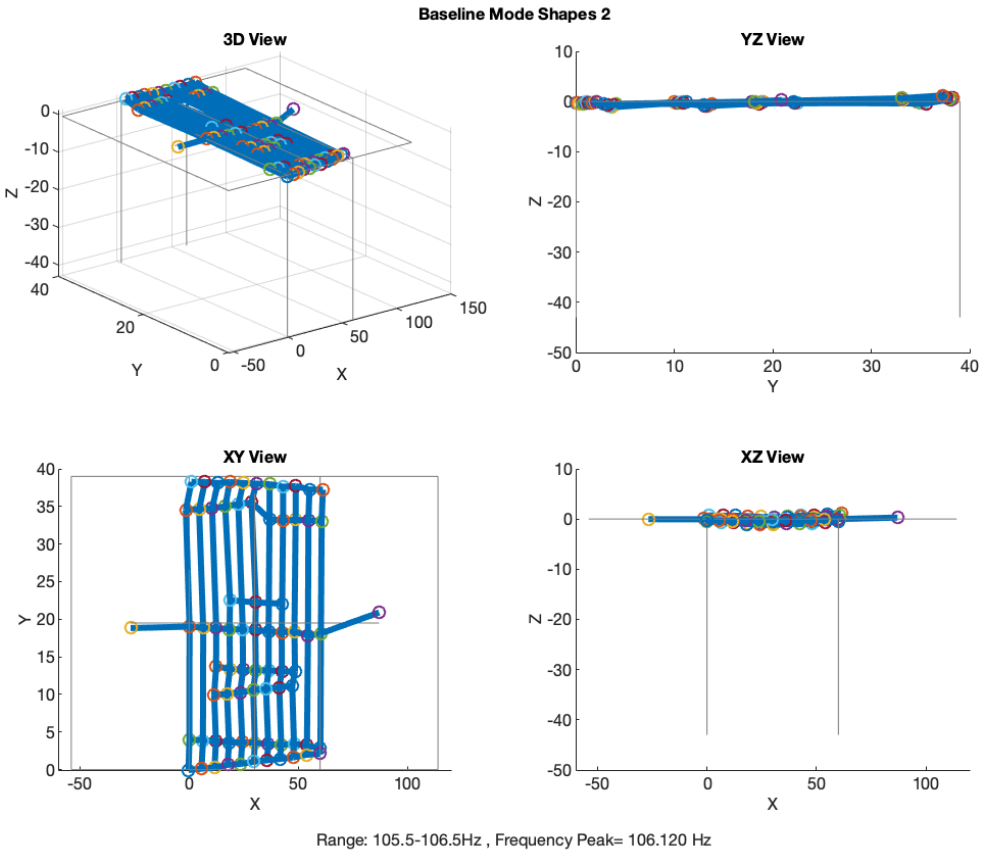

Mode Shape 19: 116.715Hz

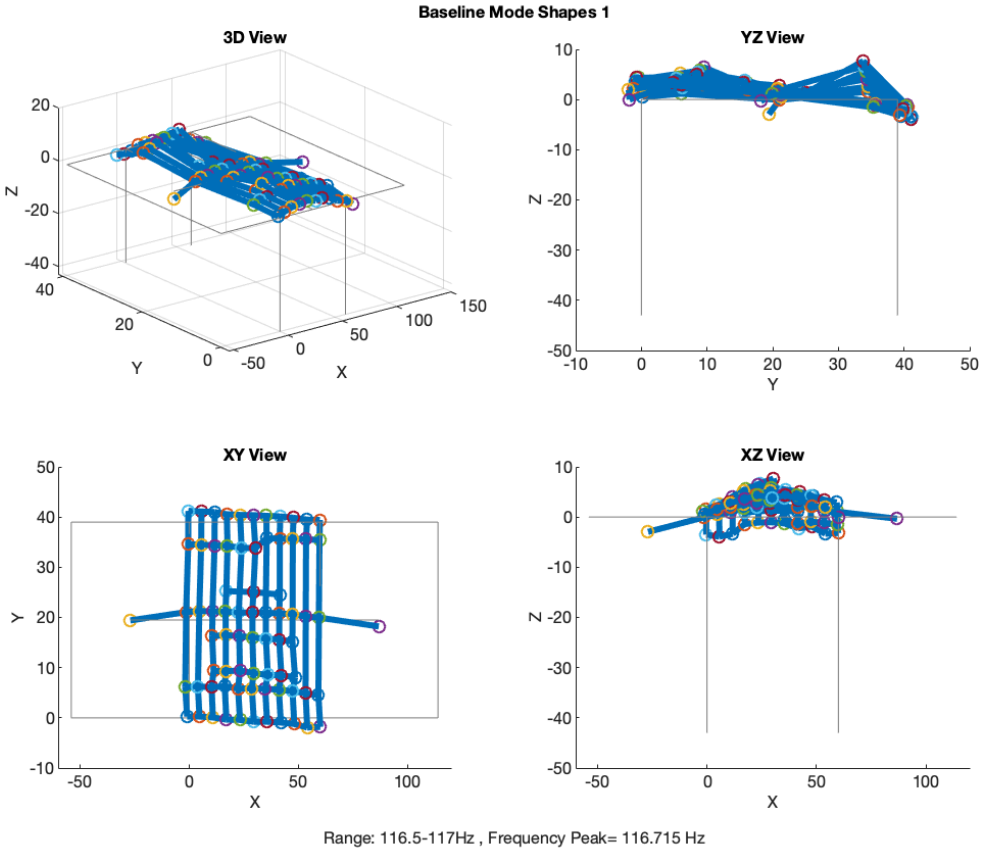

Mode Shape 20: 125.146Hz

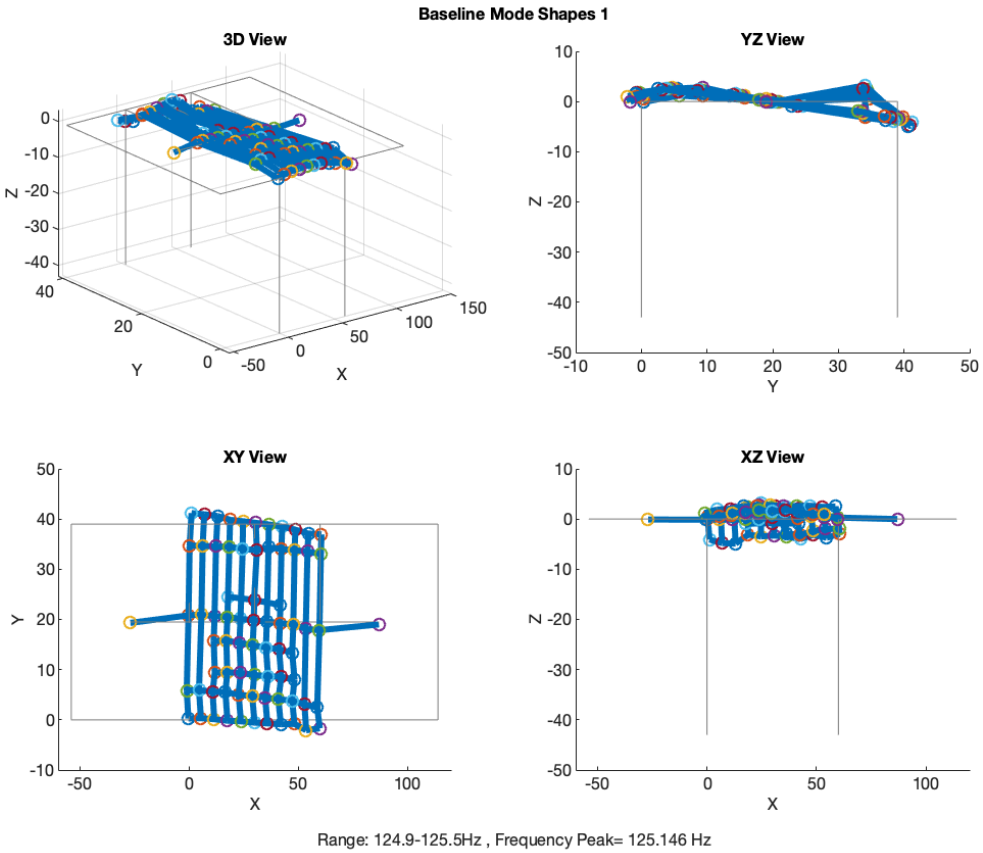

Mode Shape 21: 150.000Hz

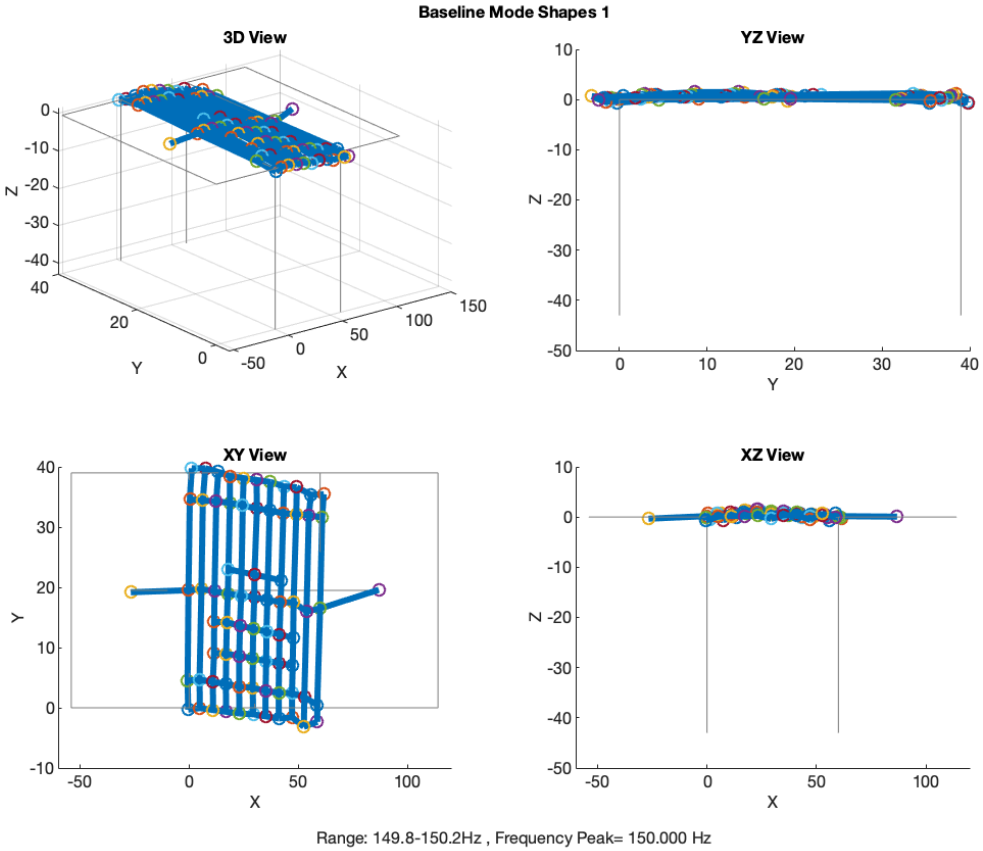

Mode Shape 22: 166.325Hz

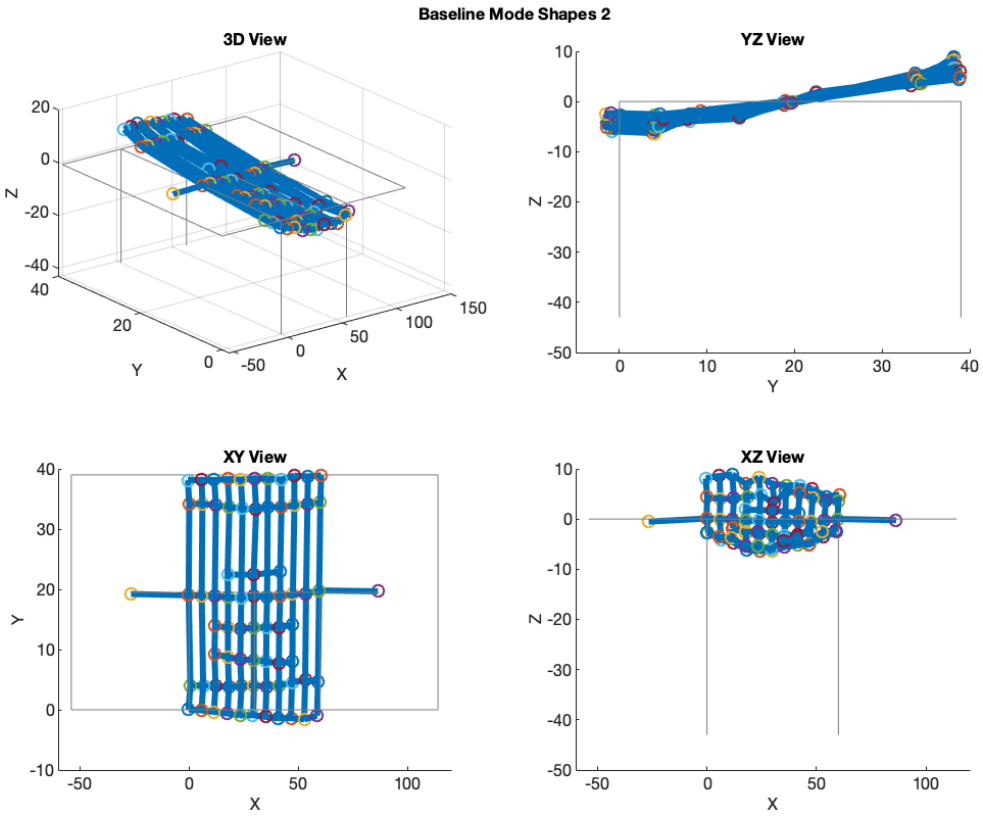

Mode Shape 23: 179.753Hz

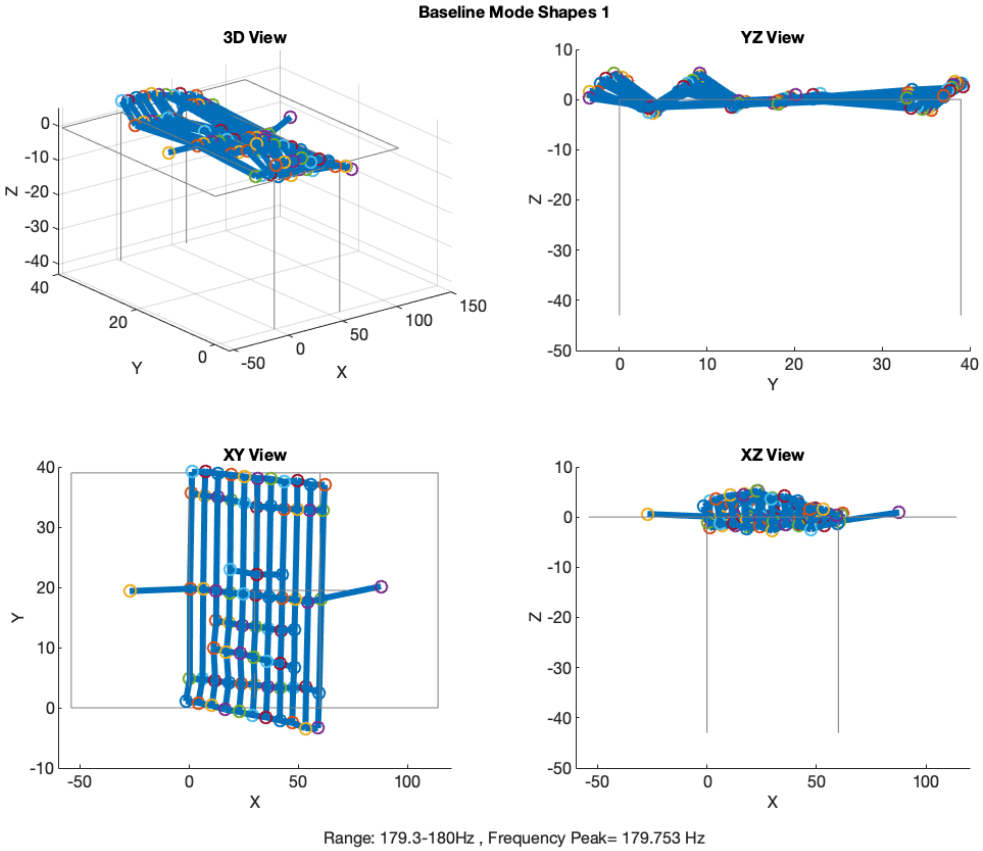

Mode Shape 24: 246.077Hz

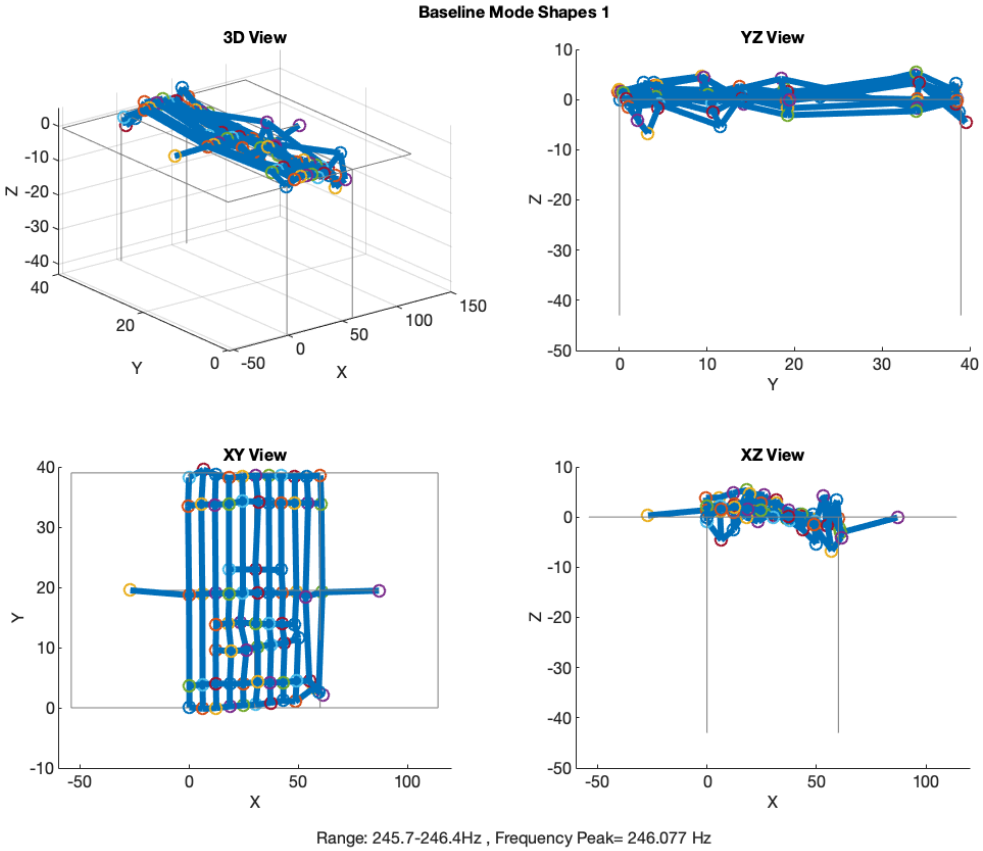

Mode Shape 25: 275.146Hz

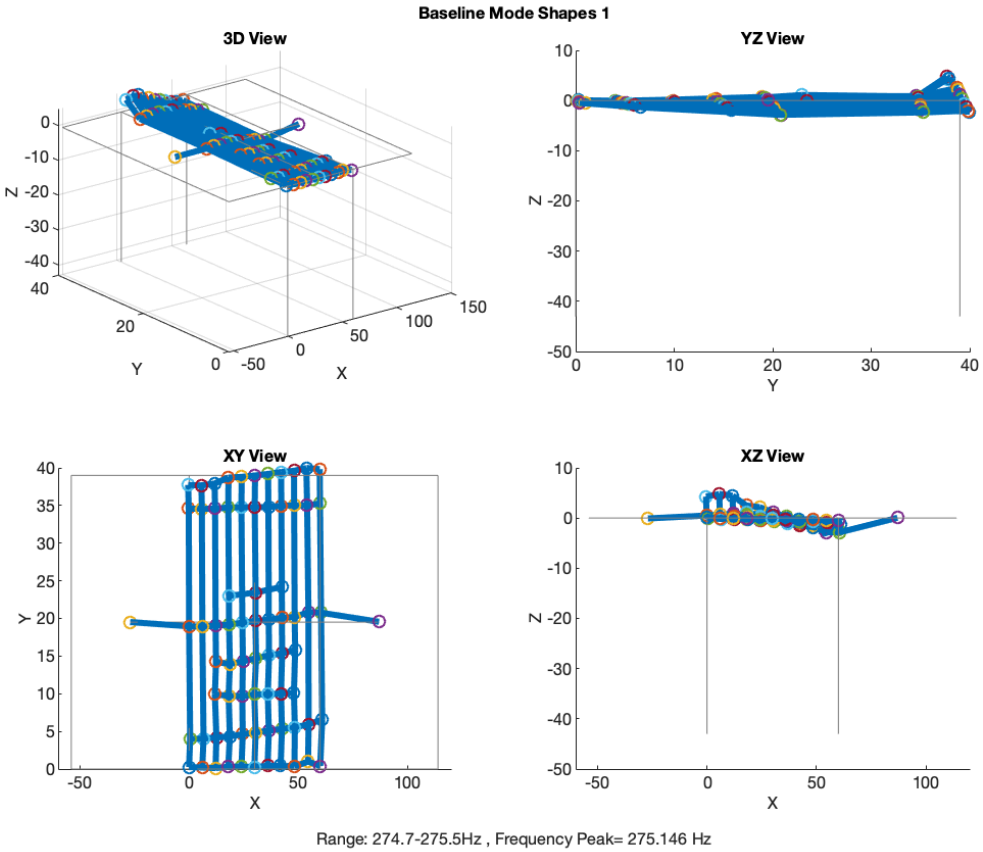

APPENDIX B: STIFFNESS CHANGE

DC1 vs DC7

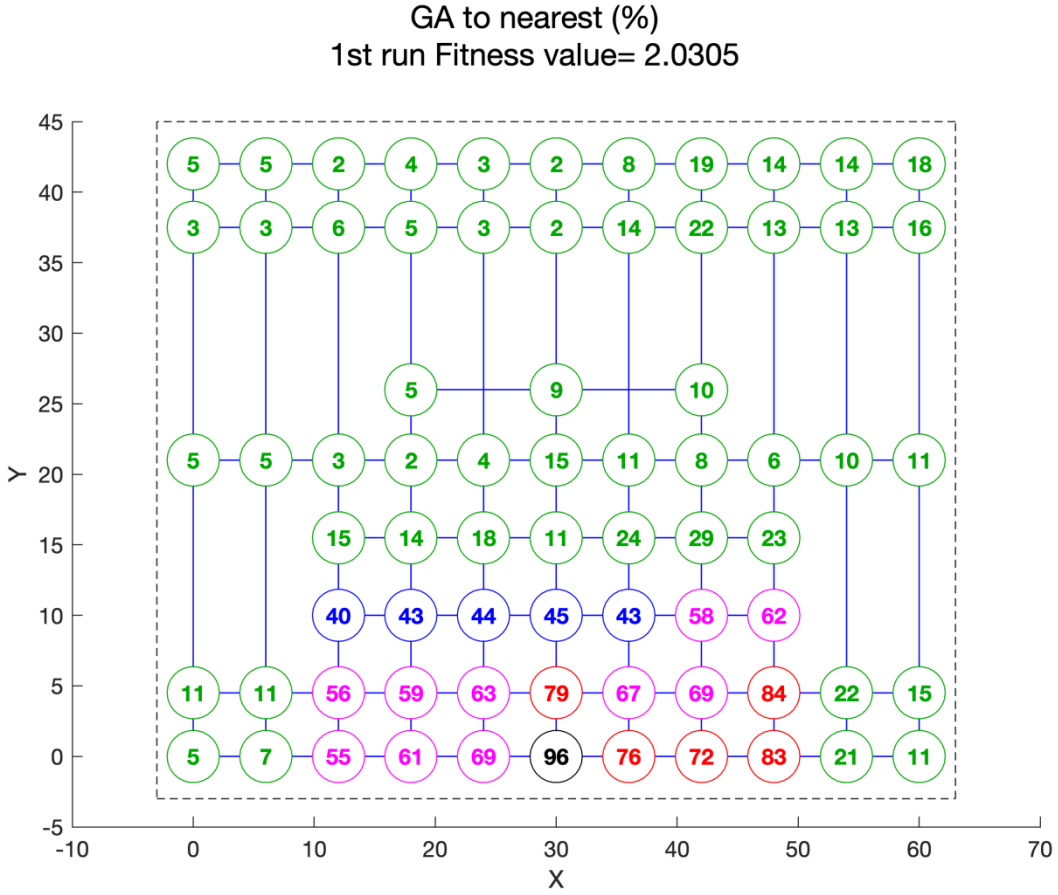
GA to nearest (%)
1st run Fitness value= 2.0305
Y
X
45
40
35
30
25
20
15
10
5
0
-5
-10
0
10
20
30
40
50
60
70
5 5 2 4 3 2 8 19 14 14 18
3 3 6 5 3 2 14 22 13 13 16
5 9 10
5 5 3 2 4 15 11 8 6 10 11
15 14 18 11 24 29 23
40 43 44 45 43 58 62
11 11 56 59 63 79 67 69 84 22 15
5 7 55 61 69 96 76 72 83 21 11

DC1 vs DC7

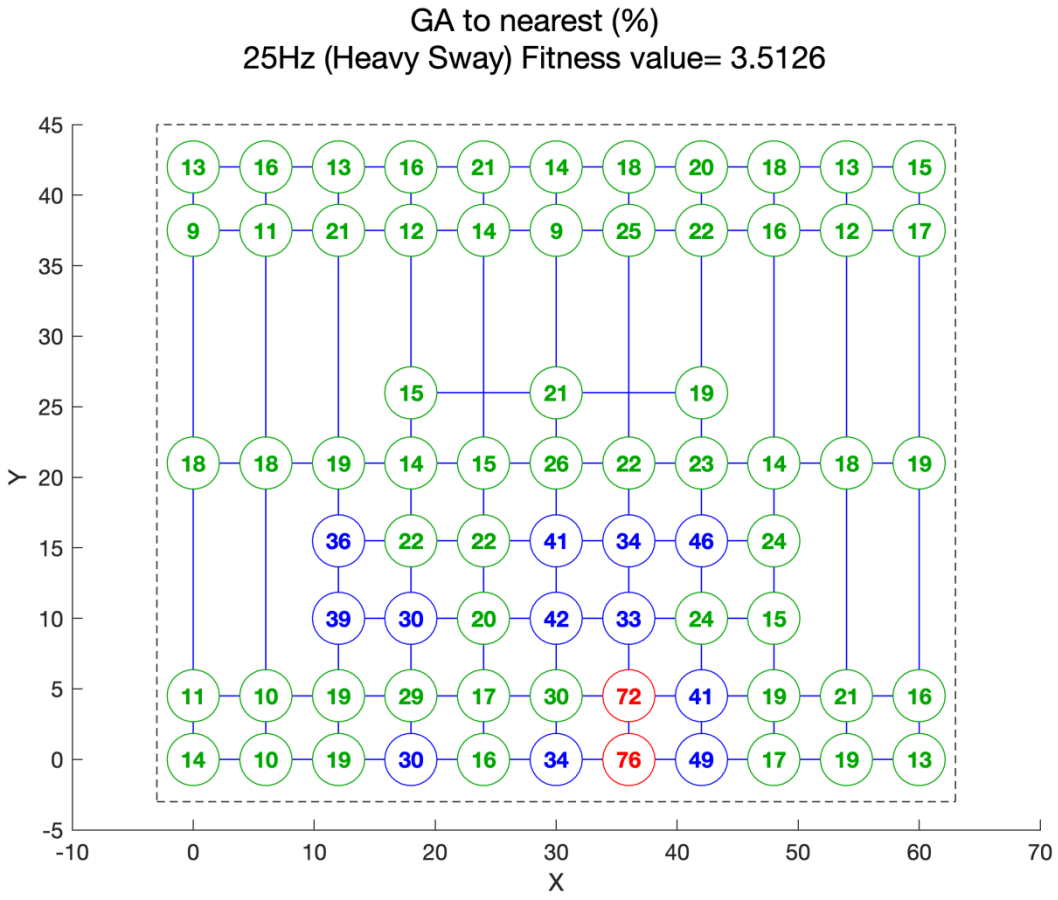
GA to nearest (%)
25Hz (Heavy Sway) Fitness value= 3.5126
Y
X
45
40
35
30
25
20
15
10
5
0
-5
-10
0
10
20
30
40
50
60
70
13 16 13 16 21 14 18 20 18 13 15
9 11 21 12 14 9 25 22 16 12 17
15 21 19
18 18 19 14 15 26 22 23 14 18 19
36 22 22 41 34 46 24
39 30 20 42 33 24 15
11 10 19 29 17 30 72 41 19 21 16
14 10 19 30 16 34 76 49 17 19 13

DC1 vs DC7

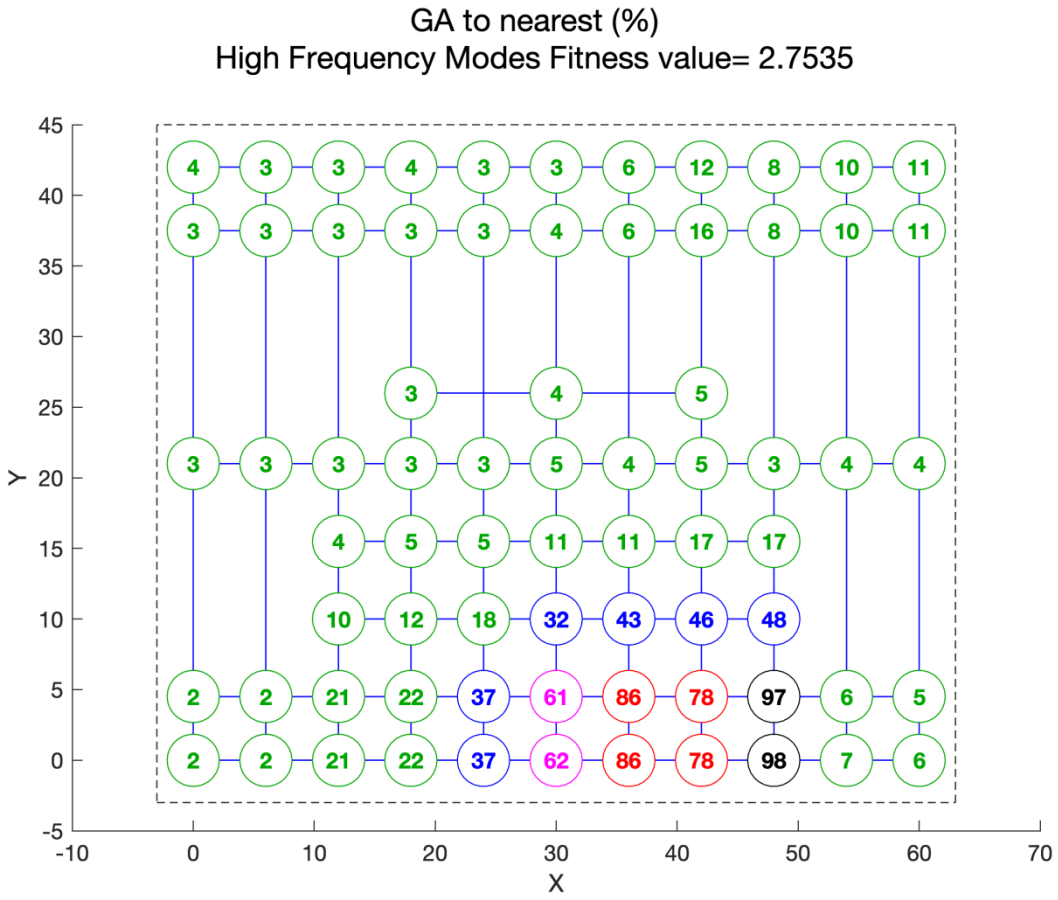
GA to nearest (%)
High Frequency Modes Fitness value= 2.7535
Y
X
45
40
35
30
25
20
15
10
5
0
-5
-10
0
10
20
30
40
50
60
70
4 3 3 4 3 3 6 12 8 10 11
3 3 3 3 3 4 6 16 8 10 11
3 4 5
3 3 3 3 3 5 4 5 3 4 4
4 5 5 11 11 17 17
10 12 18 32 43 46 48
2 2 21 22 37 61 86 78 97 6 5
2 2 21 22 37 62 86 78 98 7 6

DC1 vs DC7

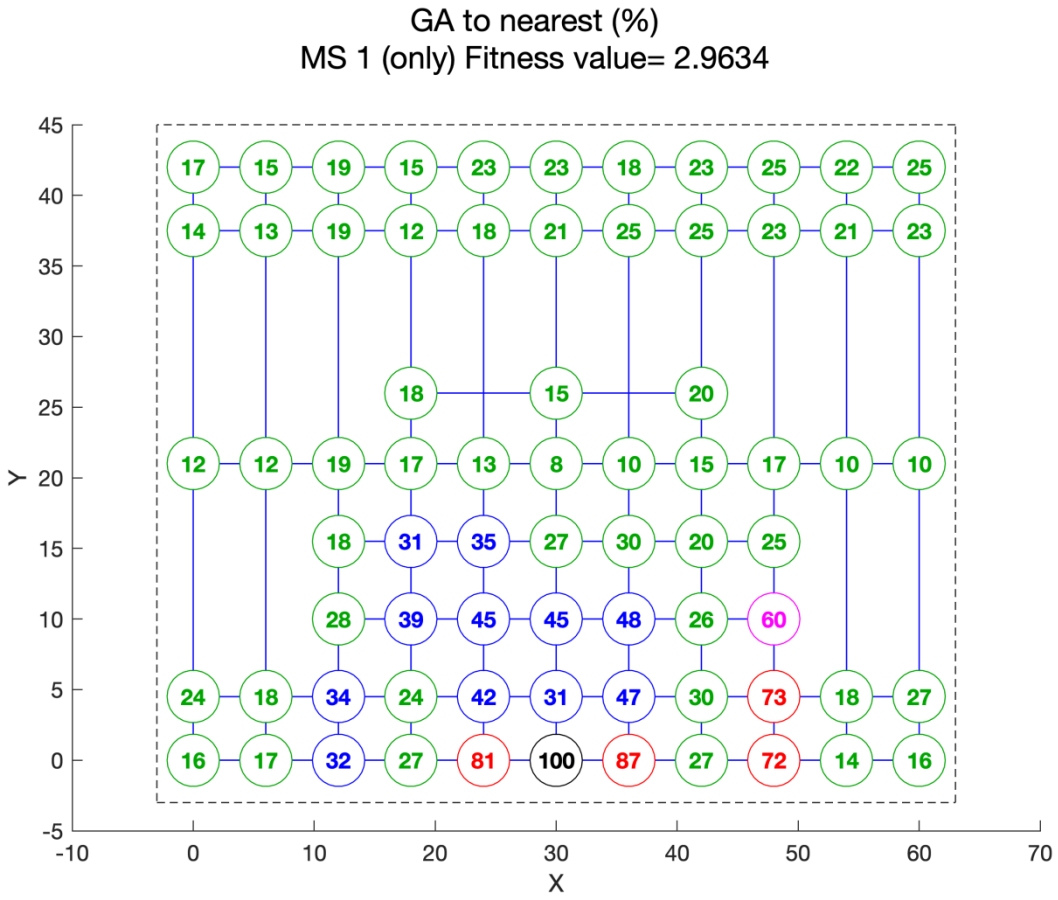
GA to nearest (%)
MS 1 (only) Fitness value= 2.9634
Y
X
45
40
35
30
25
20
15
10
5
0
-5
-10
0
10
20
30
40
50
60
70
17 15 19 15 23 23 18 23 25 22 25
14 13 19 12 18 21 25 25 23 21 23
18 15 20
12 12 19 17 13 8 10 15 17 10 10
18 31 35 27 30 20 25
28 39 45 45 48 26 60
24 18 34 24 42 31 47 30 73 18 27
16 17 32 27 81 100 87 27 72 14 16

DC1 vs DC7

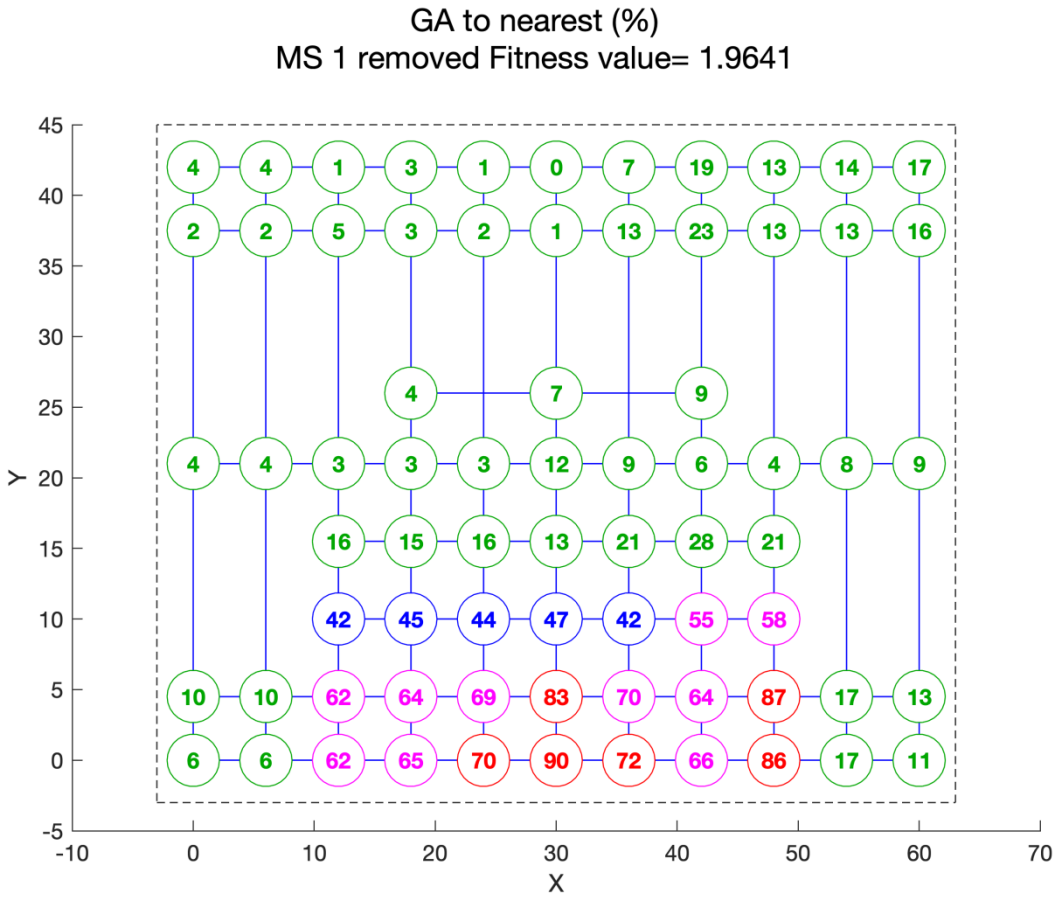
GA to nearest (%)
MS 1 removed Fitness value= 1.9641
Y
X
45
40
35
30
25
20
15
10
5
0
-5
-10
0
10
20
30
40
50
60
70
4 4 1 3 1 0 7 19 13 14 17
2 2 5 3 2 1 13 23 13 13 16
4 7 9
4 4 3 3 3 12 9 6 4 8 9
16 15 16 13 21 28 21
42 45 44 47 42 55 58
10 10 62 64 69 83 70 64 87 17 13
6 6 62 65 70 90 72 66 86 17 11

DC1 vs DC7

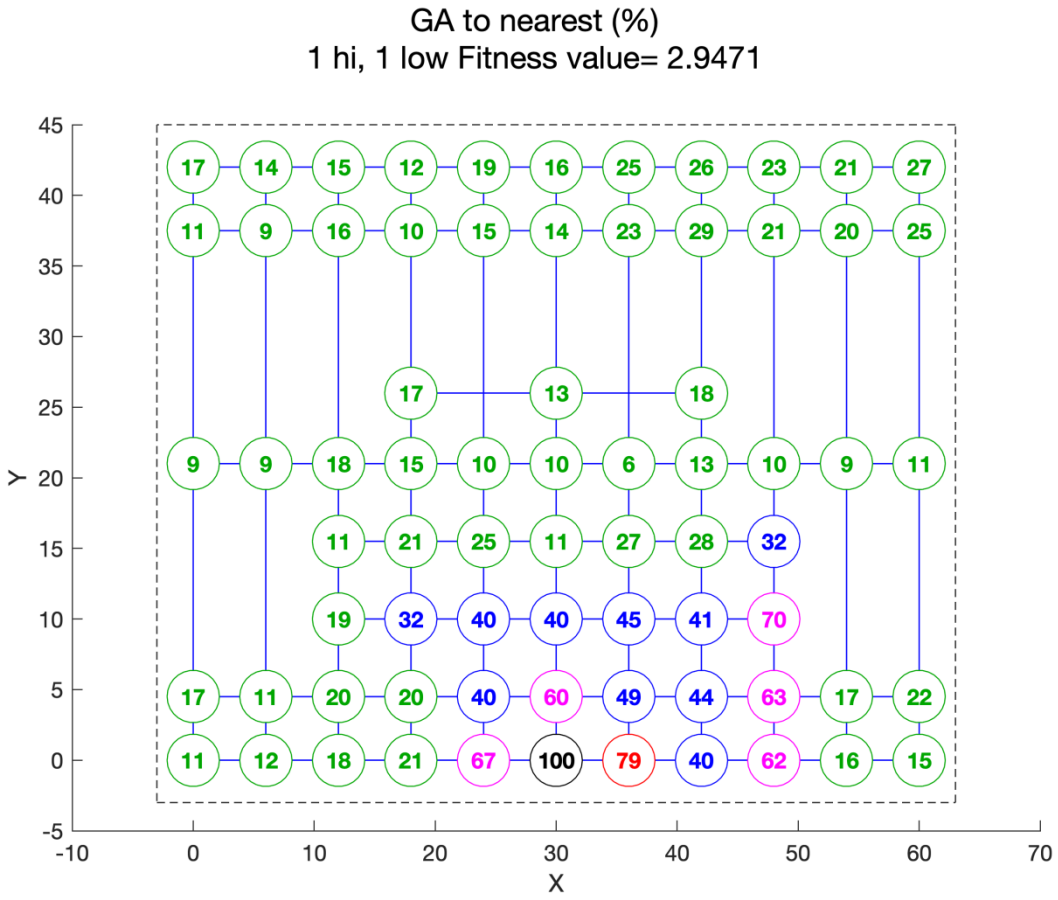
GA to nearest (%)
1 hi, 1 low Fitness value= 2.9471
Y
X
45
40
35
30
25
20
15
10
5
0
-5
-10
0
10
20
30
40
50
60
70
17 14 15 12 19 16 25 26 23 21 27
11 9 16 10 15 14 23 29 21 20 25
17 13 18
9 9 18 15 10 10 6 13 10 9 11
11 21 25 11 27 28 32
19 32 40 40 45 41 70
17 11 20 20 40 60 49 44 63 17 22
11 12 18 21 67 100 79 40 62 16 15

DC1 vs DC7

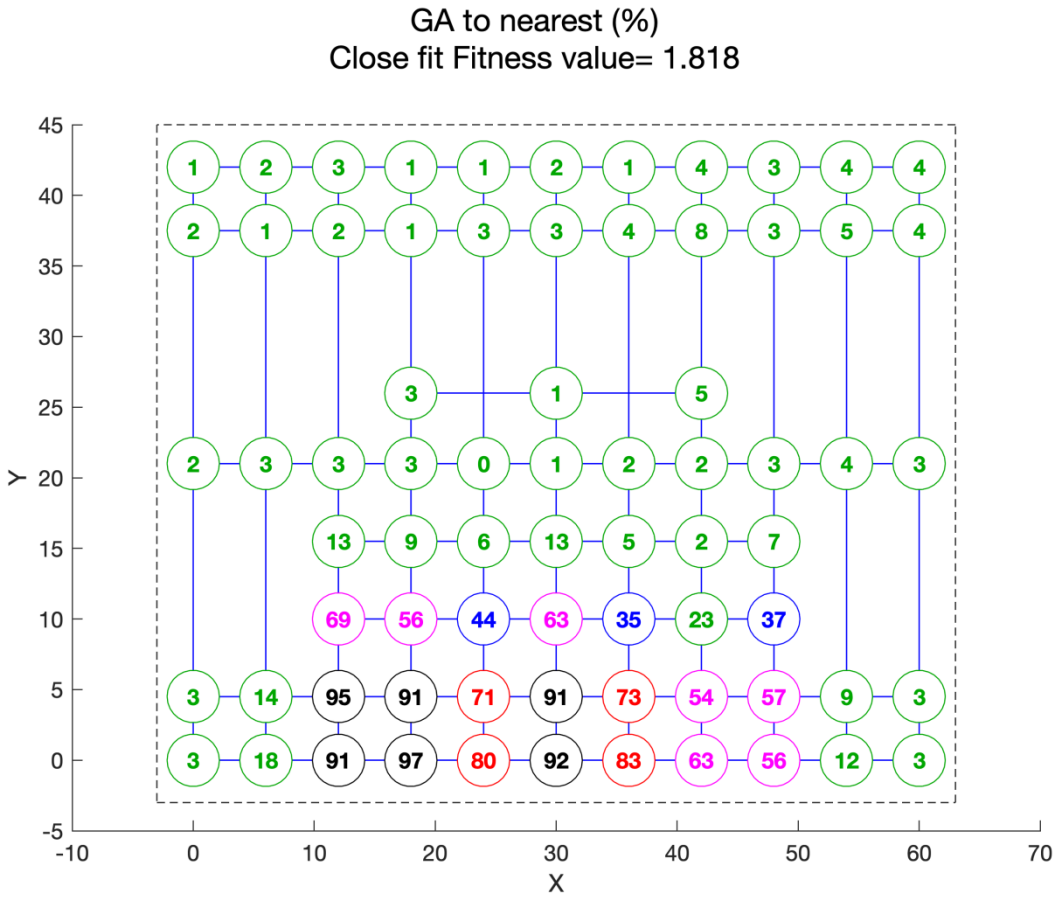
GA to nearest (%)
Close fit Fitness value= 1.818
Y
X
45
40
35
30
25
20
15
10
5
0
-5
-10
0
10
20
30
40
50
60
70
1 2 3 1 1 2 1 4 3 4 4
2 1 2 1 3 3 4 8 3 5 4
3 1 5
2 3 3 3 0 1 2 2 3 4 3
13 9 6 13 5 2 7
69 56 44 63 35 23 37
3 14 95 91 71 91 73 54 57 9 3
3 18 91 97 80 92 83 63 56 12 3

DC1 vs DC7

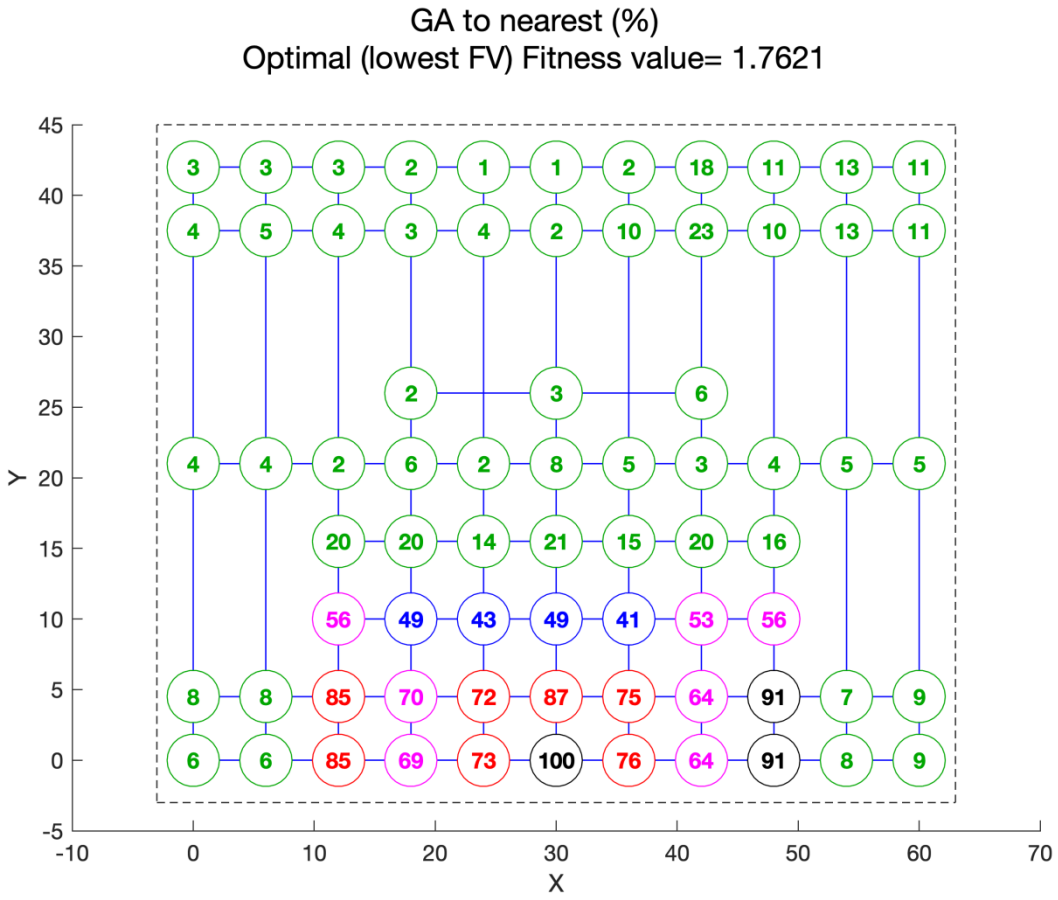
GA to nearest (%)
Optimal (lowest FV) Fitness value= 1.7621
Y
X
45
40
35
30
25
20
15
10
5
0
-5
-10
0
10
20
30
40
50
60
70
3 3 3 2 1 1 2 18 11 13 11
4 5 4 3 4 2 10 23 10 13 11
2 3 6
4 4 2 6 2 8 5 3 4 5 5
20 20 14 21 15 20 16
56 49 43 49 41 53 56
8 8 85 70 72 87 75 64 91 7 9
6 6 85 69 73 100 76 64 91 8 9

DC1 vs DC2

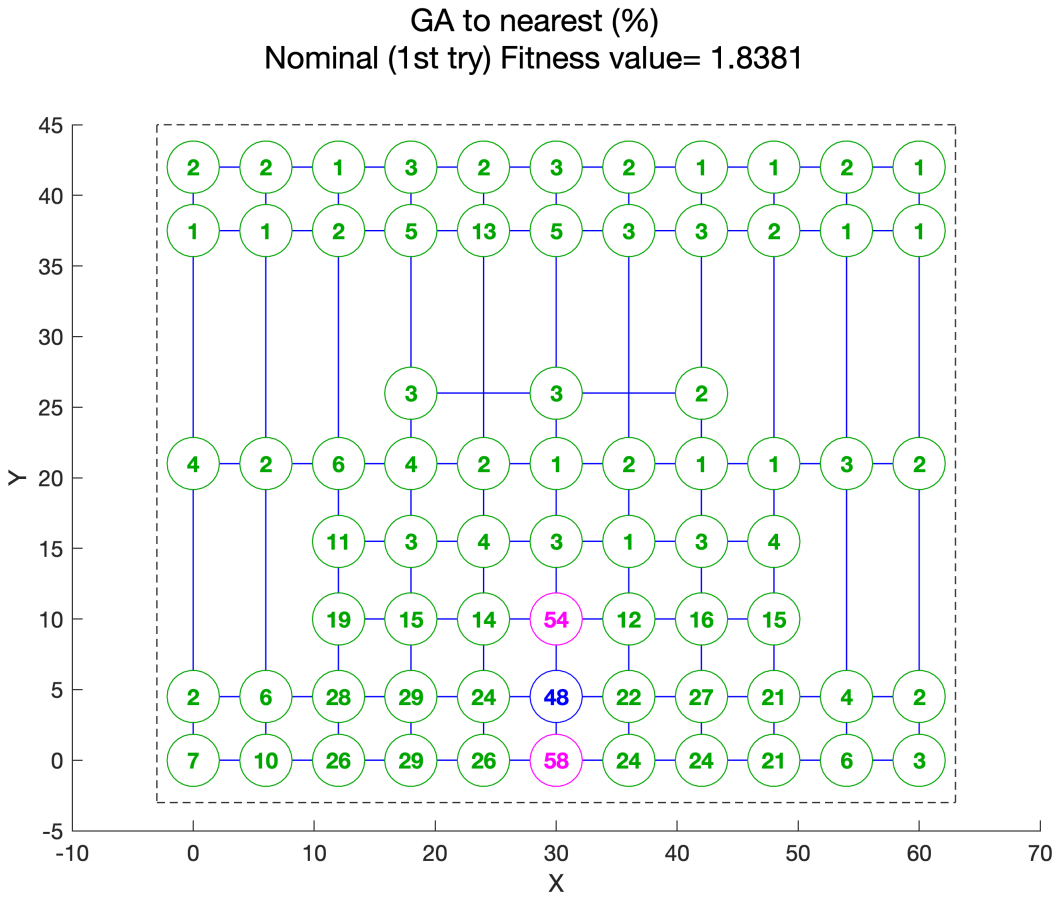
GA to nearest (%)
Nominal (1st try) Fitness value= 1.8381
Y
X
45
40
35
30
25
20
15
10
5
0
-5
-10
0
10
20
30
40
50
60
70
2 2 1 3 2 3 2 1 1 2 1
1 1 2 5 13 5 3 3 2 1 1
3 3 2
4 2 6 4 2 1 2 1 1 3 2
11 3 4 3 1 3 4
19 15 14 54 12 16 15
2 6 28 29 24 48 22 27 21 4 2
7 10 26 29 26 58 24 24 21 6 3

DC1 vs DC2

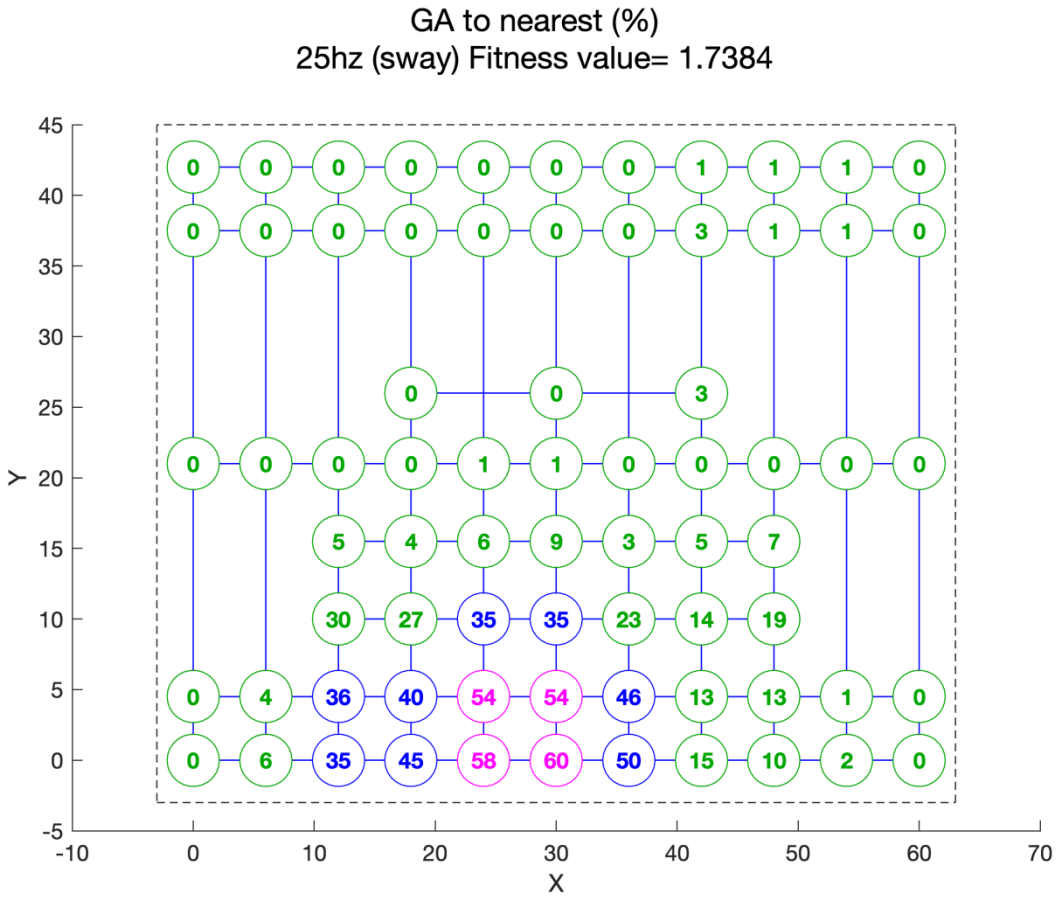
GA to nearest (%)
25hz (sway) Fitness value= 1.7384
Y
X
45
40
35
30
25
20
15
10
5
0
-5
-10
0
10
20
30
40
50
60
70
0 0 0 0 0 0 0 1 1 1 0
0 0 0 0 0 0 0 3 1 1 0
0 0 3
0 0 0 0 1 1 0 0 0 0 0
5 4 6 9 3 5 7
30 27 35 35 23 14 19
0 4 36 40 54 54 46 13 13 1 0
0 6 35 45 58 60 50 15 10 2 0

DC1 vs DC2

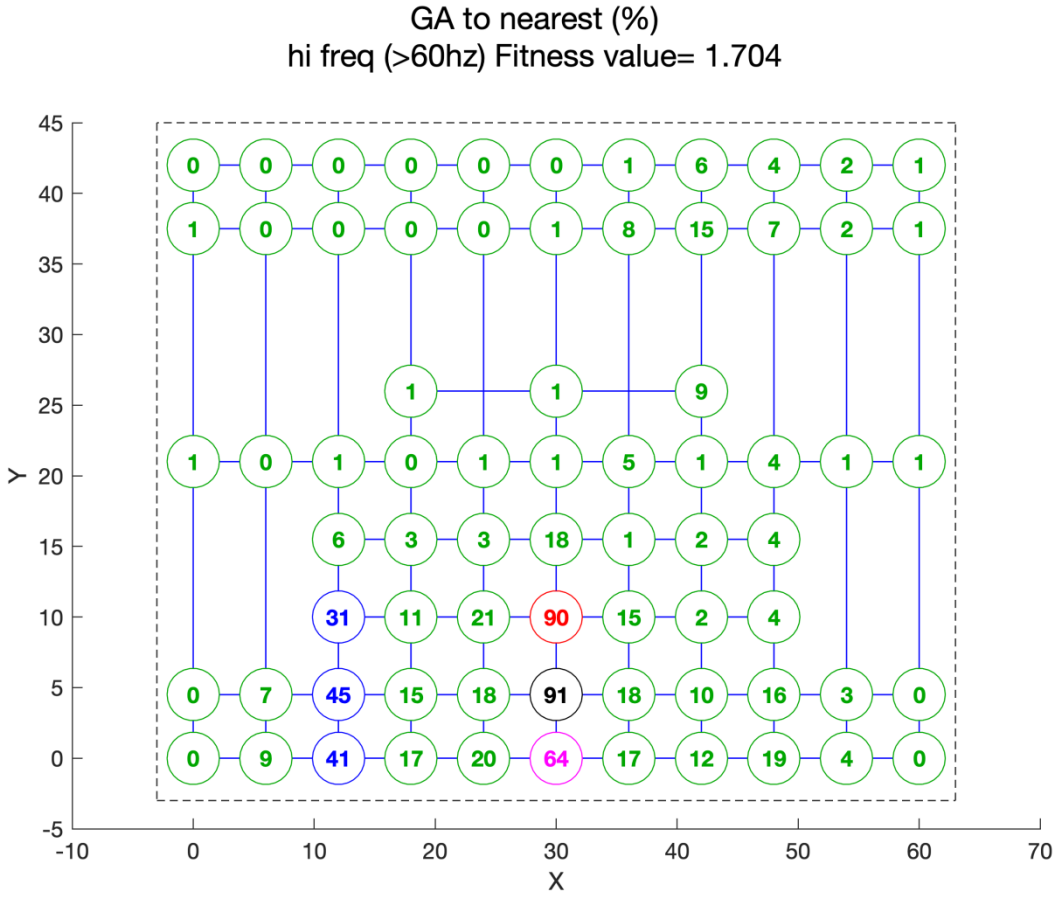
GA to nearest (%)
hi freq (>60hz) Fitness value= 1.704
Y
X
45
40
35
30
25
20
15
10
5
0
-5
-10
0
10
20
30
40
50
60
70
0 0 0 0 0 0 1 6 4 2 1
1 0 0 0 0 1 8 15 7 2 1
1 1 9
1 0 1 0 1 1 5 1 4 1 1
6 3 3 18 1 2 4
31 11 21 90 15 2 4
0 7 45 15 18 91 18 10 16 3 0
0 9 41 17 20 64 17 12 19 4 0

DC1 vs DC2

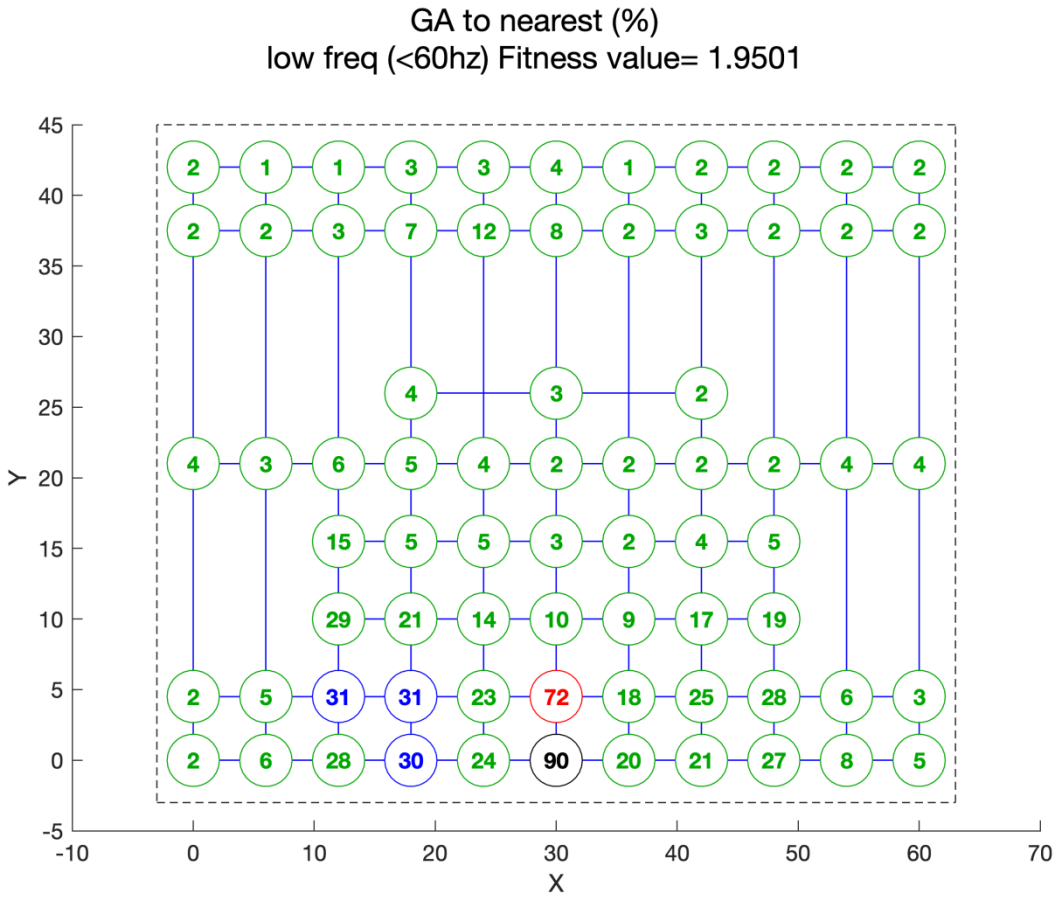
GA to nearest (%)
low freq (<60hz) Fitness value= 1.9501
Y
X
45
40
35
30
25
20
15
10
5
0
-5
-10
0
10
20
30
40
50
60
70
2 1 1 3 3 4 1 2 2 2 2
2 2 3 7 12 8 2 3 2 2 2
4 3 2
4 3 6 5 4 2 2 2 2 4 4
15 5 5 3 2 4 5
29 21 14 10 9 17 19
2 5 31 31 23 72 18 25 28 6 3
2 6 28 30 24 90 20 21 27 8 5

DC1 vs DC2

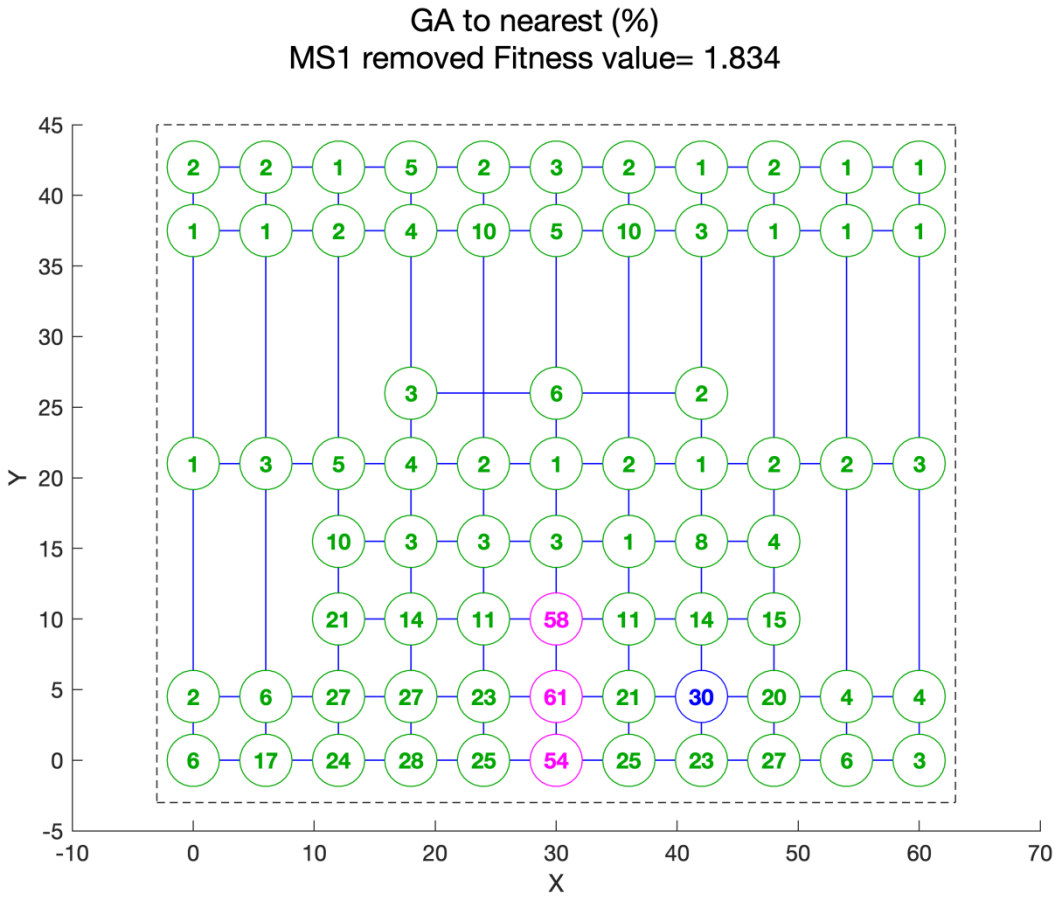
GA to nearest (%)
MS1 removed Fitness value= 1.834
Y
X
45
40
35
30
25
20
15
10
5
0
-5
-10
0
10
20
30
40
50
60
70
2 2 1 5 2 3 2 1 2 1 1
1 1 2 4 10 5 10 3 1 1 1
3 6 2
1 3 5 4 2 1 2 1 2 2 3
10 3 3 3 1 8 4
21 14 11 58 11 14 15
2 6 27 27 23 61 21 30 20 4 4
6 17 24 28 25 54 25 23 27 6 3

DC1 vs DC2

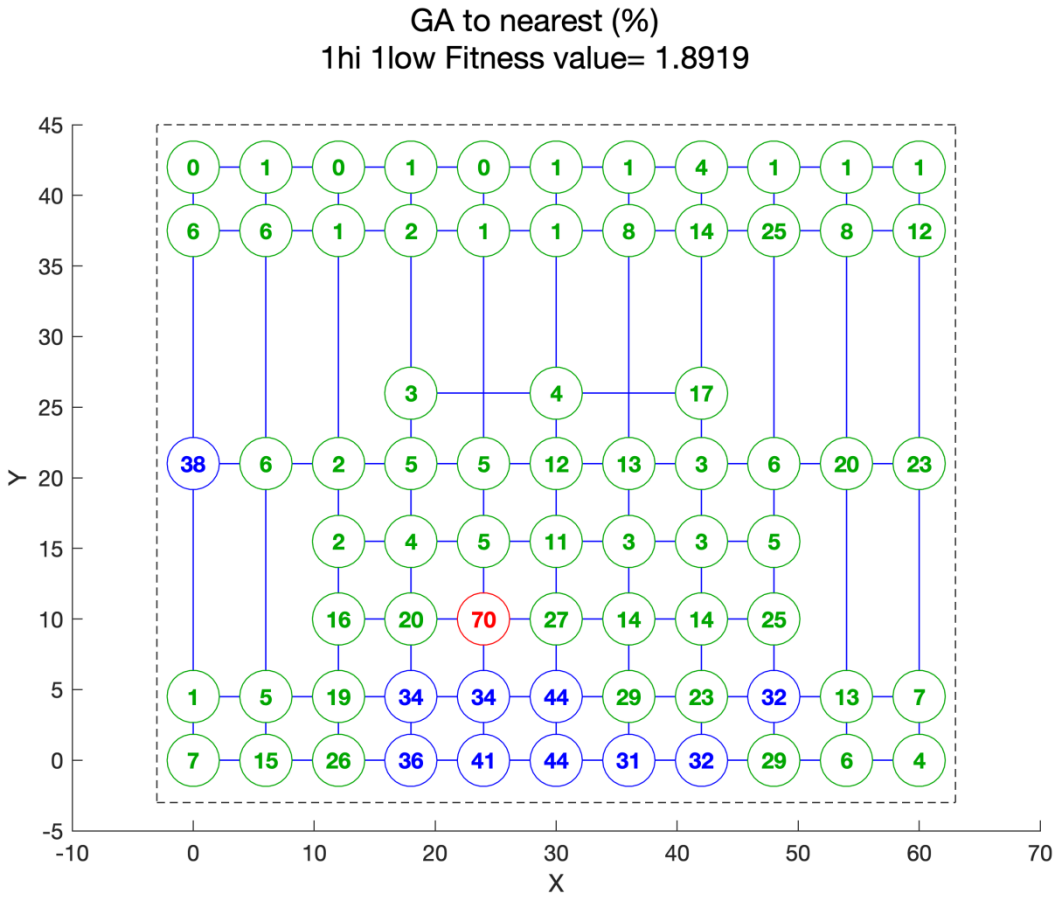
GA to nearest (%)
1hi 1low Fitness value= 1.8919
Y
X
45
40
35
30
25
20
15
10
5
0
-5
-10
0
10
20
30
40
50
60
70
0 1 0 1 0 1 1 4 1 1 1
6 6 1 2 1 1 8 14 25 8 12
3 4 17
38 6 2 5 5 12 13 3 6 20 23
2 4 5 11 3 3 5
16 20 70 27 14 14 25
1 5 19 34 34 44 29 23 32 13 7
7 15 26 36 41 44 31 32 29 6 4

DC1 vs DC2

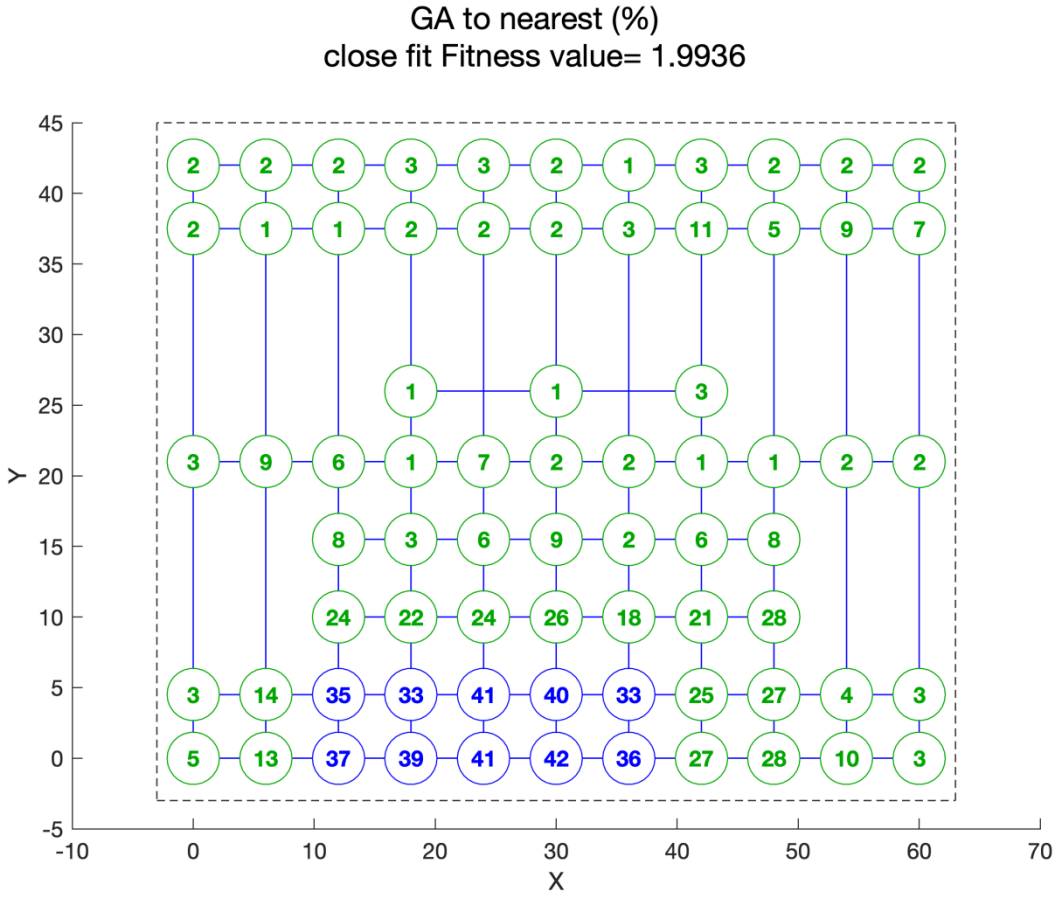
GA to nearest (%)
close fit Fitness value= 1.9936
Y
X
45
40
35
30
25
20
15
10
5
0
-5
-10
0
10
20
30
40
50
60
70
2 2 2 3 3 2 1 3 2 2 2
2 1 1 2 2 2 3 11 5 9 7
1 1 3
3 9 6 1 7 2 2 1 1 2 2
8 3 6 9 2 6 8
24 22 24 26 18 21 28
3 14 35 33 41 40 33 25 27 4 3
5 13 37 39 41 42 36 27 28 10 3

DC1 vs DC2

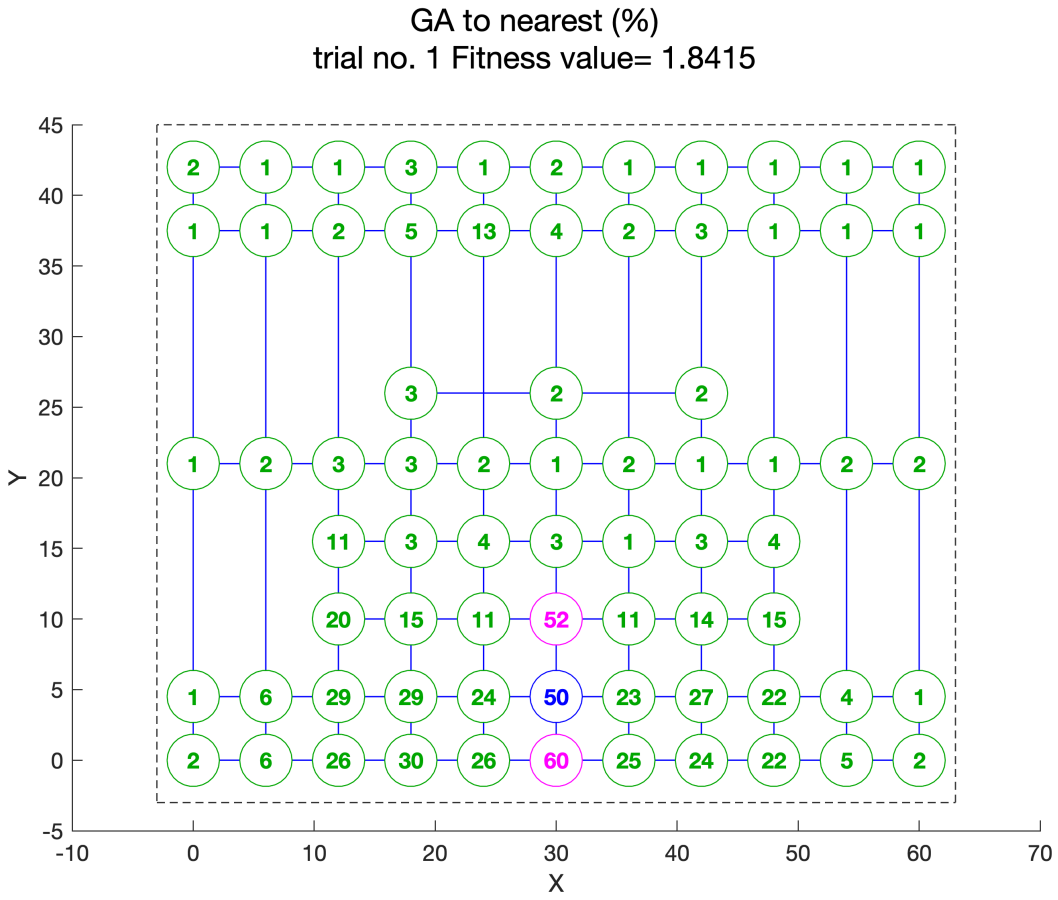
GA to nearest (%)
trial no. 1 Fitness value= 1.8415
Y
X
45
40
35
30
25
20
15
10
5
0
-5
-10
0
10
20
30
40
50
60
70
2 1 1 3 1 2 1 1 1 1 1
1 1 2 5 13 4 2 3 1 1 1
3 2 2
1 2 3 3 2 1 2 1 1 2 2
11 3 4 3 1 3 4
20 15 11 52 11 14 15
1 6 29 29 24 50 23 27 22 4 1
2 6 26 30 26 60 25 24 22 5 2

Baseline vs DC1

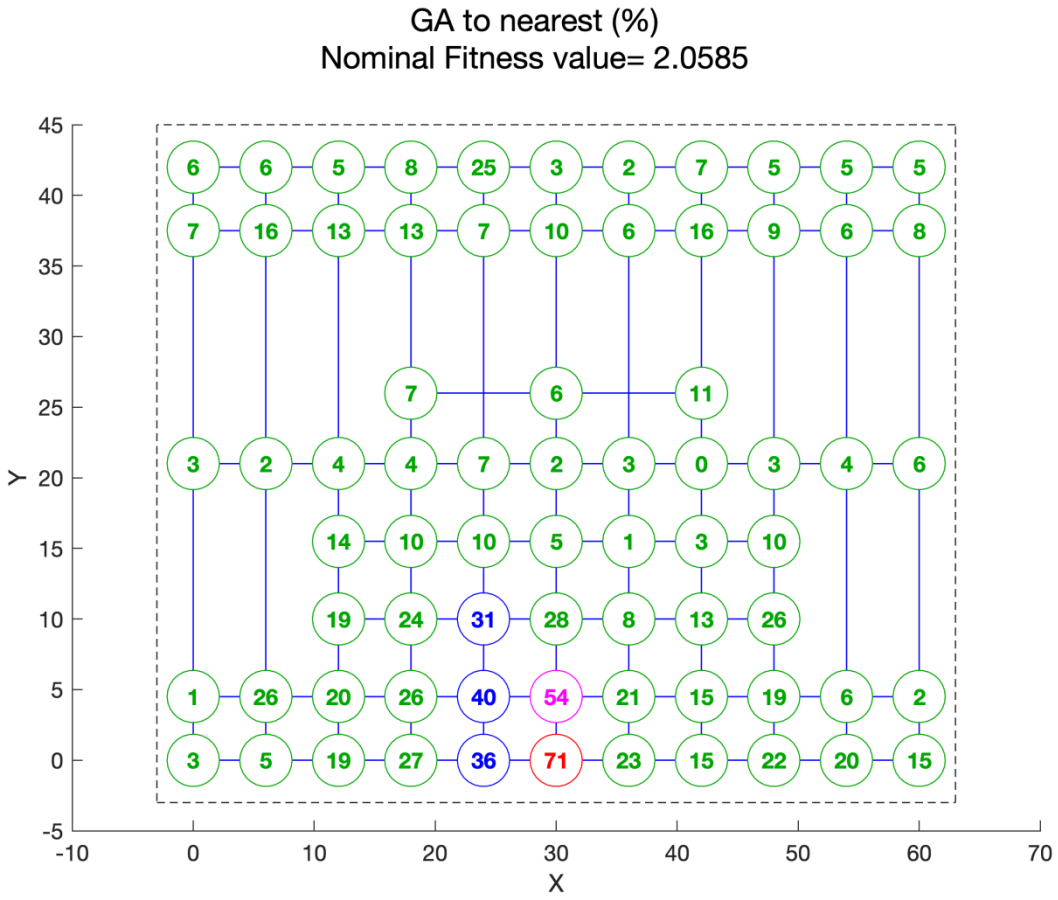

Baseline vs DC1

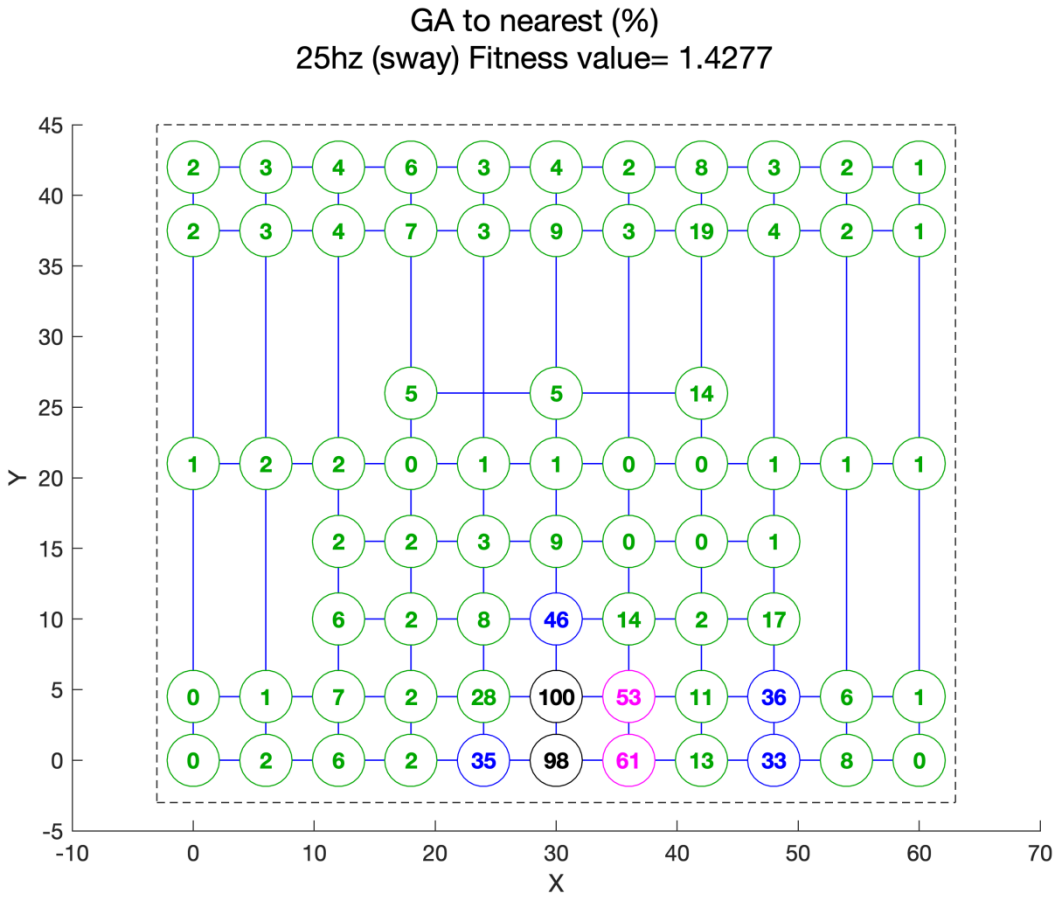

Baseline vs DC1

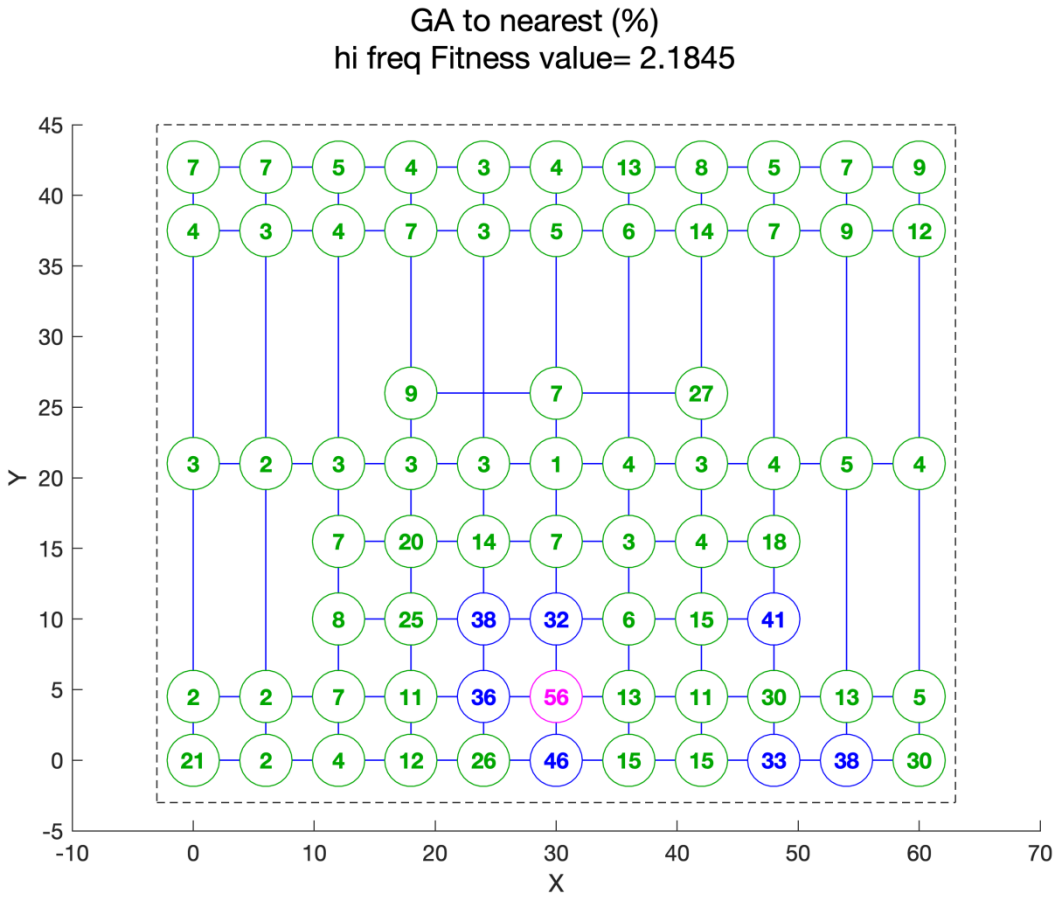

Baseline vs DC1

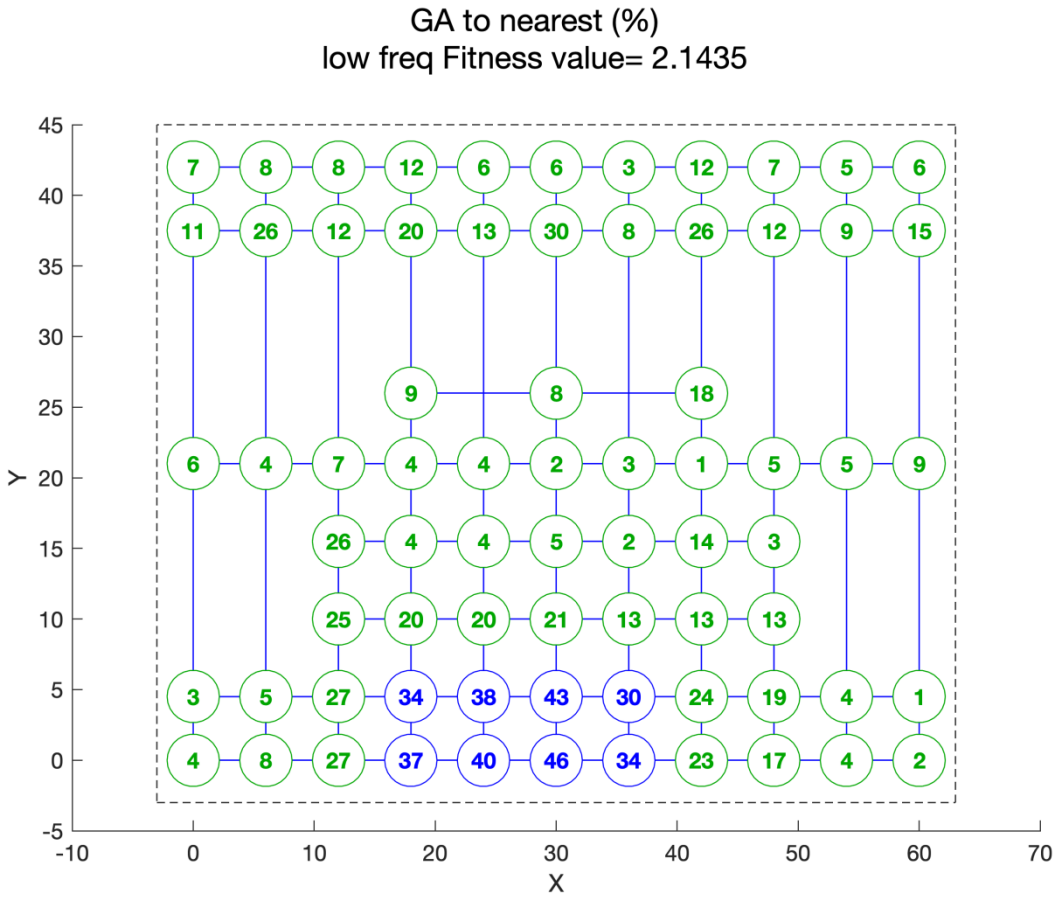

Baseline vs DC1

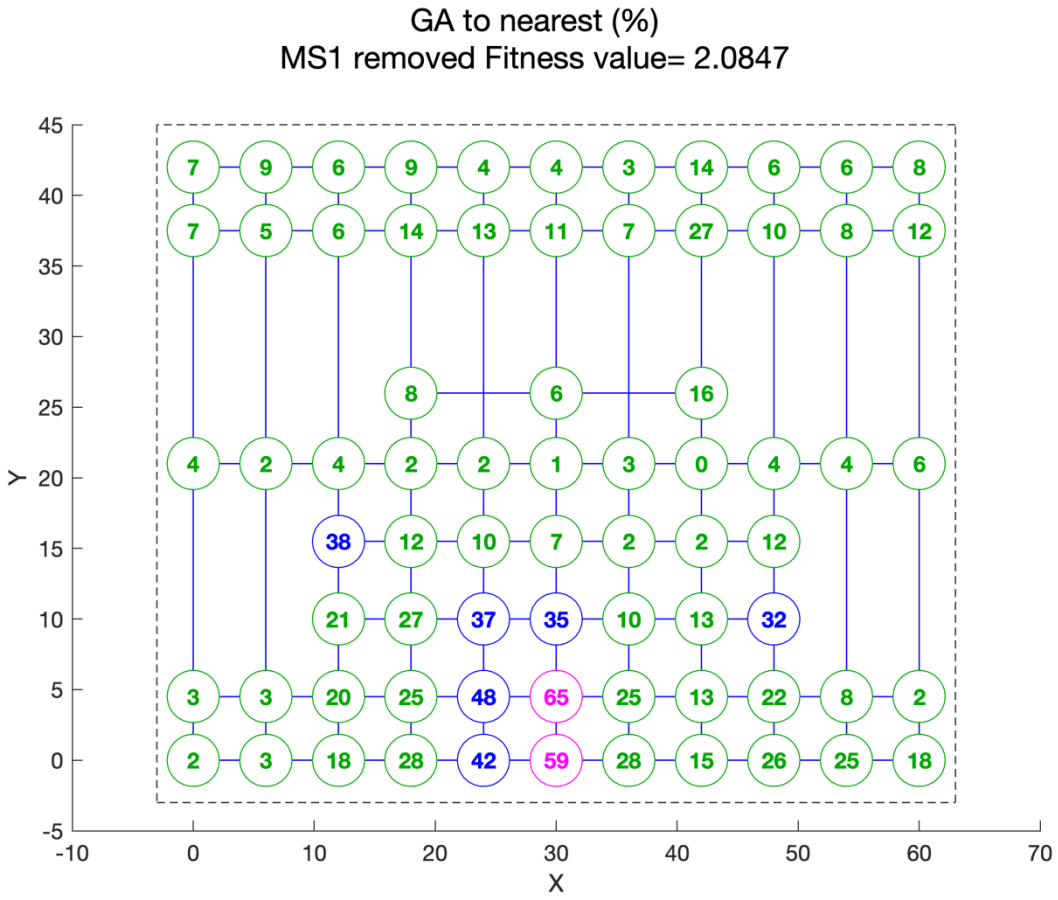

Baseline vs DC1

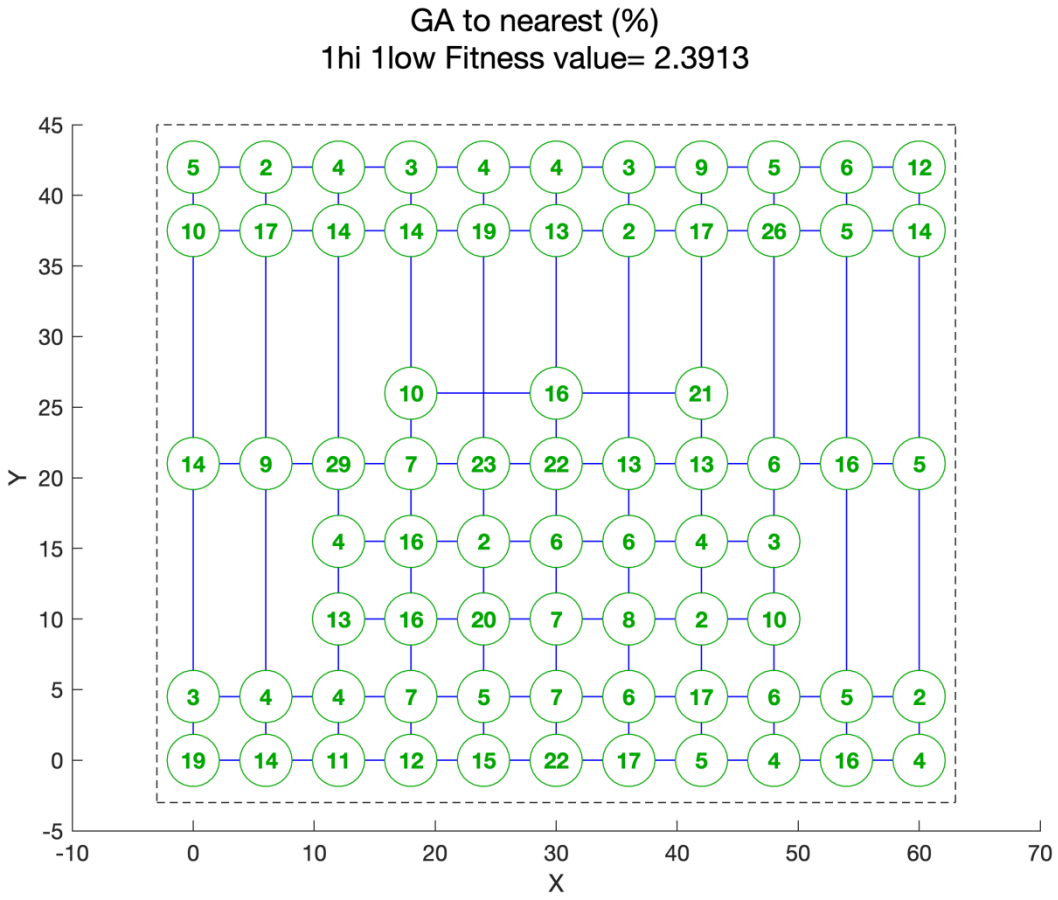

Baseline vs DC1

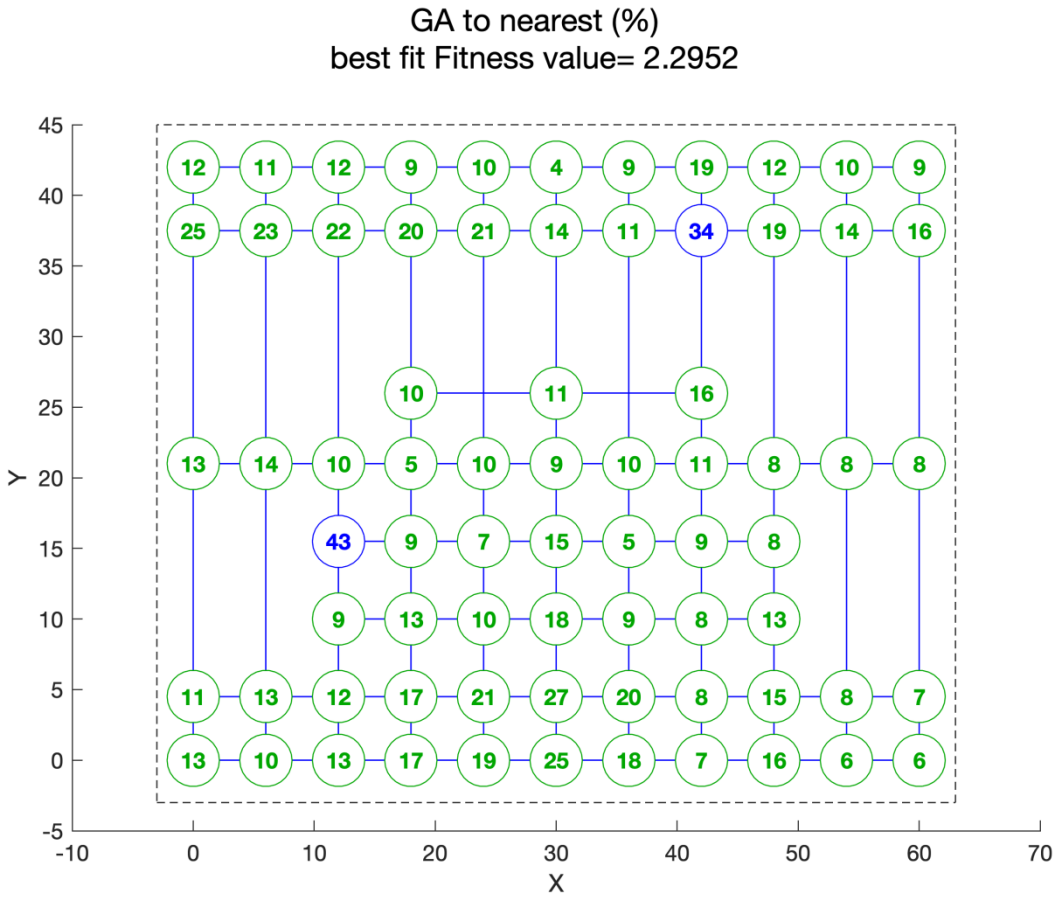

Baseline vs DC1

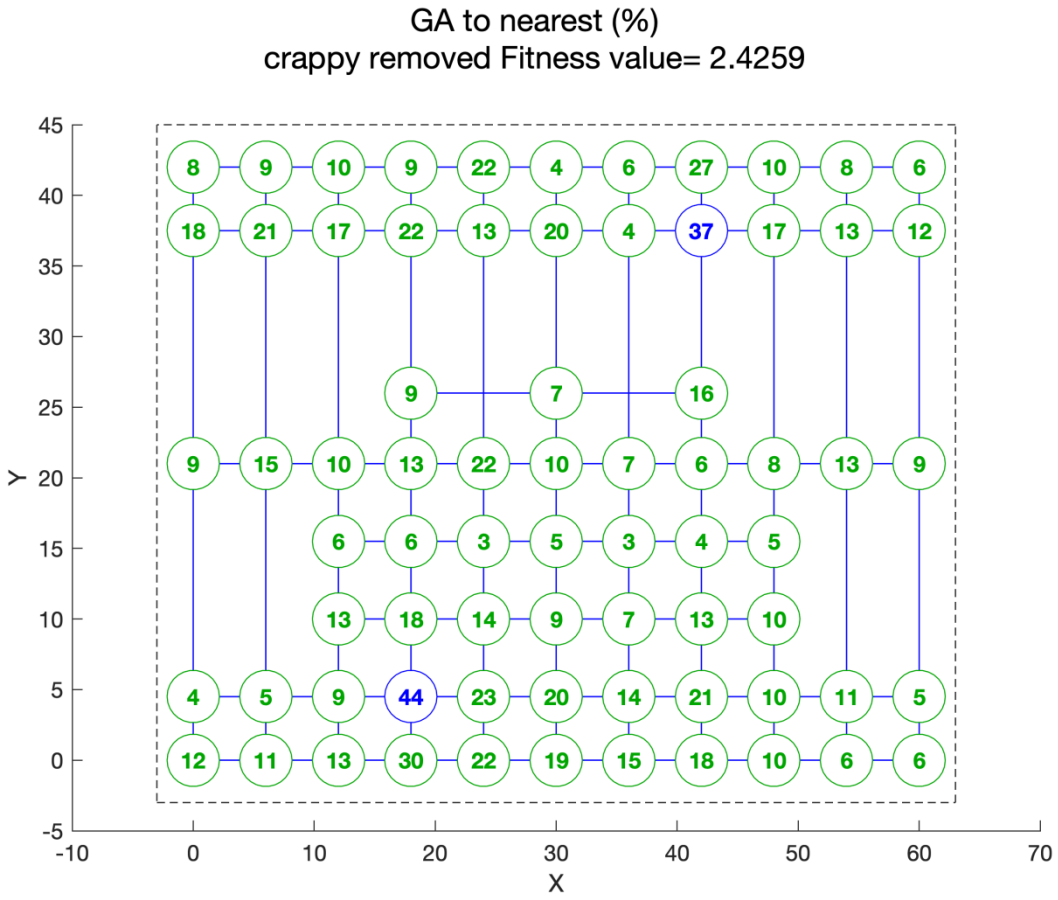

DC1 vs DC3

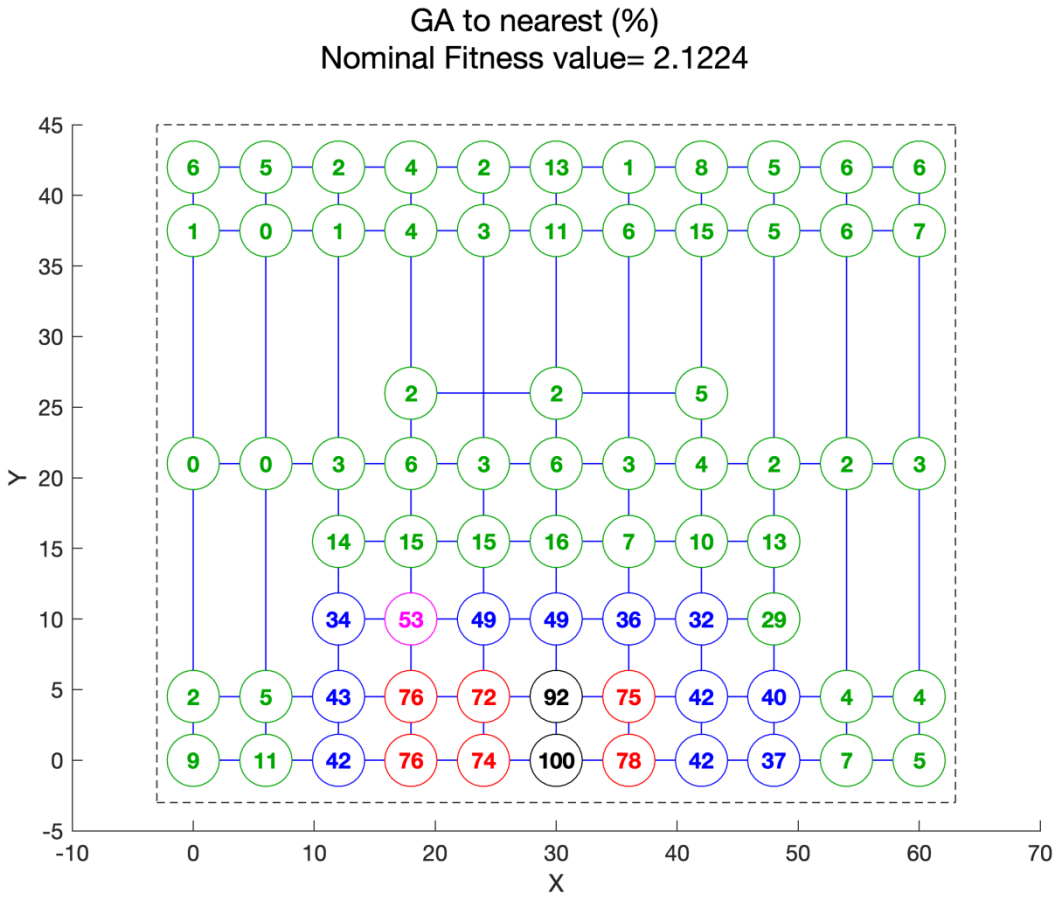
GA to nearest (%)
Nominal Fitness value= 2.1224
Y
X
45
40
35
30
25
20
15
10
5
0
-5
-10
0
10
20
30
40
50
60
70
6 5 2 4 2 13 1 8 5 6 6
1 0 1 4 3 11 6 15 5 6 7
2 2 5
0 0 3 6 3 6 3 4 2 2 3
14 15 15 16 7 10 13
34 53 49 49 36 32 29
2 5 43 76 72 92 75 42 40 4 4
9 11 42 76 74 100 78 42 37 7 5

DC1 vs DC4

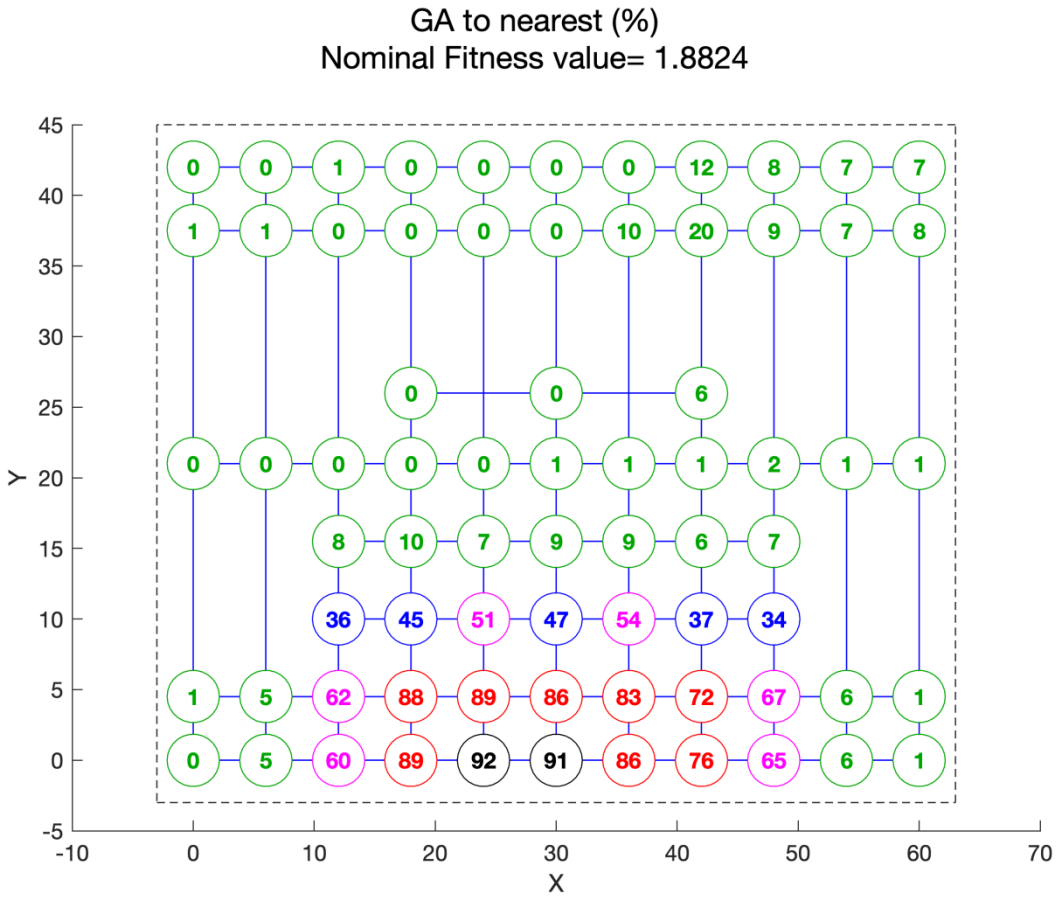
GA to nearest (%)
Nominal Fitness value= 1.8824
Y
X
45
40
35
30
25
20
15
10
5
0
-5
-10
0
10
20
30
40
50
60
70
0 0 1 0 0 0 0 12 8 7 7
1 1 0 0 0 0 10 20 9 7 8
0 0 6
0 0 0 0 0 1 1 1 2 1 1
8 10 7 9 9 6 7
36 45 51 47 54 37 34
1 5 62 88 89 86 83 72 67 6 1
0 5 60 89 92 91 86 76 65 6 1

DC1 vs DC5

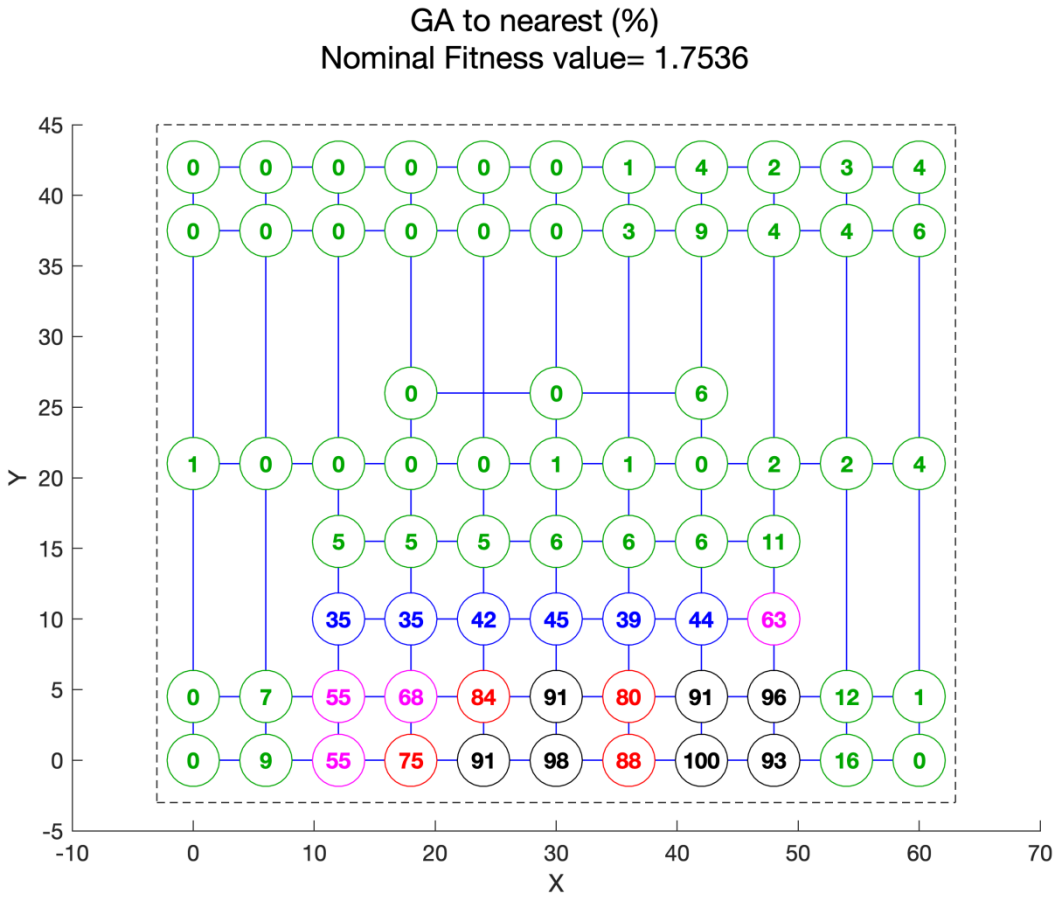
GA to nearest (%)
Nominal Fitness value= 1.7536
Y
X
45
40
35
30
25
20
15
10
5
0
-5
-10
0
10
20
30
40
50
60
70
0 0 0 0 0 0 1 4 2 3 4
0 0 0 0 0 0 3 9 4 4 6
0 0 6
1 0 0 0 0 1 1 0 2 2 4
5 5 5 6 6 6 11
35 35 42 45 39 44 63
0 7 55 68 84 91 80 91 96 12 1
0 9 55 75 91 98 88 100 93 16 0

DC1 vs DC6

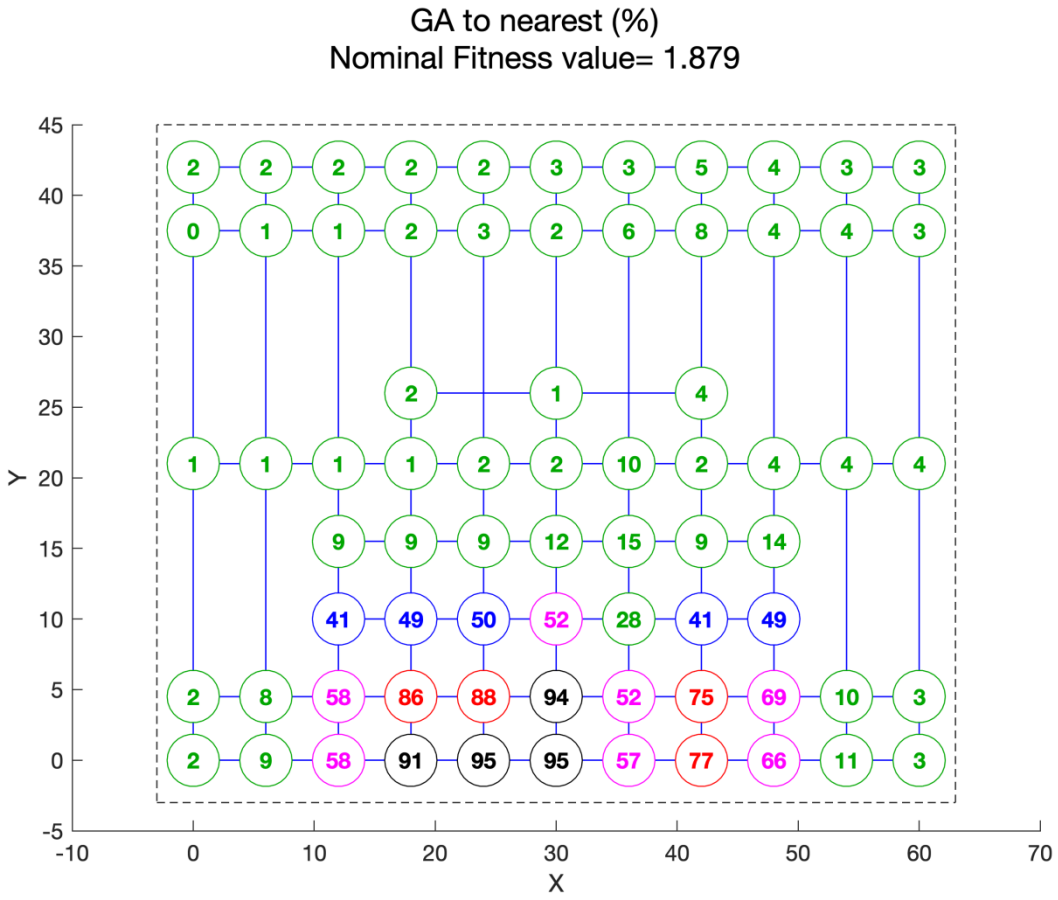
GA to nearest (%)
Nominal Fitness value= 1.879
Y
X
45
40
35
30
25
20
15
10
5
0
-5
-10
0
10
20
30
40
50
60
70
2 2 2 2 2 3 3 5 4 3 3
0 1 1 2 3 2 6 8 4 4 3
2 1 4
1 1 1 1 2 2 10 2 4 4 4
9 9 9 12 15 9 14
41 49 50 52 28 41 49
2 8 58 86 88 94 52 75 69 10 3
2 9 58 91 95 95 57 77 66 11 3

APPENDIX C: MASS LOSS

DC 7 to 8

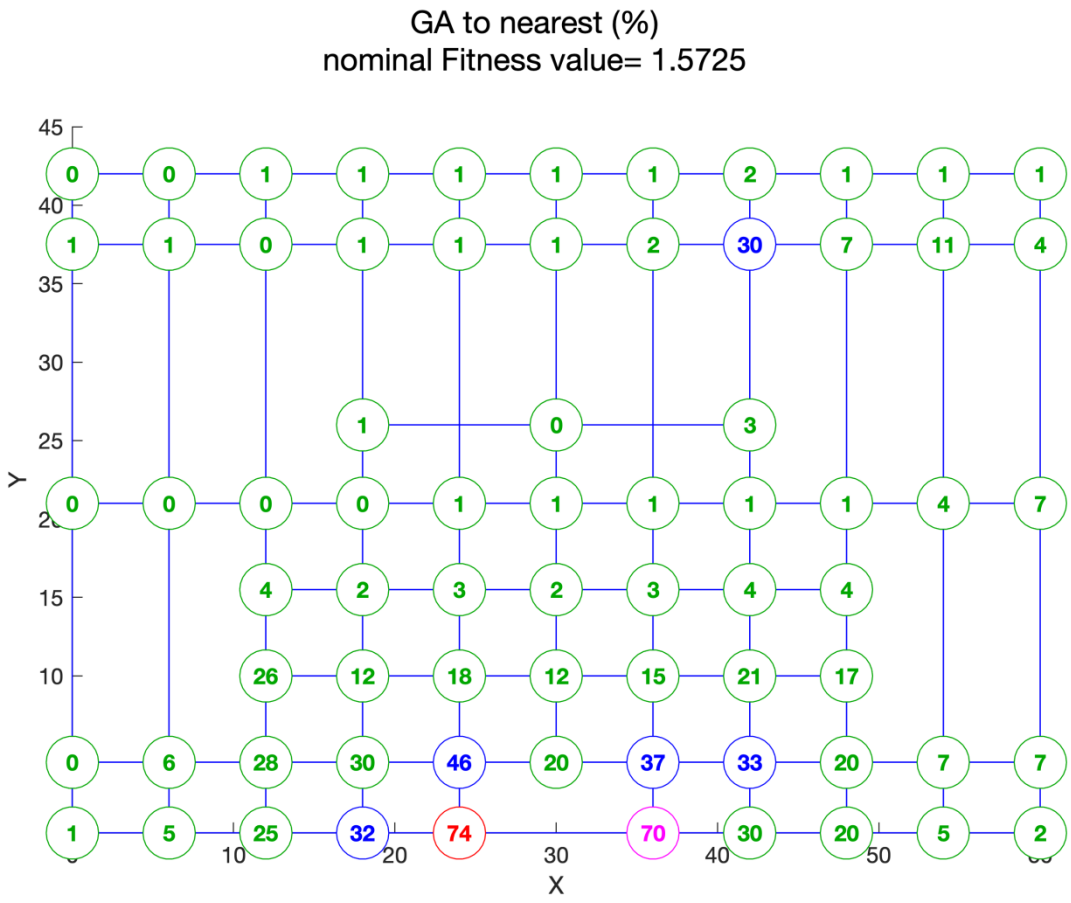
GA to nearest (%)
nominal Fitness value= 1.5725
Y
X
45
40
35
30
25
15
10
10
20
30
40
50

DC 7 to 9

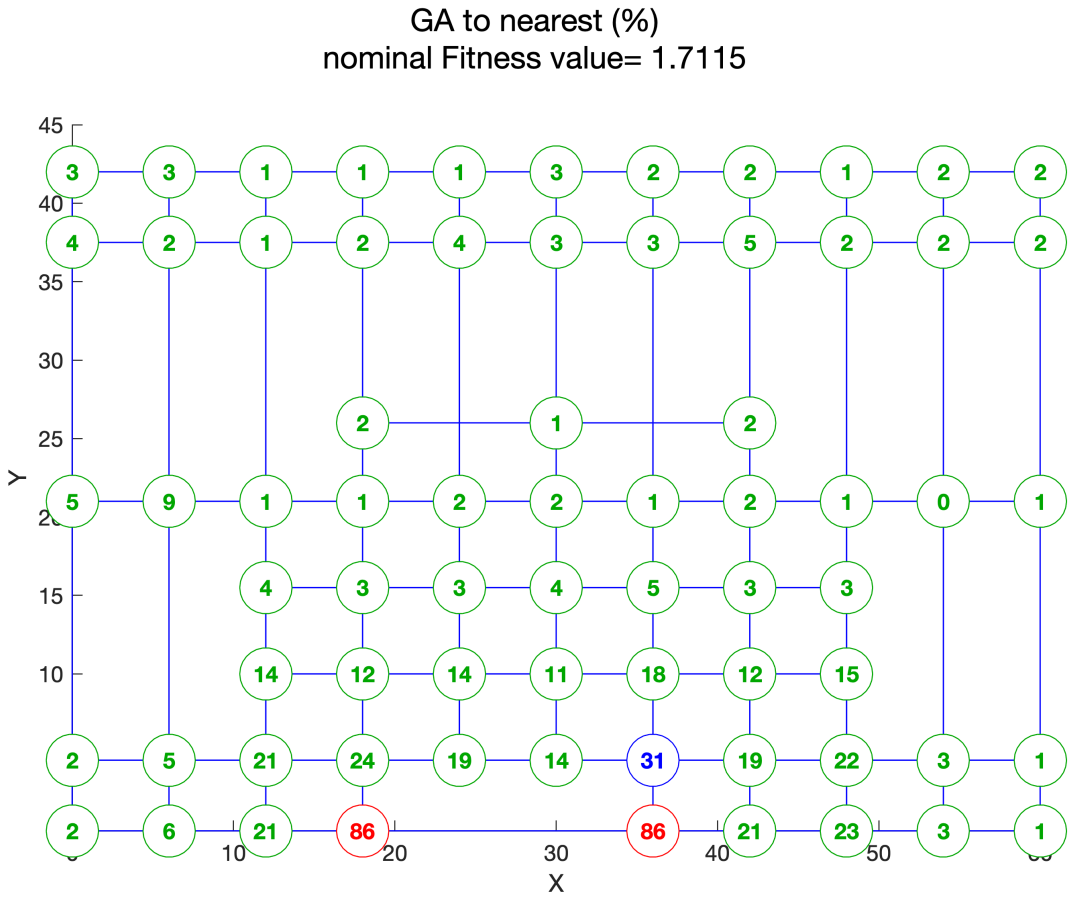
GA to nearest (%)
nominal Fitness value= 1.7115
Y
X
45
40
35
30
25
15
10
10
20
30
40
50
3 3 1 1 1 3 2 2 1 2 2
4 2 1 2 4 3 3 5 2 2 2
2 1 2
5 9 1 1 2 2 1 2 1 0 1
4 3 3 4 5 3 3
14 12 14 11 18 12 15
2 5 21 24 19 14 31 19 22 3 1
2 6 21 86 86 21 23 3 1

DC 7 to 10

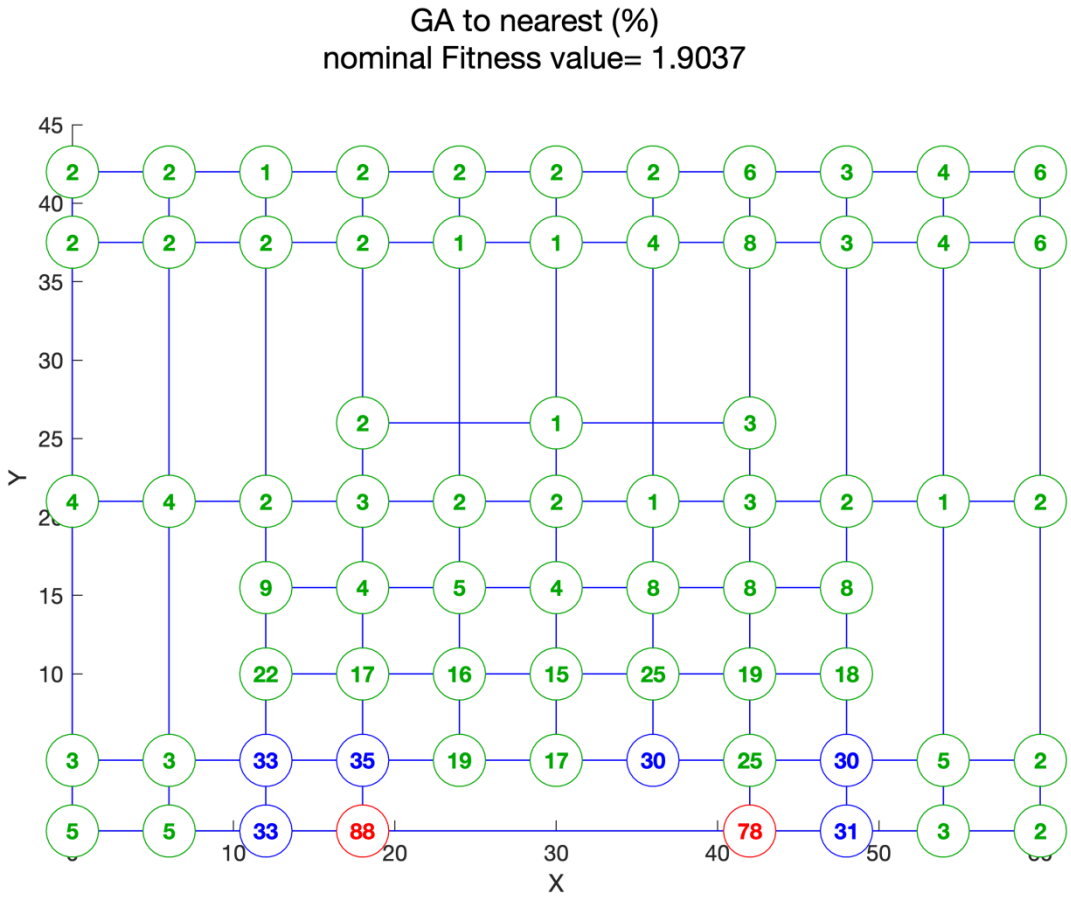
GA to nearest (%)
nominal Fitness value= 1.9037
Y
X
45
40
35
30
25
15
10
10
20
30
40
50

DC 7 to 11

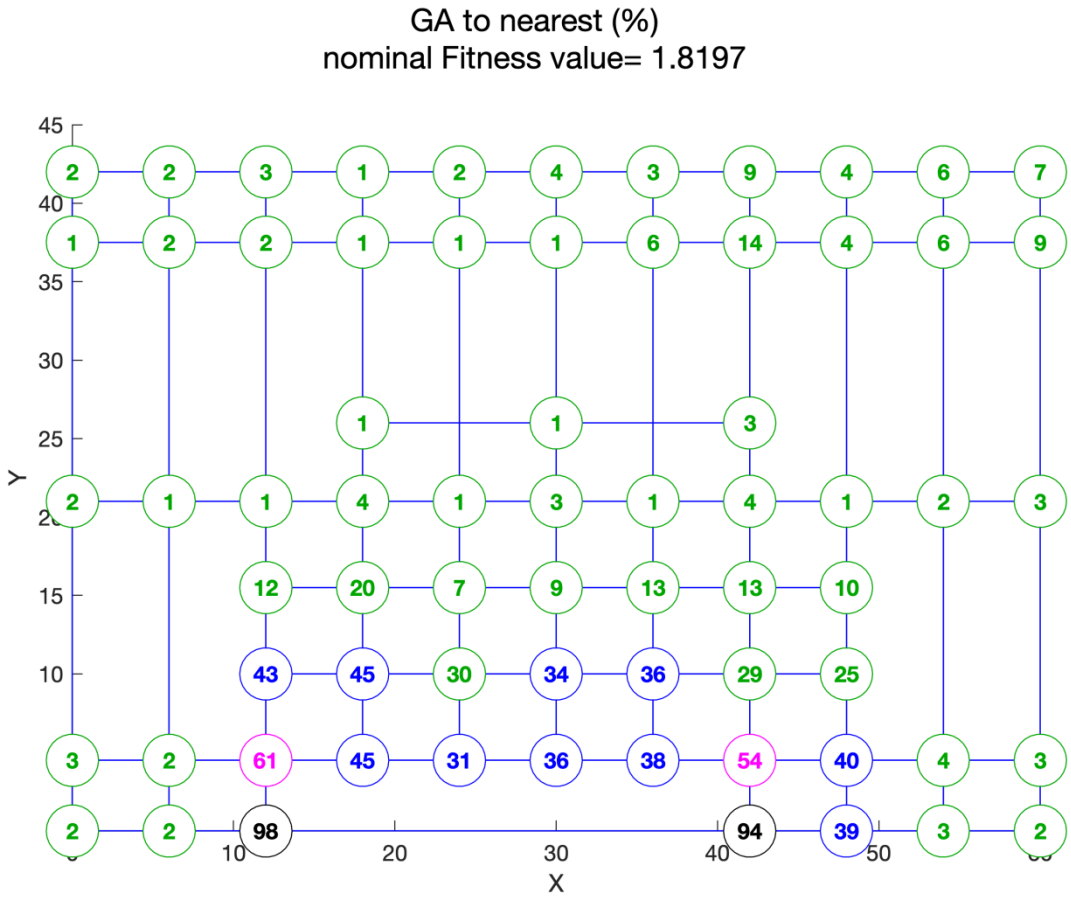
GA to nearest (%)
nominal Fitness value= 1.8197
Y
X
45
40
35
30
25
15
10
10
20
30
40
50
2 2 3 1 2 4 3 9 4 6 7
1 2 2 1 1 1 6 14 4 6 9
1 1 3
2 1 1 4 1 3 1 4 1 2 3
12 20 7 9 13 13 10
43 45 30 34 36 29 25
3 2 61 45 31 36 38 54 40 4 3
2 2 98 94 39 3 2

DC 7 to 12

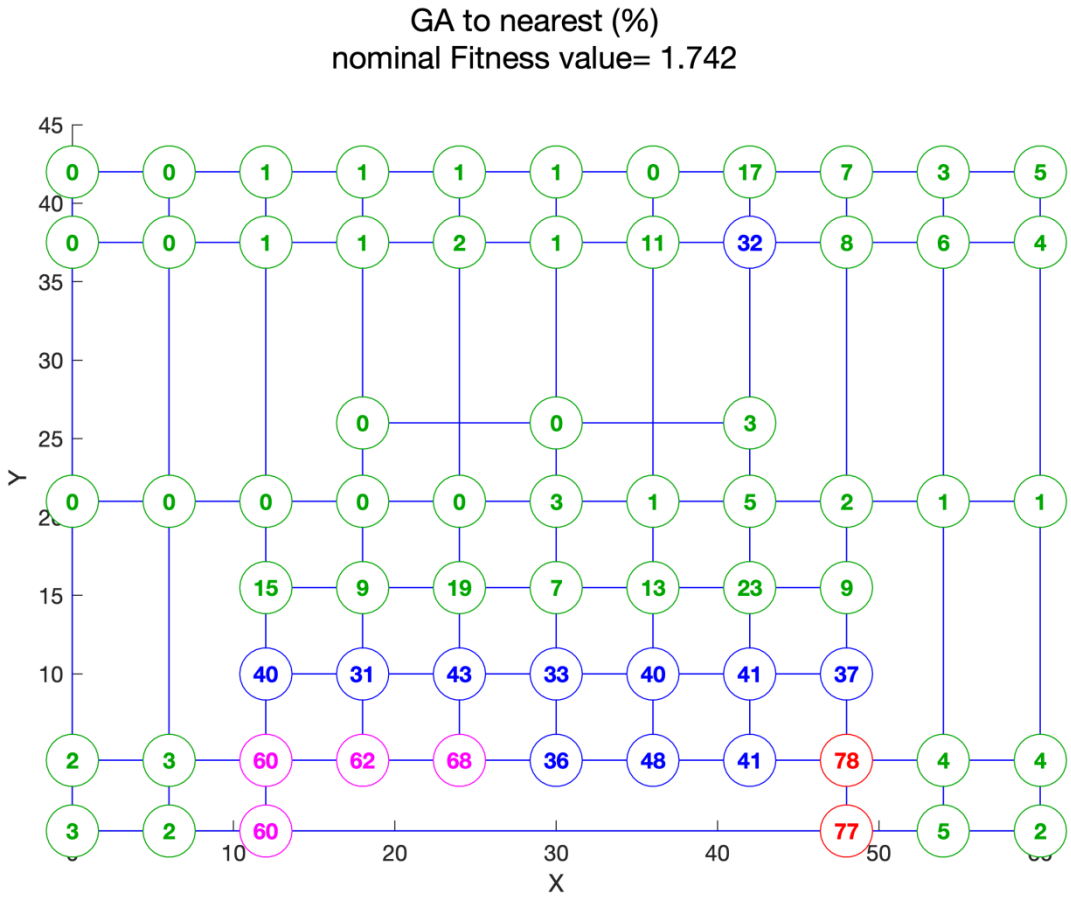
GA to nearest (%)
nominal Fitness value= 1.742
Y
X
45
40
35
30
25
20
15
10
10
20
30
40
50
0 0 1 1 1 1 0 17 7 3 5
0 0 1 1 2 1 11 32 8 6 4
0 0 3
0 0 0 0 0 3 1 5 2 1 1
15 9 19 7 13 23 9
40 31 43 33 40 41 37
2 3 60 62 68 36 48 41 78 4 4
3 2 60 77 5 2

DC 7 to 13

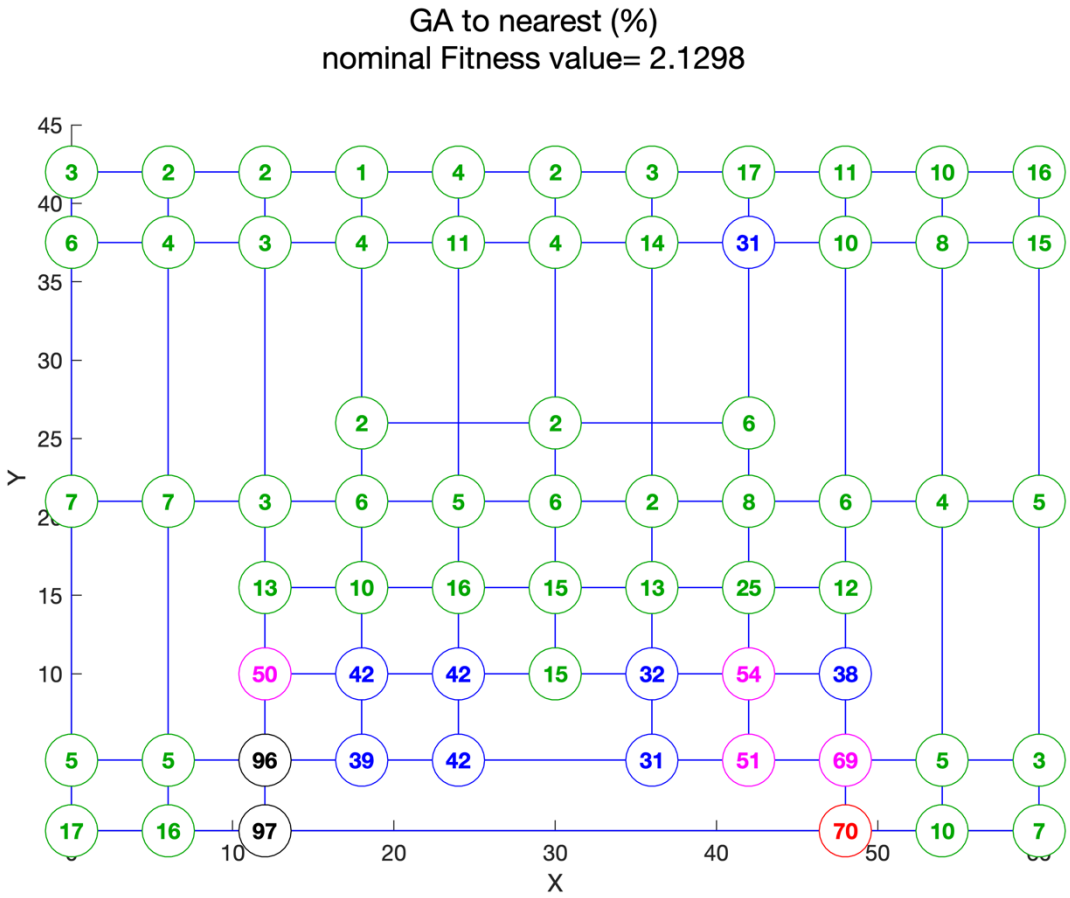
GA to nearest (%)
nominal Fitness value= 2.1298
Y
X
45
40
35
30
25
15
10
10
20
30
40
50
3 2 2 1 4 2 3 17 11 10 16
6 4 3 4 11 4 14 31 10 8 15
2 2 6
7 7 3 6 5 6 2 8 6 4 5
13 10 16 15 13 25 12
50 42 42 15 32 54 38
5 5 96 39 42 31 51 69 5 3
17 16 97 70 10 7

DC 7 to 14

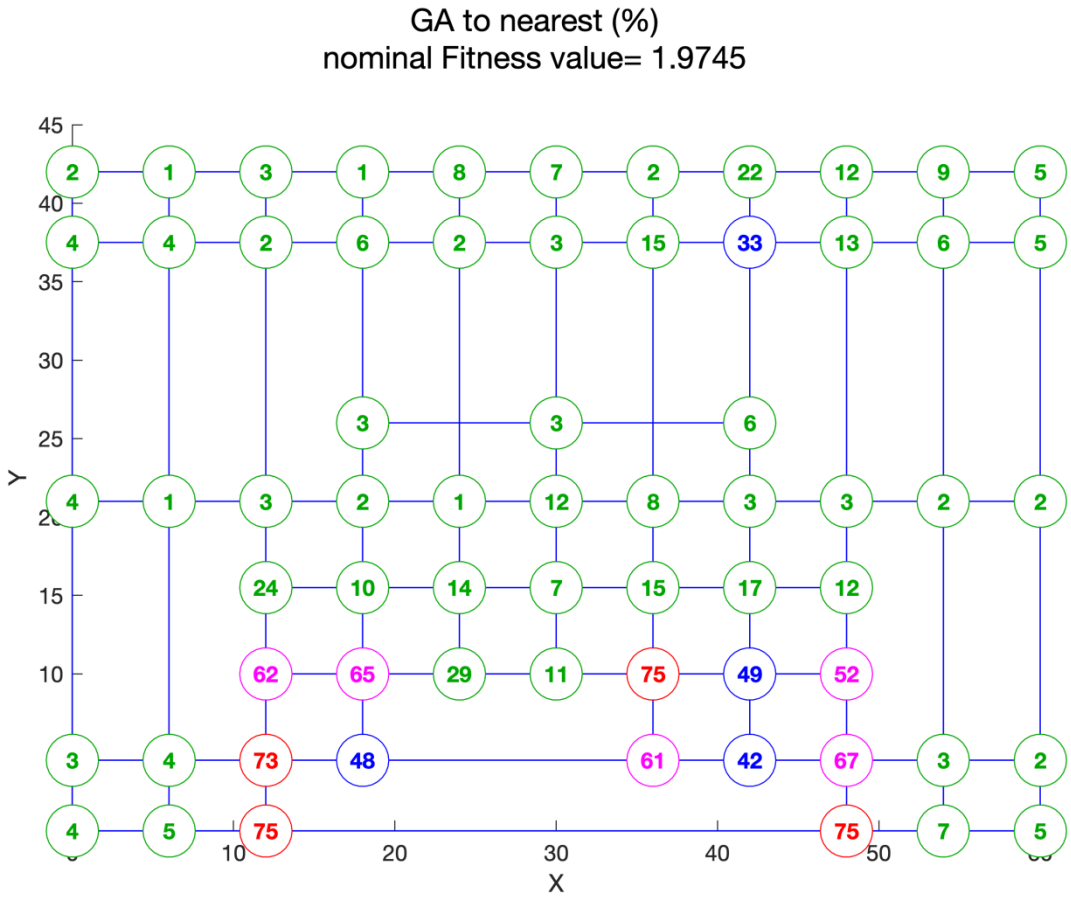
GA to nearest (%)
nominal Fitness value= 1.9745
Y
X
45
40
35
30
25
15
10
10
20
30
40
50
2 1 3 1 8 7 2 22 12 9 5
4 4 2 6 2 3 15 33 13 6 5
3 3 6
4 1 3 2 1 12 8 3 3 2 2
24 10 14 7 15 17 12
62 65 29 11 75 49 52
3 4 73 48 61 42 67 3 2
4 5 75 75 7 5

DC 7 to 15

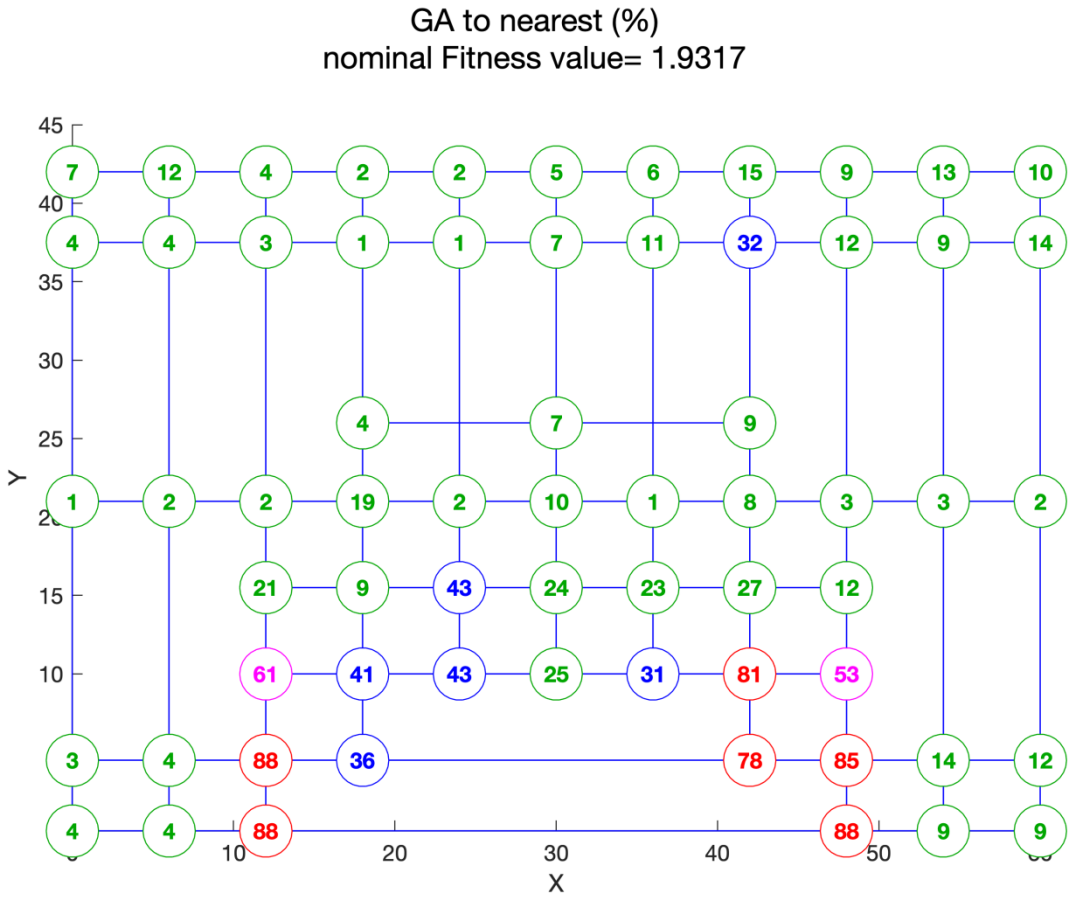
GA to nearest (%)
nominal Fitness value= 1.9317
Y
X
45
40
35
30
25
15
10
10
20
30
40
50
7 12 4 2 2 5 6 15 9 13 10
4 4 3 1 1 7 11 32 12 9 14
4 7 9
1 2 2 19 2 10 1 8 3 3 2
21 9 43 24 23 27 12
61 41 43 25 31 81 53
3 4 88 36 78 85 14 12
4 4 88 88 9 9

DC 7 to 16

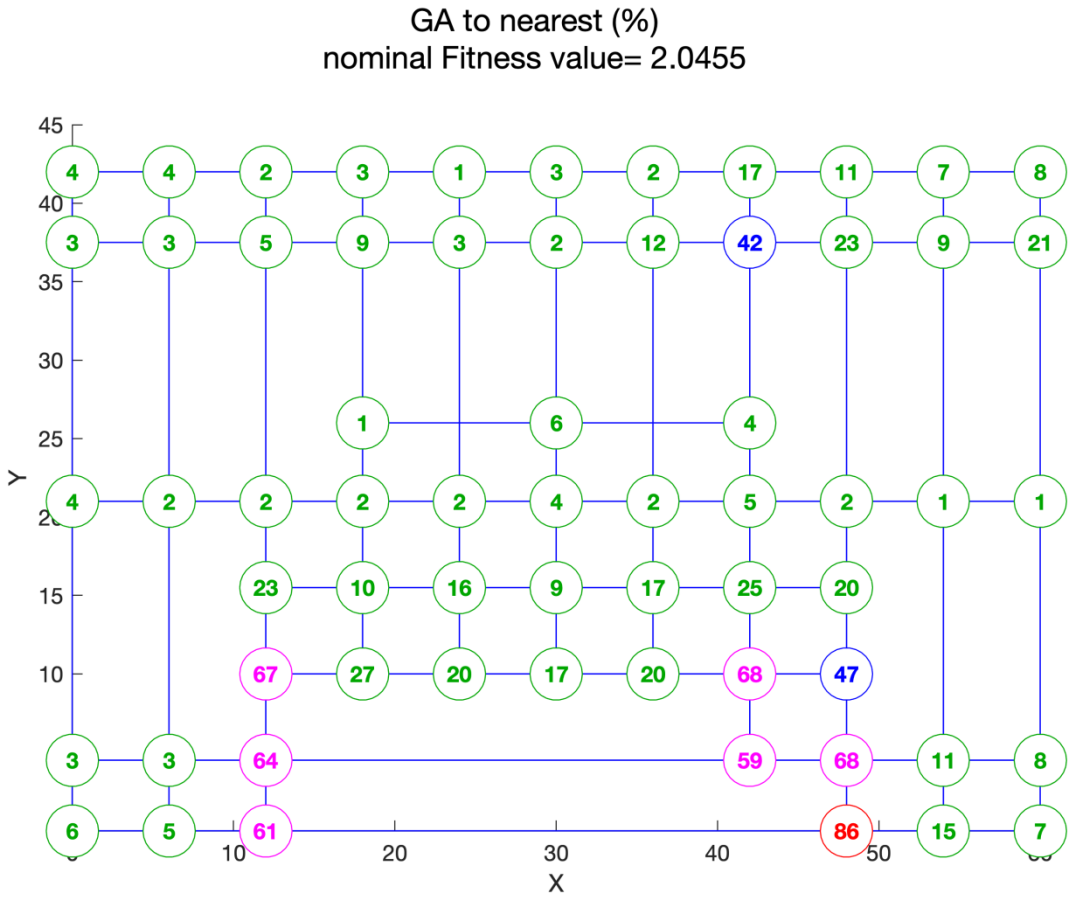
GA to nearest (%)
nominal Fitness value= 2.0455
Y
X
45
40
35
30
25
15
10
10
20
30
40
50
4 4 2 3 1 3 2 17 11 7 8
3 3 5 9 3 2 12 42 23 9 21
1 6 4
4 2 2 2 2 4 2 5 2 1 1
23 10 16 9 17 25 20
67 27 20 17 20 68 47
3 3 64 59 68 11 8
6 5 61 86 15 7

DC 7 to 17

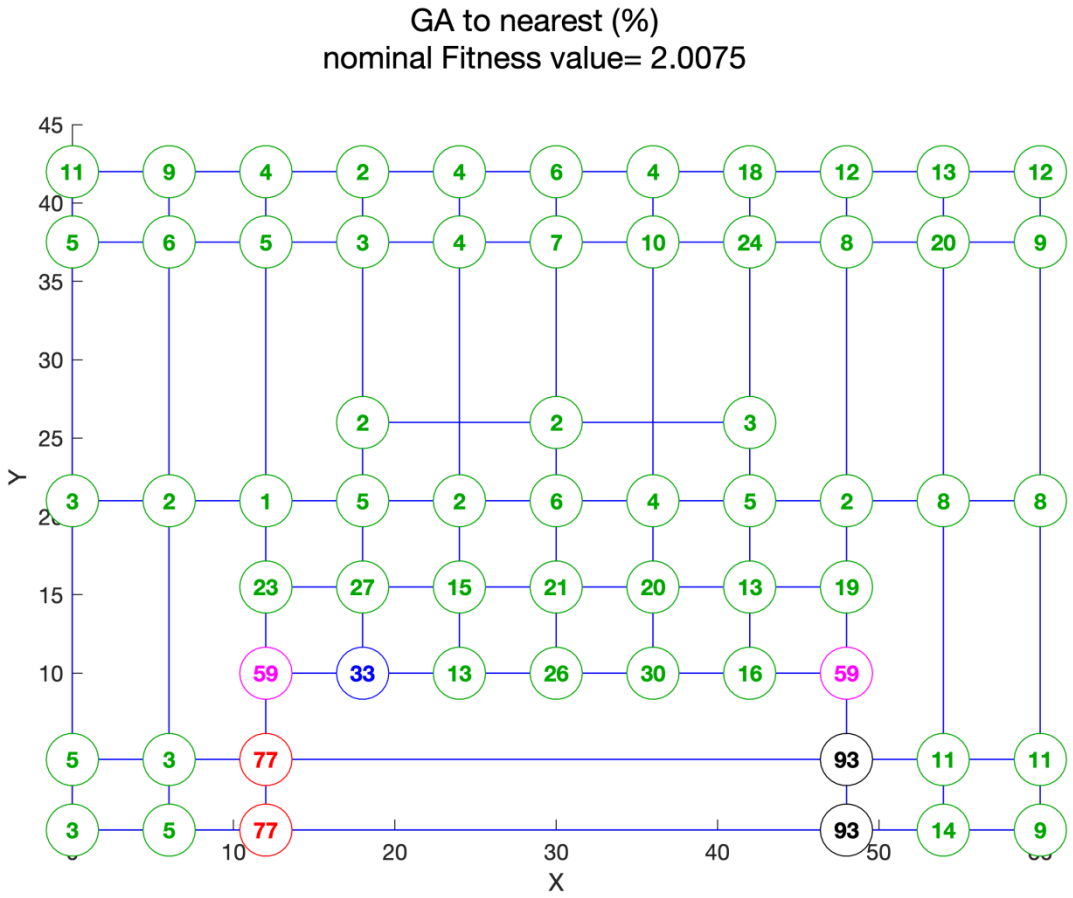
GA to nearest (%)
nominal Fitness value= 2.0075
Y
X
45
40
35
30
25
15
10
10
20
30
40
50
11 9 4 2 4 6 4 18 12 13 12
5 6 5 3 4 7 10 24 8 20 9
2 2 3
3 2 1 5 2 6 4 5 2 8 8
23 27 15 21 20 13 19
59 33 13 26 30 16 59
5 3 77 93 11 11
3 5 77 93 14 9

DC 7 to 18

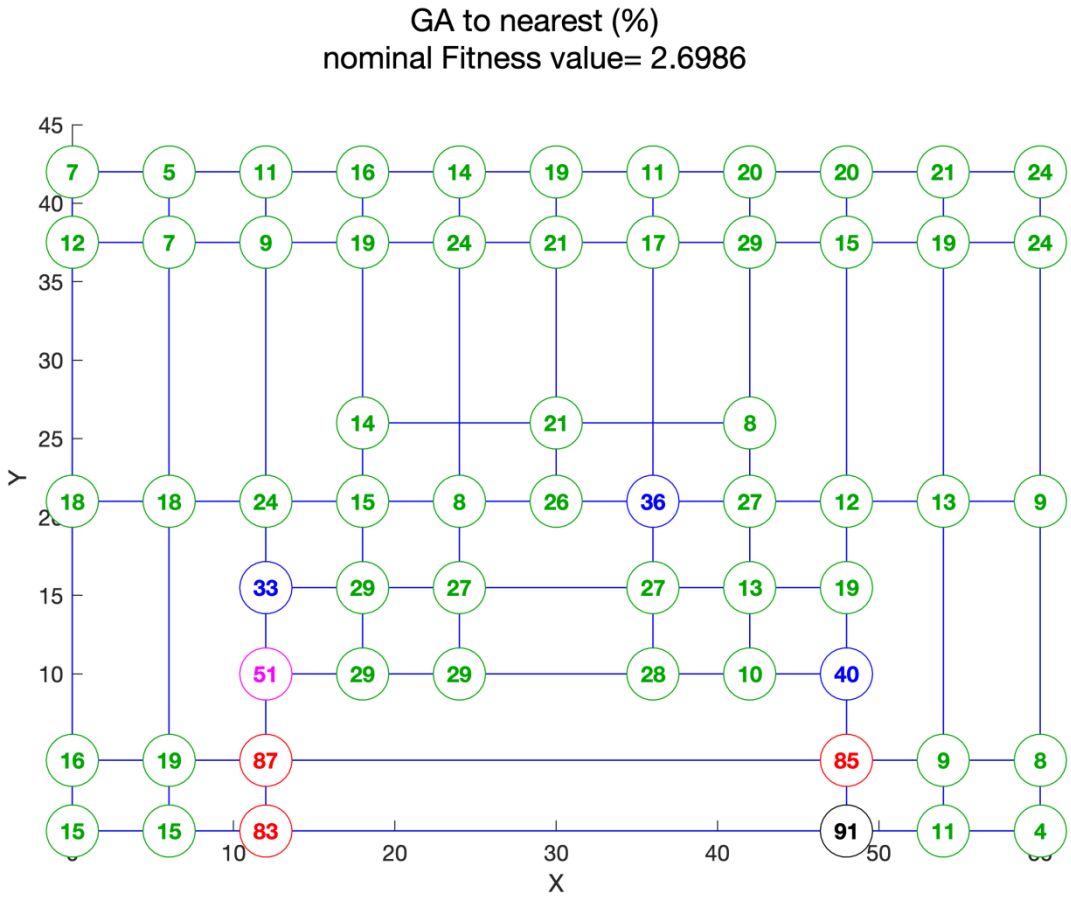
GA to nearest (%)
nominal Fitness value= 2.6986
Y
X
45
40
35
30
25
15
10
10
20
30
40
50
7 5 11 16 14 19 11 20 20 21 24
12 7 9 19 24 21 17 29 15 19 24
14 21 8
18 18 24 15 8 26 36 27 12 13 9
33 29 27 27 13 19
51 29 29 28 10 40
16 19 87 85 9 8
15 15 83 91 11 4

DC 7 to 19

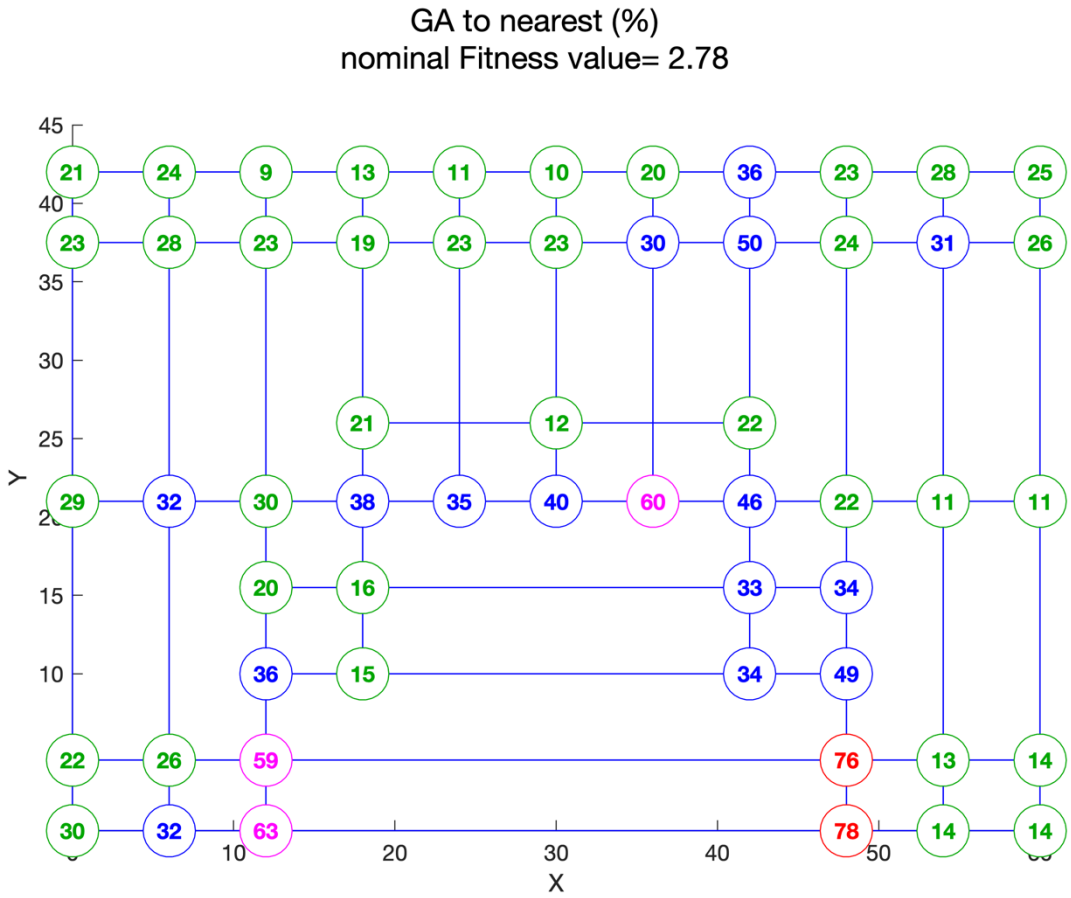
GA to nearest (%)
nominal Fitness value= 2.78
Y
X
45
40
35
30
25
15
10
10
20
30
40
50
21 24 9 13 11 10 20 36 23 28 25
23 28 23 19 23 23 30 50 24 31 26
21 12 22
29 32 30 38 35 40 60 46 22 11 11
20 16 33 34
36 15 34 49
22 26 59 76 13 14
30 32 63 78 14 14

DC 7 to 20

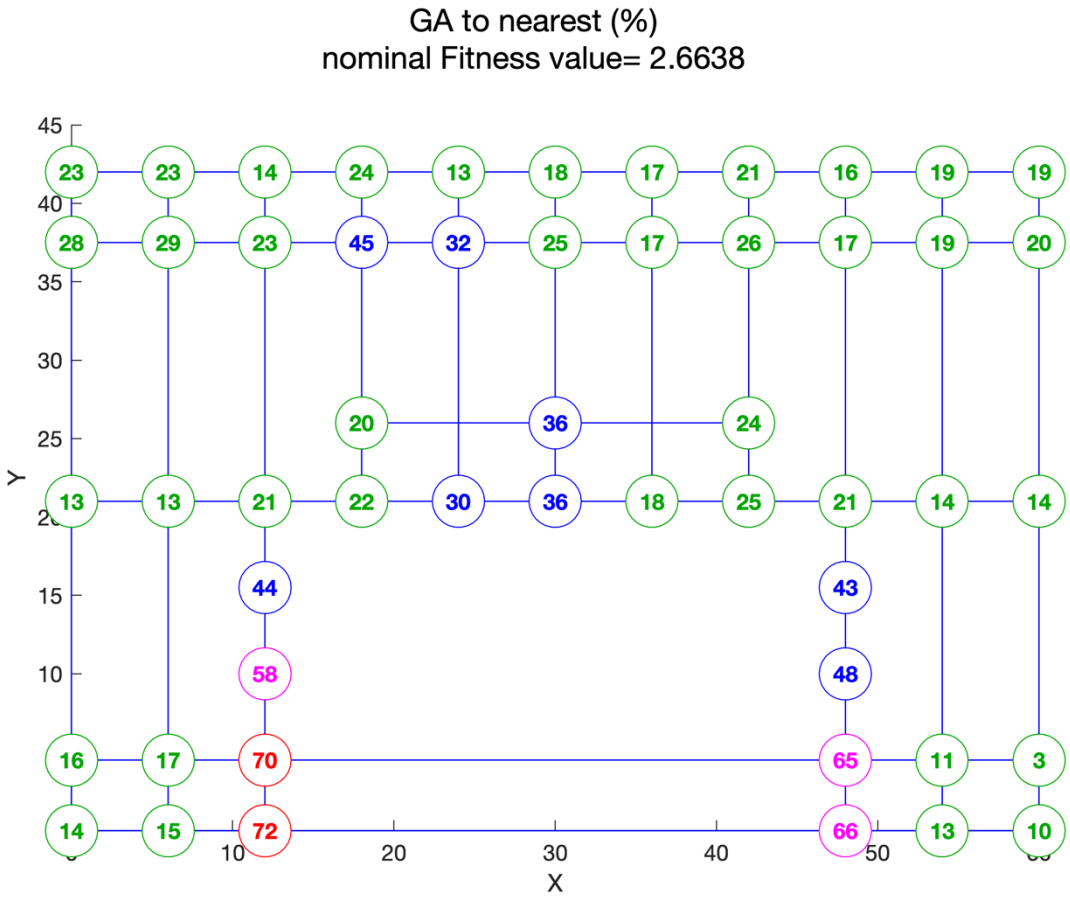
GA to nearest (%)
nominal Fitness value= 2.6638
Y
X
45
40
35
30
25
15
10
10
20
30
40
50
23 23 14 24 13 18 17 21 16 19 19
28 29 23 45 32 25 17 26 17 19 20
20 36 24
13 13 21 22 30 36 18 25 21 14 14
44 43
58 48
16 17 70 65 11 3
14 15 72 66 13 10

DC 7 to 8

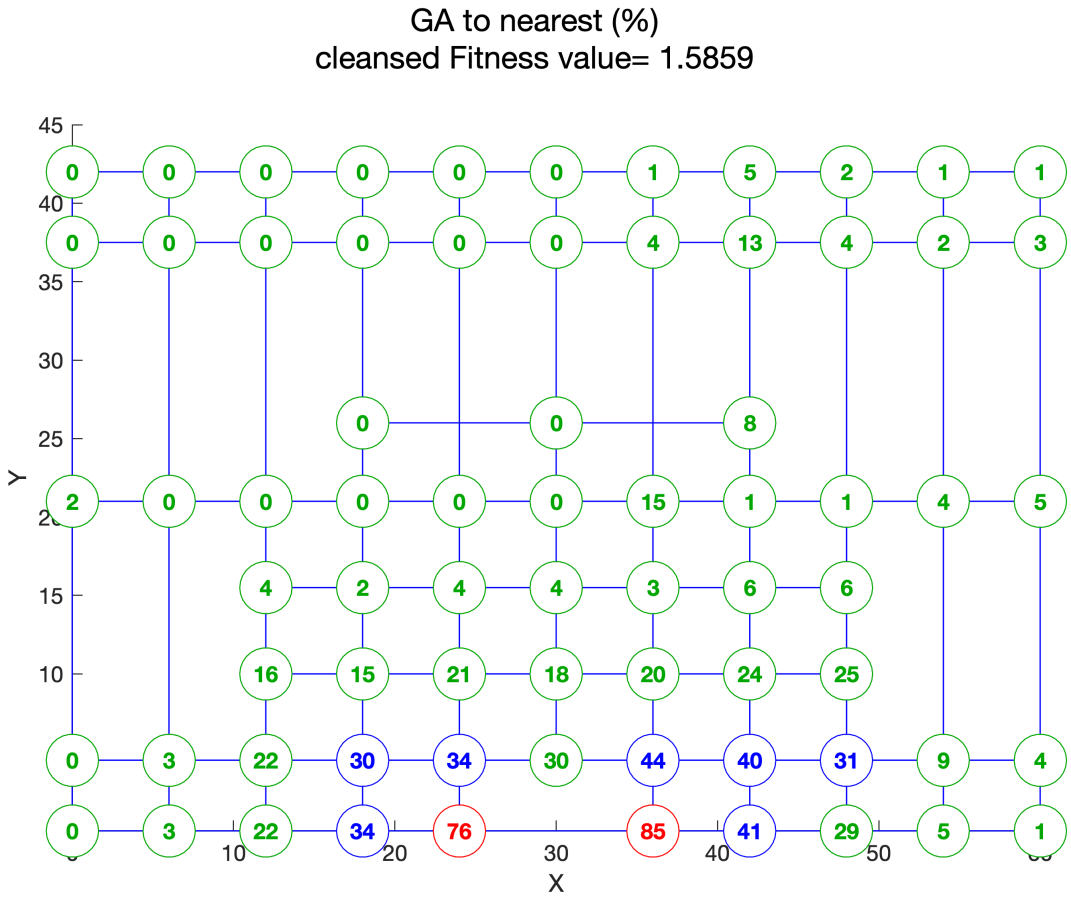
GA to nearest (%)
cleansed Fitness value= 1.5859
Y
X
45
40
35
30
25
15
10
10
20
30
40
50
0 0 0 0 0 0 1 5 2 1 1
0 0 0 0 0 0 4 13 4 2 3
0 0 8
2 0 0 0 0 0 15 1 1 4 5
4 2 4 4 3 6 6
16 15 21 18 20 24 25
0 3 22 30 34 30 44 40 31 9 4
0 3 22 34 76 85 41 29 5 1

DC 7 to 9

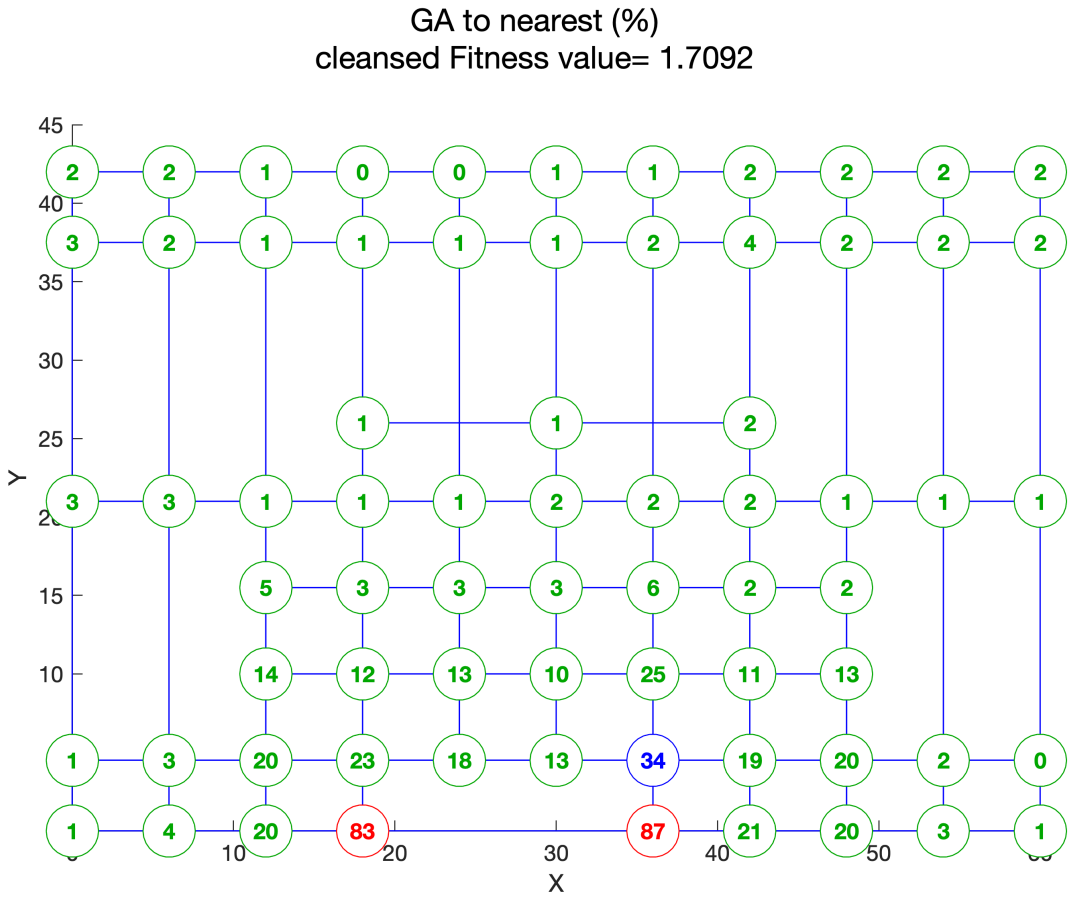
GA to nearest (%)
cleansed Fitness value= 1.7092
Y
X
45
40
35
30
25
15
10
10
20
30
40
50
2 2 1 0 0 1 1 2 2 2 2
3 2 1 1 1 1 2 4 2 2 2
1 1 2
3 3 1 1 1 2 2 2 1 1 1
5 3 3 3 6 2 2
14 12 13 10 25 11 13
1 3 20 23 18 13 34 19 20 2 0
1 4 20 83 87 21 20 3 1

DC 7 to 10

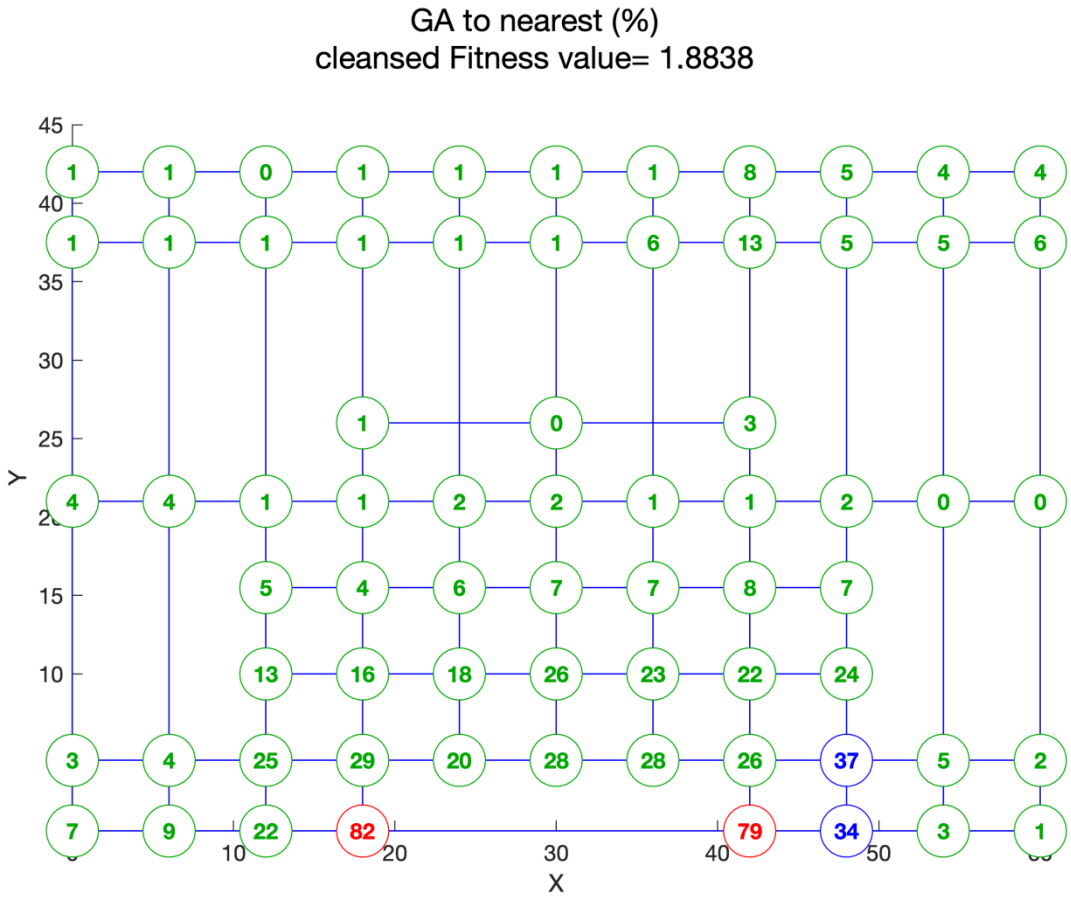
GA to nearest (%)
cleansed Fitness value= 1.8838
Y
X
45
40
35
30
25
15
10
10
20
30
40
50
1 1 0 1 1 1 1 8 5 4 4
1 1 1 1 1 1 6 13 5 5 6
1 0 3
4 4 1 1 2 2 1 1 2 0 0
5 4 6 7 7 8 7
13 16 18 26 23 22 24
3 4 25 29 20 28 28 26 37 5 2
7 9 22 82 79 34 3 1

DC 7 to 11

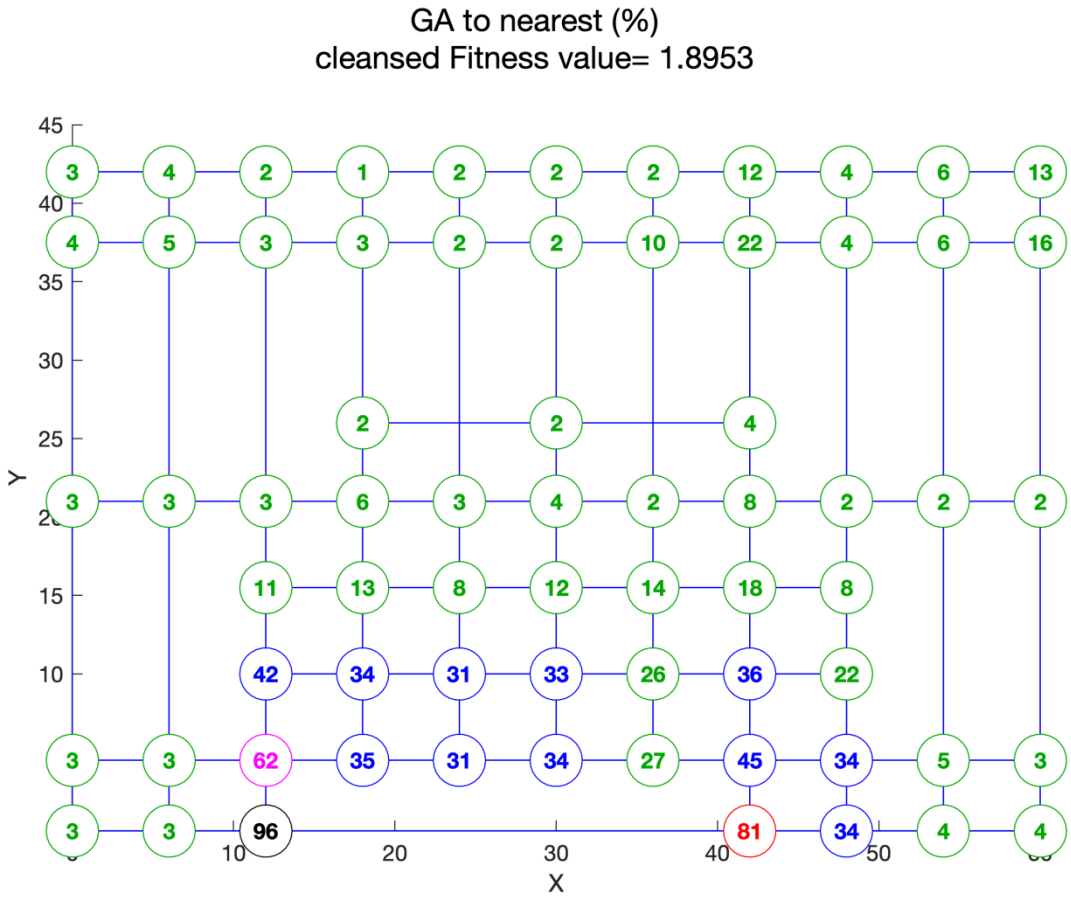
GA to nearest (%)
cleansed Fitness value= 1.8953
Y
X
45
40
35
30
25
15
10
10
20
30
40
50
3 4 2 1 2 2 2 12 4 6 13
4 5 3 3 2 2 10 22 4 6 16
2 2 4
3 3 3 6 3 4 2 8 2 2 2
11 13 8 12 14 18 8
42 34 31 33 26 36 22
3 3 62 35 31 34 27 45 34 5 3
3 3 96 81 34 4 4

DC 7 to 12

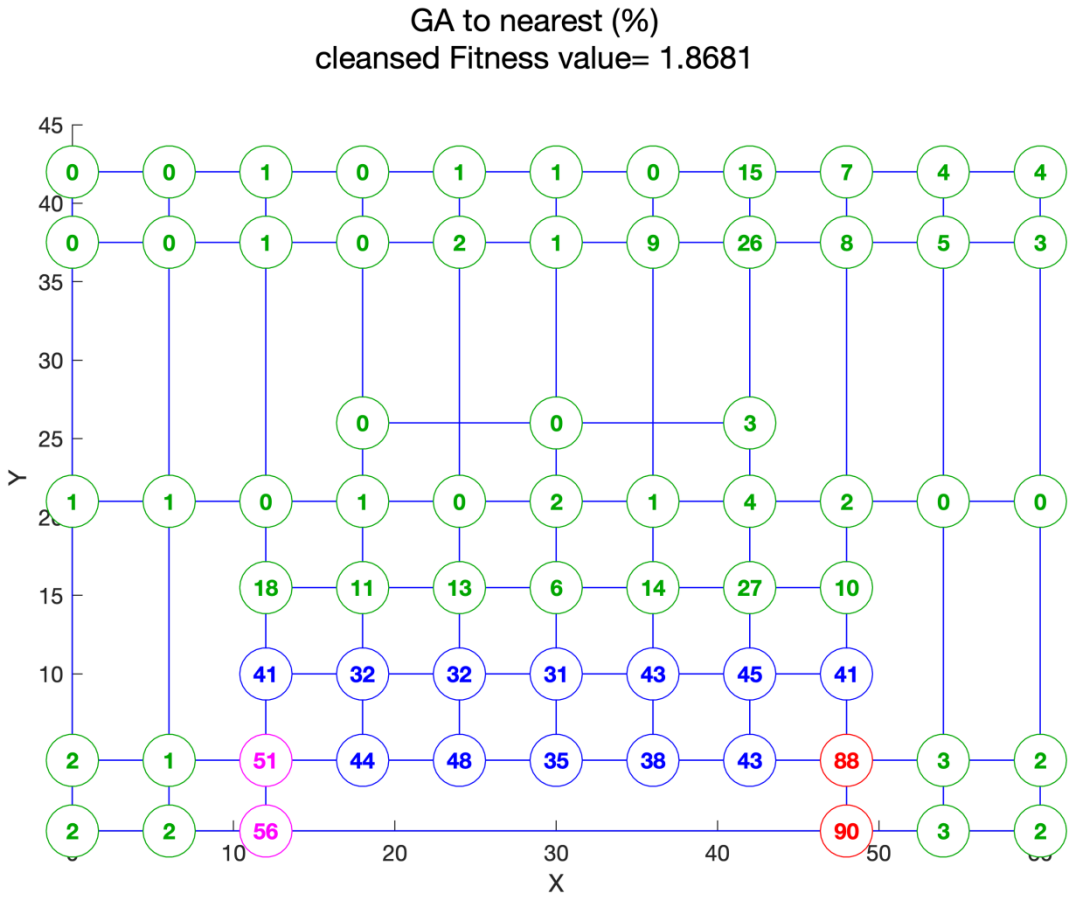
GA to nearest (%)
cleansed Fitness value= 1.8681
Y
X
45
40
35
30
25
15
10
10
20
30
40
50
0 0 1 0 1 1 0 15 7 4 4
0 0 1 0 2 1 9 26 8 5 3
0 0 3
1 1 0 1 0 2 1 4 2 0 0
18 11 13 6 14 27 10
41 32 32 31 43 45 41
2 1 51 44 48 35 38 43 88 3 2
2 2 56 90 3 2

DC 7 to 13

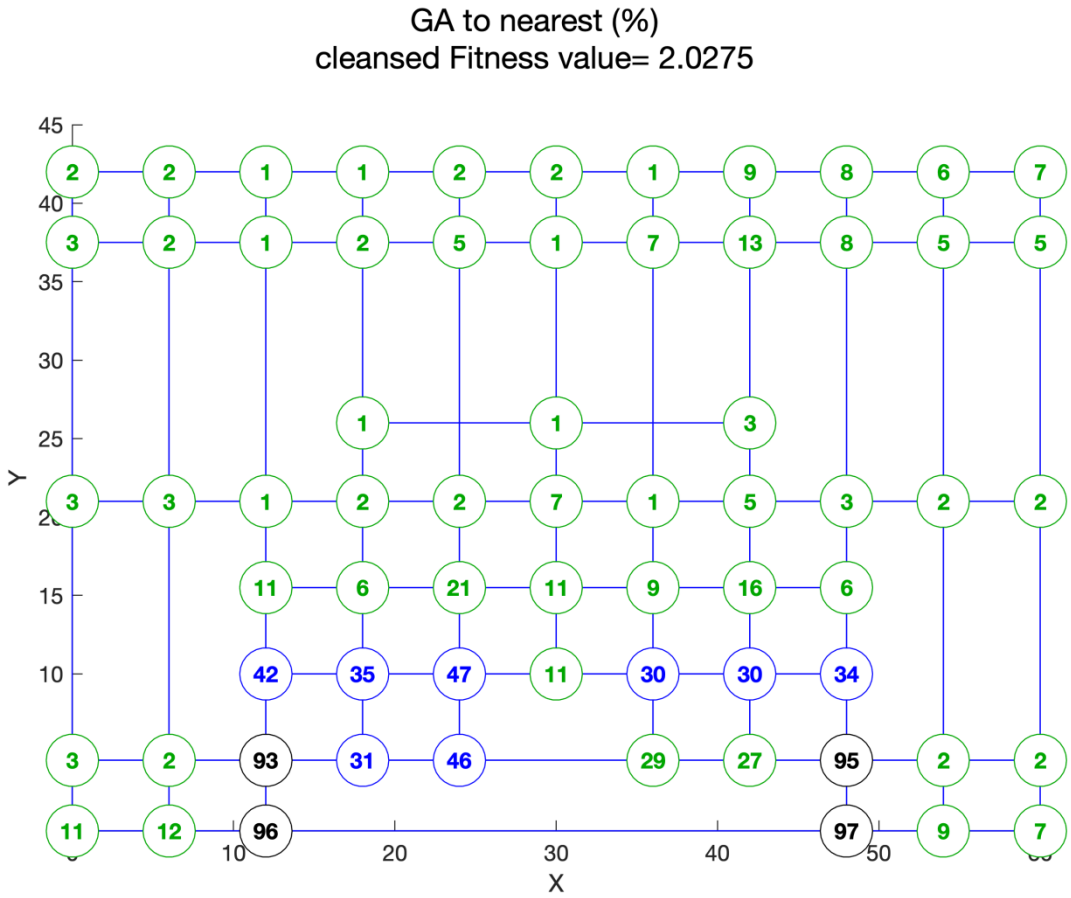
GA to nearest (%)
cleansed Fitness value= 2.0275
Y
X
45
40
35
30
25
15
10
10
20
30
40
50

DC 7 to 14

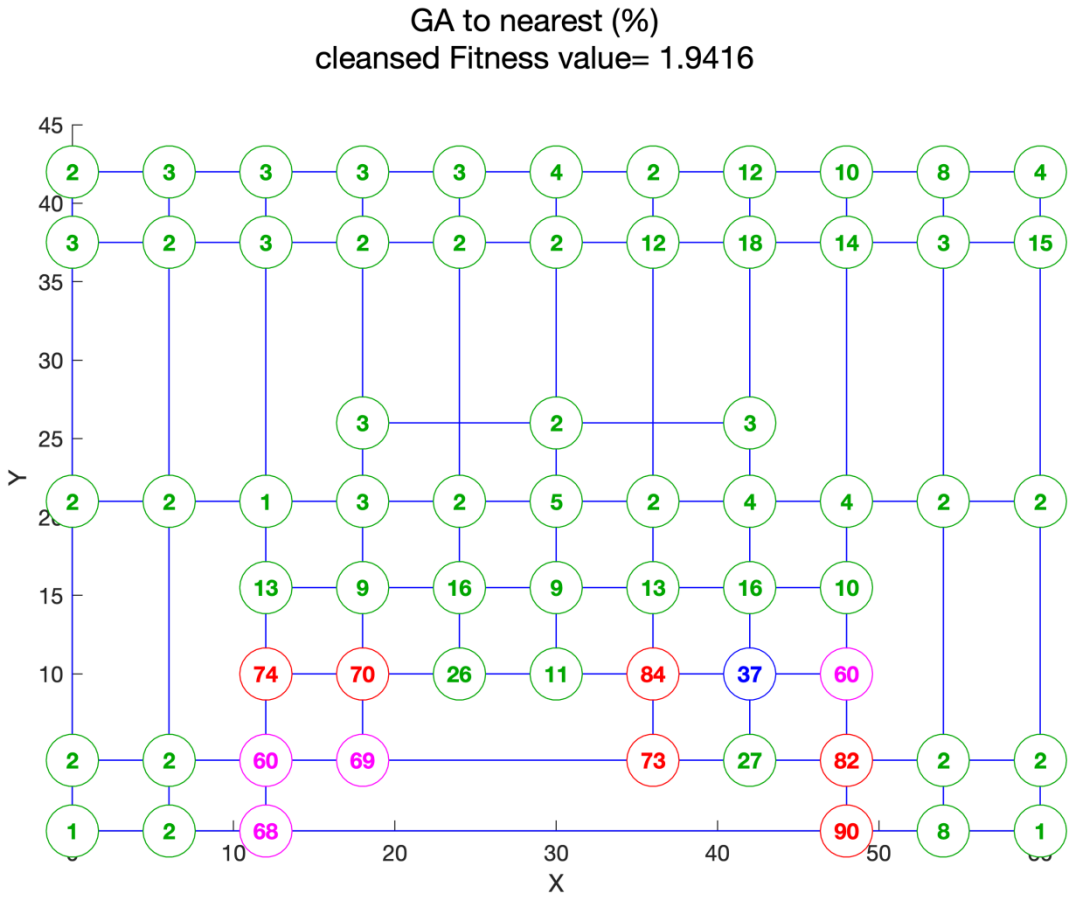
GA to nearest (%)
cleansed Fitness value= 1.9416
Y
X
45
40
35
30
25
15
10
10
20
30
40
50
2 3 3 3 3 4 2 12 10 8 4
3 2 3 2 2 2 12 18 14 3 15
3 2 3
2 2 1 3 2 5 2 4 4 2 2
13 9 16 9 13 16 10
74 70 26 11 84 37 60
2 2 60 69 73 27 82 2 2
1 2 68 90 8 1

DC 7 to 15

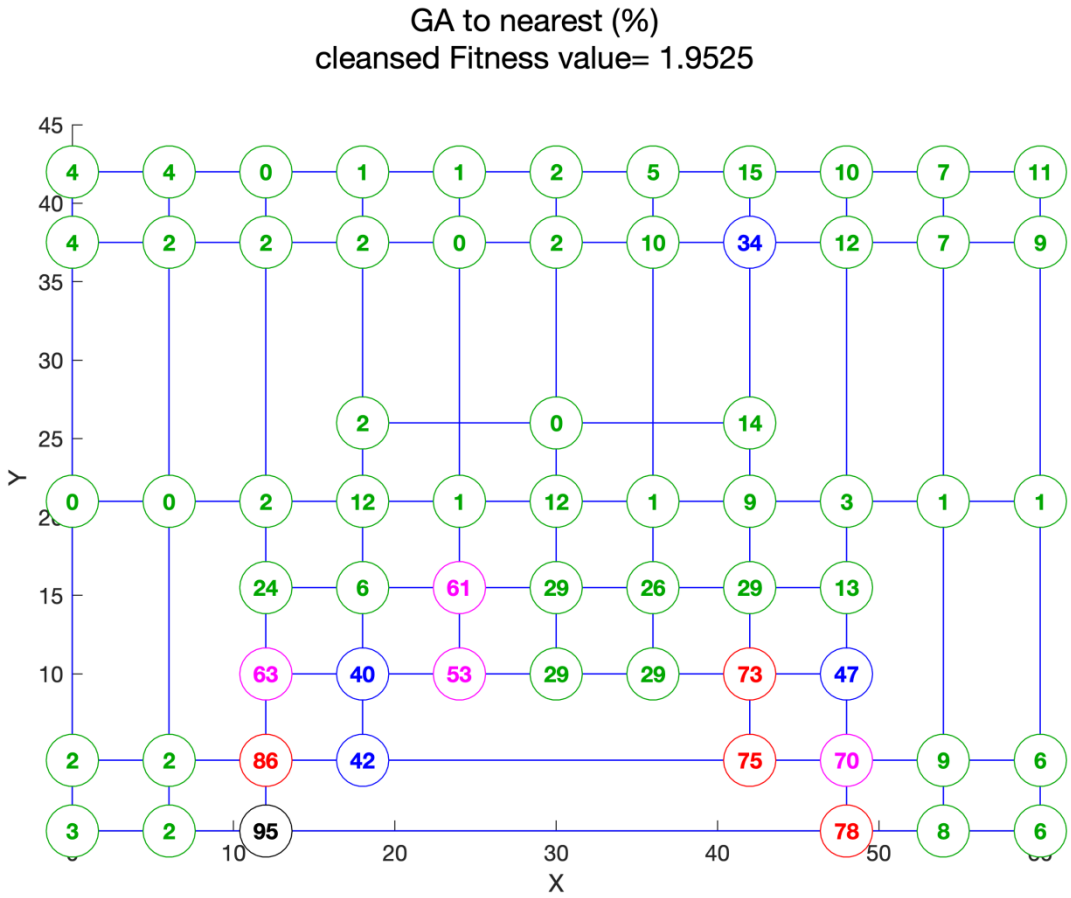
GA to nearest (%)
cleansed Fitness value= 1.9525
Y
X
45
40
35
30
25
15
10
10
20
30
40
50
4 4 0 1 1 2 5 15 10 7 11
4 2 2 2 0 2 10 34 12 7 9
2 0 14
0 0 2 12 1 12 1 9 3 1 1
24 6 61 29 26 29 13
63 40 53 29 29 73 47
2 2 86 42 75 70 9 6
3 2 95 78 8 6

DC 7 to 16

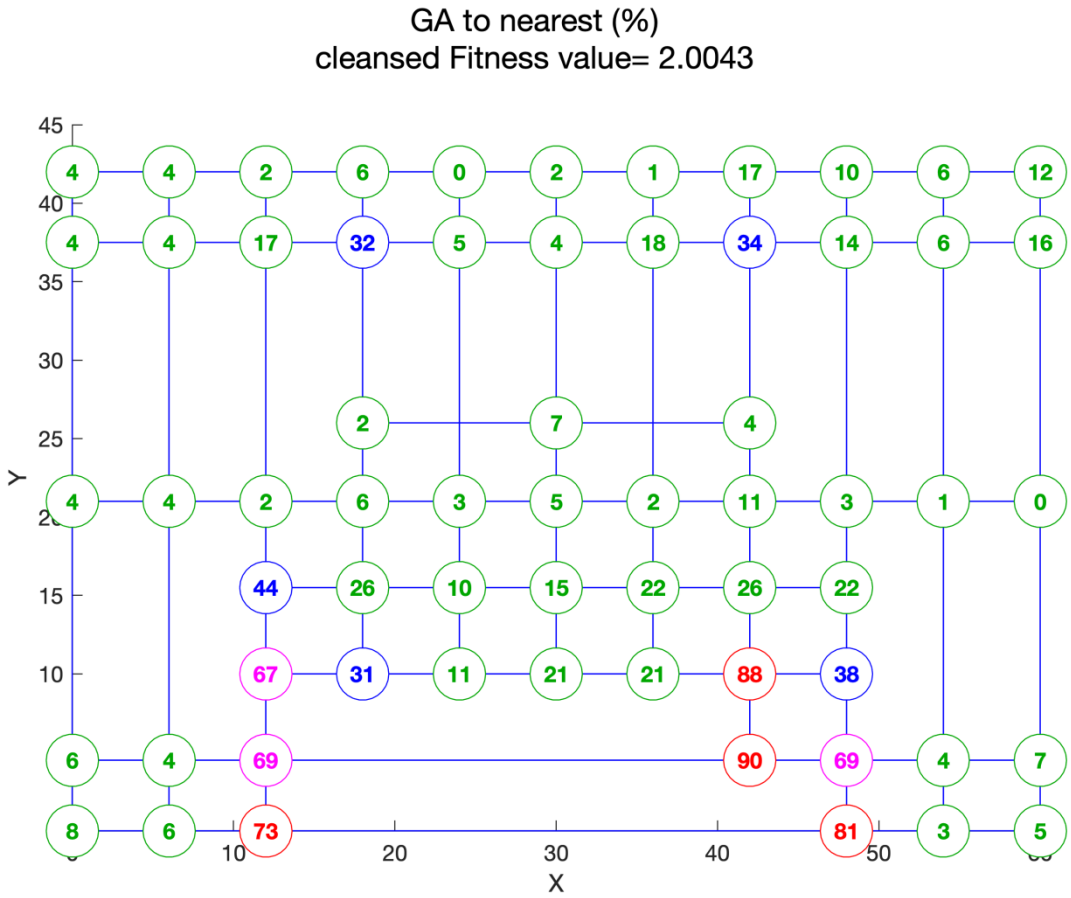
GA to nearest (%)
cleansed Fitness value= 2.0043
Y
X
45
40
35
30
25
15
10
10
20
30
40
50
4 4 2 6 0 2 1 17 10 6 12
4 4 17 32 5 4 18 34 14 6 16
2 7 4
4 4 2 6 3 5 2 11 3 1 0
44 26 10 15 22 26 22
67 31 11 21 21 88 38
6 4 69 90 69 4 7
8 6 73 81 3 5

DC 7 to 17

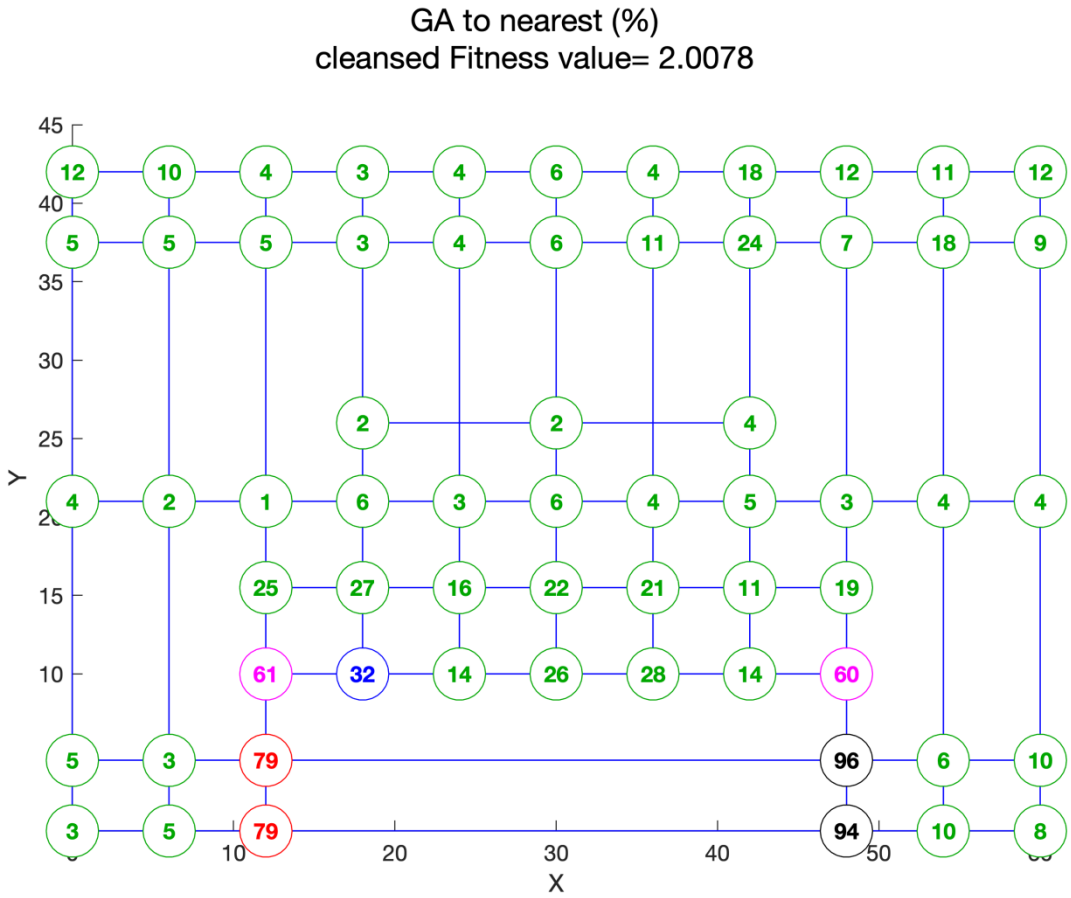
GA to nearest (%)
cleansed Fitness value= 2.0078
Y
X
45
40
35
30
25
15
10
10
20
30
40
50
12 10 4 3 4 6 4 18 12 11 12
5 5 5 3 4 6 11 24 7 18 9
2 2 4
4 2 1 6 3 6 4 5 3 4 4
25 27 16 22 21 11 19
61 32 14 26 28 14 60
5 3 79 96 6 10
3 5 79 94 10 8

DC 7 to 18

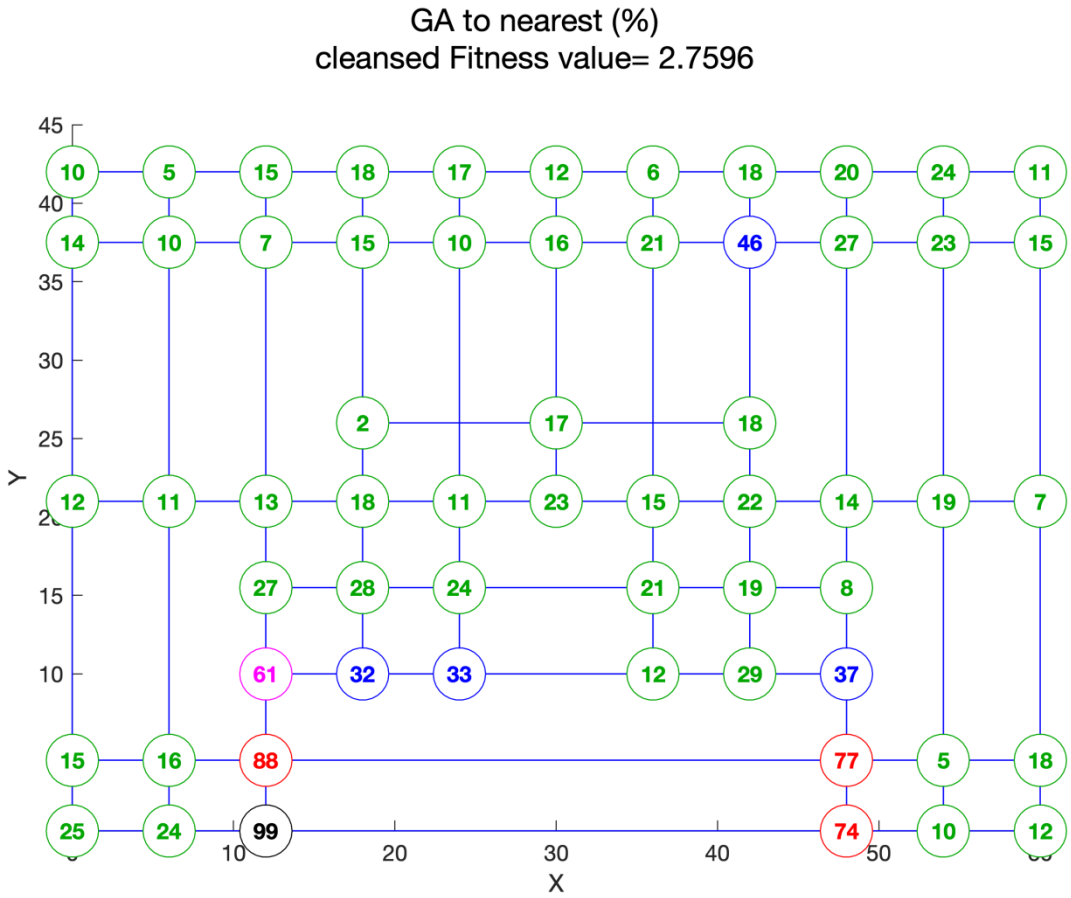
GA to nearest (%)
cleansed Fitness value= 2.7596
Y
X
45
40
35
30
25
15
10
10
20
30
40
50
10 5 15 18 17 12 6 18 20 24 11
14 10 7 15 10 16 21 46 27 23 15
2 17 18
12 11 13 18 11 23 15 22 14 19 7
27 28 24 21 19 8
61 32 33 12 29 37
15 16 88 77 5 18
25 24 99 74 10 12

DC 7 to 19

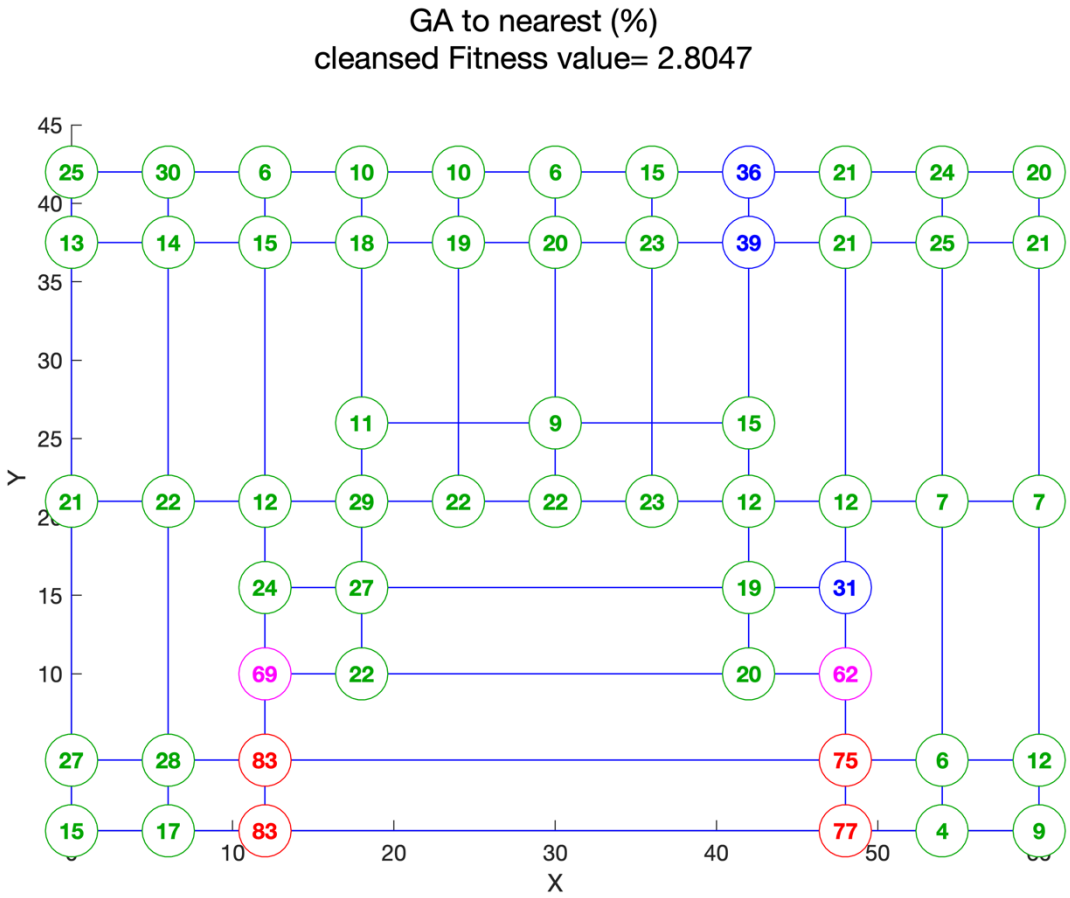
GA to nearest (%)
cleansed Fitness value= 2.8047
Y
X
45
40
35
30
25
15
10
10
20
30
40
50
25 30 6 10 10 6 15 36 21 24 20
13 14 15 18 19 20 23 39 21 25 21
11 9 15
21 22 12 29 22 22 23 12 12 7 7
24 27 19 31
69 22 20 62
27 28 83 75 6 12
15 17 83 77 4 9

DC 7 to 20

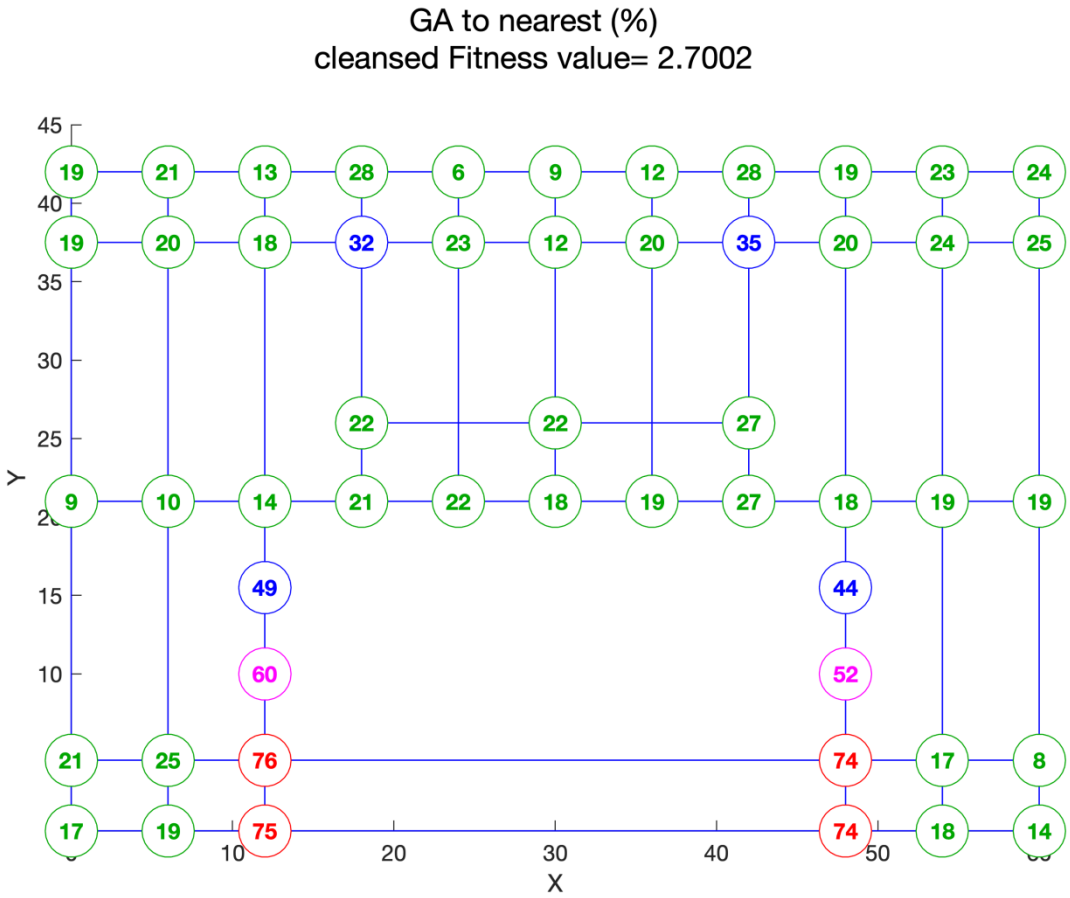
GA to nearest (%)
cleansed Fitness value= 2.7002
Y
X
45
40
35
30
25
15
10
10
20
30
40
50
19 21 13 28 6 9 12 28 19 23 24
19 20 18 32 23 12 20 35 20 24 25
22 22 27
9 10 14 21 22 18 19 27 18 19 19
49 44
60 52
21 25 76 74 17 8
17 19 75 74 18 14

APPENDIX D: OPTIMAL DAMAGE INDICES

DC1-DC2

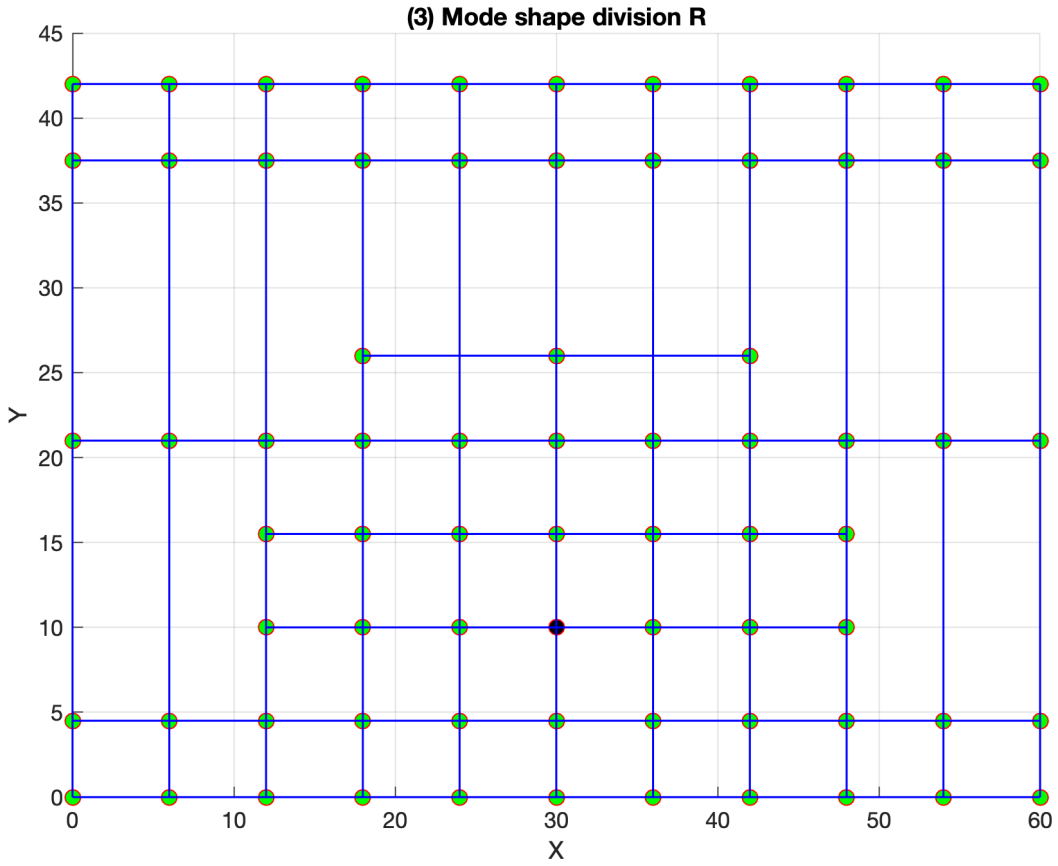
(3) Mode shape division R
45
40
35
30
25
20
15
10
5
0
Y
0
10
20
30
40
50
60
X

DC1-DC3

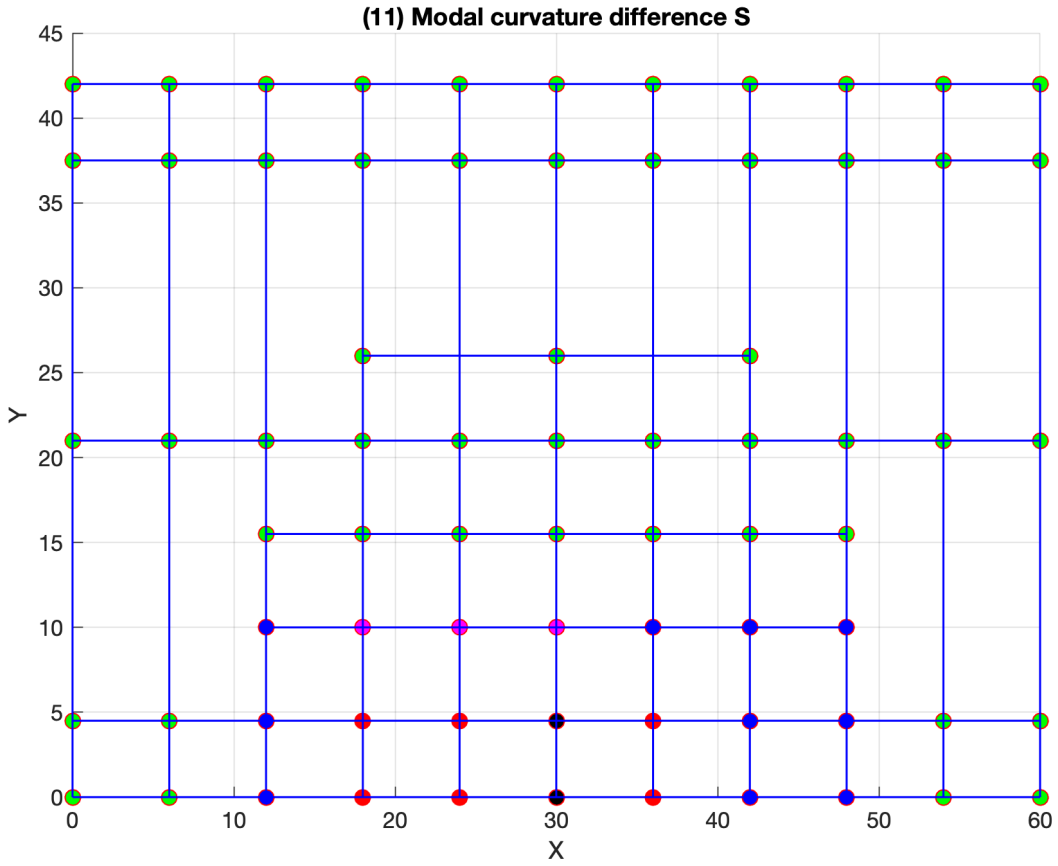
(11) Modal curvature difference S
45
40
35
30
25
20
15
10
5
0
Y
0
10
20
30
40
50
60
X

DC1-DC4

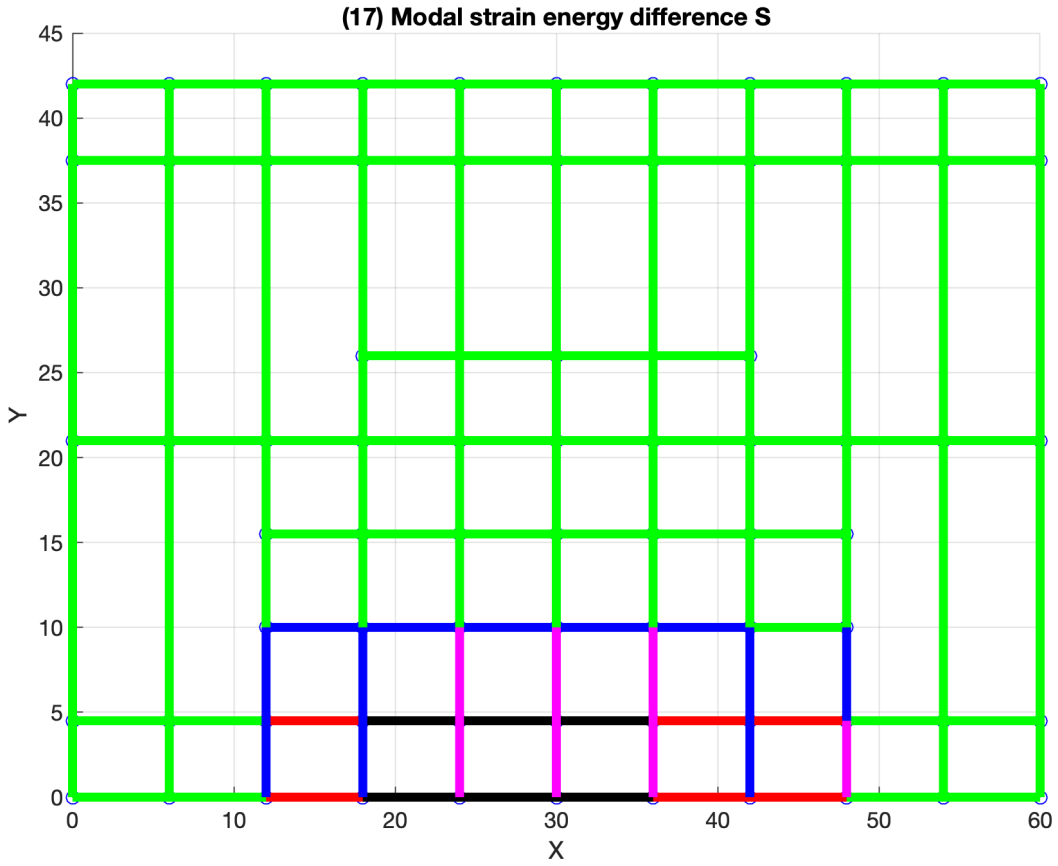
(17) Modal strain energy difference S
45
40
35
30
25
20
15
10
5
0
Y
0
10
20
30
40
50
60
X

DC1-DC5

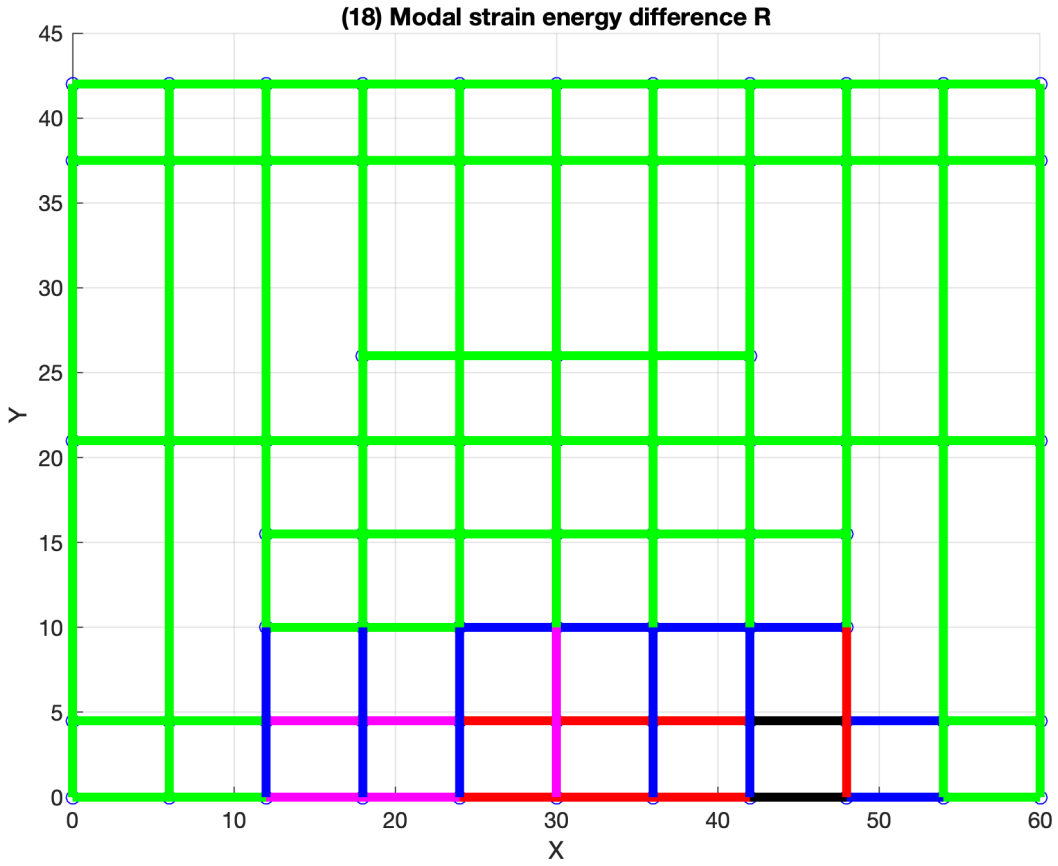
(18) Modal strain energy difference R
45
40
35
30
25
20
15
10
5
0
Y
0
10
20
30
40
50
60
X

DC1-DC6

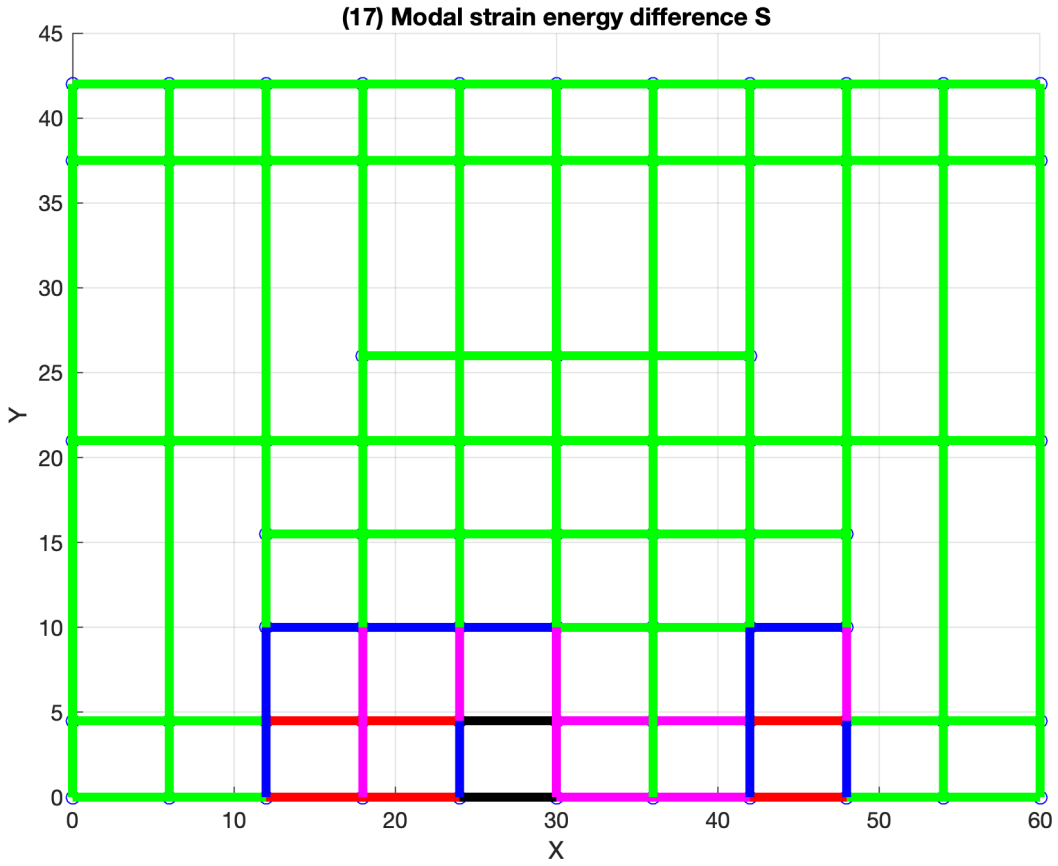
(17) Modal strain energy difference S
45
40
35
30
25
20
15
10
5
0
Y
0
10
20
30
40
50
60
X

DC1-DC7

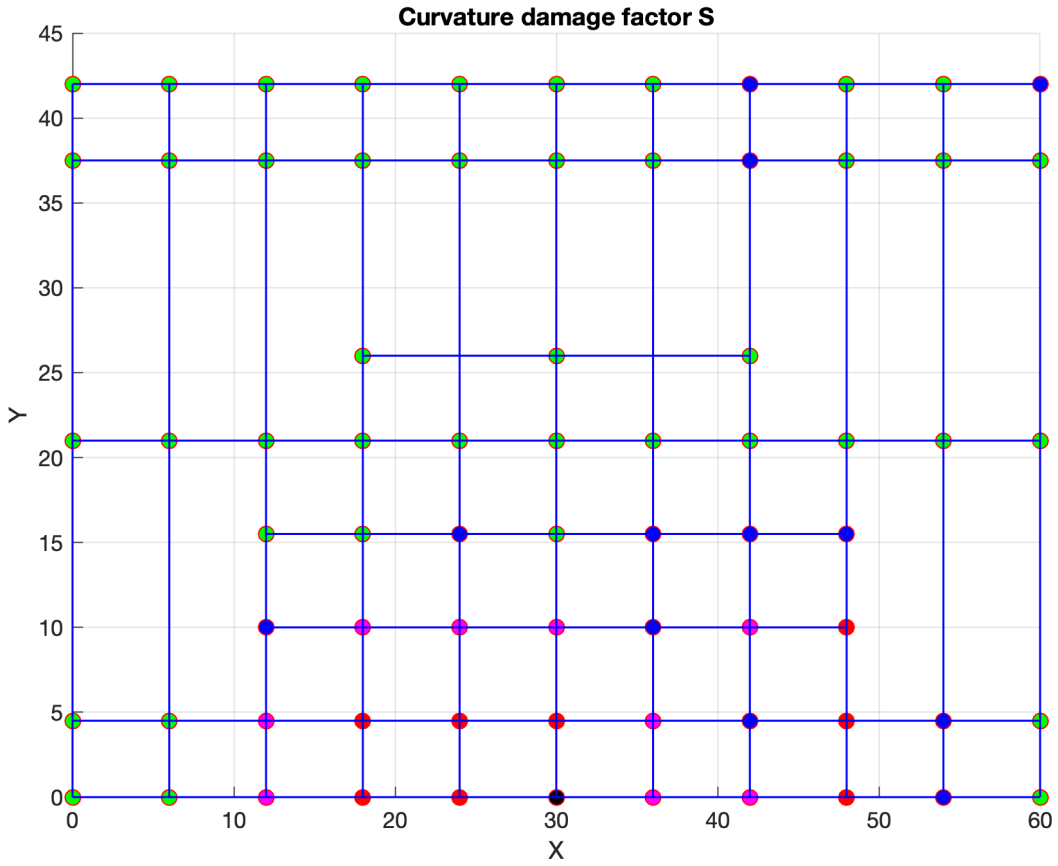
Curvature damage factor S
45
40
35
30
25
20
15
10
5
0
Y
0
10
20
30
40
50
60
X

DC7-DC8

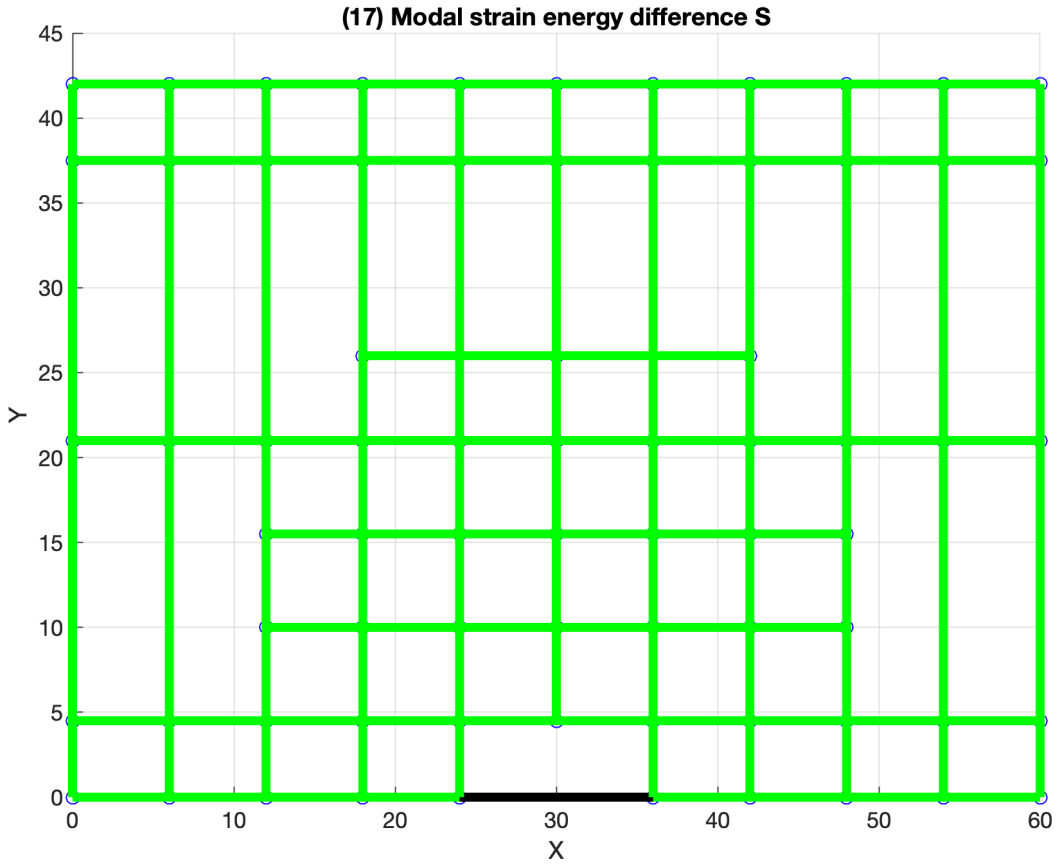
(17) Modal strain energy difference S
45
40
35
30
25
20
15
10
5
0
Y
0
10
20
30
40
50
60
X

DC7-DC9

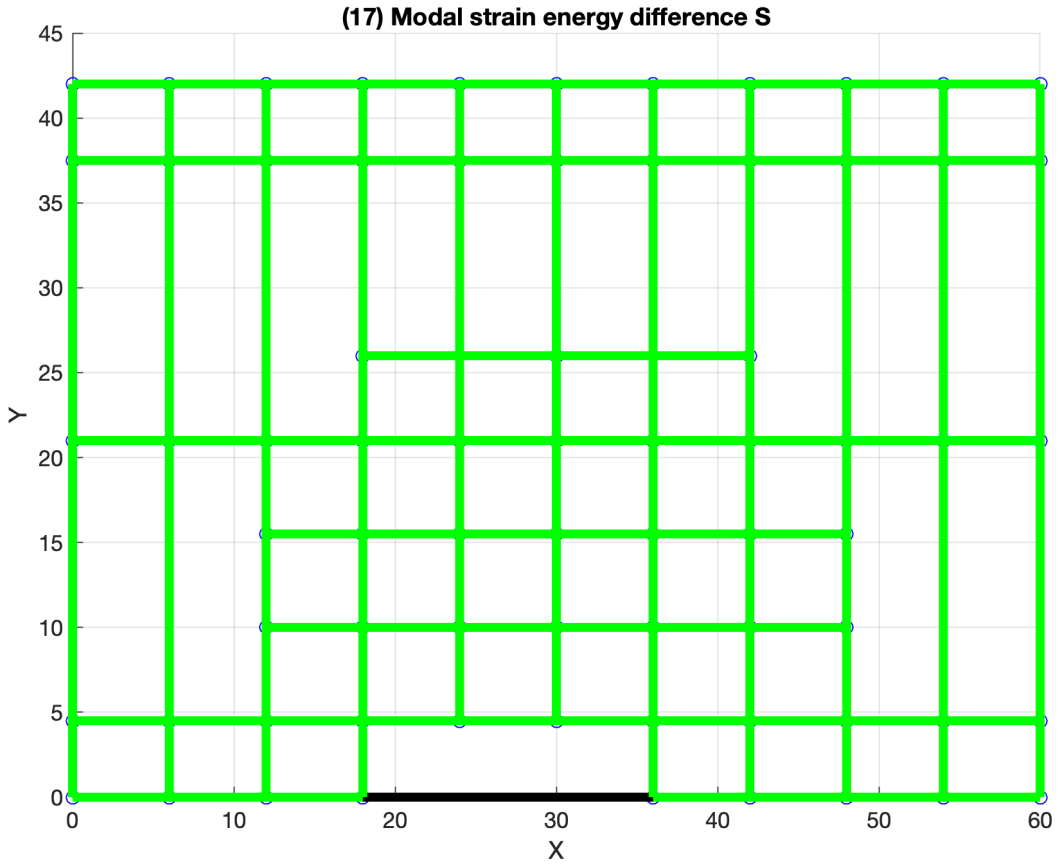
(17) Modal strain energy difference S
45
40
35
30
25
20
15
10
5
0
Y
0
10
20
30
40
50
60
X

DC7-DC10

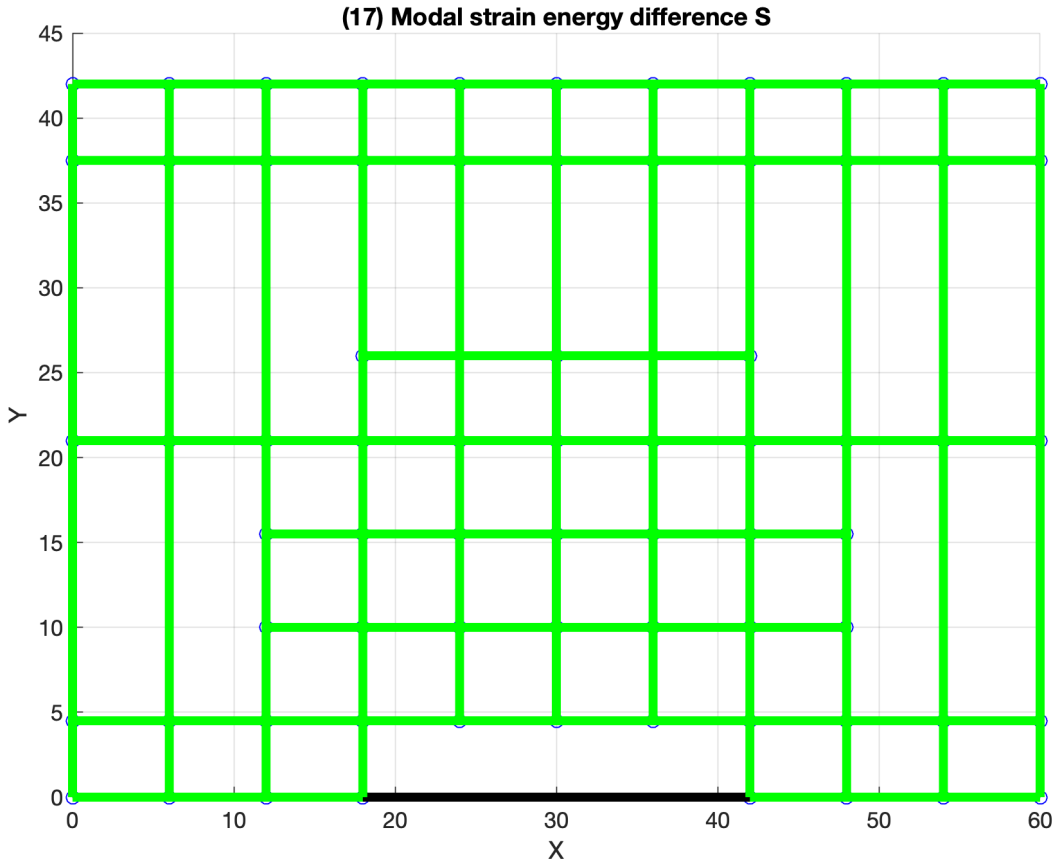
(17) Modal strain energy difference S
45
40
35
30
25
20
15
10
5
0
Y
0
10
20
30
40
50
60
X

DC7-DC11

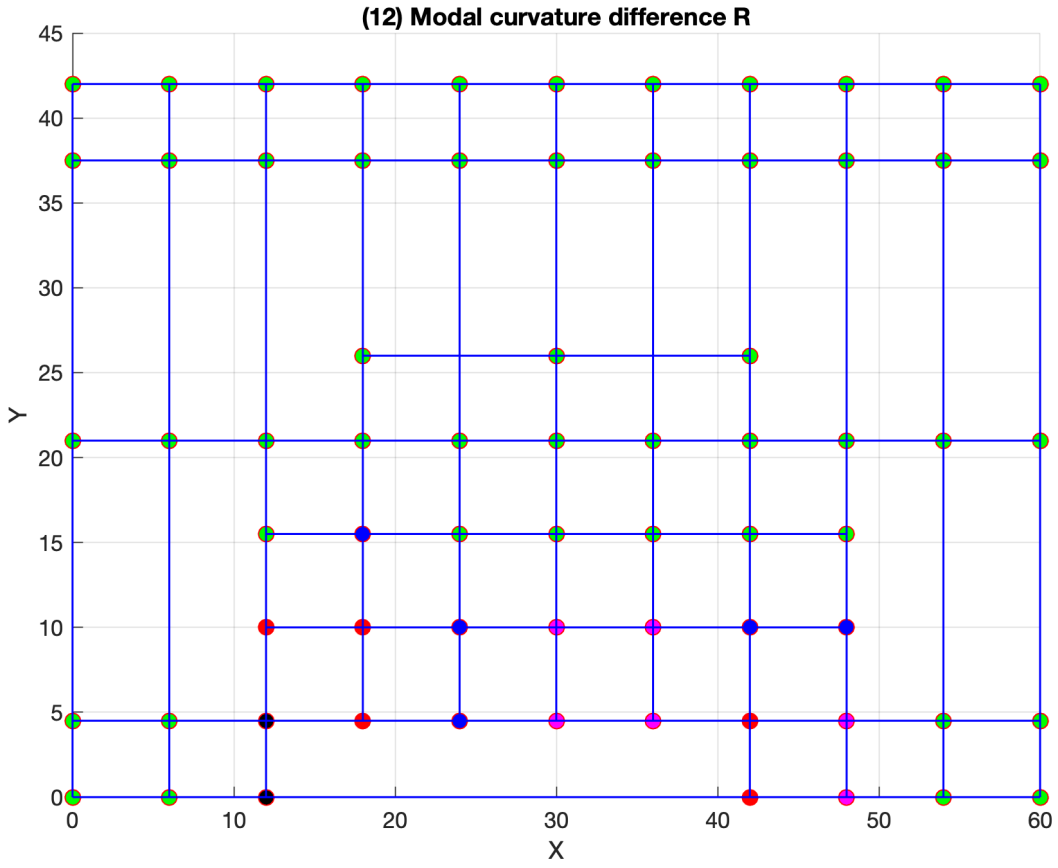
(12) Modal curvature difference R
45
40
35
30
25
20
15
10
5
0
Y
0
10
20
30
40
50
60
X

DC7-DC12

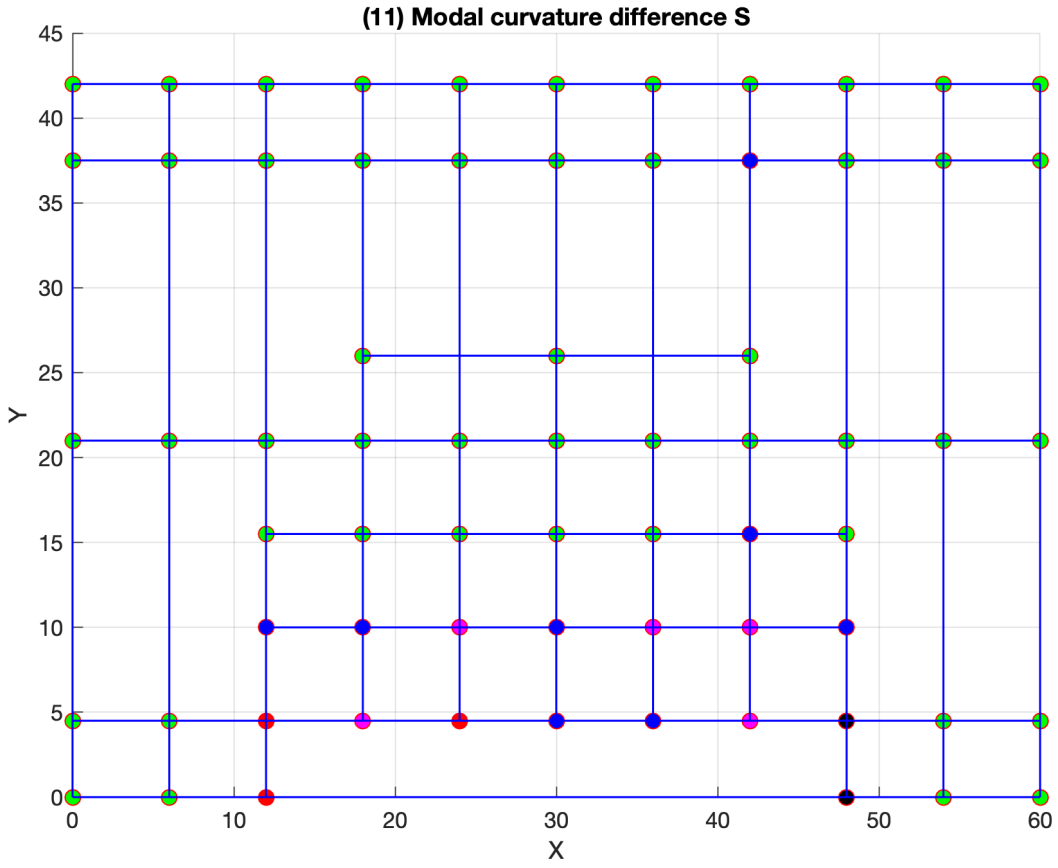
(11) Modal curvature difference S
45
40
35
30
25
20
15
10
5
0
Y
0
10
20
30
40
50
60
X

DC7-DC13

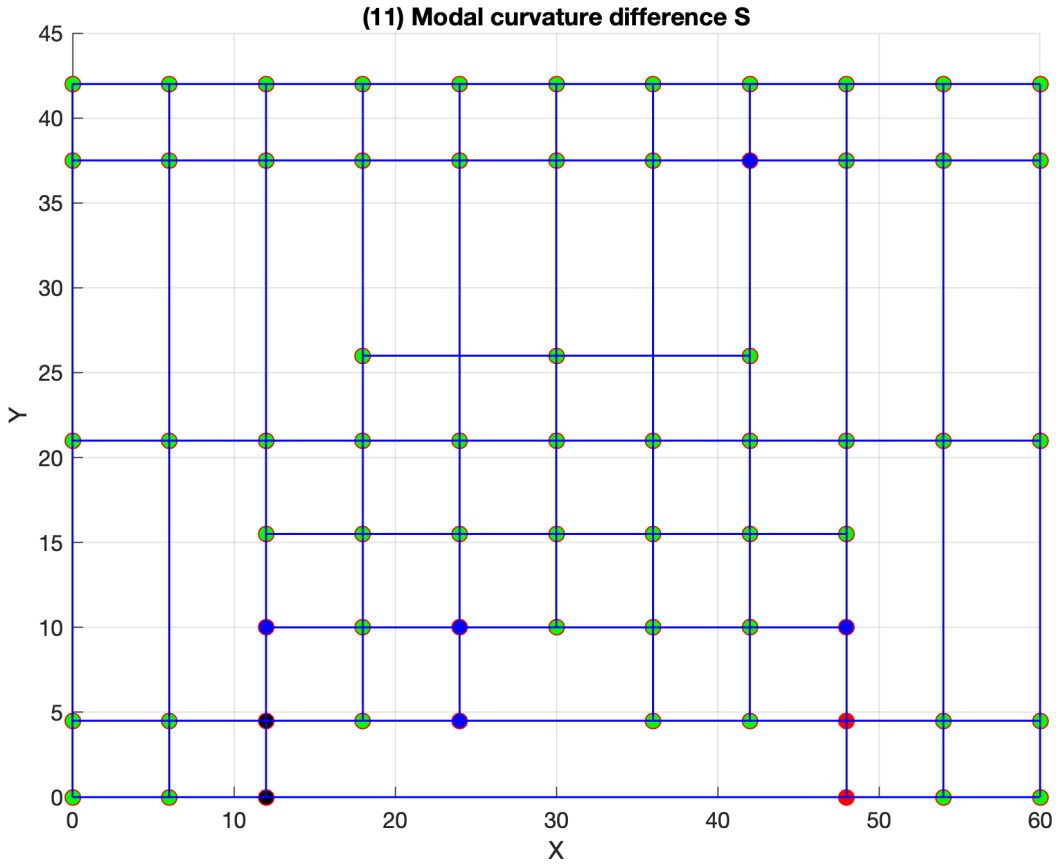
(11) Modal curvature difference S
45
40
35
30
25
20
15
10
5
0
Y
0
10
20
30
40
50
60
X

DC7-DC14

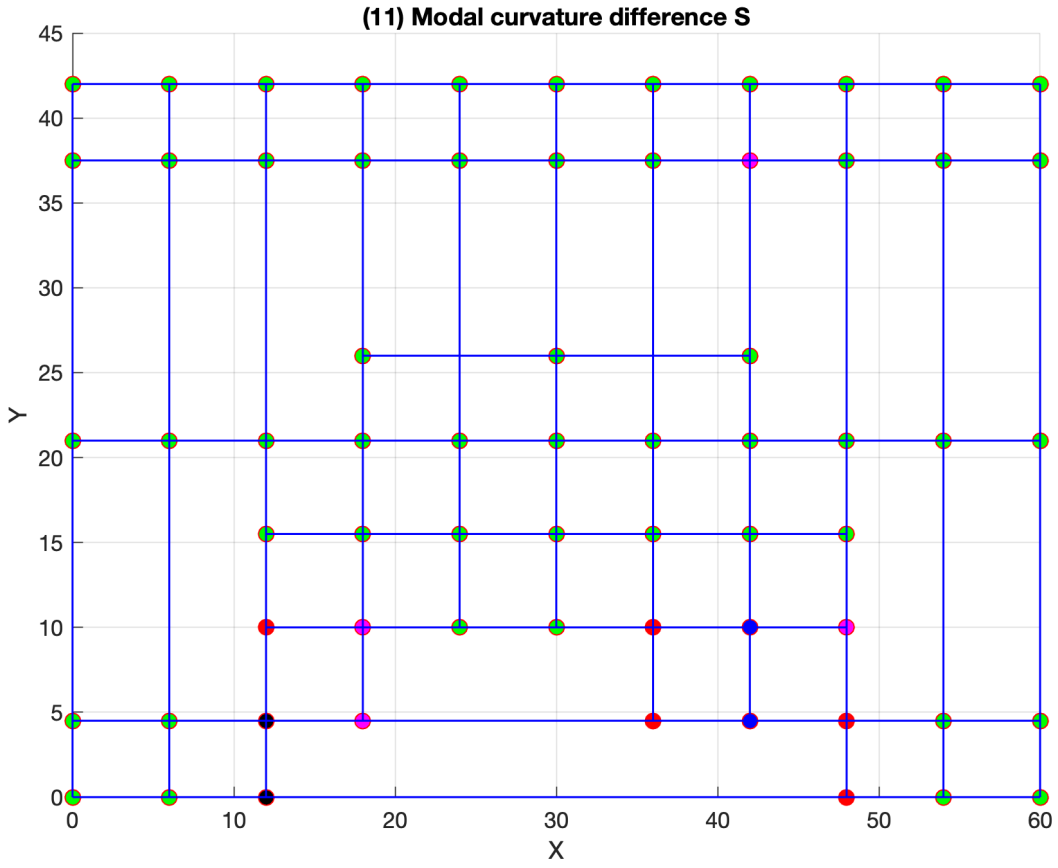
(11) Modal curvature difference S
45
40
35
30
25
20
15
10
5
0
Y
0
10
20
30
40
50
60
X

DC7-DC15

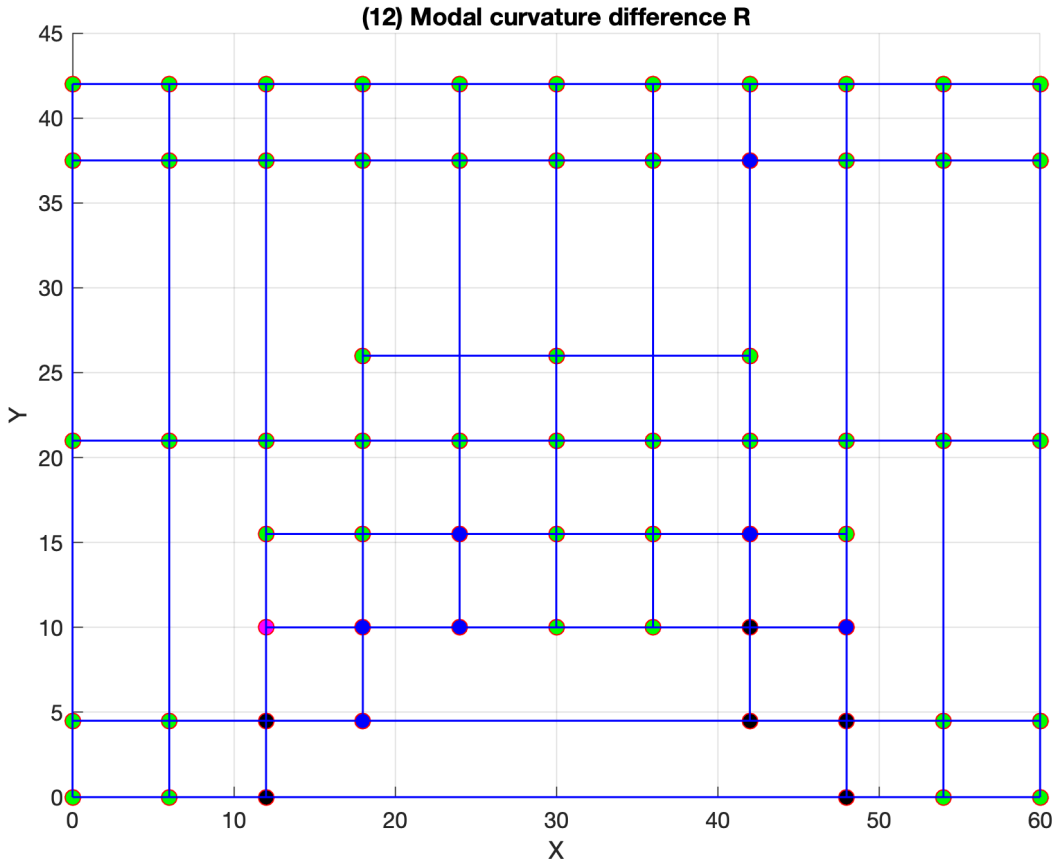
(12) Modal curvature difference R
45
40
35
30
25
20
15
10
5
0
Y
0
10
20
30
40
50
60
X

DC7-DC16

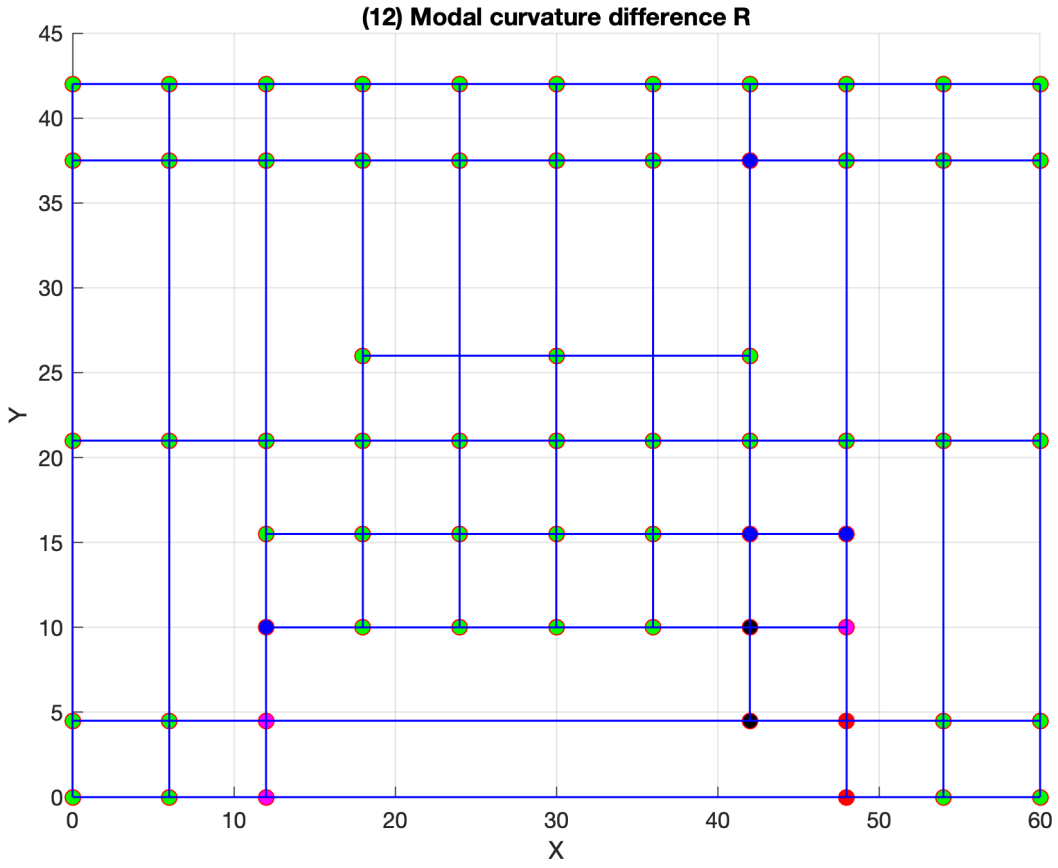
(12) Modal curvature difference R
45
40
35
30
25
20
15
10
5
0
Y
0
10
20
30
40
50
60
X

DC7-DC17

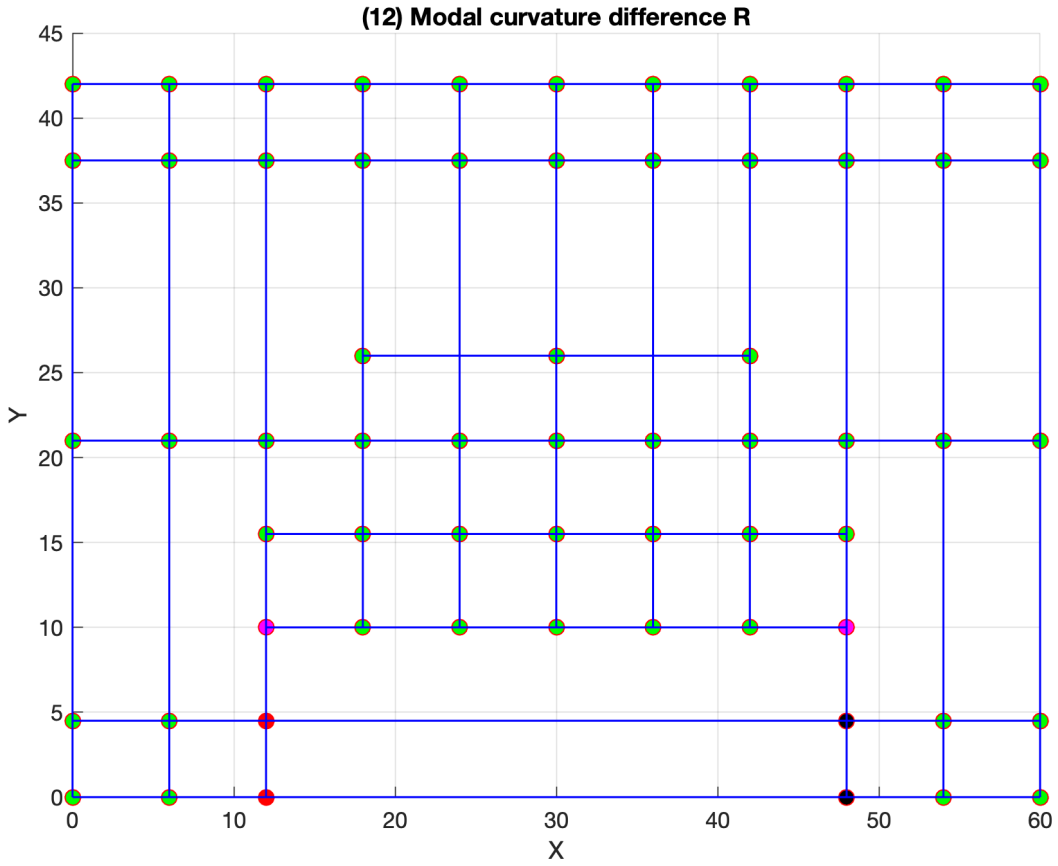
(12) Modal curvature difference R
45
40
35
30
25
20
15
10
5
0
Y
0
10
20
30
40
50
60
X

DC7-DC18

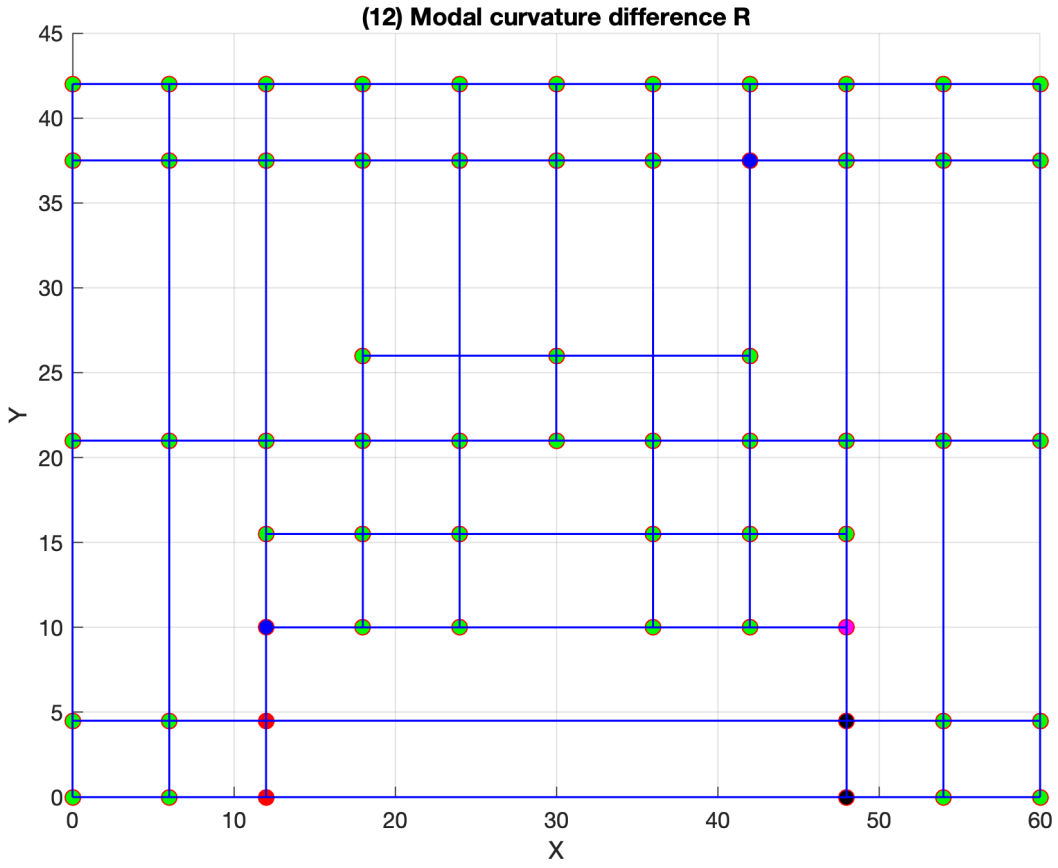
(12) Modal curvature difference R
45
40
35
30
25
20
15
10
5
0
Y
0
10
20
30
40
50
60
X

DC7-DC19

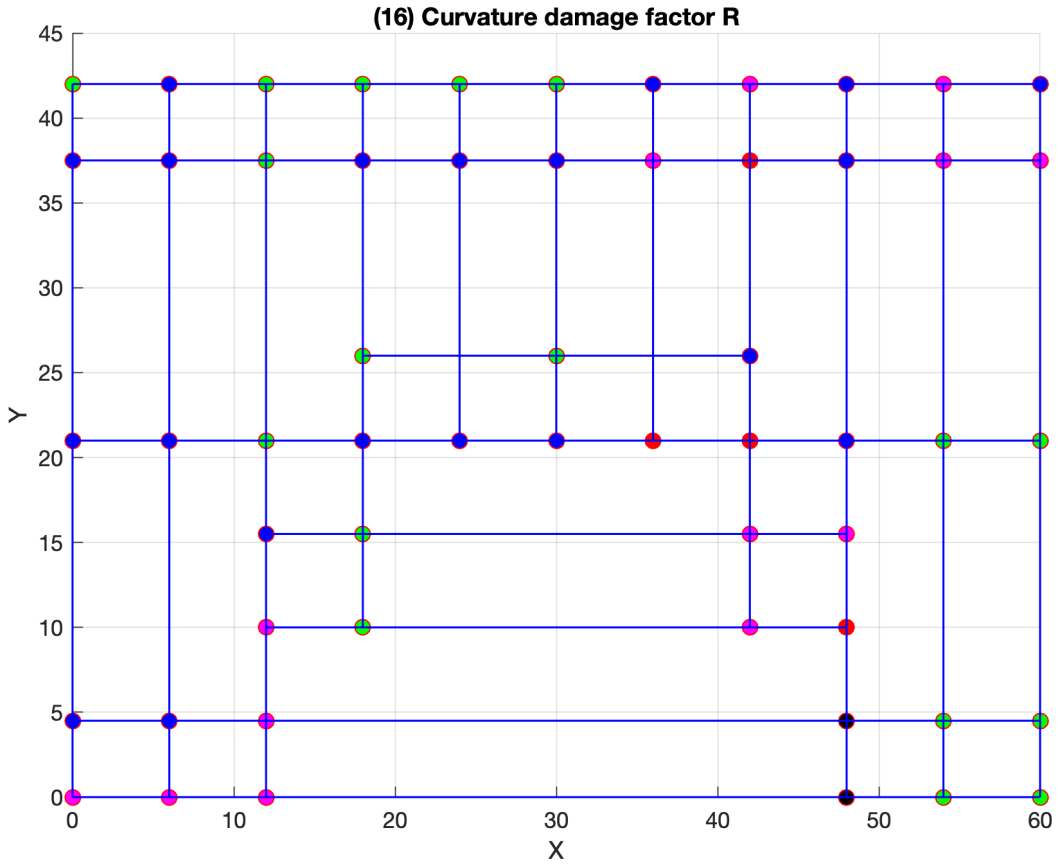
(16) Curvature damage factor R
45
40
35
30
25
20
15
10
5
0
Y
0
10
20
30
40
50
60
X

DC7-DC20

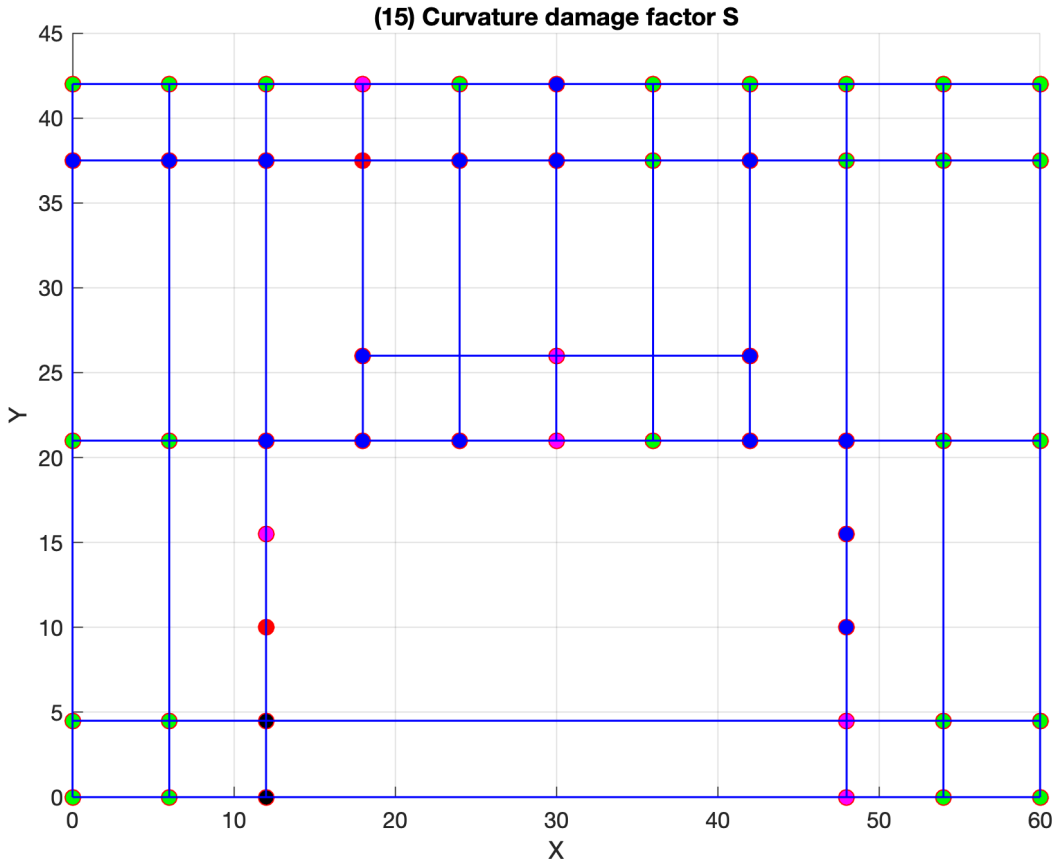
(15) Curvature damage factor S
45
40
35
30
25
20
15
10
5
0
Y
0
10
20
30
40
50
60
X

VITA

Born a Mississippian, Michael grew up in Fairhope, Alabama where he will return in order to begin work for Hargrove Engineers and Constructors in Mobile, Alabama. Michael is an Eagle Scout and graduated from high school at Bayside Academy in 2013. In, 2017 he received his Bachelors of Science degree in Civil Engineering. He passed the Fundamentals of Engineering Exam and gained his Engineering Intern status in March 2018. Two journal papers are planned come from the work in this thesis.